University of Kent

Doctoral Thesis

The Solitonic Waltz: Abelian Higgs Vortex Dynamics

Morgan Rees

A thesis submitted to the University of Kent
for the degree of Doctor of Philosophy
Mathematics

School of Mathematics, Statistics and Actuarial Science

March 2025

A long, long time ago

I can still remember how that music

Used to make me smile

And I knew if I had my chance

That I could make those people dance

And maybe they'd be happy for a while...

Don McLean

Abstract

This thesis investigates soliton dynamics in non-integrable field theories, with a primary focus on the Abelian Higgs model for vortices.

In the Baby Skyrme model, we introduce a novel family of solutions exhibiting nested ring structures with dihedral symmetry. In addition, we examine periodic solutions in cylindrical domains, enhancing the understanding of soliton solutions in two dimensions.

For the Abelian Higgs model, we develop robust numerical methods to study vortex dynamics. Our results reveal rich dynamical phenomena, such as quasi-bound states in vortex scattering and the emergence of spectral walls; a non-linear effect arising when internal modes transition to the continuous spectrum, altering vortex trajectories. Beyond critical coupling, we explore vortex interactions in Type I and Type II superconductivity, identifying attractive and repulsive regimes, uncovering non-trivial quasi-stationary states influenced by excited normal modes. Furthermore, we investigate orbiting vortex solutions, including vortex-antivortex pairs and 2-vortex systems, demonstrating sustained rotational motion induced by linear perturbations.

A significant finding is the observation of spectral walls not only in critically coupled vortices but also away from critical coupling, suggesting their broader relevance across topological field theories. These results deepen the understanding of soliton dynamics, bridging one-dimensional kinks and vortex interactions in gauge theories. The thesis concludes by proposing future research directions, including multi-vortex scattering, the role of impurities, and extensions to cosmic strings and Chern-Simons systems, laying a foundation for further exploration of soliton phenomena in theoretical and experimental contexts.

Declaration

I, Morgan John Rees, hereby declare that this thesis, entitled "The Solitonic Waltz: Abelian Higgs Vortex Dynamics", submitted for the degree of Doctor of Philosophy in Mathematics at the University of Kent, is the result of my own work and includes nothing which is the result of work done in collaboration except where specifically indicated in the text.

This thesis has not been submitted, in whole or in part, for any other degree or qualification at this or any other university or institution. The work presented herein is original, except where due acknowledgement has been made, and, to the best of my knowledge, does not contain material previously published or written by another person unless appropriately referenced.

Where applicable, I confirm that any computational code, mathematical proofs, or derivations included in this thesis are my own, unless otherwise stated. This thesis incorporates material from my publications [47, 48] co-authored with Steffen Krusch and Thomas Winyard, as well as [13] co-authored with Alberto Alonso-Izquierdo, Juan Mateos Guillarte, and Andrzej Wereszczynski, and finally [11], co-authored with Alberto Alonso-Izquierdo, Nick Manton, Juan Mateos Guillarte, and Andrzej Wereszczynski, as detailed in part III. My contributions to these works are explicitly outlined therein. All publications were submitted and published to Physical Review D.

Signed: 

Morgan John Rees

Date: 17 March 2025

Acknowledgements

First and foremost, I would like to express my gratitude to my supervisor, Steffen Krusch, who has provided excellent guidance and mentorship throughout my PhD. Thank you for always taking the time to have creative discussions with me and for helping me through every struggle. I would also like thank my second supervisor, Thomas Winyard, whose guidance has been fundamental in my journey as a researcher. Even after leaving the University, you have made time for our discussions. Both of you have encouraged me to be an independent researcher and have helped me grow as an individual. I acknowledge the UK Engineering and Physical Sciences Research Council (EPSRC) and the School of Mathematics, Statistics, and Actuarial Science at the University of Kent for a PhD studentship.

I am incredibly grateful to my better half, Mollie Tzanetis. You are my source of inspiration in all that I do. You have been there at every step of this journey and it would not have been possible without you.

An honourable mention to my big sis, Bethan Rees. Thank you for all your support, kindness and for keeping me humble in life. Thank you for being my sister.

I would like to thank my parents, Kerrie and Jason Rees, for helping me find my passion for mathematics at an early age. I am grateful to my family for all your love and support. Thank you for listening to my mathematical ramblings and doing your best to understand them.

I would like to thank my Nan, Joy Birdsey for believing in me and encouraging me to always think outside the box and beyond. I am thankful to my grandparents Hilda and Peter Saunders, you inspire and guide me more than you know.

Special thanks to my collaborators Andrzej Wereszczynski and Alberto Alonso-Izquierdo who offered many insightful discussions and opportunities to share my work.

To my friends, colleagues, and many others that I have not mentioned. Your support has meant everything to me and has been truly invaluable.

Contents

List of Tables

List of Figures

Part I

Introduction to Solitons

Chapter 1

Introduction

Solitons are stable solutions to nonlinear field equations with finite energy. We are particularly interested in field theories stabilised by a topological charge. Solitons are distinguished by their energy density being smoothly varying and localised around a specific point. An example is vortices in the Abelian Higgs model, which behave like point-like particles, or skyrmions in nuclear physics.

In this thesis, we focus on non-integrable field theories, specifically the Abelian Higgs model for vortices, which requires numerical methods to find soliton solutions.

The thesis is structured as follows. In part I we introduce soliton theory, highlighting the role of the topological charge in stabilising nonlinear field configurations. The discussion begins with one-dimensional solitons, including kinks in ϕ^4 theory and sine-Gordon kinks. The existence conditions for solitons are explored, incorporating key concepts such as topology and Derrick's theorem.

Part II explores the Baby Skyrme model, a two-dimensional analogue of the Skyrme model, which serves as a simplified framework for studying solitonic solutions. In chapter 2, we discuss the model and field equations. We discuss the Bogomolny bound and axially symmetric ring-like solutions. In chapter 3, a new family of solutions is introduced, characterised by nested ring structures that exhibit dihedral symmetry. These are compared with traditional axially symmetric ring solutions, and their energy properties are analysed. In section 4.4, we discuss Baby Skyrmions in cylindrical domains, leading to periodic solitonic structures

and an examination of infinite-charge configurations. Finally, in chapter 4, domain walls in the Baby Skyrme model are investigated, focussing on their stability, symmetry properties, and exact solutions. The findings contribute to a broader understanding of soliton interactions in non-integrable field theories.

Part III of this thesis focusses on the Abelian Higgs model, which describes vortices in a two-dimensional gauge field theory. In chapter 6, we introduce the model, followed by an exploration of the moduli space approximation and static vortex solutions. Since the field equations governing vortex dynamics are often impossible to solve analytically, numerical methods are developed and described in chapter 7. These methods include Lorentz transformations to generate boosted solutions, numerical time integration schemes for evolving vortex systems, and techniques to enforce appropriate gauge choices and boundary conditions. Particular emphasis is placed on ensuring numerical stability and accuracy, comparing results with predictions from the moduli space approximation to validate the methods.

In chapter 9, we focus on vortex scattering in the presence of excited normal modes, revealing novel dynamical features beyond the standard geodesic motion on the moduli space. The existence of quasi-bound states, where vortices undergo multiple bounces before eventually separating, is demonstrated through numerical simulations. Additionally, we observe spectral walls, a non-linear effect that alters vortex trajectories when an internal mode flows to the continuous spectrum. These results highlight the richness of vortex dynamics beyond the BPS regime and suggest deeper connections to solitonic interactions in other field theories.

In chapter 10, we move beyond critically coupled vortices, exploring vortex interactions in regimes analogous to Type I and Type II superconductivity. In the Type I regime ($\lambda < 1$), vortices exhibit attractive interactions. In the Type II regime ($\lambda > 1$), repulsive interactions dominate. We explore the impact of non-zero energy modes on vortex behaviour, finding non-trivial quasi-stationary states. Furthermore, our findings suggest the presence of spectral walls away from critical coupling.

Finally, in chapter 11, we focus on orbiting vortex solutions, where vortices undergo rotational motion around a central point. These orbits arise in various contexts,

including vortex-antivortex pairs, where mutual attraction can lead to stable rotational states. In addition, orbits are studied in 2-vortex systems, where linear perturbations induce sustained rotational motion. These findings contribute to the understanding of vortex interactions in confined geometries and suggest potential experimental realisations in condensed matter systems.

The thesis concludes in part IV with an overview of the key findings and a discussion of potential future research directions.

1.1 Soliton Theory

1.1.1 Topology

For topological solitons to exist, the solutions to a given energy functional must be continuous maps between distinct manifolds, classified by a conserved topological invariant or charge [53].

Consider two compact manifolds X and Y without boundary. If a continuous map $\phi : X \to Y$ can be continuously deformed into another map $\psi : X \to Y$, then ϕ is homotopic to ψ. This defines an equivalence relation, partitioning the maps into homotopy classes.

The set of homotopy classes of maps from X to Y is denoted $[X, Y]$. When $X = S^n$ (the n-sphere), this set is the nth homotopy group $\pi_n(Y)$, which forms a group for $n \geq 1$.

For example, if $Y = S^n$ with $n \geq 1$, then $\pi_n(S^n) \cong \mathbb{Z}$, the integers.

If $\phi : X \to Y$ is a differentiable map between oriented closed manifolds of the same dimension, the topological charge is the degree of the map,

$$B_\phi = \deg(\phi) = \int_X \phi^*(\Omega), \tag{1.1.1}$$

where Ω is the normalised volume form on Y (with $\int_Y \Omega = 1$), and ϕ^* denotes the pullback.

This degree is a homotopy invariant, taking integer values and often interpreted as a winding number in field theories.

Topological solitons arise in theories where field configurations cannot be continuously deformed to the vacuum, belonging to non-trivial homotopy classes. In flat space $\mathbb{R}^d$, boundary conditions at infinity (e.g., fields approaching vacuum values) enable compactification, allowing classification via homotopy groups such as $\pi_{d-1}(V)$ for linear target spaces V (vacuum manifold) or $\pi_d(Y)$ for nonlinear fields with closed target Y.
Examples include vortices ($\pi_1(V)$) and Skyrmions ($\pi_3(Y)$) [53].

1.1.2 Derrick's Argument

There is an additional constraint for topological solitons to exist, by means of evading Derrick's argument. Regarding field theories in flat space, for a given field configuration to be a stationary point of the energy functional, it must be stable under spatial rescaling [29].
Derrick's argument states that a field theory will not admit topological solitons if the static energy functional has no stationary points under spatial rescaling, apart from the vacuum solution. To avoid this constraint, the energy functional must contain terms that scale differently under rescaling; specifically, it must include both an expanding term (such as a potential or mass term) and a contracting term (such as a gradient or kinetic term). Without this balance, the solution would either shrink to a point or expand indefinitely. One way to evaluate an energy functional $E[\phi]$ is to consider it on a one-parameter family of field configurations $\phi^{(\lambda)}$, yielding

$$e(\lambda) = E[\phi^{(\lambda)}]. \tag{1.1.2}$$

In general, for a critical point of the energy functional, the derivative $de/d\lambda = 0$ must hold at $\lambda = 1$ (where $\phi^{(1)} = \phi$) for all such one-parameter families. This can be thought of in terms of a small deformation parameter ϵ, with $\lambda = 1 + \epsilon$ (or $\lambda = e^{\epsilon}$), and differentiating at $\epsilon = 0$, equivalent to $\lambda = 1$.
Derrick's argument arises from considering a specific one-parameter family induced by spatial scaling, $x \mapsto \lambda x$ with $\lambda > 0$, defining the rescaled field configuration as

$\phi^{(\lambda)}(x) = \phi(\lambda x)$. The energy functional evaluated on this family is

$$e(\lambda) = E[\phi^{(\lambda)}], \tag{1.1.3}$$

and the condition for a critical point is $de/d\lambda\big|_{\lambda=1} = 0$.

To derive $e(\lambda)$, consider a general static energy functional in d spatial dimensions. For simplicity, take a scalar field theory with a gradient term and a potential term:

$$E[\phi] = \int_{\mathbb{R}^d} \left(\frac{1}{2} |\nabla\phi|^2 + V(\phi) \right) d^d x = E_2[\phi] + E_0[\phi], \tag{1.1.4}$$

where $E_2[\phi] = \int \frac{1}{2} |\nabla\phi|^2 \, d^d x$ and $E_0[\phi] = \int V(\phi) \, d^d x$.

For the energy functional on the rescaled fields, first evaluate the potential term:

$$E_0[\phi^{(\lambda)}] = \int_{\mathbb{R}^d} V\left(\phi(\lambda x)\right) \, d^d x. \tag{1.1.5}$$

Make the change of variables $\tilde{x} = \lambda x$, so $d^d x = d^d \tilde{x}/\lambda^d$. This gives

$$E_0[\phi^{(\lambda)}] = \frac{1}{\lambda^d} \int_{\mathbb{R}^d} V\left(\phi(\tilde{x})\right) \, d^d \tilde{x} = \lambda^{-d} E_0[\phi]. \tag{1.1.6}$$

Now for the gradient term:

$$E_2[\phi^{(\lambda)}] = \int_{\mathbb{R}^d} \frac{1}{2} \left|\nabla\phi(\lambda x)\right|^2 \, d^d x. \tag{1.1.7}$$

Since $\nabla\phi(\lambda x) = \lambda(\nabla\phi)(\lambda x)$, we have $\left|\nabla\phi(\lambda x)\right|^2 = \lambda^2 \left|(\nabla\phi)(\lambda x)\right|^2$. Substituting the variable change,

$$E_2[\phi^{(\lambda)}] = \frac{\lambda^2}{\lambda^d} \int_{\mathbb{R}^d} \frac{1}{2} \left|(\nabla\phi)(\tilde{x})\right|^2 \, d^d \tilde{x} = \lambda^{2-d} E_2[\phi]. \tag{1.1.8}$$

Thus, the value of the energy functional on the rescaled fields is

$$e(\lambda) = \lambda^{2-d} E_2[\phi] + \lambda^{-d} E_0[\phi]. \tag{1.1.9}$$

The existence of a critical point in $e(\lambda)$ at $\lambda = 1$ determines whether stable solitons are possible. For $d = 1$, $e(\lambda) = \lambda E_2[\phi] + \lambda^{-1} E_0[\phi]$, which has a critical point at

$\lambda = \sqrt{E_0[\phi]/E_2[\phi]}$, allowing kinks. For $d > 1$, there is typically no such point unless additional terms (e.g., higher derivatives or gauge fields) are included to balance the scaling.

For a solution, the condition $\frac{de}{d\lambda}\big|_{\lambda=1} = 0$ provides virial relations, such as $(2-d)E_2[\phi] = dE_0[\phi]$ in this case.

1.2 Kinks

In this section, we will discuss some of the key concepts of topological solitons by considering 1-dimensional solitons known as kinks.

The Lagrange density admitting kink solutions is

$$\mathcal{L} = \frac{1}{2}\partial_\mu\phi\partial^\mu\phi - U(\phi), \tag{1.2.1}$$

where ϕ is a real scalar field, and the potential $U(\phi)$ is a real function with $U(\phi) \geq 0$ and multiple degenerate minima (vacua), ensuring non-trivial homotopy group $\pi_0(V)$ for the vacuum manifold $V \subset \mathbb{R}$.

To derive the Euler-Lagrange equation, we start from the action $S = \int \mathcal{L}\, d^{1+1}x$. The principle of least action requires that $\delta S = 0$ for variations $\delta\phi$. The variation of $\mathcal{L}$ is

$$\delta\mathcal{L} = \partial_\mu\phi\,\partial^\mu(\delta\phi) - \frac{dU}{d\phi}\delta\phi. \tag{1.2.2}$$

Integrating by parts on the first term gives

$$\delta S = \int \left(-\partial_\mu\partial^\mu\phi - \frac{dU}{d\phi}\right)\delta\phi\, d^{1+1}x + \text{boundary terms}, \tag{1.2.3}$$

assuming boundary terms vanish. Setting $\delta S = 0$ for arbitrary $\delta\phi$ yields the Euler-Lagrange equation

$$\partial_\mu\partial^\mu\phi + \frac{dU}{d\phi} = 0. \tag{1.2.4}$$

Kinks are finite-energy solutions to this equation that are topologically distinct from the vacuum. For finite energy, the field must approach vacua at spatial infinity, $\lim_{x\to\pm\infty}\phi(x) = \phi_\pm$ where $U(\phi_\pm) = 0$. If $\phi_+ = \phi_-$, the solution can be

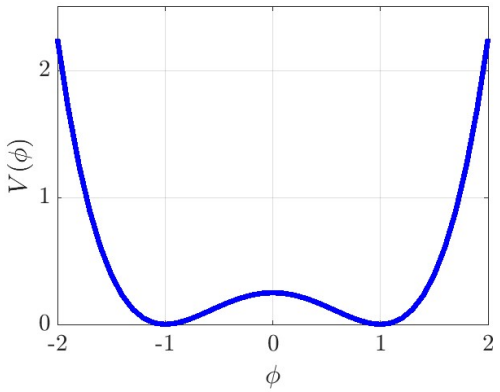

Figure 1.2.1: Potential of ϕ^4 kink, $V(\phi) = \frac{1}{2}(1-\phi^2)^2$.

continuously deformed to the constant vacuum $\phi(x) = \phi_\pm$ everywhere, making it topologically trivial.

However, if $\phi_+ \neq \phi_-$, the solution interpolates between distinct vacua, giving it topological charge and preventing continuous deformation to the vacuum. Kinks are classified by elements of $\pi_0(V) \times \pi_0(V)$.

We have a vacuum value when the potential $V = 0$, which are points forming a submanifold $\mathcal{V} \subset \mathbb{R}$, known as the vacuum manifold of the field theory. For the solution to be topologically stable, there must be multiple vacua, otherwise the homotopy group $\pi_0(\mathcal{V})$ is trivial.

We consider 1-dimensional ϕ^4 kinks as an example, the potential term is $V(\phi) = \frac{1}{2}(1-\phi^2)^2$, see figure 1.2.1. The ϕ^4 kink potential can be seen in figure 1.2.1. We can clearly see that this potential has two minima at -1 and 1 respectively, which we label as the vacua of the field.

The ϕ^4 kink solution interpolates between these vacua, so the kinks are classified by elements of $\pi_0(\mathcal{V}) \times \pi_0(\mathcal{V})$. We can then write the topological charge as

$$B_\phi = \frac{1}{2}\int_{-\infty}^{\infty} \frac{d\phi}{dx}\, dx = \frac{1}{2}\left[\phi(+\infty) - \phi(-\infty)\right], \tag{1.2.5}$$

which fits the general form $B_\phi = \deg(\phi) = \int_X \phi^*(\Omega)$ by considering the compactified real line as $X \simeq S^1$ and the target effectively as the interval between vacua, with the charge counting the net transitions between distinct components of $\mathcal{V}$.

This charge is an integer. Here, B_ϕ can only be one of three values. If $B_\phi = 0$, we have the vacuum solution; hence, the kink solution is a straight line at either

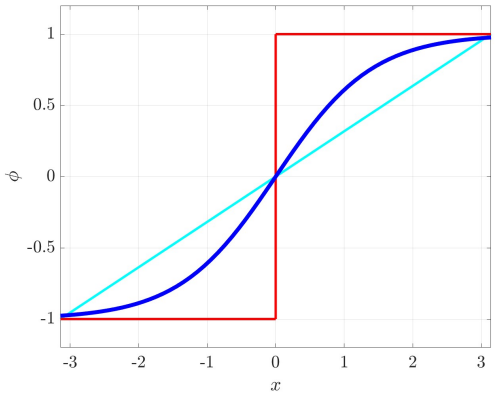

Figure 1.2.2: Exact ϕ^4 kink solution in blue, shortest path from the vacua in cyan, and vacuum values in red.

vacuum value. If $B_\phi = 1$, then the kink solution interpolates from the negative vacuum value to the positive one. Finally, if $B_\phi = -1$, we have an anti-kink that interpolates from the positive vacuum value to the negative one.

Unlike most topological systems, ϕ^4 kinks have the exact static solution of the field equation (1.2.4) for time-independent configurations,

$$\phi(x) = \tanh(x - a), \tag{1.2.6}$$

where a is a constant of integration, representing the translation symmetry of the system. We can therefore plot this solution; see figure 1.2.2. We interpolate between the two vacua in figure 1.2.2, whereby we have a non-trivial topology. We arrive at a solution which appears to be a tanh line. The solution is formulated this way because the solution is governed by both the potential term and the gradient of ϕ.

Ignoring the potential, the best solution for the kink would be the straight line from $(-1, -\infty)$ to $(+1, +\infty)$, as this would be the shortest path; however, the potential term also acts on the kink. If we study the potential in the region $\phi \in (-1, 1)$, then we can see that as ϕ approaches 0, the potential term wants to increase the slope of ϕ, however, this is battling with the straight line.

Note that ϕ^4 kink solutions take the vacuum values at $\pm\infty$, which is analogous to vortices, which are the main focus of this thesis.

The soliton also evades Derrick's theorem [29]. As derived in the general case for $d = 1$, applying a spatial rescaling to the energy functional, we obtain

$$e(\lambda) = \lambda E_2 + \lambda^{-1} E_0, \tag{1.2.7}$$

where the subscripts denote the degree of spatial derivatives for each term, $E_2 = \int \frac{1}{2} \left(\frac{d\phi}{dx}\right)^2 dx$ and $E_0 = \int V(\phi) dx$.
This has a critical point at $\lambda = \sqrt{E_0/E_2}$. For the physical solution, this occurs at $\lambda = 1$, implying the virial relation $E_2 = E_0$, which balances the expanding potential term (minimised by steep interpolation) and the contracting gradient term (minimised by shallow interpolation), resulting in a finite size for the kink.
Furthermore, the energy can be bounded below using the Bogomolny approach. Completing the square in the energy functional,

$$E = \int \left[\frac{1}{2} \left(\frac{d\phi}{dx} \mp \sqrt{2V(\phi)} \right)^2 \pm \sqrt{2V(\phi)} \frac{d\phi}{dx} \right] dx \geq \pm \int_{\phi(-\infty)}^{\phi(+\infty)} \sqrt{2V(\phi)}\, d\phi, \tag{1.2.8}$$

since the square term is non-negative. For the kink (+ sign), the bound is

$$E \geq \int_{-1}^{1} \sqrt{2 \cdot \frac{1}{2}(1-\phi^2)^2}\, d\phi = \int_{-1}^{1} (1-\phi^2)\, d\phi = \frac{4}{3}, \tag{1.2.9}$$

with equality when $\frac{d\phi}{dx} = \sqrt{2V(\phi)} = 1 - \phi^2$, which is satisfied by the exact solution $\phi = \tanh(x - a)$. Thus, the kink saturates the Bogomolny bound, confirming its stability and minimal energy for the given topological charge.

1.2.1 Sine-Gordon Kinks

We can also explore another model that admits kink solutions, known as the sine-Gordon model. Here, we have the potential, visually displayed in figure 1.2.3.

$$V(\phi) = 1 - \cos\phi. \tag{1.2.10}$$

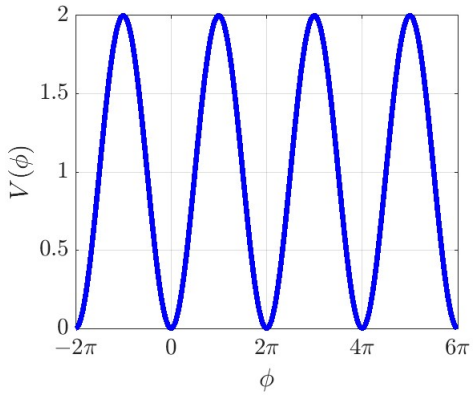

Figure 1.2.3: Plot for the potential term of the sine-Gordon kink; $V(\phi) = 1 - \cos\phi$.

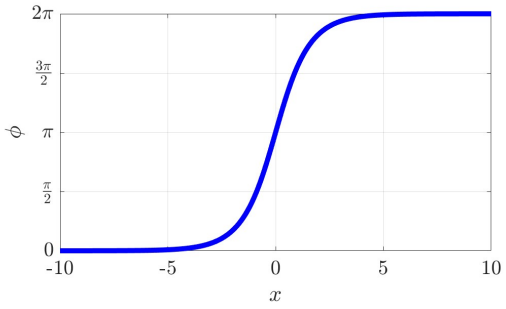

Figure 1.2.4: Degree 1 sine-Gordon kink solution.

We are interested in the sine-Gordon system as it provides a clear example of topology analogous to vortices. The Euler-Lagrange equation for static configurations is

$$\frac{d^2\phi}{dx^2} = \sin(\phi), \tag{1.2.11}$$

which has the analytical solution

$$\phi(x) = 4\arctan(e^{x-a}), \tag{1.2.12}$$

where a is a translation coordinate.

We can consider the target space as cyclic, where $\phi \in [0, 2\pi)$, and identify 0 and 2π as the same point, effectively compactifying the target to S^1.

In figure 1.2.4, we see a degree 1 solution, where $a = 0$.

We can write the topological charge as

$$\begin{aligned} B_\phi &= \frac{1}{2\pi}\int_{-\infty}^{\infty} \frac{d\phi}{dx}\, dx \\ &= \frac{1}{2\pi}\left[\phi(+\infty) - \phi(-\infty)\right] \\ &= \sum_{k=1}^{M} \text{sign}\left(\frac{\mathrm{d}\phi}{\mathrm{dx}}(\mathrm{x_k})\right), \end{aligned} \tag{1.2.13}$$

where M is the number of preimages x_k of a regular points in the target space (e.g., a point not at vacua). This can be interpreted as counting the signed preimages of ϕ at these points x_k. We can therefore see that the kink solution in figure 1.2.4 is indeed of degree 1 by the use of (1.2.13), and counting the preimages of ϕ.

We impose a one-point compactification by identifying spatial infinities, hence the domain becomes topologically a circle S^1. We can transform our target space by considering the periodic potential. In the case of the sine-Gordon model, our potential is periodic, hence we can compactify the target space to the unit 1-sphere such that, $\phi_\pm = \lim_{|x|\to\pm\infty} \phi(x) = 2\pi n$ for integer n.

This gives us a map from a circle to a circle; hence, we can interpret the winding number as the number of times the domain circle wraps around the target circle. This leads to the interpretation that the winding number is determined by considering the homotopy group of the map. Since we have constricted our map to the circle, we consider the homotopy group $\pi_1(S^1) = \mathbb{Z}$, hence we can interpret the degree as an integer winding number.

Note that this is analogous to Baby Skyrmions, which we discuss next.

Part II

Baby Skyrmions

Chapter 2

The Baby Skyrme Model

2.1 Introduction

The Baby Skyrme model is a 2-dimensional analogue of the Skyrme model, which is a (3+1)-dimensional model for pions, first introduced by T.H. Skyrme [65], which is a low energy effective model for the high quark colour limit of quantum chromodynamics (QCD).

The motivation for Baby Skyrmions is as a toy model for the Skyrme model, whereby calculations and numerical simulations are simplified by dimensional reduction. Terms of the model are chosen based on the components of the Lagrangian in the Skyrme model; however, it is worth noting that the potential term is not needed in the Skyrme model, and hence its choice is solely based on the stability of the theory and the solutions it presents.

Another interpretation of the model is as a stabilisation of the $O(3)$ sigma model, whereby the introduction of a Skyrme term and potential term balance to stop the soliton from expanding infinitely or shrinking to a localised point. This is achieved by evading Derrick's theorem, as the sigma model term is scale-invariant in two dimensions, while the Skyrme term (quartic in derivatives) scales as λ^{-2} under rescaling (contracting against shrinkage), and the potential term scales as λ^2 (expanding against growth), providing a stable minimum at finite scale.

In recent years, there has been a growing interest in Baby Skyrmions in condensed matter systems, where they have been observed in various materials, namely in the

context of magnetic systems. In this case, the model often features an additional Dzyaloshinskii-Moriya interaction (DMI) term, which can induce topologically stable spin textures analogous to Skyrmions. The inclusion of the DMI term stabilises the configuration by breaking the inversion symmetry [24, 32, 43, 82].

In addition, there has been some interest in Baby Skyrmion lattices [52], whereby the lattice structure formed by Baby Skyrmions under various potential terms is discussed. It is demonstrated that different potentials lead to distinct crystalline arrangements, such as hexagonal and square lattices. Alternative potential choices, such as the easy plane potential, have also been shown to break the residual $SO(2)$ symmetry and produce solitons with only discrete symmetry [44]. Furthermore, the study of Baby Skyrmions in curved backgrounds, such as anti-de Sitter space, has revealed that higher charge solutions form concentric ring-like layered structures, with transitions between different numbers of layers occurring at specific topological charges [31, 79]. Similar layered structures have been studied in the full Skyrme model using rational map methods, whereby multi-shell configurations can be constructed from multiple rational maps [57].

The particular model under consideration in this part includes the potential term $V(\phi) = (1-\phi_3^2)$ [78]. We aim to study a new family of solutions of the Baby Skyrme model that admits a dihedral symmetry. Historically, solutions of this model have displayed axial symmetry for all charges. The introduction of dihedral symmetry could provide new insights into the underlying topological and geometric properties of Baby Skyrmions, and might have broader implications in the context of condensed matter systems. Previous work on breaking the global $O(3)$ symmetry to the dihedral group D_N has demonstrated that soliton solutions exhibit a constituent structure composed of topologically confined partons [40, 45]. The statics and dynamics of such broken symmetry models reveal that multi-soliton solutions are related to polyform structures, with scattering behaviour governed by parton interactions [40].

2.2 The Model

The Baby Skyrme model is given by the Lagrangian density

$$\mathcal{L} = \frac{1}{2}\partial_\mu\phi \cdot \partial^\mu\phi - \frac{1}{4}(\partial_\mu\phi \times \partial_\nu\phi) \cdot (\partial^\mu\phi \times \partial^\nu\phi) - V(\phi), \tag{2.2.1}$$

where ϕ is the 3-component scalar Baby Skyrme field, and $V(\phi)$ is the potential term. The first term is known as the sigma term and contains terms up to second degree in derivatives, the second term is known as the Skyrme term, motivated by the Skyrme term of the Skyrme model and contains terms of degree 4 in derivatives. The Lagrangian functional is $L = \int \mathcal{L}\, d^2x$, and the action $S = \int L\, dt$.

We seek only static solutions of the equations of motion, which are obtained by varying the Lagrangian density eq. (2.2.1) with respect to the field ϕ. We obtain the Euler-Lagrange equations of motion by calculating the variation of (2.2.5).

The resulting field equations, projected orthogonal to ϕ due to the constraint $\phi \cdot \phi = 1$, are

$$\phi \times \left(\partial^\mu\partial_\mu\phi - \partial_\mu \left[(\partial^\mu\phi \cdot \partial^\nu\phi)(\partial_\nu\phi) - (\partial_\nu\phi \cdot \partial^\nu\phi)(\partial^\mu\phi) \right] - \frac{\partial V}{\partial \phi} \right) = 0. \tag{2.2.2}$$

The field ϕ is defined on (2+1)-dimensional spacetime, where ϕ is a map $\phi : X \to Y$, where the domain $X = \mathbb{R}^2$, and the target $Y = \mathbb{R}^3$, since we represent ϕ with a 3 component unit vector. A one point compactification of the domain space defines a point at $\pm\infty$ which is mapped to the vacuum value. By including a point at infinity, the domain becomes $\mathbb{R}^2 \cup \{\infty\}$ which is isomorphic to the unit 2-sphere. We constrain ϕ to the 2-sphere by imposing the normalisation $\phi \cdot \phi \equiv \phi_1^2 + \phi_2^2 + \phi_3^2 = 1$. We hence have that $X \cong \mathbb{R}^2 \cup \{\infty\} = S^2$, and $Y = S^2$, and $\phi : S^2 \to S^2$. $\dim X = \dim Y = 2$, hence ϕ is classified by the homotopy group $\pi_2(S^2) = \mathbb{Z}$.

The topological charge is defined by the integral of the pullback of the normalised volume form on S^2

$$B = \int_{\mathbb{R}^2} \phi^*\Omega = -\frac{1}{4\pi} \int_{\mathbb{R}^2} \phi \cdot (\partial_1\phi \times \partial_2\phi)\, d^2x, \tag{2.2.3}$$

Additionally, we impose that both X and Y are path-connected such that we can connect any two points with a path that stays in the manifold, i.e. the image of X always lies on a path-connected component of Y.

We choose a point $y \in Y$, whereby the set of preimages of y is defined by the points on X mapped to y. We define this as a set of isolated points $\{x^{(1)}, \ldots, x^{(M)}\}$, where M is the number of preimages $x^{(k)}$, such that at each point, the Jacobian of the map is non-zero.

The topological charge can also be interpreted as

$$B = \deg(\phi) = \sum_{k=1}^{M} \text{sign}(J(x^{(k)})), \tag{2.2.4}$$

where J is the determinant of the Jacobian matrix of all first-order partial derivatives. We hence count the signs of the Jacobian, that is, we count the preimages of ϕ including multiplicity.

The energy functional we are interested in is a map E from the space of field configurations to $\mathbb{R}$ $E : \phi \to \mathbb{R}$ defined by the integral

$$E[\phi] = \int \left[\frac{1}{2}[(\partial_1 \phi)^2 + (\partial_2 \phi)^2] + \frac{1}{2}(\partial_1 \phi \times \partial_2 \phi)^2 + m^2 V(\phi) \right] d^2x, \tag{2.2.5}$$

where x_1, x_2 are spatial coordinates, ϕ is a scalar field, and $V[\phi]$ is the potential. In this chapter, we use the potential term introduced by [78]

$$V(\phi) = m^2(1 - \phi_3^2), \tag{2.2.6}$$

This choice of potential depends only on ϕ_3, so we break the $O(3)$ symmetry of the model to an $O(2)$ symmetry.

For topological solitons to exist, the theory must evade Derrick's theorem. We can apply a Derrick's scaling argument to the energy functional. Consider a spatial rescaling such that $x \to \lambda x$, with $\lambda > 0$, and hence we get the expression for the rescaled energy as

$$e(\lambda) = \lambda^2 E_0 + E_2 + \lambda^{-2} E_4, \tag{2.2.7}$$

where $E_0 = \int m^2(1-\phi_3^2)\, d^2x$ is the potential term, $E_2 = \int \frac{1}{2}(\partial_i \phi)^2\, d^2x$ is the sigma

term, and $E_4 = \int \frac{1}{2}(\partial_1\phi \times \partial_2\phi)^2 \, d^2x$ is the Skyrme term, with E_n denoting the term of the energy functional that is of degree n in its derivatives. We hence have that

$$\frac{de}{d\lambda}\Big|_{\lambda=1} = \lambda E_0 - \lambda^{-1} E_4 = 0, \tag{2.2.8}$$

leading to the constraint that, in order for the soliton solution to be stable, the energy contributions of the Skyrme term and potential term must be equal for $\lambda > 0$. This constraint allows us to assess the validity of our numerical calculations, as we can calculate these energy contributions, and stable solutions only exist for $E_0[\phi] = E_4[\phi]$.

2.3 Bogomolny Bound

We will study later in Chapter 4.4 a lower bound derived from periodic boundary conditions; however, we can impose another well-studied lower bound on the energy known as the Bogomolny bound.

We can then rewrite the static energy functional eq. (2.2.5)

$$\begin{aligned} E &= \frac{1}{2}\int (\partial_1\phi)^2 + (\partial_2\phi)^2 d^2x + \frac{1}{2}\int (\partial_1\phi \times \partial_2\phi)^2 d^2x + \int m^2 V(\phi) d^2x, \\ &\geq \frac{1}{2}\int (\partial_1\phi)^2 + (\partial_2\phi)^2 d^2x. \end{aligned} \tag{2.3.1}$$

We can then write vector ϕ in terms of its components,

$$E = \int \frac{1}{4}\Big[(\partial_i\phi_a + \epsilon_{abc}\epsilon_{ij}\phi_b\partial_j\phi_c)(\partial_i\phi_a + \epsilon_{agh}\epsilon_{ik}\phi_g\partial_k\phi_h) \pm \partial_i\phi_a\epsilon_{abc}\epsilon_{ij}\phi_b\partial_j\phi_c - \partial_i\phi_a\epsilon_{agh}\epsilon_{ik}\phi_g\partial_k\phi_h\Big] d^2x. \tag{2.3.2}$$

where $a, b, c, g, h \in \mathbb{Z}_3$, and $i, j, k \in \mathbb{Z}_2$, and ϵ_{ij} is the 2-dimensional Levi-Civita symbol, defined as $\epsilon_{12} = 1$, $\epsilon_{21} = -1$, and 0 if indices repeat.

To derive a lower bound, we complete the square in the sigma and Skyrme terms:

$$\begin{aligned} E &= \int \frac{1}{4}\left[(\partial_i\phi \pm \epsilon_{ij}\phi \times \partial_j\phi) \cdot (\partial_i\phi \pm \epsilon_{ik}\phi \times \partial_k\phi)\right] d^2x \pm \int \frac{1}{2}\epsilon_{ij}\phi \cdot (\partial_i\phi \times \partial_j\phi)\, d^2x \\ &\geq \frac{1}{2}\int \partial_i\phi \cdot (\epsilon_{ij}\phi \times \partial_j\phi) d^2x \\ &= \int \phi \cdot (\partial_i\phi \times \partial_j\phi)\, d^2x = 4\pi|B|, \end{aligned} \tag{2.3.3}$$

where the Levi-Civita tensor $(a \times b)_i = \epsilon_{ijk} a_j b_k$ can be written as a cross product on S^2 since it is the Lie algebra of $SO(3)$.

The energy of a Baby Skyrmion exceeds this lower bound, tending towards 4π as $m \to 0$. It however cannot attain this bound as the mass term is required for stable solutions and the size of the solution becomes infinite in the limit. We choose $m^2 = 0.1$ throughout this chapter to stay consistent with the literature.

2.4 Static Solutions

This model was previously studied in [78], whereby the solutions studied admit an axial symmetry for all charges. These solutions are given by the axially symmetric ansatz

$$\phi = \begin{pmatrix} \phi_1 \\ \phi_2 \\ \phi_3 \end{pmatrix} = \begin{pmatrix} \sin f \cos(B\theta) \\ \sin f \sin(B\theta) \\ \cos f \end{pmatrix}, \tag{2.4.1}$$

where $f(\rho)$ is the monotonically decreasing profile function in polar coordinates (ρ, θ), with boundary conditions $f(0) = \pi$ and $f(\infty) = 0$, and B is the topological charge. It should be noted that this ansatz is stable for all B, as shown in [78] unlike the standard model with potential with only one vacuum. This ansatz can be substituted into the energy functional to reduce the dimensionality of the problem. Moreover, we can use the ansatz as an initial configuration to simulate axially symmetric lumps or rings of energy in a 2-dimensional space. We then use an arrested Newton flow algorithm, see chapter 7, to vary the fields using the equations of motion to converge to a solution with a minimised energy density.

Some examples of minimised energy solutions for two-dimensional axial rings are displayed as a heat plot for the energy density in figure 2.4.1.

We observe that the axial rings increase with size as the topological charge increases; however, the energy decreases per soliton. At higher charges, the axial rings grow larger and the cost of the curvature of the rings decreases, resulting in an exponential tail in the energy per soliton values, which can be seen in figure 3.3.5.

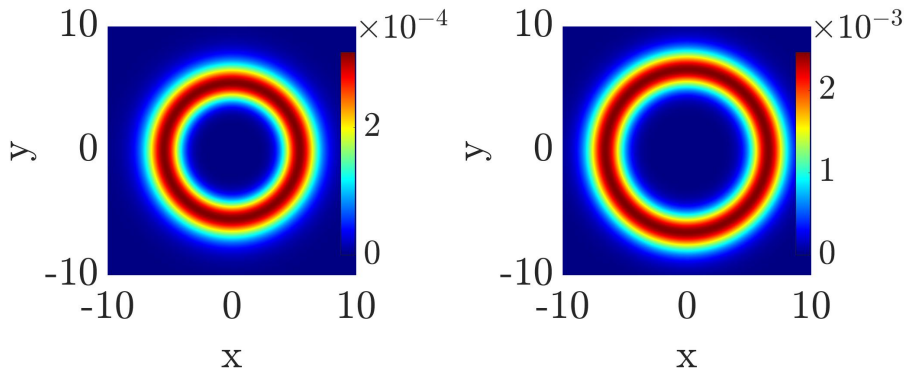

$B = 4$.

$B = 5$.

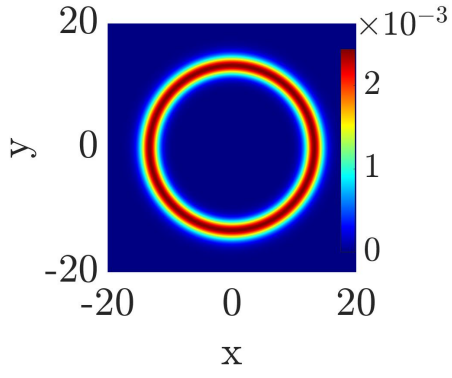

$B = 10$.

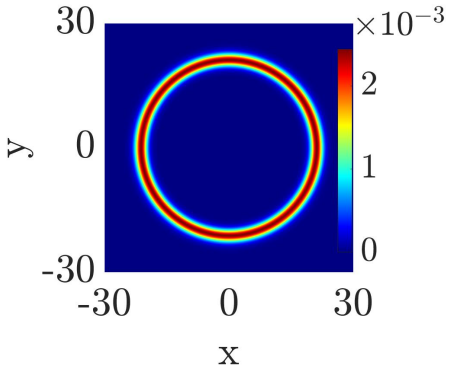

$B = 16$.

Figure 2.4.1: Heat plots for the minimised Energy Density for a sample of topological charges B, found under the axially symmetric ansatz. We find that the energy per soliton decreases as the total topological charge of the solution increases, as a result of the increasing size of the solutions, resulting in a lower energy cost from the curvature of the solution.

Chapter 3

Multi-Layered Rings

3.1 Introduction

In this chapter, we explore a new family of solutions of the Baby Skyrme model with two vacua. We introduce a configuration with nested layers of rings in which the solutions appear to admit dihedral symmetry. We compare the previously studied axial solutions to this new family of solutions.

3.2 Dihedral Solutions

We choose an initial configuration that places N charge 1 lumps in a circle, with the phase orientated so that they are all facing the origin. This initial configuration allows our 2-dimensional algorithm to find a critical point of the energy functional that differs from the axially symmetric solution. For example, see in figure 3.2.1 a new $B = 5$ solution.

The phase in the 2-dimensional plane, shown in the right of figure 3.2.1 is calculated as

$$\theta = \tan^{-1}\left(\frac{\phi_2}{\phi_1}\right) = \begin{cases} \tan^{-1}\left(\frac{\phi_2}{\phi_1}\right), & \phi_1 > 0; \\ \tan^{-1}\left(\frac{\phi_2}{\phi_1}\right) + \pi, & \phi_1 < 0 \text{ and } \phi_2 \geq 0; \\ \tan^{-1}\left(\frac{\phi_2}{\phi_1}\right) - \pi, & \phi_1 < 0 \text{ and } \phi_2 < 0; \\ \frac{\pi}{2}, & \phi_1 = 0 \text{ and } \phi_2 > 0; \\ -\frac{\pi}{2}, & \phi_1 = 0 \text{ and } \phi_2 < 0; \\ \text{undefined}, & \phi_1 = 0 \text{ and } \phi_2 = 0. \end{cases} \tag{3.2.1}$$

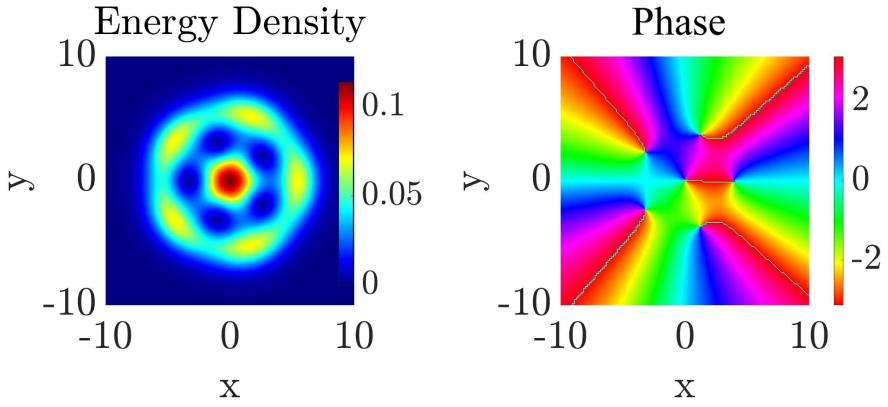

Figure 3.2.1: Heat plot for the minimised energy solution (left) of the Euler-Lagrange equations and phase coloured plots to indicate winding (right) for a $B = 5$ solution.

where ϕ_1 and ϕ_2 are the corresponding components of the vector field ϕ, and undefined indicates that this computation is not possible. We see that the phase of the solution is distributed between the different layers, indicating that the topological charge is also distributed between the layers. This particular solution hence has $B = 1$ in the centre and $B = 4$ in the outer layer.

The energy per soliton of the $B = 5$ solution, shown on the left of figure 3.2.1 is $E = 1.4245$ (normalised by the Bogomolny bound), larger than that of the axial ring, hence this solution is a local minimum of the energy functional.

To confirm that the field ϕ has dihedral symmetry, we must show invariance under a symmetry pair consisting of a spatial rotation and an isorotation. Specifically, apply a spatial rotation S: $\theta \to \theta + \beta$, where $\beta = \frac{2\pi}{B}$, which transforms the ansatz eq. (2.4.1) to

$$\phi' = \begin{pmatrix} \sin f \cos(B(\theta+\beta)) \\ \sin f \sin(B(\theta+\beta)) \\ \cos f \end{pmatrix}.$$

This is equivalent to the original ϕ after an isorotation $R\phi$, where R is the SO(3) rotation matrix around the ϕ_3-axis by $-B\beta$:

$$R = \begin{pmatrix} \cos(-B\beta) & -\sin(-B\beta) & 0 \\ \sin(-B\beta) & \cos(-B\beta) & 0 \\ 0 & 0 & 1 \end{pmatrix} = \begin{pmatrix} \cos(2\pi) & \sin(2\pi) & 0 \\ -\sin(2\pi) & \cos(2\pi) & 0 \\ 0 & 0 & 1 \end{pmatrix} = I,$$

since $B\beta = 2\pi$. Thus, $\phi' = R\phi = \phi$, confirming rotational invariance under the pair (S, R).

We can plot the field values, see figure 3.2.2, and perform an $SO(3)$ rotation as a linear combination of the field components. This shows us that the fields are invariant under a chiral rotation.

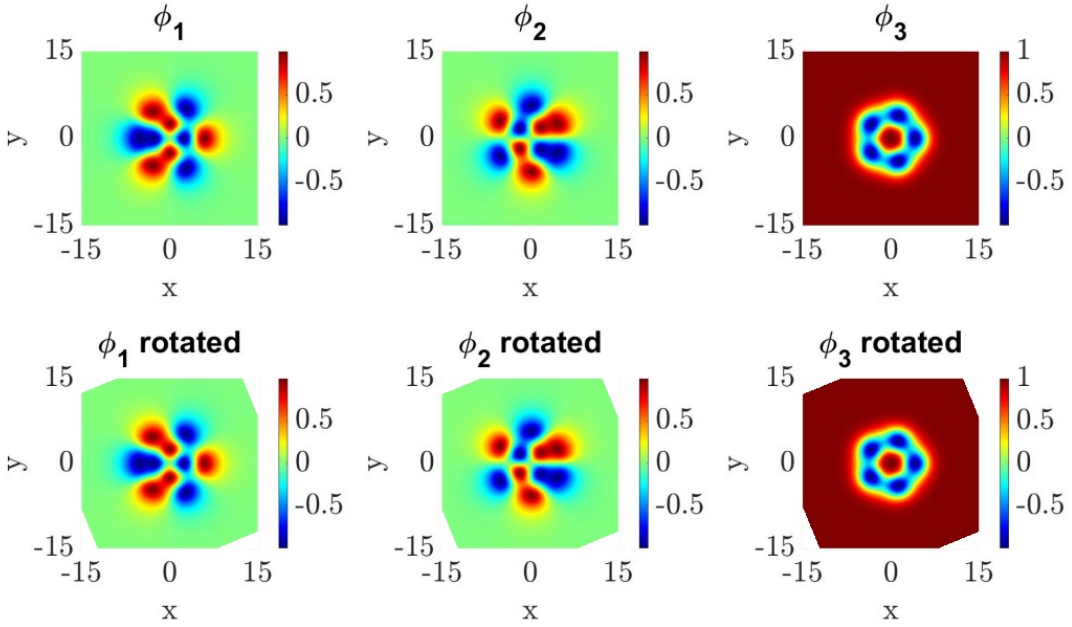

Figure 3.2.2: Heat plot for the field values of the minimised solution of the equations of motion for charge B = 5 solution, admitting a dihedral symmetry.

We can similarly verify that the Baby Skyrme solution to the energy functional allows for a Z_2 symmetry with the spatial reflection $\theta \to -\theta$, which can be shown by the global reflection

$$(\phi_1, \phi_2, \phi_3) \to (\phi_1, -\phi_2, \phi_3), \tag{3.2.2}$$

or alternatively

$$\tilde{\phi} = \begin{pmatrix} \sin(f)\cos(B(-\theta)) \\ \sin(f)\sin(B(-\theta)) \\ \cos(f) \end{pmatrix} = \begin{pmatrix} \sin(f)\cos(B\theta) \\ -\sin(f)\sin(B\theta) \\ \cos(f) \end{pmatrix}, \tag{3.2.3}$$

since sine is anti-symmetric and cosine is symmetric.

Thus we confirm that this solution has dihedral symmetry D_5, since the dihedral group can be expressed as $D_n \cong C_n \rtimes \mathbb{Z}_2$.

3.2.1 Initial Configuration

We have identified new local minimum solution of the energy functional. In this section, we aim to generate these dihedral solutions, such that we can choose the charges of the layers of the solution.

Therefore, let us consider the initial configuration

$$\phi = (\phi_1, \phi_2, \phi_3) = \begin{cases} (\sin f \cos(-B_1\theta), \sin f \sin(-B_1\theta), \cos f), & \rho < \rho_0; \\ (\sin f \cos(B_2\theta), \sin f \sin(B_2\theta), \cos f), & r_0 \leq \rho \leq \rho_1; \\ (0, 0, 1), & \rho > \rho_1. \end{cases} \tag{3.2.4}$$

We simulate an inner ring of topological charge B_1, and an outer ring of topological charge B_2 that winds in the opposite direction. Note that $f(\rho) = 0$ for $\rho > \rho_1$, hence here $\phi = (0, 0, 1)$. (ρ, θ) are polar coordinates, ρ_0, ρ_1 are constants chosen such that there is enough space for the ring to exist in the space, and $f(\rho)$ is a profile function, denoted by the map, $f : \mathbb{R} \to \mathbb{R}$, such that

$$f(\rho) = \begin{cases} 2\pi - \pi\frac{\rho}{\rho_0}, & \rho < \rho_0; \\ \pi - \pi\frac{\rho - \rho_0}{\rho_1 - \rho_0}, & \rho_0 \leq \rho \leq \rho_1; \\ 0, & \rho > \rho_1, \end{cases} \tag{3.2.5}$$

where the profile function, f, winds around the target space for the number of layers. We denote a charge B solution as a (B_1, B_2) solution.

This continuous model is discretised using a finite lattice of size 600×600, suitably large such that the asymptotic energy cutoff is negligible, with a fixed step size in space of $h = 0.2$ in both the x_1 and x_2 directions. A step size of this magnitude was chosen because it allows for suitable accuracy without significantly increasing the run time of the simulations. Moreover, the derivatives were approximated using a finite-difference scheme of 4^{th} order. Note that larger solutions were computed on sufficiently large grids; however, in all cases, the figures presented have been truncated to provide a clear result.

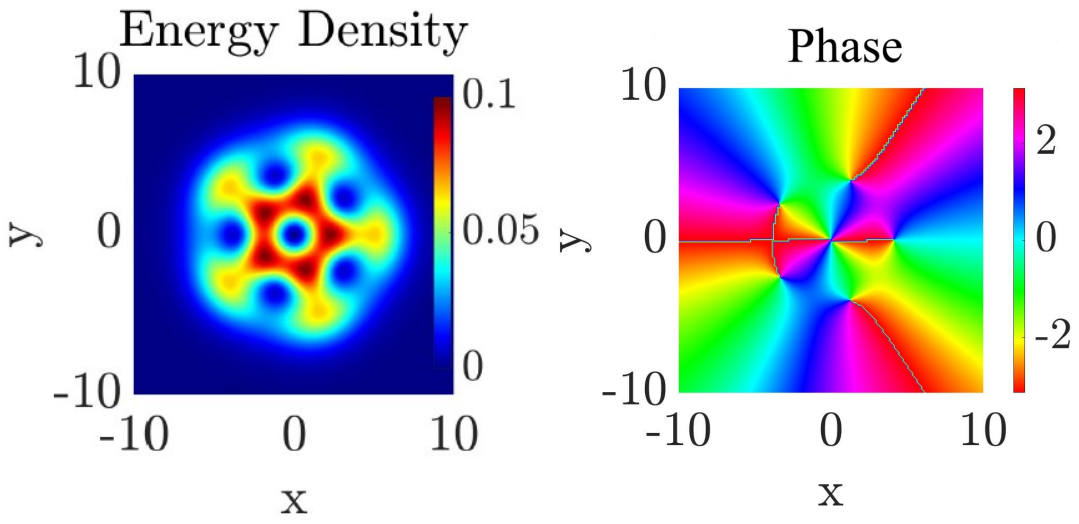

Figure 3.3.1: Heat plot for the minimised energy solutions of the equations of motion and phase coloured plots to indicate winding, respectively of a $(2,3)$ solution created using the new initial condition (3.2.4).

3.3 Results

3.3.1 Low charge solutions and Symmetries

In the previous section, we have shown a $(1,4)$ solution (see figure 3.2.1). Using eq. (3.2.4) as an initial configuration, we find another $B = 5$ solution. The solution is still only a local minimum, but we discover that many configurations of the same overall topological charge may exist. Figure 3.3.1 shows a $(2,3)$ solution which has the highest energy out of all $B = 5$ solutions, however, it is interesting to study as the energy density also appears to admit a dihedral symmetry in this case.

The energy per soliton of the $(2,3)$ solution is $E = 1.4693$, and the energy per soliton of the axially symmetric $B = 5$ solution is $E = 1.3737$. The axial ring is the global minimum at this charge, but within the new family of solutions, the $(1,4)$ ring is the local minimum.

Next, we consider a charge $(2,4)$ solution.

We conjecture that we can understand the symmetry of the solution by plotting the phase (as given in eq. (3.2.1) against the domain angle θ, the angle in the $2D$ domain at fixed radius ρ, which determines the angular position along a circle in the Baby Skyrmion's domain. We observe this for a charge (2,4) solution in figure 3.3.4.

We see that there are 6*crossings*. This suggests that there are six localised points where the energy is minimal, which we can interpret as a reason for the $B = 6$ solutions

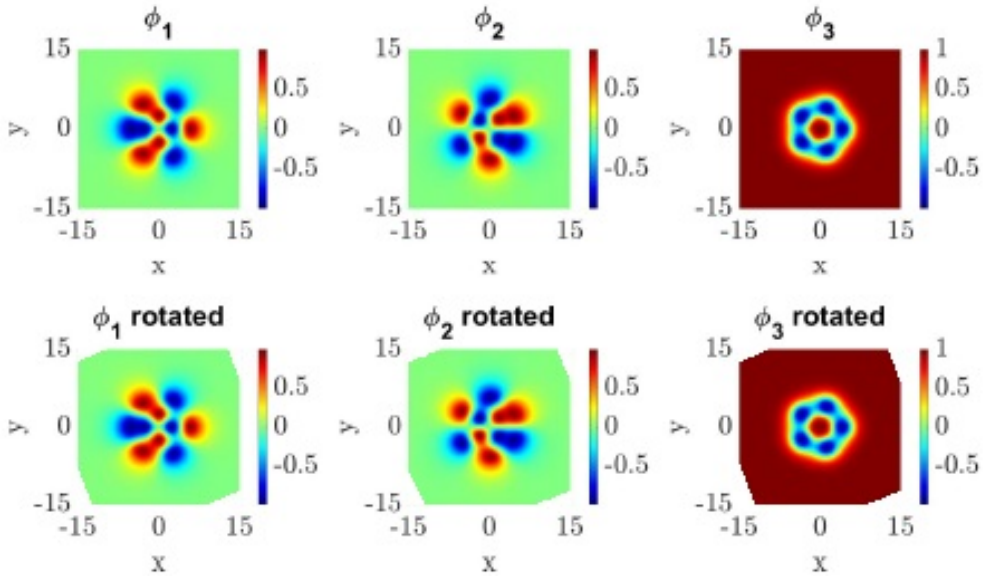

Figure 3.3.2: Heat plots for the field values for a $(2, 3)$ solution to illustrate the invariance of the fields under a dihedral symmetry.

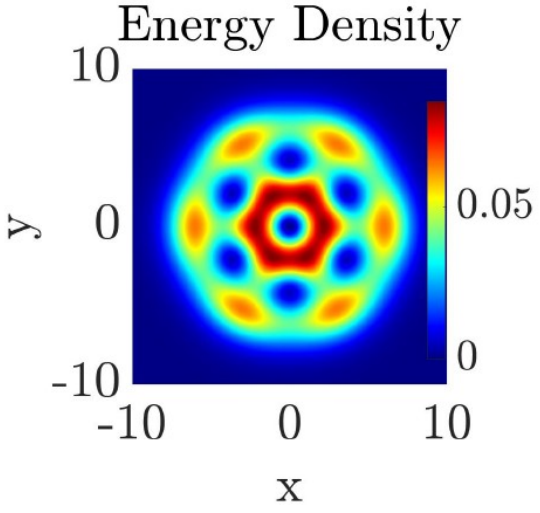

Figure 3.3.3: Heat plot for the energy density of a $(2, 4)$ solution with energy per soliton $E = 1.4183$. This figure shows the 2 inner layers of the 4 layered solution figure 5.2, which has a lower energy per soliton than this solution. This provided promise for the energy being reduced by the attraction of the layers.

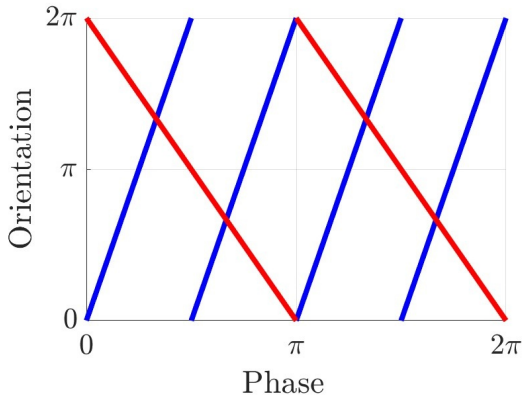

Figure 3.3.4: Plot to illustrate an explanation for the symmetry of a $(2, 4)$ solution. The phase of the inner ring is shown in blue, and the phase of the outer ring is shown in red, where the phase is calculated in eq. (3.2.1) and plotted against the domain angle θ, which determines the angular position along a circle in the Baby Skyrmion's domain. This figure shows that there are 6 localised points where the inner and outer rings are in phase with each other. It follows that the energy density has lumps of energy at these localised points, whereby the inner and outer rings pass in and out of phase.

B	E_{axial}	$(1, B-1)$	$(2, B-2)$	$(3, B-3)$	$(4, B-4)$	$(5, B-5)$
4	*1.3798*	**1.4595**	N/A	N/A	N/A	N/A
5	*1.3737*	**1.4245**	1.4693	N/A	N/A	N/A
6	*1.3703*	**1.4097**	1.4183	N/A	N/A	N/A
7	*1.3683*	1.4017	**1.3954**	1.4335	N/A	N/A
8	*1.3669*	1.3962	**1.3859**	1.4002	N/A	N/A
9	*1.3660*	1.3919	**1.3817**	1.3841	1.4135	N/A
10	*1.3654*	1.3887	1.3792	**1.3771**	1.3902	N/A
11	*1.3649*	1.3861	1.3774	**1.3743**	1.3783	1.4013
12	*1.3645*	-	1.3758	1.3729	**1.3727**	1.3841
13	*1.3642*	-	-	-	**1.3705**	1.3746

Table 3.1: Energy per baryon for the historically studied axial solutions versus new dihedral symmetric solutions for topological charges $B = 4$ to $B = 13$. Italic entries indicate axial solutions, bold entries indicate local minimum of new solutions.

admitting dihedral D_6 symmetry, and similarly for all B.

3.3.2 Energy Comparisons for Different Solutions

We compare the energy per soliton for axially symmetric and dihedral solutions across various topological charges B. Table 3.1 summarises these results.

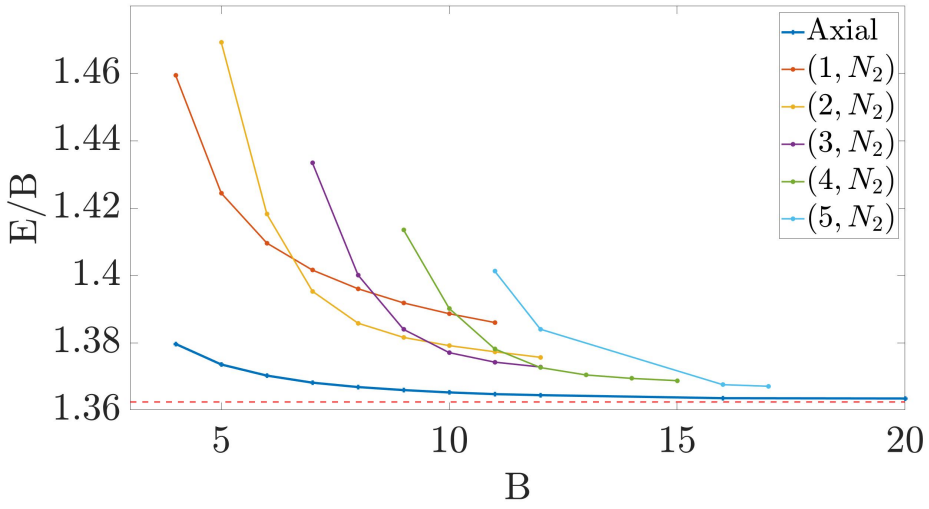

Figure 3.3.5: Energy per baryon of axial configuration vs. multiple nested rings with 2 layers. This figure plots the data of table 3.1. The dotted red line indicates a lower bound for the energy per baryon of the axial rings, calculated using an infinite domain wall on a cylinder, which is synonymous to a ring of infinite curvature.

We can see from figure 3.3.5 that the global minimum is an axial ring for all charges studied so far, however, it is interesting that as the charge of the total configuration increases, the minimum of the nested rings change so that the charge of the inner ring increases when the difference between the charges of the 2 rings is too great.

3.3.3 B = 9 Family of Solutions

We can also study the charge $B = 9$ configurations, to give an example of how the same overall charge configurations differ from each other, see figure 3.3.6.

For the nested ring solutions with two layers, the size of the solution is smaller, hence the contribution from the curvature is larger than that of an axial solution of the same size. At low charges, it is clear that the minimised energy is dominated by the contribution of the curvature. However, we have an attraction between the layers that pull them together, as a result of the inner and outer layers moving in and out of phase with each other, creating localised lumps of energy, thus a dihedral symmetry for the solution.

This attraction reduces the total energy of the solution. The smaller the difference between the charges of the layers, the smaller the solution, and hence the larger the cost of the curvature of the solution.

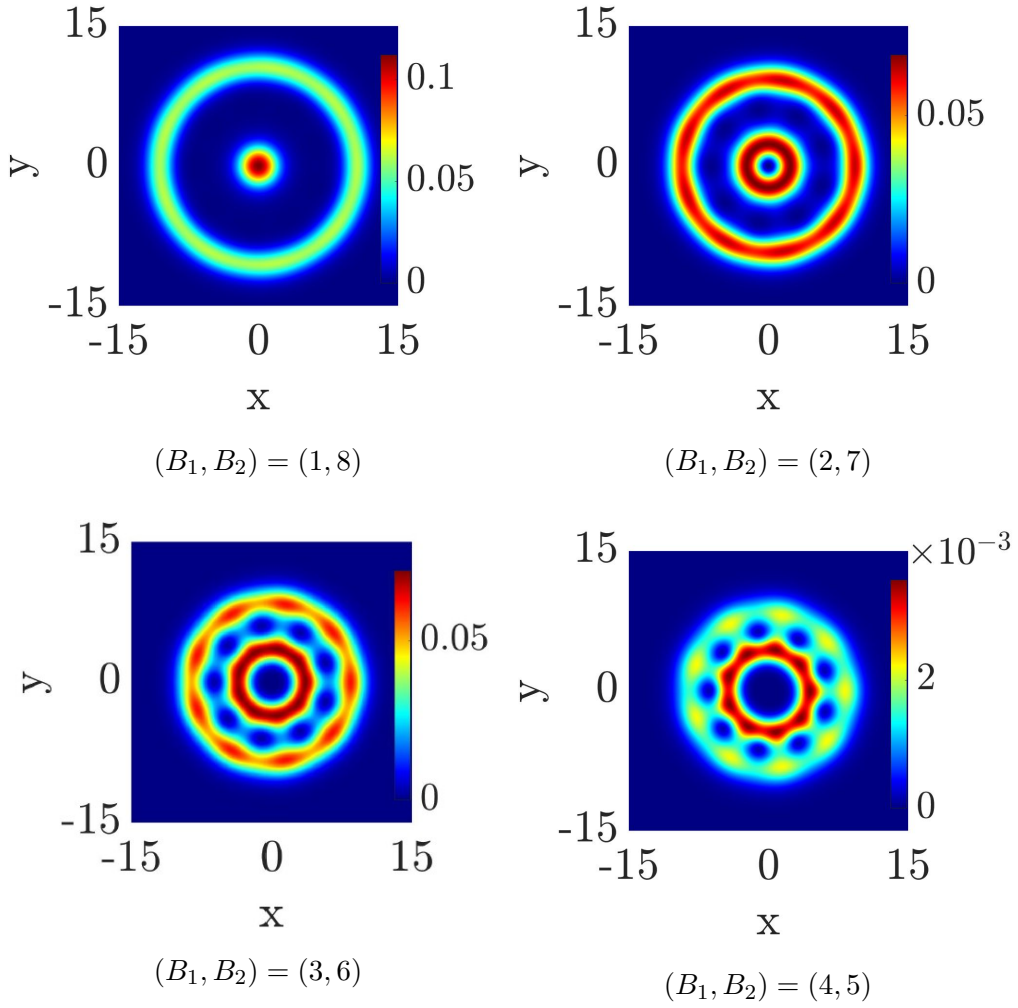

Figure 3.3.6: Heat plots for the minimized energy solutions of the equations of motion for $(1, 8)$, $(2, 7)$, $(3, 6)$, and $(4, 5)$ solutions. The $(2, 7)$ configuration has evenly distributed energy density, while $(3, 6)$ shows a higher peak in the inner ring. Configurations $(1, 8)$ and $(4, 5)$ have the highest energy. The local minimum for $B = 9$ occurs at $(2, 7)$, with energy per soliton $E = 1.3817$.

Since the $(2, 7)$ configuration is the local minimum, we can assume that such minimum occur when the cost of the curvature is balanced with the attraction between the layers. Figure 3.3.7 illustrates the phase eq. (3.2.1) of the $B = 9$ configurations. This helps us to understand how the topological charge is distributed throughout the solution. In all cases, the D_9 symmetry is preserved, with $(2, 7)$ and $(3, 6)$ being the minimal energy configurations in this family.

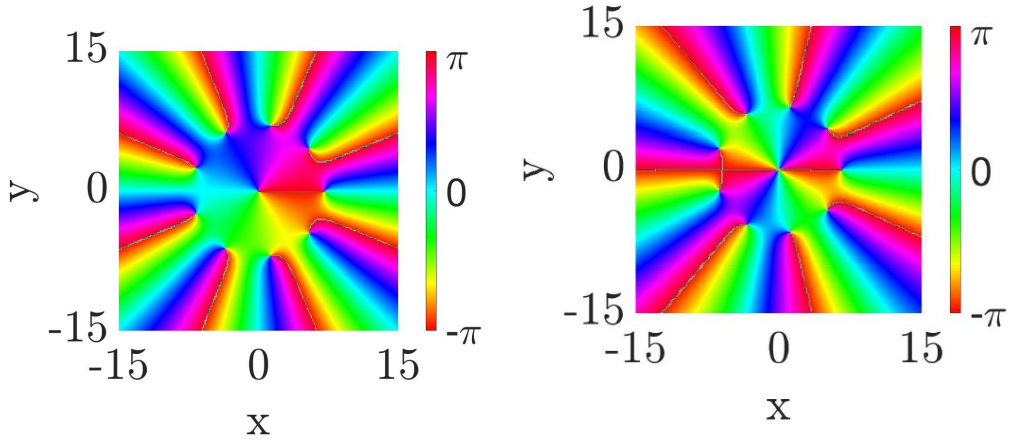

$(B_1, B_2) = (1, 8)$

$(B_1, B_2) = (2, 7)$

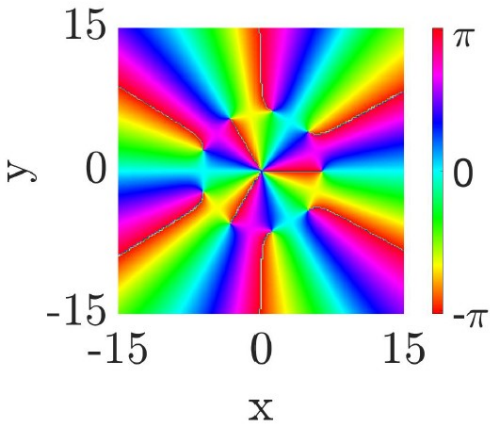

$(B_1, B_2) = (3, 6)$

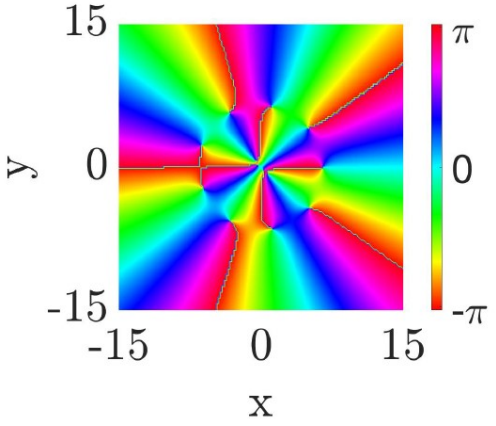

$(B_1, B_2) = (4, 5)$

Figure 3.3.7: Plots of the phase eq. (3.2.1) for $(1, 8)$, $(2, 7)$, $(3, 6)$, and $(4, 5)$ solutions.

3.4 Higher Charge Solutions

Next we explore configurations with higher charges by introducing more layers and analysing their symmetries. Some symmetries might be preserved if the symmetry group of the inner two rings is a subgroup of the outer layers.

3.4.1 $(11, 25)$ Solution

An example of the breakdown of the layers is the $(11, 25)$ ring, which is expected to have D_{36} symmetry, since $B = 36$. However, numerical simulations suggest that the solution evolves into a $(5, 7, 11, 13)$ ring with D_6 symmetry, as shown in figure 3.4.1. The inner two rings sum to charge $B = 12$, and the outer two rings sum to charge

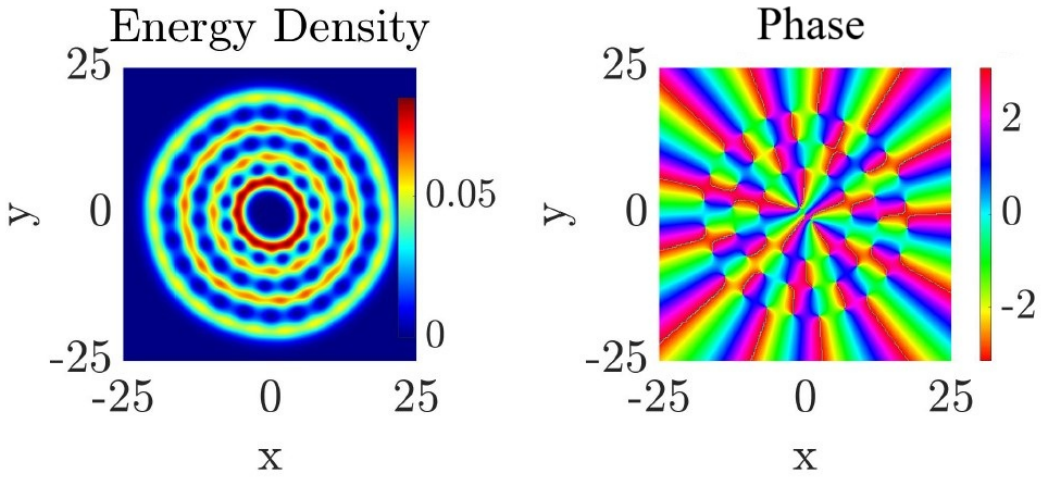

Figure 3.4.1: Heat plot for a $(5, 7, 11, 13)$ nested ring solution. The energy per baryon is $E = 1.37974$. The D_6 symmetry results from the balance of charges across layers.

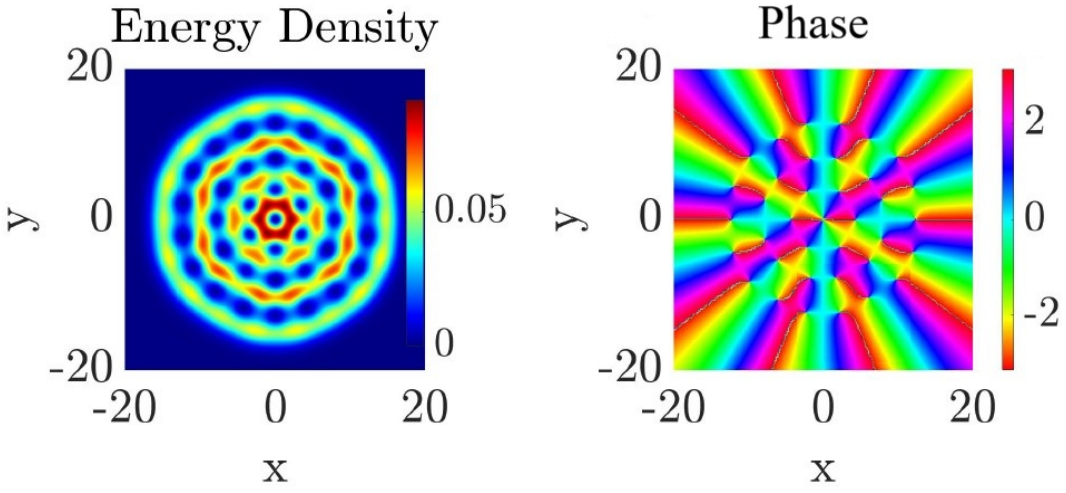

Figure 3.4.2: Heat plot for the minimised energy solution of the equations of motion for a $(2, 4, 8, 10)$ nested ring, with energy per baryon $E = 1.3901$, and topological winding for the same configuration respectively. We see a clear D_6 symmetry, which is verified in figure 3.4.3

$B = 24$. Although D_{12} is the largest subgroup, the solution prefers D_6 symmetry due to numerical constraints and lattice limitations.

3.4.2 $(2, 4, 8, 10)$ Solution

The maximum symmetry we would be able to achieve from a multi-layered ring at this charge would be D_{24} if the ring only had 2 layers, however, since the rings flow into more

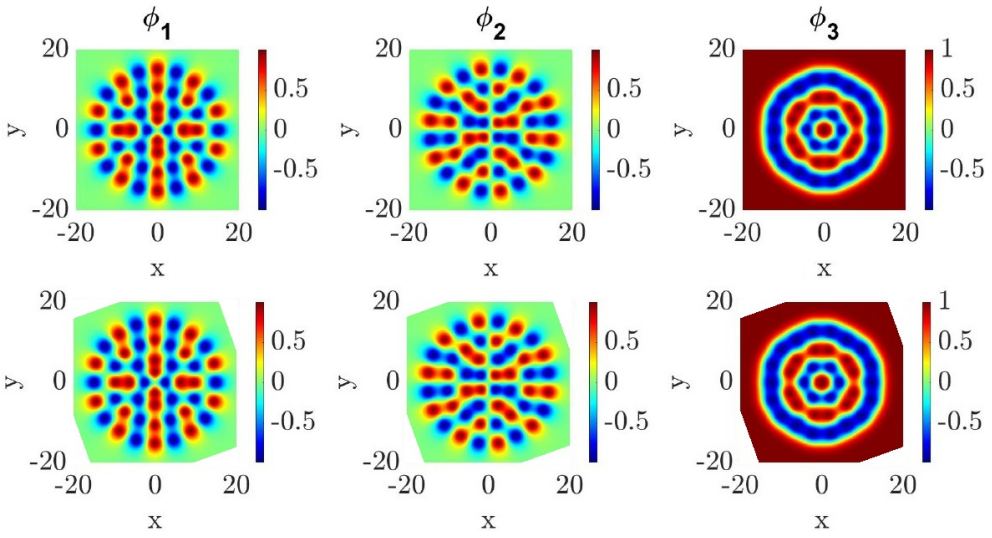

Figure 3.4.3: Heat plot for the field values of the fields of a $(2, 4, 8, 10)$ nested ring, and the fields after a D_6 rotation, with the space rotated the other way for comparison.

layers, the highest symmetry we should be able to achieve would be a D_{12} symmetry, as this would be the largest subgroup.

A clear hexagonal structure can be seen in the shape of the energy density. Furthermore, we can verify the D_6 symmetry by showing that the fields are invariant under this rotation. It appears as though the symmetry group of these configurations is the greatest subgroup of the total charge of the inner two rings compared to the total charge of the outer two rings. We attempt to validate this symmetry in figure 3.4.3.

Furthermore, the inner 2 layers are a $(2, 4)$ ring, and hence we can compare these 2 D_6 solutions. The $(2, 4)$ solution has energy per soliton $E = 1.4183$, whereas the $(2, 4, 8, 10)$ solution has energy per soliton $E = 1.3901$, suggesting that the interaction between layers has indeed lowered the energy of the solution.

Chapter 4

Domain Walls

4.1 Introduction

A domain wall is a boundary between two vacua. In this case, we use the same Baby Skyrme model as before, as the potential term allows for two vacua. Hence, we can have a domain wall interpolating between these two vacua

A domain wall occurs due to the fixation of the vacua at the boundaries. We simulate space as a cylinder, by parametrising the space as a rectangle, periodic in the x_1-direction, where $\lim_{x_2\to\infty}\phi = (0,0,-1)$ and $\lim_{x_2\to-\infty}\phi = (0,0,1)$. This breaks the $O(3)$ symmetry into a $O(2)$ symmetry.

For the solution to be a topological soliton, it must evade Derrick's theorem. Due to the nature of the solution being on a cylinder, scaling in the x_1-direction would result in a different solution, so in order to check the solution numerically, we must ensure that it is invariant under scaling in the x_2 direction. We hence use a slightly different version of Derrick's theorem, where we apply the rescaling [53] $x_2 \to \lambda_2 x_2$. By studying the limit definition of the derivative, it is clear that

$$\partial_2\phi \mapsto \frac{1}{\mu_2}\partial_2\phi, \tag{4.1.1}$$

where we have chosen λ_2 to be the scaling parameter in the x_2 direction. Applying this rescaling to eq. (2.2.5),

$$E = \frac{1}{2\pi}\cdot\frac{1}{\lambda_2}\int\frac{1}{4}\left[\lambda_2^2(\partial_1\phi)^2 + (\partial_2\phi)^2\right] + \frac{\lambda_2^2}{4}|\partial_1\phi\times\partial_2\phi|^2 + V(\phi)d^2\,x$$

$$= \frac{1}{2\pi} \int \frac{1}{4} \left[\frac{1}{\lambda_2} (\partial_1 \phi)^2 + \lambda_2 (\partial_2 \phi)^2 \right] + \frac{\lambda_2}{2} |\partial_1 \phi \times \partial_2 \phi|^2 + \frac{1}{\lambda_2} V(\phi) \, d^2x. \tag{4.1.2}$$

This leads to the transformation for the energy

$$e(\lambda_2) = \frac{1}{\lambda_2} E_{2,1} + \lambda_2 E_{2,2} + \lambda_2 E_4 + \frac{E_0}{\lambda_2}. \tag{4.1.3}$$

To ensure the stability of the soliton, we apply Derrick's theorem by requiring the energy to be stationary with respect to the scaling parameter λ_2. Taking the derivative of $e(\lambda_2)$ with respect to λ_2 and evaluating at $\lambda_2 = 1$, we obtain

$$\frac{de}{d\lambda_2}\Big|_{\lambda_2=1} = -\frac{1}{\lambda_2^2} E_{2,1} + E_{2,2} + E_4 - \frac{E_0}{\lambda_2^2}\Big|_{\lambda_2=1} = -E_{2,1} + E_{2,2} + E_4 - E_0 = 0,$$

where $E_{2,1} = \frac{1}{4} \int (\partial_1 \phi)^2, d^2x$, $E_{2,2} = \frac{1}{4} \int (\partial_2 \phi)^2, d^2x$, $E_4 = \frac{1}{2} \int |\partial_1 \phi \times \partial_2 \phi|^2, d^2x$, and $E_0 = \int V(\phi), d^2x$ represent the contributions to the energy functional from the respective terms. For the soliton to be stable, this condition must hold, implying a balance between the energy contributions. Specifically, stable solutions require $E_0 + E_{2,1} = E_{2,2} + E_4$. This constraint allows us to numerically verify the stability of the soliton by computing these energy terms and ensuring that they satisfy the derived equality, consistent with the requirements for a topological soliton to evade Derrick's theorem on a cylindrical geometry.

We will first reduce the dimensionality of the system to a one-field model, in order to give some insight into what the optimal length L might be and also to give verification of the two-field code.

4.2 Symmetry Reduction

We consider the same Lagrangian density eq. (2.2.1). For an initial configuration, we let

$$\phi = \begin{pmatrix} \phi_1 \\ \phi_2 \\ \phi_3 \end{pmatrix} = \begin{pmatrix} \sin f \cos(B\theta) \\ \sin f \sin(B\theta) \\ \cos f \end{pmatrix}, \tag{4.2.1}$$

where $f(\rho)$ is the monotonically decreasing profile function with polar coordinates (ρ, θ), with boundary conditions $f(0) = \pi$ and $f(\infty) = 0$, and B is the topological charge.

Substituting this ansatz into eq. (2.2.1), we can reduce the dimension of the Lagrangian. We again choose the mass term $m^2 = 0.1$. We perform a change of variables from the field ϕ to the one-dimensional scalar field f, where we note that $\rho = \sqrt{x_1^2 + x_2^2}$.

$$\mathcal{L} = \frac{1}{2}\left((\partial_t f)^2 - (\partial_1 f)^2 - (\partial_2 f)^2\right) + \frac{\sin^2(f)}{2}[(\partial_t f \partial_1 f - \partial_1 f \partial_t f)^2 + (\partial_t f \partial_2 f - \partial_2 f \partial_t f)^2 - (\partial_1 f \partial_2 f - \partial_2 f \partial_1 f)^2] - \frac{m^2}{2}\sin^2(f),$$

If we consider static solutions with $\theta = \frac{2\pi x_1}{L}$, where L is the size of the unit cell in the periodic x_1 direction, then the Lagrangian density is

$$\mathcal{L} = -\frac{1}{2}(\partial_2 f)^2 - \frac{\sin^2(f)}{2}(\partial_2 f)^2(\partial_1 \theta)^2 - \frac{m^2}{2}\sin^2(f), \tag{4.2.2}$$

with resulting field equation

$$-\partial_{22} f(1 + \sin^2(f)(\partial_1\theta)^2) - \frac{(\partial_1\theta)^2}{2}(\partial_2 f)^2 \sin(2f) + \frac{m^2}{2}\sin(2f) = 0. \tag{4.2.3}$$

We can solve (4.2.3) numerically using an arrested newton flow algorithm and compare the energy values per soliton for various periodic lengths L to minimise the energy for this parameter L.

For $B = 1$, figure 4.2.1 shows that the optimal value for the periodic length is $L = 8.43$, with a minimal energy of $E = 1.3625539$, which we will consider to be a lower bound of the energy.

4.3 $B = 1$ Baby Skyrmion on a cylinder

Using our one-field results as guidance, we study the domain wall in two dimensions. Figure 4.3.2 shows plots for the energy density and topological winding of the charge $B = 1$ two-dimensional domain wall of optimal cell size.

We interpret the domain wall as an infinitely large ring with zero curvature, making this a lower bound for the axially symmetric solution. We find, with less precision, that the optimal length is $L = 8.4$ (the optimal cell size), with minimal energy $E = 1.362561$, which is within 0.0001% of the one-field result.

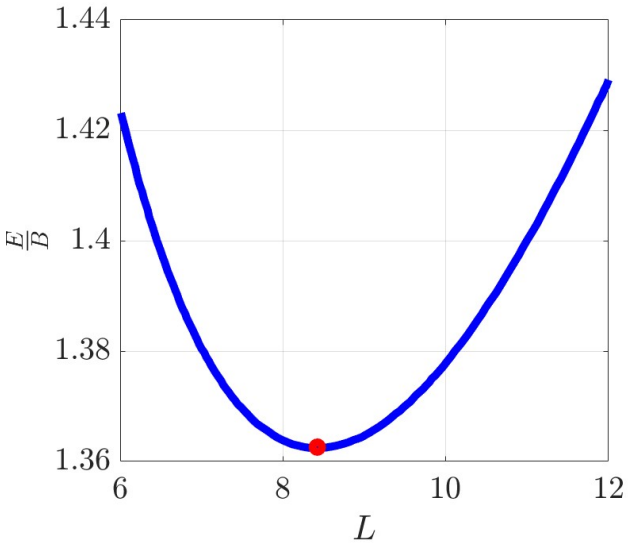

Figure 4.2.1: Comparison of the energy for the one-dimensional charge $B = 1$ domain wall for each periodic length L, computed using 8000 points, with a space step of 0.01. We find an optimal periodic length $L = 8.43$, with energy per soliton $E = 1.3625$, which agrees with the two-dimensional results.

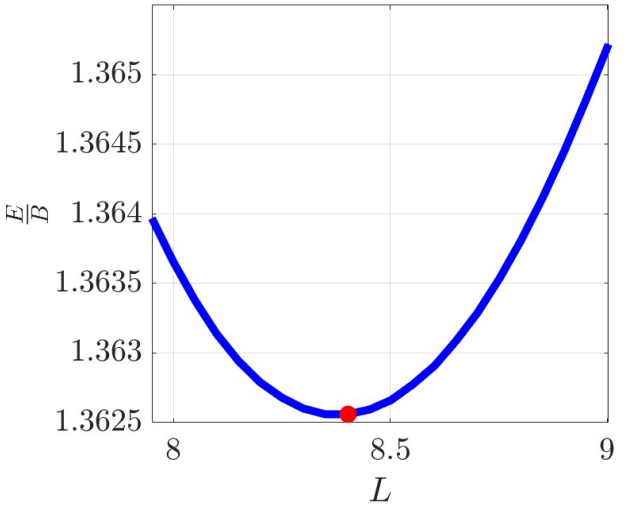

Figure 4.3.1: Energy per soliton against periodic length L for a domain wall on a cylinder, computed using 2-dimensional numerics. We minimised the fields on a fixed length L, then varied L to find the optimal cell size. We find that The optimal L is 8.4, with energy per soliton $E = 1.3625$

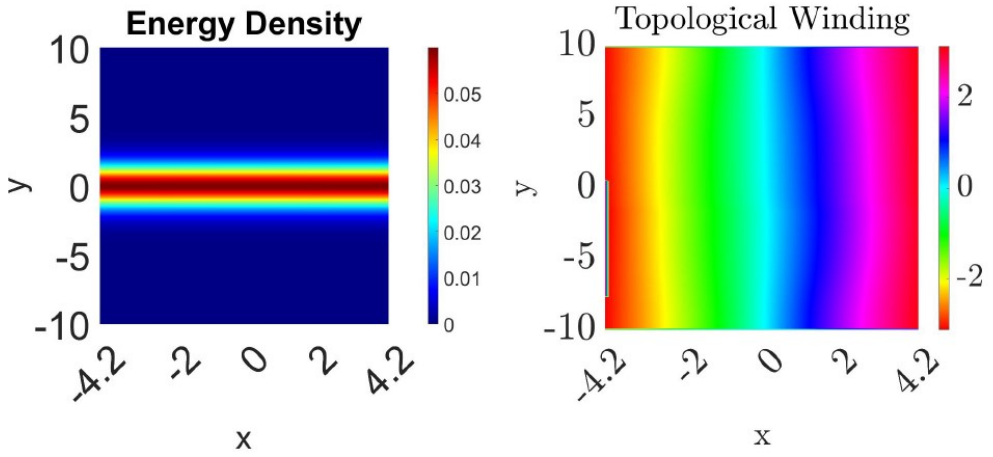

Figure 4.3.2: Heat plot for the minimised energy solution of the equation of motion for a $B = 1$ domain wall in 2 dimensions. This is the solution of the optimal length $L = 8.4$, with energy per soliton $E = 1.3625$. On the right hand side we have the energy density coloured by the phase. The shows that the domain wall winds from $-\pi$ to π across the cell.

4.4 $B = 2$ Baby Skyrmion on a cylinder

We simulate a $B = 2$ Baby Skyrmion on a cylinder of periodic length L.

Figure 4.4.1 plots the energy per soliton for different periodic lengths L. We use a minimisation algorithm whereby we minimise the fields for a fixed L, then vary L to find the optimal cell size. We gradually increased the lattice, starting with small L, to find the minimal energy. Moreover, to verify these solutions, we also started the system with a large L, gradually removing points in the $x-$direction to reduce the cell size, to minimise for L.

We find that the optimal configuration for the Baby Skyrmion on a cylinder is a charge $B = 2$ configuration with periodic length $L = 8.4$. This simulated a layered solution with zero curvature, hence we have a lower bound on the energy of $E \geq 1.3630$ for the dihedral solutions.

We show a heat plot for the minimised energy solution of the equations of motion for a charge 2 solution on a cylinder with optimal L in figure 4.4.2. We see that the configuration splits into two $B = 1$ domain walls (axial rings with zero curvature). This could imply that the global minimum would be a compound structure of multiple rings, which suggests that at some charge the double rings could be the global minimum. Further studying of these infinite rings suggests that the solution is in fact 2 parallel domain walls. This could imply that this solution is not stable as 2 parallel charge 1

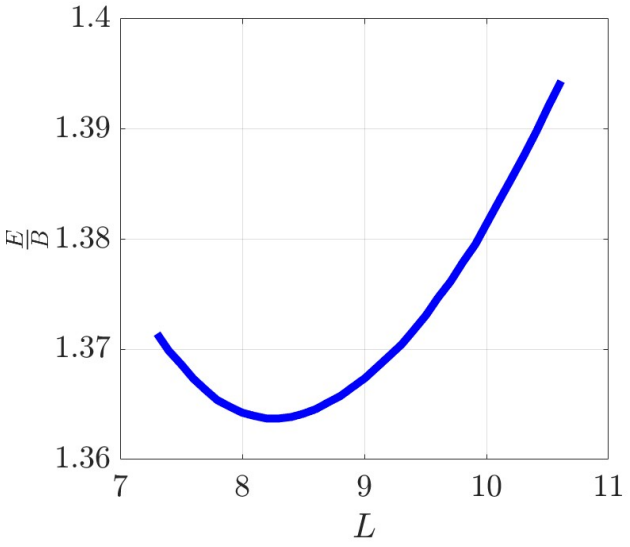

Figure 4.4.1: Energy per soliton against periodic length L for a $B = 2$ Baby Skyrmion on a cylinder. The optimal periodic length is $L = 8.4$, with energy per soliton $E = 1.3630$.

domain walls will want to infinitely repel because of their relative phase never being in the attractive channel.

Furthermore, we can study the phase of the solution to ensure that it has the correct topological winding, and we can clearly see that the phase winds around each wall once, suggesting that each infinite chain is of charge 1 per unit cell. An illustration of the phase of the infinite $B = 2$ solution can be seen in figure 4.4.2. We see in the next chapter that the minimised energy for the domain wall is found at the same minimised length L, however, the minimised energy in this case is $E = 1.3626$, suggesting that there is indeed a slight energy cost for the 2 parallel domain walls.

The energy minimum found for the domain wall is slightly lower than that of the $B = 2$ Baby Skyrmion on a cylinder. However, by studying the model, it appears that the $B = 2$ solution is indeed two parallel domain walls passing in and out of phase with each other, suggesting that there is an energy interaction cost between the two walls.

We can confirm the interaction between the walls in two ways: first, by shifting the two walls apart and observing if they flow back to the original solution or remain where they are with lower energy (which indeed is the case), and second, by adjusting the phase of one of the walls. The latter method suggests that the interaction is not influenced by phase differences but rather by the proximity of the walls. From this we conclude that the lower bound on the energy is the single domain wall, with energy per soliton

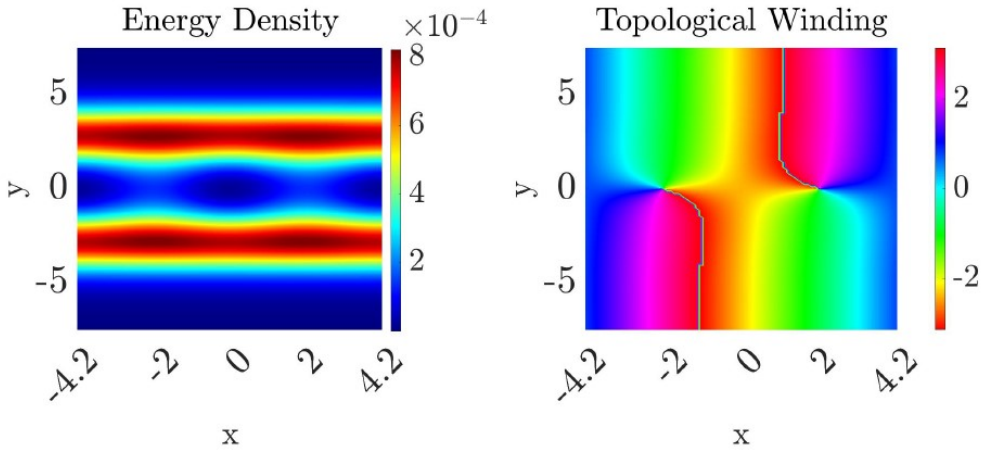

Figure 4.4.2: Heat plot for the minimised energy density of a topologically charged $B = 2$ Baby Skyrmion on a cylinder with periodic lattice in the x-direction on the left, and the plot for the phase winding of the same solution. We can see from the energy density that there is a clear interaction between the 2 walls, which can be interpreted from the topological winding as a result of the 2 layers being out of phase with each other, resulting in a repulsion. The result can be interpreted as 2 parallel domain walls, which further supports the argument of repulsion.

$E = 1.3625$.

The charge 2 solution on a cylinder is then considered the lower bound for double rings. Although this bound is higher than that of the domain wall, it is possible that other solutions on the cylinder could represent global minimum.

Chapter 5

Conclusions

In this part of the thesis, we have investigated families of solutions within the Baby Skyrme model, employing the potential $V(\phi) = (1 - \phi_3^2)$ as introduced in [78]. These solutions depart from the historically observed axial symmetry, instead exhibiting dihedral symmetry, which was previously unseen in this context. Our exploration reveals a diverse and intricate space of solutions, particularly pronounced at higher topological charges, where multi-layered configurations emerge. The introduction of nested rings demonstrates that interlayer attractions can lower the energy per soliton compared to isolated layers, as evidenced by comparing the $(2, 4)$ solution ($E = 1.4183$) with the $(2, 4, 8, 10)$ configuration ($E = 1.3901$).

We have also discussed lower bounds on the energy through the analysis of infinite rings and domain walls. By simulating the model on a cylinder with periodic boundary conditions, we identified a lower energy bound of $\frac{E}{B} \geq 1.3630$ for a charge $B = 2$ Baby Skyrmion, while a single domain wall yielded an even lower bound of $\frac{E}{B} = 1.3625$ at an optimal periodic length of $L = 8.4$. These findings suggest that the global minimum for axial rings may approximate an infinitely large ring with vanishing curvature, while double-layered rings are bounded by the charge $B = 2$ cylindrical solution. Intriguingly, the slight increase in energy of the $B = 2$ solution on the domain wall hints at a repulsive interaction between parallel walls, a phenomenon that deserves further investigation.

Our results indicate that the Baby Skyrme model has a richer structure than previously appreciated, with dihedral solutions offering stable local minimum and axial solutions retaining their status as global minimum across the charges studied.

Part III

Vortices

Chapter 6

Abelian Higgs Vortices

6.1 Introduction

The Abelian Higgs model [38] is a relativistic field theory whose excitations in $(2+1)$-dimensions take the form of topologically stable solitons known as vortices.

The field theory consists of a complex scalar field ϕ coupled to a $U(1)$ gauge field A_μ. The static theory is equivalent to the effective Ginzburg-Landau theory [35], describing a magnetic field penetrating a superconductor, where the total flux is quantised by the number of vortices. The dynamics of vortex solutions is where these two theories diverge; the Abelian Higgs model exhibits second-order dynamics with Lorentz invariance [59, 60, 64], whereas the time-dependent Ginzburg-Landau model exhibits first-order dynamics [30, 55]. It is the former second-order dynamics that we will focus on in this thesis. Note that in $(3+1)$ dimensions vortices appear as string-like objects, known as cosmic strings, which if they exist, may be detected through the gravitational contribution to early universe cosmology [77].

Vortex scattering has been well studied for all values of the single parameter λ [18, 28, 59, 60, 64]. This parameter splits the model into two types; type I ($\lambda < 1$) where vortices exhibit long-range attraction and type II ($\lambda > 1$) where vortices repel at long-range. In contrast, at critical coupling ($\lambda = 1$), there are no static long-range intervortex forces, and the N-vortex solutions can be represented by an unordered set of dimension $2N$ or $\mathcal{M}_N = \mathbb{C}^N/S_N$ where S_N is the set of permutations. At critical coupling, low-energy second-order dynamics can then be approximated as free geodesic motion on the moduli space $\mathcal{M}_N$. This moduli space naturally captures the most striking result, namely that vortices exhibit head-on 90° scattering [73].

6.2 The Abelian Higgs model

The $(2+1)$-dimensional Abelian Higgs model [38] is described by the action

$$S = \int\int_{\mathbb{R}^2} \mathcal{L}\, dt\, d^2x = \int\int_{\mathbb{R}^2} \left[-\frac{1}{4} f_{\mu\nu} f^{\mu\nu} + \frac{1}{2} \overline{D_\mu \phi}\, D^\mu \phi - \frac{\lambda}{8} (|\phi|^2 - 1)^2 \right] dt\, d^2x, \quad (6.2.1)$$

where $\phi(t,x) = \phi_1(t,x) + i\phi_2(t,x)$ is a complex scalar field (the Higgs field), with spatial coordinate $x \in \mathbb{R}^2$, and $A_\mu(t,x) = (A_0, A_1, A_2)$ is a real $U(1)$ gauge potential. The covariant derivative is $D_\mu \phi = (\partial_\mu - iA_\mu)\phi$, and the field strength tensor is $f_{\mu\nu} = \partial_\mu A_\nu - \partial_\nu A_\mu$. λ is the coupling constant. We will assume the spacetime $\mathbb{R}^{2+1}$ has the metric signature $(+,-,-)$. All parameters (e.g., electric charge, vacuum expectation value) are normalised, leaving λ as the Higgs field mass parameter, and the speed of light is set to $c = 1$.

The model is invariant under the gauge transformation

$$\phi(x) \mapsto e^{i\alpha(x)} \phi(x), \qquad A_\mu(x) \mapsto A_\mu(x) + \partial_\mu \alpha(x). \quad (6.2.2)$$

The static energy for field configurations is

$$V = \frac{1}{2} \int_{\mathbb{R}^2} \left[\overline{D_i \phi} D_i \phi + B^2 + \frac{\lambda}{4} (1 - |\phi|^2)^2 \right] d^2x, \quad (6.2.3)$$

where $B = f_{12} = \partial_1 A_2 - \partial_2 A_1$ represents the magnetic field orthogonal to the plane.

For field configurations to have finite energy we require that $B \to 0$, $D_\mu \phi \to 0$ and $|\phi| \to 1$ as $\rho \to \infty$, where $\rho = |x|$. This fixes the Higgs field on the boundary

$$\phi_\infty := \lim_{\rho \to \infty} \phi(x)$$

to take values on the unit circle such that $\phi_\infty : S^1_\infty \to S^1$, where S^1_∞ is the circle on the boundary of $\mathbb{R}^2$. This map is encapsulated by an integer degree or winding number $N \in \mathbb{Z}$. This winding number counts the number of zeros of the continuous Higgs field ϕ including multiplicity. Since a given field configuration cannot be deformed from one homotopy class to a different one by a continuous deformation, the field configurations are separated into infinitely many disjoint components, indexed by the integer degree N.

Therefore, the dynamic field equations must preserve the integer degree N. To relate

the total magnetic flux to N, consider the boundary condition $D_i\phi \to 0$ as $\rho \to \infty$, which implies $\partial_i\phi = iA_i\phi$ on the boundary circle S^1_∞. Writing $\phi = |\phi|e^{i\theta}$, where $|\phi| \to 1$ and θ is the phase, we have $\partial_i\theta = A_i$ on the boundary. The winding number N is the number of times θ winds around S^1 as one traverses S^1_∞, given by

$$N = \frac{1}{2\pi}\int_{S^1_\infty} d\theta = \frac{1}{2\pi}\int_{S^1_\infty} \partial_i\theta\, dx^i = \frac{1}{2\pi}\int_{S^1_\infty} A_i\, dx^i. \tag{6.2.4}$$

By Stokes' theorem, the line integral of A_i over the boundary S^1_∞ equals the integral of the magnetic field $B = f_{12} = \partial_1 A_2 - \partial_2 A_1$ over $\mathbb{R}^2$:

$$\int_{S^1_\infty} A_i\, dx^i = \int_{\mathbb{R}^2} (\partial_1 A_2 - \partial_2 A_1)\, d^2x = \int_{\mathbb{R}^2} f_{12}\, d^2x. \tag{6.2.5}$$

Thus, the magnetic flux is quantised in terms of the winding number:

$$\frac{1}{2\pi}\int_{\mathbb{R}^2} f_{12} = N. \tag{6.2.6}$$

To ensure that finite-energy configurations, such as vortices, are stable topological solitons, they must evade Derrick's theorem [53]. Consider a spatial rescaling

$$x \to \kappa x, \tag{6.2.7}$$

with $\kappa > 0$, applied to the static energy (6.2.3). Under this rescaling, the Higgs field ϕ scales as,

$$\phi(x) \to \phi(\kappa x), \tag{6.2.8}$$

the spatial derivatives transform as

$$\partial_i \to \frac{1}{\kappa}\partial_i \tag{6.2.9}$$

, so the covariant derivative transforms as

$$D_i\phi \to \frac{1}{\kappa}D_i\phi \tag{6.2.10}$$

. We are working in a gauge theory, hence both terms of the covariant derivative must scale consistently, hence the magnetic field transforms as

$$B = \partial_1 A_2 - \partial_2 A_1 \to \frac{1}{\kappa^2} B \tag{6.2.11}$$

since

$$A_i \to \frac{1}{\kappa} A_i. \tag{6.2.12}$$

The metric transforms as $d^2x \to \kappa^2 d^2x$. Thus, the static energy becomes

$$V(\mu) = \frac{1}{2} \int_{\mathbb{R}^2} \left[\frac{1}{\mu^2} \overline{D_i \phi} D_i \phi + \frac{1}{\mu^4} B^2 + \frac{\mu^2 \lambda}{4} (1 - |\phi|^2)^2 \right] d^2x. \tag{6.2.13}$$

This can be written as

$$V(\kappa) = \frac{1}{\kappa^2} E_2 + \frac{1}{\kappa^4} E_4 + \kappa^2 E_0, \tag{6.2.14}$$

where $E_2 = \frac{1}{2} \int_{\mathbb{R}^2} \overline{D_i \phi} D_i \phi \, d^2x$ is the kinetic term, $E_4 = \frac{1}{2} \int_{\mathbb{R}^2} B^2 \, d^2x$ is the magnetic term, and $E_0 = \frac{1}{2} \int_{\mathbb{R}^2} \frac{\lambda}{4} (1 - |\phi|^2)^2 \, d^2x$ is the potential term. For the energy to be stationary with respect to κ, we compute the derivative and evaluate at $\kappa = 1$:

$$\frac{dV}{d\kappa}\Big|_{\kappa=1} = -\frac{2}{\kappa^3} E_2 - \frac{4}{\kappa^5} E_4 + 2\kappa E_0 \Big|_{\kappa=1} = -2E_2 - 4E_4 + 2E_0 = 0. \tag{6.2.15}$$

This yields the stability condition

$$E_0 = E_2 + 2E_4. \tag{6.2.16}$$

This condition ensures that vortex solutions with non-zero winding number N can be stable, as it balances the contributions of the potential, kinetic, and magnetic terms, allowing the Abelian Higgs model to support topological solitons that evade Derrick's theorem. This constraint can be used to numerically verify the stability of vortex configurations by computing E_0, E_2, and E_4.

Varying the action with respect to ϕ and A_μ yields the second-order Euler-Lagrange equations of motion

$$D_\mu D^\mu \phi - \frac{\lambda}{2} (1 - |\phi|^2) \phi = 0, \tag{6.2.17}$$

$$\partial_\mu f^{\mu\nu} + \frac{i}{2} \left(\bar{\phi} D^\nu \phi - \phi \overline{D^\nu \phi} \right) = 0. \tag{6.2.18}$$

.

6.3 BPS Equations

We can derive a lower bound on the energy, known as the Bogomolny bound [25]. We complete the square of the integrand of eq. (6.2.3). The covariant derivative term expands as

$$\overline{D_i\phi}D_i\phi = |D_1\phi|^2 + |D_2\phi|^2 = |D_1\phi \pm iD_2\phi|^2 \mp i\left(D_1\phi\overline{D_2\phi} - D_2\phi\overline{D_1\phi}\right).$$

The magnetic field term and potential term transform together as

$$B^2 + \frac{\lambda}{4}(|\phi|^2-1)^2 = \left(B \pm \frac{1}{2}(|\phi|^2-1)\right)^2 \mp B(|\phi|^2-1).$$

Hence

$$V = \frac{1}{2}\int d^2x \Bigg[\left(B - \frac{1}{2}(1-|\phi|^2)\right)^2 + \overline{(D_1\phi + iD_2\phi)}(D_1\phi + iD_2\phi) \\ + B - i\left(\partial_1(\phi D_2\phi) - \partial_2(\phi D_1\phi)\right) + \frac{\lambda-1}{4}(1-|\phi|^2)^2\Bigg] \tag{6.3.1}$$

The term $i\left(\partial_1(\phi D_2\phi) - \partial_2(\phi D_1\phi)\right)$ represents the divergence of the vector field $\vec{F} = i(\phi D_2\phi, -\phi D_1\phi)$, since $\nabla\cdot\vec{F} = \partial_1(i\phi D_2\phi) - \partial_2(i\phi D_1\phi) = i(\partial_1(\phi D_2\phi) - \partial_2(\phi D_1\phi))$. By Stokes' theorem, this divergence over $\mathbb{R}^2$ can be expressed as a line integral over the boundary circle at infinity S^1_∞

$$i\int_{\mathbb{R}^2}\left(\partial_1(\phi D_2\phi) - \partial_2(\phi D_1\phi)\right)d^2x = i\int_{S^1_\infty}(\phi D_2\phi)dx_1 - (\phi D_1\phi)dx_2, \tag{6.3.2}$$

where (dx_1, dx_2) is the line element along S^1_∞. The finite energy conditions require $D_i\phi \to 0$ and $|\phi| \to 1$ as $\rho \to \infty$. Since $D_i\phi = (\partial_i - iA_i)\phi$, the condition $D_i\phi \to 0$ implies $\partial_i\phi = iA_i\phi$ on the boundary, so $\phi D_i\phi = \phi(\partial_i\phi - iA_i\phi) = \phi(iA_i\phi - iA_i\phi) = 0$. Thus, the integrand in (6.3.2) vanishes, making the line integral zero [53].

Finally, by evaluating the integral of B using eq. (6.2.6) we have a lower bound on the energy

$$V[\phi, A_i] \geq \pi|N| + \frac{\lambda-1}{8}\int(1-|\phi|^2)^2\, d^2x. \tag{6.3.3}$$

where N is the integer degree.

At critical coupling, we therefore have the Bogomolny bound [25]

$$V \geq \pi |N|, \tag{6.3.4}$$

which is saturated for solutions of the Bogomolny equations

$$\begin{aligned} D_1\phi \pm iD_2\phi &= 0 \\ B \mp \frac{1}{2}(1 - |\phi|^2) &= 0. \end{aligned} \tag{6.3.5}$$

6.4 Moduli Space Approximation

In the case of N vortices at critical coupling, the solutions to the field equations can be represented by an unordered set of positions, which form a moduli space of dimension $2N$. The moduli space, $\mathcal{M}_N$, is the configuration space for the positions of the vortices and can be written as the quotient,

$$\mathcal{M}_N = \frac{\mathbb{R}^{2N}}{S_N} \cong \frac{\mathbb{C}^N}{S^N},$$

where S_N is the symmetric group that accounts for the indistinguishability of the vortices under permutation. This moduli space accounts for the fact that the vortices are indistinguishable except for their positions. At critical coupling, the moduli space of the N-vortex system is thus a reduced configuration space that reflects the internal symmetry of the system.

6.4.1 Geodesic Motion at Critical Coupling

At critical coupling ($\lambda = 1$), the low-energy dynamics of N vortices in the Abelian Higgs model are described by geodesic motion on the moduli space $\mathcal{M}_N$ [53]. This approximation holds when vortices move slowly compared to the internal field dynamics, reducing the field equations to motion on $\mathcal{M}_N$. A distinctive feature of this regime is the head-on 90° scattering of vortices, governed by the geometry of $\mathcal{M}_N$ [63].

The vortex positions are parametrised by complex coordinates $z_r \in \mathbb{C}$, $r = 1, \ldots, N$, corresponding to points in the plane $\mathbb{R}^2 \cong \mathbb{C}$. The metric on $\mathcal{M}_N$, derived from the kinetic energy of field configurations satisfying the Bogomolny equations eq. (6.3.5), is

given by

$$ds^2 = \sum_{r,s=1}^{N} g_{r\bar{s}} dz_r d\bar{z}_s, \tag{6.4.1}$$

where $g_{r\bar{s}} = \pi\left(\delta_{rs} + 2\frac{\partial b_r}{\partial \bar{z}_s}\right)$ forms an $N \times N$ Hermitian matrix ($g_{r\bar{s}} = \overline{g_{s\bar{r}}}$), with b_r being coefficients in the expansion of the Higgs field logarithm, as described below [63].

The reduced Lagrangian, capturing the kinetic energy of the fields at critical coupling, is

$$L_{\text{red}} = \frac{\pi}{2} \sum_{r,s=1}^{N} g_{r\bar{s}} \dot{z}_r \dot{\bar{z}}_s, \tag{6.4.2}$$

where $\dot{z}_r = dz_r/dt$ denotes the velocity of the r-th vortex, and the factor $\pi/2$ normalises the vortex energy to $\pi|N|$ for winding number N. Varying (6.4.2) yields the geodesic equations, describing free motion at constant speed on $\mathcal{M}_N$, which accounts for the 90° scattering observed in head-on vortex collisions [60, 63].

To compute the metric coefficients, we apply Samols' method [63]. The Higgs field is expressed as $\phi = e^{\frac{1}{2}(h+i\chi)}$, where $h = \log|\phi|^2$ satisfies the Bogomolny equation $\nabla^2 h + 1 - e^h = 4\pi \sum_{r=1}^{N} \delta^2(z - z_r)$ away from the vortex positions. Near each vortex at z_r, h expands as $h = 2\log|z - z_r| + a_r + b_r(z - z_r) + \bar{b}_r(\bar{z} - \bar{z}_r) + \ldots$, with a_r and b_r depending on all vortex positions. The kinetic energy $T = \frac{1}{2}\int_{\mathbb{R}^2}(|\partial_t \phi|^2 + \partial_t A_i \partial_t A^i) d^2x$ is evaluated for slowly moving vortices, using the time derivatives of eq. (6.3.5) and Gauss' law, yielding

$$T = \pi \sum_{r,s=1}^{N} \left(\delta_{rs} + 2\frac{\partial b_r}{\partial \bar{z}_s}\right) \dot{z}_r \dot{\bar{z}}_s. \tag{6.4.3}$$

Thus, the metric coefficients are

$$g_{r\bar{s}} = \pi\left(\delta_{rs} + 2\frac{\partial b_r}{\partial \bar{z}_s}\right). \tag{6.4.4}$$

The Hermitian property follows from $\frac{\partial b_r}{\partial \bar{z}_s} = \frac{\partial \bar{b}_s}{\partial z_r}$. For well-separated vortices, $b_r \to 0$, reducing the metric to $ds^2 = \pi \sum_{r=1}^{N} dz_r d\bar{z}_r$, corresponding to independent vortex motion [53, 63].

The metric on $\mathcal{M}_N$ is Kähler, as the associated 2-form $\omega = \frac{i}{2}\sum_{r,s=1}^{N} g_{r\bar{s}} dz_r \wedge d\bar{z}_s$ is closed, due to the symmetry $\frac{\partial b_r}{\partial \bar{z}_s} = \frac{\partial \bar{b}_s}{\partial z_r}$ [53, 62]. This Kähler structure supports the use of complex coordinates z_r and enables global calculations on $\mathcal{M}_N$. The geodesic motion described by (6.4.2) governs the low-energy dynamics, with the 90° scattering arising from the geometry of $\mathcal{M}_N$, as confirmed by numerical studies [60, 63].

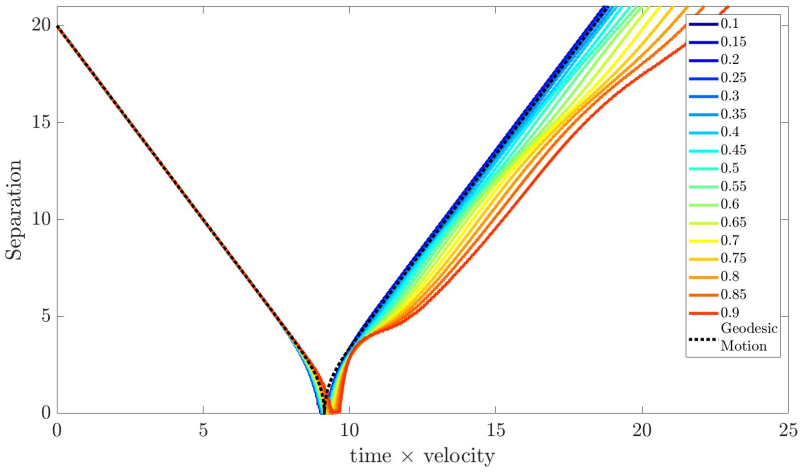

Figure 6.4.1: Separation of the zeros of the Higgs field (interpreted as the vortex position) of 2 vortices scattering at various initial velocities against time. Here the time is rescaled by the velocity such that $t \mapsto v_{\text{in}}t$, where v_{in} is the initial velocity of the vortices. The dotted black line is geodesic motion on the moduli space.

We can solve this 1-dimensional dynamical system, and plot the geodesic path of the vortices, see figure 6.4.1. To confirm that our numerics are working correctly, we can simulate the scattering of vortices at critical coupling, using the configuration eq. (9.1.3), and setting the perturbations to zero. We can then track the zeros of the condensate to plot the separation for a set of initial velocities.

In the moduli space approximation, the trajectories are independent of the initial velocity. This leads us to rescale our trajectories to $t \to v_{\text{in}}t$, where v_{in} is the initial velocity of the vortices. Figure 6.4.1 shows the scattering of two $N = 1$ vortices over a range of initial velocities. As expected, the trajectories initially lie on the same curve until $t \approx 8$. For small velocities $v_{\text{in}} < 0.3$, our numerics match the expected behaviour from the moduli space approximation (dotted line) whereby they travel with constant velocity and scatter at 90°. For larger velocities, the numerics deviate significantly from the moduli space approximation, which is only valid for small velocities. For velocities close to one, the trajectories show new kinds of behaviour which goes beyond the scope of this thesis.

6.5 Symmetry Reduction

To simulate vortex solutions, we take advantage of the radial symmetry of the soliton. We can hence reduce the dimensionality of the field theory by exploiting this symmetry

argument.

Consider polar coordinates, with radial coordinate ρ and angular coordinate θ, related to Cartesian coordinates by $x_1 = \rho\cos\theta$, $x_2 = \rho\sin\theta$ [53]. The gauge potential $A_i = (A_1, A_2)$ in Cartesian coordinates transforms to polar coordinates as

$$A_\rho = A_1\cos\theta + A_2\sin\theta, \quad A_\theta = -A_1\rho\sin\theta + A_2\rho\cos\theta, \tag{6.5.1}$$

where A_ρ and A_θ are the radial and angular components of the gauge potential, with the area element $d^2x = \rho d\rho d\theta$. Hence the magnetic field tensor becomes $f_{\rho\theta} = \rho f_{12}$. The static energy is then

$$V = \frac{1}{2}\int_0^\infty \int_0^{2\pi} \left(\frac{1}{\rho^2} f_{\rho\theta}^2 + \overline{D_\rho\phi} D_\rho\phi + \frac{1}{\rho^2}\overline{D_\theta\phi} D_\theta\phi + \frac{\lambda}{4}(1-|\phi|^2)^2 \right) \rho\, d\rho\, d\theta, \tag{6.5.2}$$

where $D_\rho\phi = \partial_\rho\phi - iA_\rho\phi$ and $D_\theta\phi = \partial_\theta\phi - iA_\theta\phi$ are the covariant derivatives in polar coordinates. We first consider an axially symmetric static isolated vortex of degree N at the origin using the ansatz

$$\phi = f(\rho)\, e^{iN\theta}, \quad (A_0, A_\rho, A_\theta) = (0, 0, a_\theta(\rho)), \tag{6.5.3}$$

where we choose the temporal gauge $A_0 = 0$ and the radial gauge $A_\rho = 0$, with $f(\rho)$ a radial profile function and $a_\theta(\rho)$ the angular component of the gauge potential. By the principle of symmetric criticality, this axially symmetric configuration, which satisfies the field equations restricted to radial dependence, is also a static solution of the full field equations [53].

Substituting this radially symmetric ansatz into eq. (6.5.2), we have the reduced static energy

$$V = \pi\int_0^\infty \left(\frac{1}{\rho^2}\left(\frac{da_\theta}{d\rho}\right)^2 + \left(\frac{df}{d\rho}\right)^2 + \frac{1}{\rho^2}(N-a_\theta)^2 f^2 + \frac{\lambda}{4}(1-f^2)^2 \right) \rho\, d\rho, \tag{6.5.4}$$

which has the resulting Euler-Lagrange equations of motion

$$\begin{aligned} f'' + \frac{1}{\rho}f' - \frac{1}{\rho^2}f(N-a_\theta)^2 - \frac{\lambda}{2}f(f^2-1) = 0\,, \\ a_\theta'' - \frac{1}{\rho}a_\theta' + (N-a_\theta)f^2 = 0\,. \end{aligned} \tag{6.5.5}$$

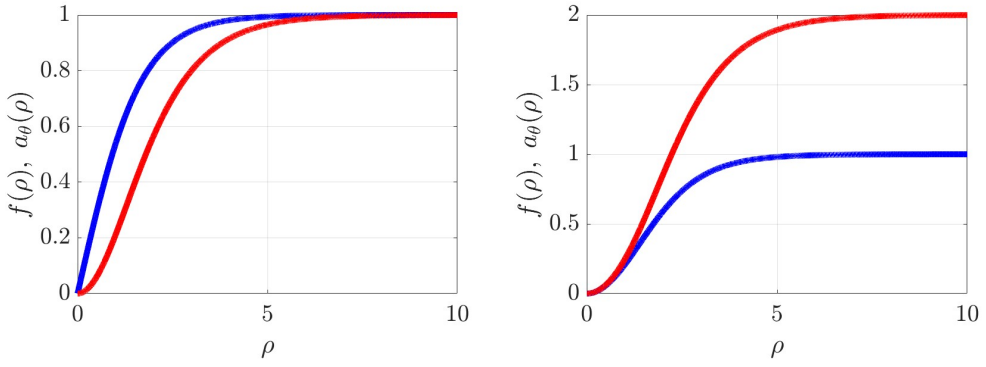

$N = 1$ $N = 2$

Figure 6.5.1: Profile functions for critically couple ($\lambda = 1$) vortex solutions, where blue is $f(\rho)$, and red is $a_\theta(\rho)$.

Regularity gives us the profiles at the origin $f(0) = 0$ and $a(0) = 0$ while the boundary conditions at infinity are,

$$\lim_{\rho\to\infty} f(\rho) = 1 \quad \text{and} \quad \lim_{\rho\to\infty} a_\theta(\rho) = N\,.$$

The coupled system eq. (6.5.5) is nonlinear and must be solved numerically, which is done using an arrested Newton flow algorithm, with 4^{th}-order finite difference for derivatives to minimise the energy.

Although there is no known analytic solution, we can study the asymptotic form of the solutions for both $\rho \sim 0$ and $\rho \to \infty$. First, we will consider f and a_θ near the origin, which admits the expansion

$$f(\rho) = \rho^N F(\rho^2), \qquad a_\theta(\rho) = \rho^2\, G(\rho^2), \tag{6.5.6}$$

where F and G are power series in ρ^2 with a non-zero coefficient for the leading term. Hence, we can write any general cylindrically symmetric solution of degree N as

$$\begin{aligned} \Phi &= (x_1 + ix_2)^N\, F(x_1^2 + x_2^2)\,, \\ A_\mu = (A_0, A_1, A_2) &= \begin{pmatrix} 0 \\ -x_2\, G(x_1^2 + x_2^2) \\ x_1\, G(x_1^2 + x_2^2) \end{pmatrix}, \end{aligned} \tag{6.5.7}$$

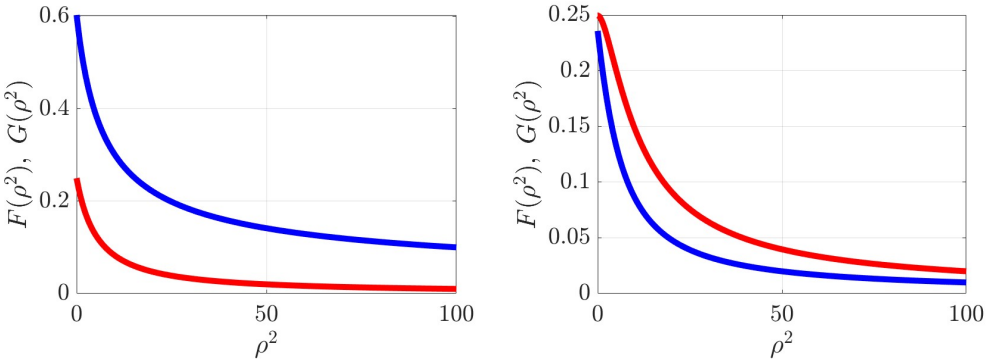

$N = 1$ $N = 2$

Figure 6.5.2: Profile functions for critically coupled ($\lambda = 1$) vortex solutions, where blue is $F(\rho^2)$, and red is $G(\rho^2)$.

where $F(\rho^2)$ and $G(\rho^2)$ are now nonlinear functions across the whole space, but can be expanded as a power series near zero.

The reduced energy functional is thus

$$V = \int \left(2\left(\sigma \frac{dG}{d\sigma} + G\right)^2 + \left(2\left(\frac{dF}{d\sigma}\right)^2 \sigma^2 + 2NF\frac{dF}{d\sigma}\sigma \right.\right. \\ \left.\left. + F^2\left(\frac{\sigma^2 G^2}{2} - NG\sigma + N^2\right)\right)\sigma^{N-1} + \frac{\lambda}{8}\left(\sigma^N F^2 - 1\right)^2 \right) \pi \, d\sigma, \tag{6.5.8}$$

with field equations

$$8\rho^2 F'' + 8F' - \lambda\rho^{2N}F^3 + \lambda F - 2\rho^2 FG^2 + 4N(FG + 2F') = 0\,, \\ 4\rho^2 G'' + 8G' + \rho^{2(N-1)}F^2(N - \rho^2 G) = 0\,. \tag{6.5.9}$$

6.6 Static Interaction

To consider the tails of the solutions, we linearise the system eq. (6.5.5) around the vacuum $(f, a_\theta) = (1, N)$ which produces a decoupled system of two ODEs which yield the solution

$$f(\rho) \sim 1 - \frac{q}{2\pi} K_0(\sqrt{\lambda}\rho)\,, \qquad a_\theta(\rho) \sim N - \frac{m}{2\pi}\rho\, K_1(\rho)\,. \tag{6.6.1}$$

We can now understand the long-range static intervortex forces by assuming that a vortex at long-range acts as a point source [66], each with an associated scalar charge q

and magnetic dipole moment m.

These point sources must satisfy the linear differential equations with solutions given in eq. (6.6.1). This leads to the linear interaction energy of two well separated point sources as

$$E_{\text{int}}(s) = -\frac{q}{2\pi}K_0(\sqrt{\lambda}s) + \frac{m}{2\pi}K_0(s)\,, \tag{6.6.2}$$

where s is the separation. The key result is that the contribution from the Higgs field interaction is negative, while the magnetic contribution is positive. Hence, for $\lambda < 1$ the Higgs field dominates at long range, causing vortices to attract, while for $\lambda > 1$ the magnetic field dominates at long range, causing vortices to repel [66].

At critical coupling ($\lambda = 1$), where the contributions from the Higgs field and magnetic field cancel each other out with $q = m$, which leads to no long-range interaction between static vortices.

For $s \to 0$, the interaction energy behaves as a 4^{th}-order polynomial in s [67]

$$E_{\text{int}}(s) = E_{\text{int}}(0) + \frac{1}{2}\omega^2_{\lambda;2,2}(0)\frac{s^4}{32\beta(\lambda)}, \tag{6.6.3}$$

where $E_{\text{int}}(0)$ is the static force of the radially symmetric 2-vortex and $\omega^2_{\lambda;2,2}(0)$ is the angular frequency for the 2-vortex splitting mode, see chapter 8. $\beta(\lambda)$ is a λ-dependent, numerically calculated constant.

We calculate the static force per vortex by solving the field equations in 2-dimensions at fixed separations, using an arrested Newton flow algorithm to find the minimal energy solutions. Note that we pin the vortices at desired distances d ranging from 0 to 10 in increments of 0.1. We hence have that the static interaction per vortex is

$$E_{\text{Static}}(d) = \frac{1}{2}\left(V_2^{\lambda}(d) - 2V_1^{\lambda}(0)\right), \tag{6.6.4}$$

where $V_1^{\lambda}(0)$ is the static energy of the $N = 1$ vortex, and $V_2^{\lambda}(s)$ is the static energy of the minimised $N = 2$ solution, where vortices are positioned at $\pm d$.

In figure 6.6.1, we plot the numerically calculated static interaction, eq. (6.6.4). We overlay the short-range and long-range approximation and plot for different λ.

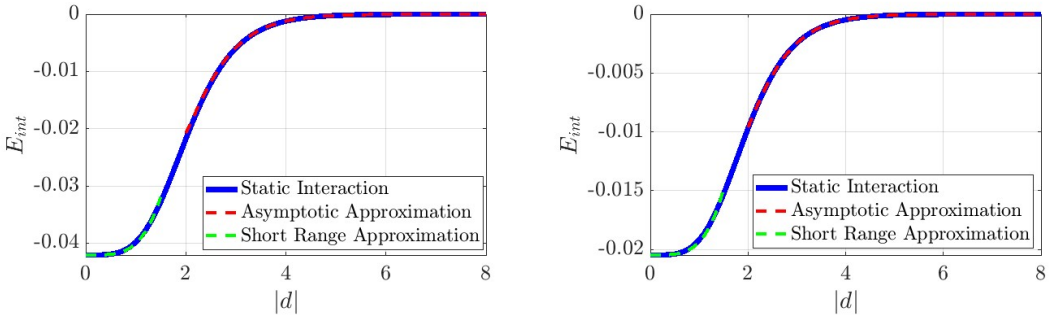

$\lambda = 0.8.$ $\lambda = 0.9.$

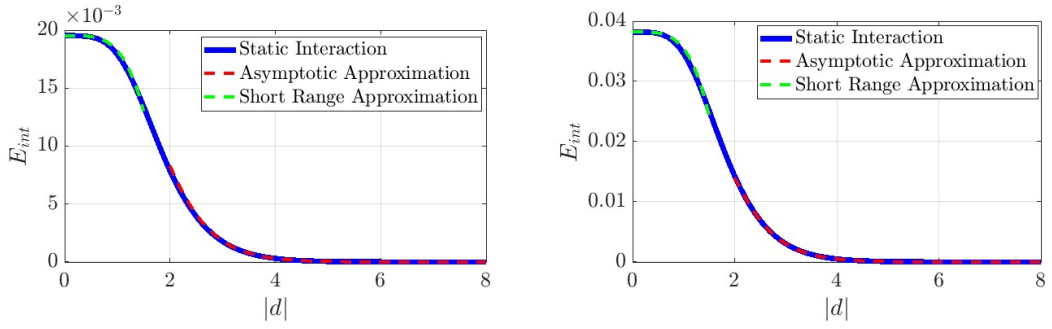

$\lambda = 1.1.$ $\lambda = 1.2.$

Figure 6.6.1: Static interaction energy per vortex for a 2-vortex system for a range of λ indicated by colour. The black dashed lines show the asymptotic fit of the interaction energy eq. (6.6.2). The dashed magenta lines show the fit for the short range interaction energy eq. (6.6.3)

6.7 Static Solutions

We now explore static vortex solutions in $2-$dimensions. We have the initial configuration

$$\begin{aligned} \phi_1(x_1, x_2) &= \mathcal{R}((x_1 + ix_2)^N) F(x_1^2 + x_2^2) \\ \phi_2(x_1, x_2) &= \mathcal{I}((x_1 + ix_2)^N) F(x_1^2 + x_2^2) \\ A_\mu(x_1, x_2) &= \begin{pmatrix} 0 \\ -x_2 G(x_1^2 + x_2^2) \\ x_1 G(x_1^2 + x_2^2) \end{pmatrix}, \end{aligned} \tag{6.7.1}$$

where F and G are the solutions of eq. (6.5.9).

We can simulate eq. (6.7.1) using a lattice of 601×601 points. We can then minimise the solution by numerically solving the gradient flow equations eqs. (6.2.17) and (6.2.18) using an arrested newton flow algorithm. We show the energy density eq. (6.2.3) and

condensate $|\phi|^2$ for a $N = 1$ vortex in figure 6.7.1 and a $N = 2$ vortex in figure 6.7.2.

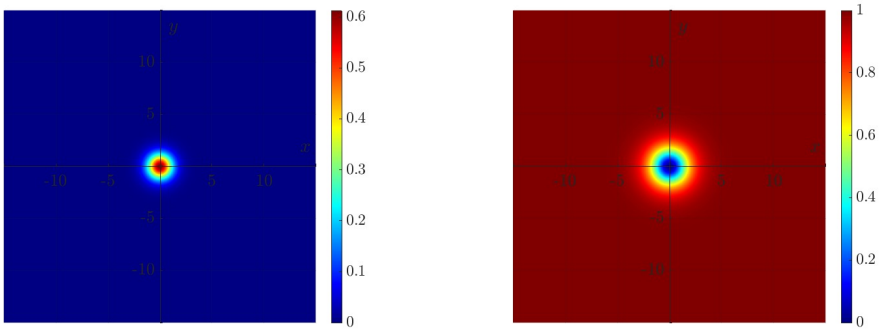

Figure 6.7.1: Static solution for a degree $N = 1$ vortex at critical coupling $\lambda = 1$). We plot the energy density (left) and the condensate $|\phi^2|$ (right).

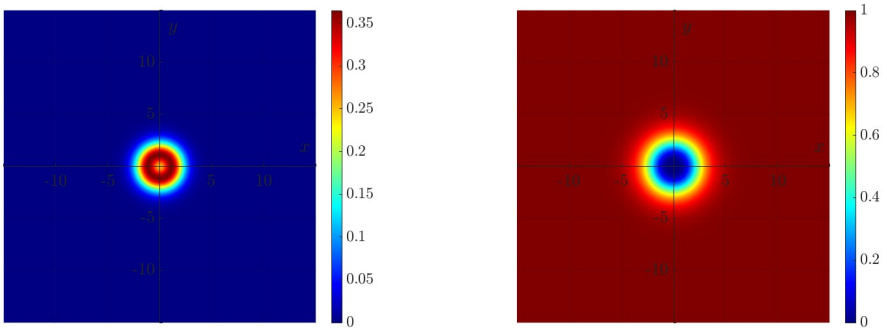

Figure 6.7.2: Static solution for a degree $N = 2$ vortex at critical coupling $\lambda = 1$). We plot the energy density (left) and the condensate $|\phi^2|$ (right).

6.8 Results

In this section, we discuss vortex scattering solutions at critical coupling ($\lambda = 1$). We only have one free parameter, being the separation of the vortices. In this chapter we consider head on scattering. We can also consider collisions with non-zero impact parameter. This can indeed be done, but is not the focus of this thesis, and is hence not presented here.

6.8.1 2-Vortex Solutions

We show snapshots from a simulation regarding BPS 2-vortex scattering, and we plot the energy density as a heat plot. The vortices are initially positioned at $(\pm 10, 0)$, with

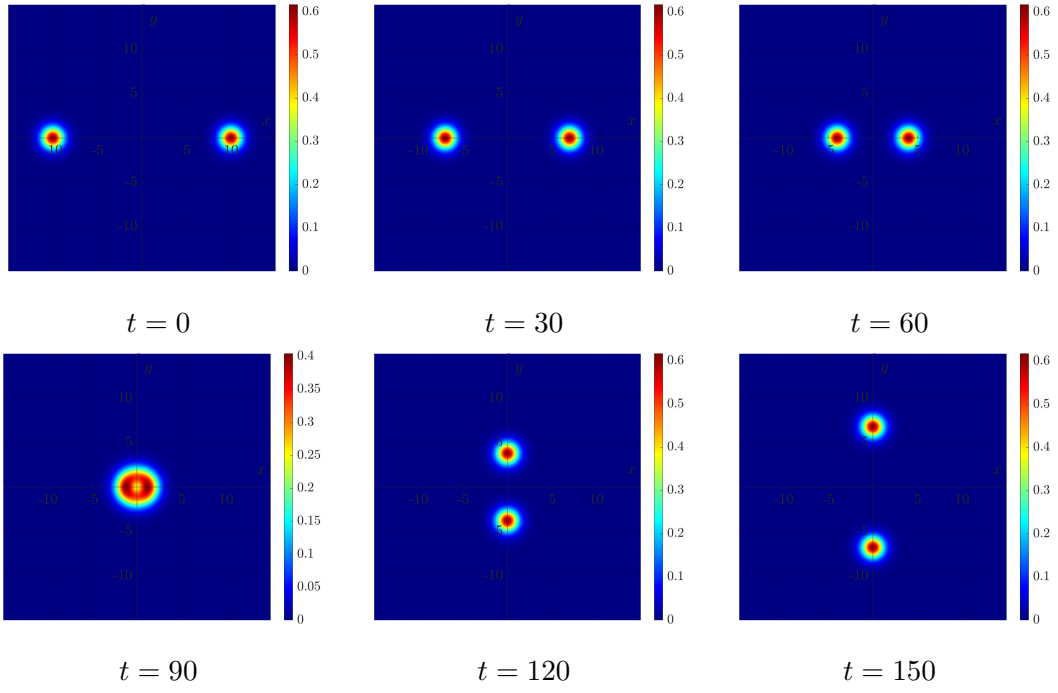

Figure 6.8.1: Heat plots for the energy density for values of $t = 0, 30, 60, 90, 120, 150$. We show 2-vortex head on scattering with with $v_i n = 0.1$.

initial velocity $v_{in} = 0.1$. We can see that the vortices scatter at right angles, and pass through each other remaining unchanged. This is confirmed in figure 6.4.1, whereby we find this is a key feature of vortex dynamics.

6.8.2 Multi-Vortex Scattering

Here we show snapshots of a head-on collision of two 2-vortices. In the case of scattering two $N = 1$ vortices, see figure 6.8.1, the vortices pass through the axially symmetric $N = 2$ configuration, before scattering at 90°. However, note that for $N > 1$ this is not the case. In fact, for the scattering of two $N = 2$ vortices, we observe that the two $N = 2$ vortices split into a configuration with four $N = 1$ vortices. An important observation is that the resulting $N = 1$ constituent vortices begin to oscillate in shape, suggesting that a shape mode for the 1-vortices has been naturally excited. This is indeed hard to see in figure 6.8.2, however, notice that the peaks in the energy density of the inner two vortices change as the vortices evolve.

We can also scatter two $N = 3$ vortices, see figure 6.8.3, where we display a heat plot for the energy density, at snapshots of a dynamical simulation. The vortices scatter head on, with initial velocity $v_{\text{in}} = 0.3$.

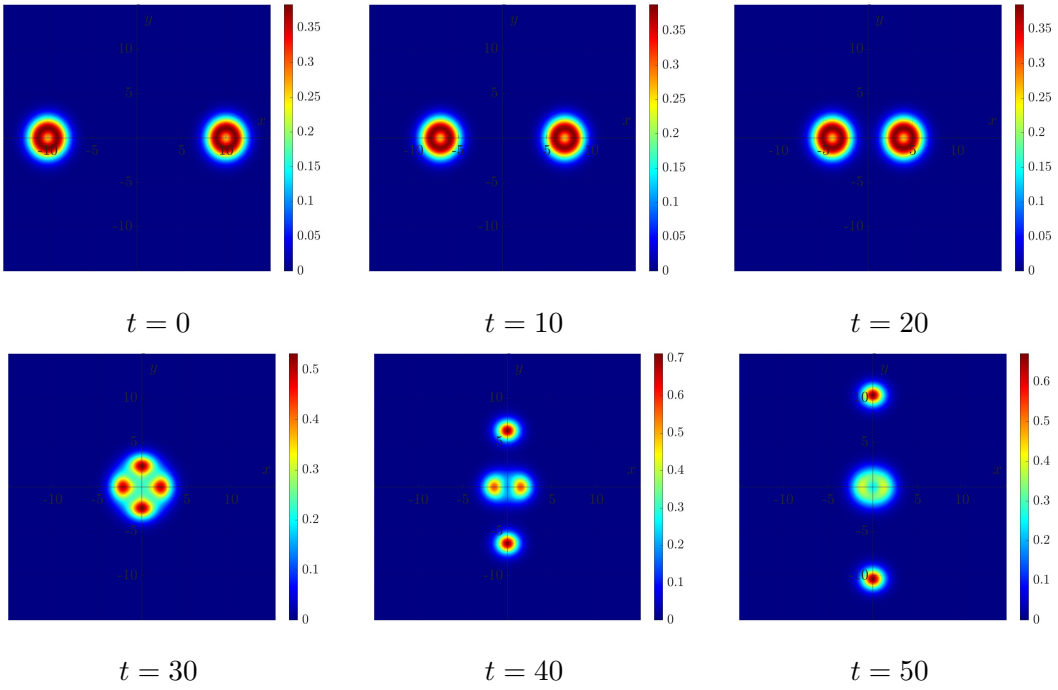

Figure 6.8.2: Heat plots for the energy density for values of $t = 0, 10, 20, 30, 40, 50$. We show two $N = 2$ vortices in a head on scattering with with $v_{\text{in}} = 0.3$.

We observe that the vortices initially travel as $N = 3$ radially symmetric solutions. When the vortices come close, they split into the constituent 1-vortex parts. Two of the vortices are accelerated towards infinity. Two are sent to infinity with a smaller velocity. Most interestingly, we notice the inner two vortices, located closest to the origin. During the scattering process, the kinetic energy from the vortices is transferred to the non-zero energy shape mode of the constituent vortices. This leads to the vortices at the centre forming a quasi-bound state, where they appear to scatter multiple times. This motivates chapter 9, where we aim to reproduce this phenomenon.

6.9 Conclusion

This chapter has explored the dynamics and static properties of vortices within the $(2+1)$-dimensional Abelian Higgs model, a relativistic field theory giving rise to topologically stable solitons. We began by introducing the model's Lagrangian and its second-order equations of motion. The single parameter λ was shown to govern vortex interactions, delineating type I ($\lambda < 1$) attractive, type II ($\lambda > 1$) repulsive, and critically coupled ($\lambda = 1$) regimes, the latter being our primary focus in this chapter.

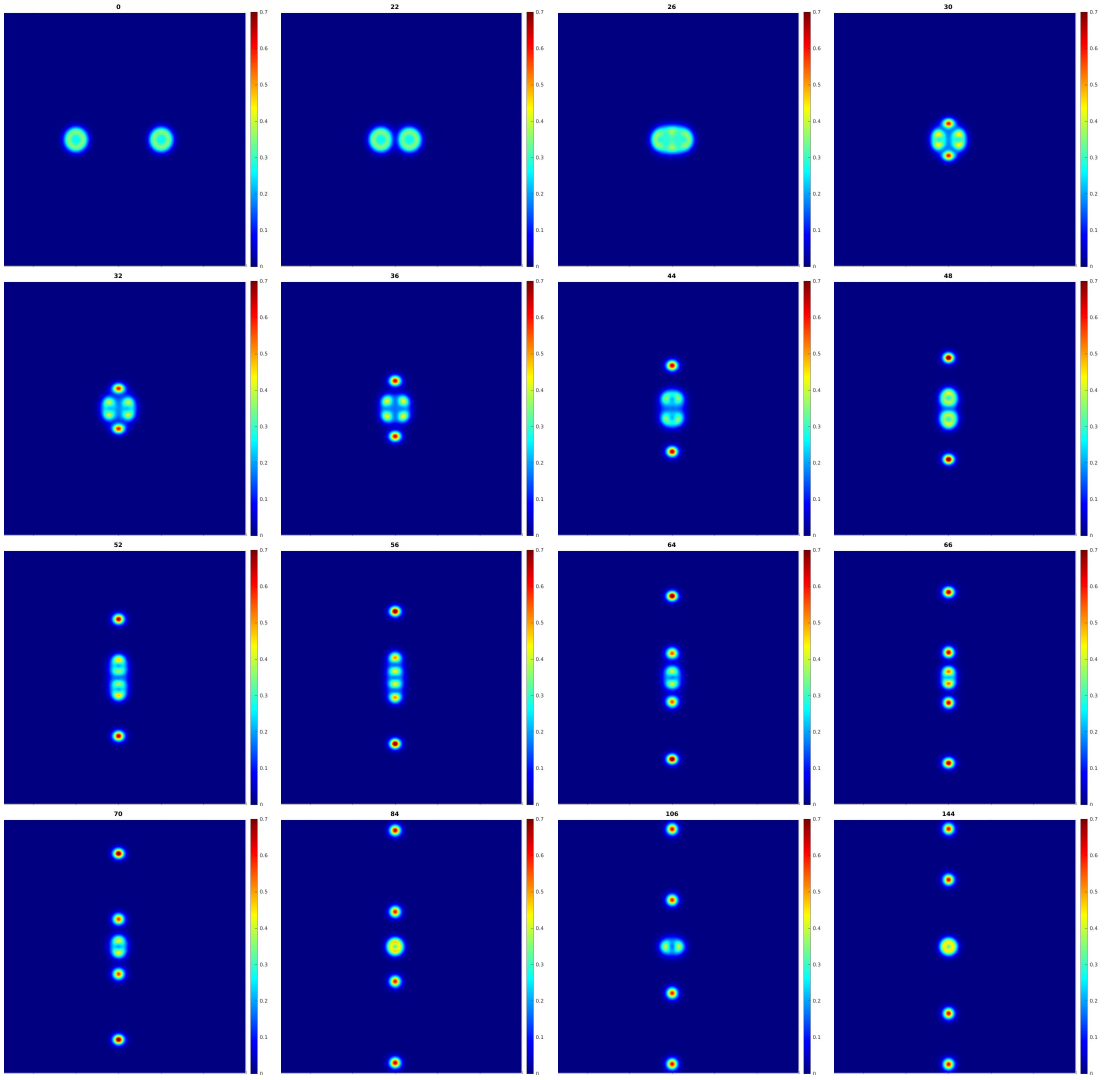

Figure 6.8.3: Heat plots for the energy density for values of $t = 0, 10, 20, 30, 40, 50$. We show 3-vortex 3-vortex head on scattering with with $v_{\text{in}} = 0.3$.

At critical coupling, we discussed that the N-vortex system is elegantly described by a moduli space $\mathcal{M}_N = \mathbb{C}^N/S_N$, where low energy dynamics reduce to geodesic motion. This framework successfully captures the hallmark 90° scattering of vortices in head-on collisions, a result numerically validated by tracking the zeros of the Higgs field across various initial velocities.

The Bogomolny bound at critical coupling, saturated by the BPS equations, provided a theoretical foundation for understanding minimal energy configurations, while numerical simulations of $N = 2$ vortex, $N = 3$ vortex, and multi-vortex scattering illuminated the complexity of their interactions. Notably, head-on collisions of higher-degree vortices (e.g. $N = 2$ and $N = 3$) showcased splitting into constituent $N = 1$ vortices, with

kinetic energy exciting shape modes that hint at quasi-bound states, an observation motivating further investigation in subsequent chapters.

In summary, this chapter has established a comprehensive picture of Abelian Higgs vortices at critical coupling, blending analytical insights from the moduli space approximation with robust numerical methods to explore their static and dynamic behaviour. These findings underscore the interplay between topological stability, geodesic motion, and field interactions, laying the groundwork for deeper studies into vortex scattering phenomena and their potential cosmological implications.

Chapter 7

Non-Linear Numerical Methods

We seek dynamic solutions of the equations of motion eqs. (6.2.17) and (6.2.18), which we find by numerically evolving the equations of motion from an initial condition of well separated Lorentz boosted vortices. We discretise the fields on a regular grid of $n_1 \times n_2$ lattice sites with spacing $h > 0$, where the discretised configuration space is the manifold $\mathcal{C} = (\mathbb{C} \times \mathbb{R}^3)^{n_1 n_2} \cong \mathbb{R}^{5n_1 n_2}$. We approximate the first- and second-order spatial derivatives using central 4^{th} order finite difference operators, generating a discrete approximation to the equations of motion. We then evolve the discretised fields using a 2^{nd} order leapfrog method with time step $\Delta_t = 0.01$ [16]. We typically use $n_1 = n_2 = 601$ and $h = 0.1$ throughout.

7.1 Lorentz Transformation

For dynamical simulations where we require the vortices to have an initial velocity, we perform a Lorentz transformation to boost the coordinates.

We will first consider a boost in the x_1-direction. Our coordinates then transform as

$$t \mapsto \tilde{t} = \gamma(t + vx_1), \qquad x \mapsto \tilde{x_1} = \gamma(x_1 + vt), \qquad x_2 \mapsto \tilde{x_2} = x_2, \tag{7.1.1}$$

where $\gamma = \frac{1}{\sqrt{1-v^2}}$ is the Lorentz factor. We write this transformation as a vector equation $\tilde{x} = \Lambda x$, where

$$\Lambda = \begin{pmatrix} \gamma & \gamma v & 0 \\ \gamma v & \gamma & 0 \\ 0 & 0 & 1 \end{pmatrix}, \qquad \Lambda^{-1} = \begin{pmatrix} \gamma & -\gamma v & 0 \\ -\gamma v & \gamma & 0 \\ 0 & 0 & 1 \end{pmatrix}, \tag{7.1.2}$$

The Higgs field transforms trivially as

$$\phi(x) \mapsto \tilde{\phi}(x) = \phi(\Lambda^{-1}x), \tag{7.1.3}$$

and the gauge field transforms the same as the derivative of ϕ, hence

$$A^{\mu}(x) \mapsto \tilde{A^{\mu}}(x) = \Lambda A^{\mu}(\Lambda^{-1}x). \tag{7.1.4}$$

If we wish to boost in any direction, then we can consider the $SO(3)$ rotation matrix

$$R = \begin{pmatrix} 1 & 0 & 0 \\ 0 & \cos\tau & -\sin\tau \\ 0 & \sin\tau & \cos\tau \end{pmatrix}, \tag{7.1.5}$$

and apply it to the boost such that $\hat{\Lambda} = R\Lambda$, where τ is angular direction of the boost. This transformation can be written as one matrix

$$\hat{\Lambda} = \begin{pmatrix} \gamma & \gamma v\cos\tau & \gamma v\sin\tau \\ \gamma v\cos\tau & \gamma\cos^2\tau + \sin^2\tau & (\gamma-1)\cos\tau\sin\tau \\ \gamma v\sin\tau & (\gamma-1)\cos\tau\sin\tau & \gamma\sin^2\tau + \cos^2\tau \end{pmatrix}. \tag{7.1.6}$$

7.2 Arrested Newton Flow

We find energy minimisers to nonlinear systems such as Baby Skyrmions and Abelian Higgs Vortices, using a gradient descent method. The model is discretised on a grid of dimension that of the field theory. For the case of vortices, we consider a two-dimensional grid. This approximates a given energy functional as a discrete approximation.

We define a vector for the fields such that

$$\xi_a = (\phi_1, \phi_2, A_1, A_2),$$

where ϕ is the Higgs field and A_i the components of the vector gauge potential.
The time evolution can hence be approximated using a simple Euler method

$$\xi_a^{(n+1)} = \xi_a^{(n)} + \Delta_t \dot{\xi}_a^{(n)}, \tag{7.2.1}$$

$$\dot{\xi}_a^{(n+1)} = \dot{\xi}_a^{(n)} + \Delta_t \ddot{\xi}_a^{(n)}, \tag{7.2.2}$$

where $\xi_a^{(n)}$ is the field configurations at a time t, and $\xi_a^{(n+1)}$ are the field configurations at the time $t + \Delta_t$, given an arbitrary constant such that $\Delta_t \ll 1$. $\dot{\xi}$ is the first order time derivatives of the fields, and we start with the initial data $\dot{\xi}_a = 0$. We denote the second-order time derivatives of the fields as $\ddot{\xi}_a$, and we find the solution, that is, the local minimum, where $\ddot{\xi}_a = 0$.
The arrested Newton flow is an evolution-based approach that halts the flow of the gradient descent by means of an arresting condition to stop the descent from overshooting the minimum and oscillating indefinitely. Rather than iteratively applying discrete updates, it defines a flow in phase space that drives an initial guess toward a zero of a vector field, with an 'arrest' mechanism to stabilise convergence near the solution [68, 69, 71]. The arresting condition is as follows. If

$$\dot{\xi}_a \cdot \ddot{\xi}_a < 0, \tag{7.2.3}$$

then we force the velocity of the fields to be zero, i.e. $\dot{\xi}_a = 0$, and resume the gradient descent. This can be interpreted as the acceleration ($\ddot{\xi}$) being in the opposite half-plane to the velocity ($\dot{\xi}$). This interpretation arises because the negative dot product in eq. (7.2.3) indicates that the angle between $\dot{\xi}_a$ and $\ddot{\xi}_a$ exceeds 90 degrees, placing them in opposite half-planes relative to the origin in phase space, which signals a potential overshoot of the minimum [68].

7.3 Numerical Time Integration Methods

The leapfrog method [16, 37] is a symplectic, second-order accurate time-stepping algorithm used to solve time-dependent second-order partial differential equations (PDEs).

It is particularly suited for evolving the equations of motion in the Abelian Higgs model due to its stability and accuracy for oscillatory systems. True to its name, the leapfrog method 'leaps' over intermediate steps.

For a given second-order ordinary or partial differential equation, let

$$\frac{\partial^2 \xi_a}{\partial t^2} = f_a(\xi, \nabla\xi, t), \tag{7.3.1}$$

which can be rewritten as a system of first-order equations

$$\dot{\xi}_a = \frac{\partial \xi_a}{\partial t}, \tag{7.3.2}$$

$$\ddot{\xi}_a = f_a(\xi, \nabla\xi, t). \tag{7.3.3}$$

We can iterate these quantities using the velocity Verlet form of the leapfrog method as

$$\xi_a^{(n+1)} = \xi_a^{(n)} + \Delta_t \dot{\xi}_a^{(n)} + \frac{\Delta_t^2}{2} f_a(\xi^{(n)}, \nabla\xi^{(n)}, t_n), \tag{7.3.4}$$

$$\dot{\xi}_a^{(n+1)} = \dot{\xi}_a^{(n)} + \frac{\Delta_t}{2}\left(f_a(\xi^{(n)}, \nabla\xi^{(n)}, t_n) + f_a(\xi^{(n+1)}, \nabla\xi^{(n+1)}, t_{n+1})\right), \tag{7.3.5}$$

where $\xi_a^{(n)}$ is the field configuration at time t_n, and $\xi_a^{(n+1)}$ is the field configuration at time $t_{n+1} = t_n + \Delta_t$. Equation (7.3.4) updates the field ξ_a using a second-order Taylor expansion, incorporating the acceleration f evaluated at time t_n. Equation (7.3.5) updates the velocity $\dot{\xi}_a$ using a trapezoidal rule, averaging the acceleration at times t_n and t_{n+1} to achieve second-order accuracy [81].

This second-order method is useful for vortex scattering as it is symplectic, meaning that geometric quantities are conserved by the integration method. This provides advantages in maintaining stability and accuracy during large integration times. The method is also of second-order. As such, it is more efficient in terms of computational resources, which is essential in our case because of the volume of results.

For longer integration times, higher-order methods can reduce truncation errors. The 6th-order leapfrog method, based on Yoshida's symplectic integrator [81], achieves this by composing multiple second-order leapfrog steps with specific weights. For a sixth-order method, we use seven stages with weights [81]

$$w_0 = w_6 = \frac{1}{2(1 - \sqrt[3]{2})}, \qquad w_1 = w_5 = \frac{1 - \sqrt[3]{2}}{2(1 - \sqrt[3]{2}) + \sqrt[3]{4}},$$

$$w_2 = w_4 = \frac{\sqrt[3]{2} - 1}{2(1 - \sqrt[3]{2}) + \sqrt[3]{4}}, \qquad w_3 = \frac{2 - \sqrt[3]{4}}{2(1 - \sqrt[3]{2}) + \sqrt[3]{4}},$$

such that $\sum_{i=0}^{6} w_i = 1$. We define cumulative time fractions $d_0 = 0$, $d_i = d_{i-1} + \frac{w_{i-1}+w_i}{2}$ for $i = 1, \ldots, 6$, where $d_6 = 1$. The fields are advanced through seven substeps as follows:

$$\xi_a^{(n+d_i)} = \xi_a^{(n+d_{i-1})} + w_i \Delta_t \dot{\xi}_a^{(n+d_{i-1})} + \cdots$$
$$\cdots + \frac{(w_i \Delta_t)^2}{2} f_a(\xi^{(n+d_{i-1})}, \nabla\xi^{(n+d_{i-1})}, t_n + d_{i-1}\Delta_t), \tag{7.3.6}$$
$$\dot{\xi}_a^{(n+d_i)} = \dot{\xi}_a^{(n+d_{i-1})} + \frac{w_i \Delta_t}{2} \big(f_a(\xi^{(n+d_{i-1})}, \nabla\xi^{(n+d_{i-1})}, t_n + d_{i-1}\Delta_t) + \cdots$$
$$\cdots + f_a(\xi^{(n+d_i)}, \nabla\xi^{(n+d_i)}, t_n + d_i\Delta_t) \big), \tag{7.3.7}$$

We advance the fields from time t_n to t_{n+1} through seven substeps, $i = 0, \ldots, 6$, with intermediate times $t_n + d_i\Delta_t$. The weights w_i scale the time increments such that the total step satisfies $\sum_i w_i = 1$. The first equation updates the field ξ_a using a second-order Taylor expansion with velocity and acceleration at the previous substep $t_n + d_{i-1}\Delta_t$. The second equation updates the velocity $\dot{\xi}_a$ using a trapezoidal rule, averaging the acceleration at substeps $t_n + d_{i-1}\Delta_t$ and $t_n + d_i\Delta_t$. The combination of these substeps with specific weights cancels lower-order error terms, achieving sixth-order accuracy [81].

7.4 Natural Boundary Conditions

We impose natural boundary conditions [69], so that radiation may leave the system by passing through the boundary. We denote the dynamical fields collectively as ξ_a, $a = 0, .., 5$, consisting of the real and imaginary components of ϕ, as well as the 3 components of the vector gauge potential. We take the variation of the action eq. (6.2.1) with respect to ξ_a, so that the action varies as

$$\delta S = \int_\Omega \left(\frac{\partial \mathcal{L}}{\partial \xi_a} - \partial_i \left(\frac{\partial \mathcal{L}}{\partial(\partial_i \xi_a)} \right) \right) \delta\xi_a + \int_{\partial\Omega} \left(-n_i \frac{\partial \mathcal{L}}{\partial(\partial_i \xi_a)} \right) \delta\xi_a, \tag{7.4.1}$$

where Ω is the finite domain in space-time that we perform our simulations on, and $\partial\Omega$ is the boundary of the domain. Furthermore, the divergence theorem has been used so that the flux of the variation of S through the boundary curve $\partial\Omega$ is the same as the surface integral of the divergence of the variation of S across the entire region Ω. It should be noted that n_i is the inward pointing normal to $\partial\Omega$. We require that $\delta S = 0$

be such that ξ_a satisfies the Euler-Lagrange equations in Ω. Henceforth, we have the boundary conditions

$$n_i \frac{\partial \mathcal{L}}{\partial(\partial_i \xi_a)} = 0 \tag{7.4.2}$$

on the boundary $\partial\Omega$. First, we consider the boundary $x_1 = \pm\infty$. For the energy eq. (6.2.3), the boundary condition eq. (7.4.2) reduces to

$$\begin{aligned}
\begin{pmatrix} 1 \\ 0 \end{pmatrix} \cdot \begin{pmatrix} \partial_1\phi_1 + A_1\phi_2 \\ \partial_2\phi_1 + A_2\phi_2 \end{pmatrix} &= 0 \Rightarrow \partial_1\phi_1 = -A_1\phi_2, \\
\begin{pmatrix} 1 \\ 0 \end{pmatrix} \cdot \begin{pmatrix} \partial_1\phi_2 - A_1\phi_1 \\ \partial_2\phi_2 - A_2\phi_1 \end{pmatrix} &= 0 \Rightarrow \partial_1\phi_2 = A_1\phi_1, \\
\begin{pmatrix} 1 \\ 0 \end{pmatrix} \cdot \begin{pmatrix} \partial_1 A_2 - \partial_2 A_1 \\ 0 \end{pmatrix} &= 0 \Rightarrow \partial_1 A_2 = \partial_2 A_1 \\
\begin{pmatrix} 1 \\ 0 \end{pmatrix} \cdot \begin{pmatrix} \partial_0 A_1 - \partial_1 A_0 \\ 0 \end{pmatrix} &= 0 \Rightarrow \partial_1 A_0 = \partial_0 A_1.
\end{aligned} \tag{7.4.3}$$

We must also consider the boundary $x_2 = \pm\infty$

$$\begin{aligned}
\begin{pmatrix} 0 \\ 1 \end{pmatrix} \cdot \begin{pmatrix} \partial_1\phi_1 + A_1\phi_2 \\ \partial_2\phi_1 + A_2\phi_2 \end{pmatrix} &= 0 \Rightarrow \partial_2\phi_1 = -A_2\phi_2, \\
\begin{pmatrix} 0 \\ 1 \end{pmatrix} \cdot \begin{pmatrix} \partial_1\phi_2 - A_1\phi_1 \\ \partial_2\phi_2 - A_2\phi_1 \end{pmatrix} &= 0 \Rightarrow \partial_2\phi_2 = A_2\phi_1, \\
\begin{pmatrix} 0 \\ 1 \end{pmatrix} \cdot \begin{pmatrix} \partial_1 A_2 - \partial_2 A_1 \\ 0 \end{pmatrix} &= 0 \\
\begin{pmatrix} 0 \\ 1 \end{pmatrix} \cdot \begin{pmatrix} \partial_0 A_2 - \partial_2 A_0 \\ 0 \end{pmatrix} &= 0 \Rightarrow \partial_2 A_0 = \partial_0 A_2.
\end{aligned} \tag{7.4.4}$$

Note that from the finite energy conditions, $B \to 0$ on $\partial\Omega$, so we have that $\partial_1 A_2 = \partial_2 A_1$. Furthermore, we are working in a discretised version of a continuous theory, so we must also discretise our boundary conditions, which give us equations for ghost points, which are temporary points that exist past the boundary. These allow us to calculate the

numerical derivatives on the boundary.

These boundary conditions can be summarised such that the covariant derivative tends to zero normal to the boundary at infinity, as well as the magnetic field, i.e.

$$\begin{aligned} \mathbf{n} \cdot (\nabla - i\mathbf{A})\Phi = n_i \cdot D_i\Phi = 0 \text{ on } \partial\Omega \\ \text{curl}\mathbf{A} = \nabla \times \mathbf{A} = \mathbf{B} = 0 \text{ on } \partial\Omega \end{aligned} \tag{7.4.5}$$

where $\mathbf{A}$ are the spatial components of a 4 component 1-form, with the x_3-dependence set to zero, and $\mathbf{B} = B\mathbf{k}$, which is a 3 vector whose only non-zero component is in the x_3-direction.

We must impose a further constraint on the boundary such that the first-order time derivative of the electric potential A_0 goes to 0 on $\partial\Omega$, i.e. $\partial_0 A_0 = 0$. This constraint is necessary for numerical stability.

We can compare the phase $\theta = \arctan(\frac{\phi_2}{\phi_1})$ (although not gauge invariant) of an axially symmetric $N = 2$ vortex, at $\lambda = 1$, moving with constant velocity in the x_1 direction, both with natural boundary conditions and without; see figure 7.4.1.

We can see from figure 7.4.1 that the natural boundary conditions are essential for stable vortex dynamics. With fixed boundary conditions (left), we see that the numerics fail after $t = 494$ and there is a discontinuity between the phase on the boundary and the phase in the bulk. This leads to radiation in the fields, likely from planar waves incoming from the boundary, as a result of the discontinuity between the field values at the boundary and the bulk.

Alternatively, we see, by implementing natural boundary conditions (right), that the phase winds smoothly around the boundary as the vortex moves, and the numerical simulation remains stable.

7.5 Gauge Choices

During the development of the numerics, we considered many gauge choices motivated by work on vortex scattering [17, 58, 59, 64]. One option is the temporal gauge $A_0 = 0$, which can be achieved by using a gauge transformation to impose this condition after the boost. Alternatively, for static solutions we choose $A_0 = 0$. When boosting the solution, A_0 becomes non-zero because of A_1, hence we can transform $A_1 = 0$ through a gauge transformation before a Lorentz boost, such that A_0 is still zero after the boost. However,

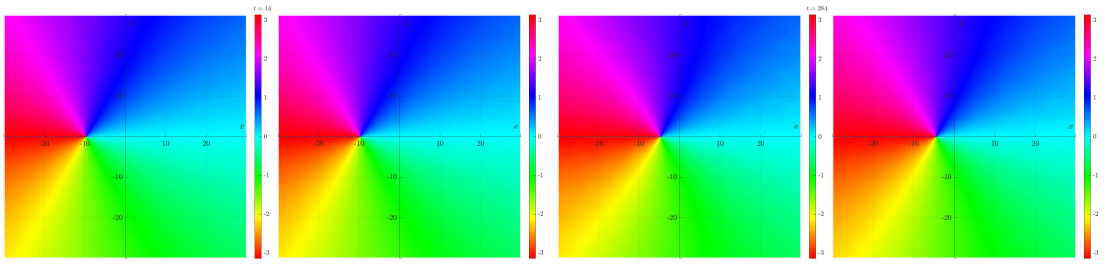

$t = 0$ $t = 284$

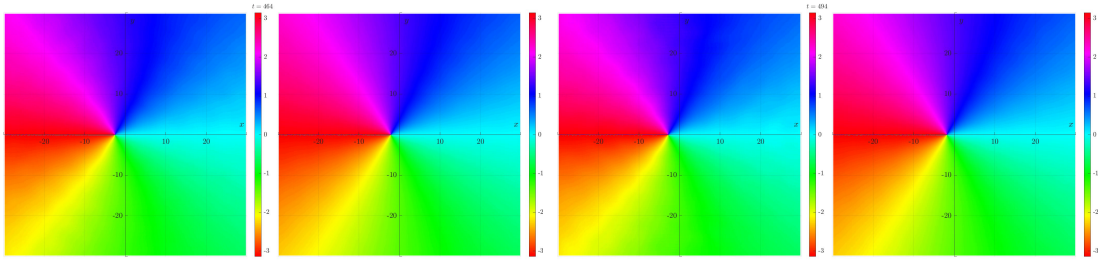

$t = 464$ $t = 494$

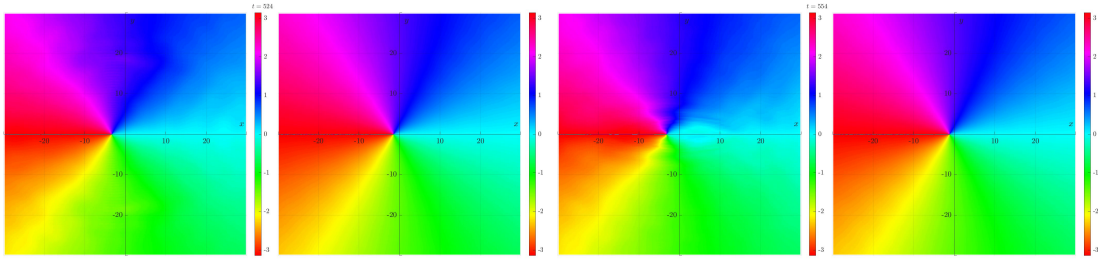

$t = 524$ $t = 554$

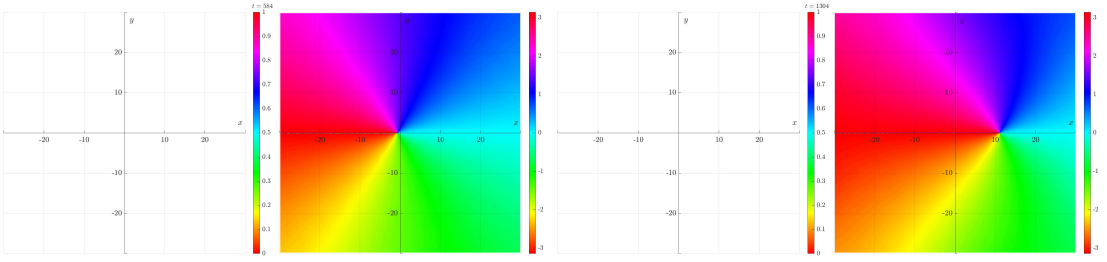

$t = 584$ $t = 1304$

Figure 7.4.1: We plot the phase $\theta = \arctan(\frac{\phi_2}{\phi_1})$ of a critically coupled $N = 2$ vortex moving with constant velocity in the x_1 direction. We display fixed boundary conditions (left) and natural boundary conditions (right).

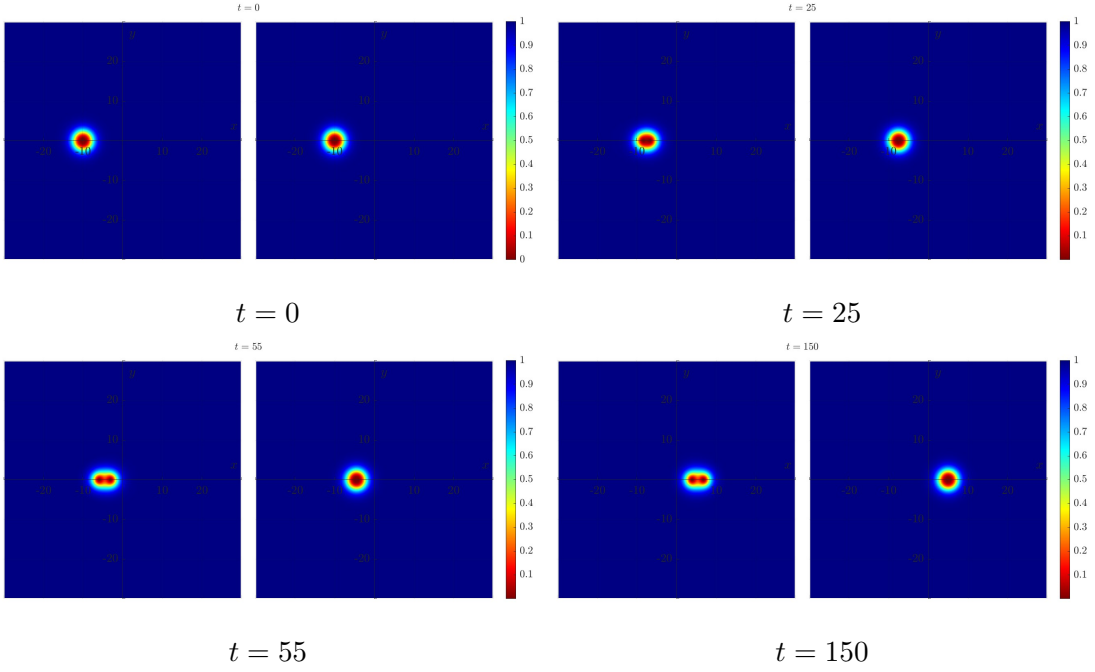

Figure 7.5.1: We show heat plots of the condensate $|\phi|^2$ of a critically coupled $N = 2$ vortex moving with constant velocity in the x_1 direction. We impose the temporal gauge $A_0 = 0$ (left) and the Lorenz gauge $\partial_\mu A^\mu = 0$ (right).

this temporal gauge is not compatible with the natural boundary conditions, as the it does not provide an equation for the derivatives of the gauge field on the boundary. Hence, we chose the Lorenz gauge $\partial_\mu A^\mu = 0$, as it is compatible with the natural boundary conditions (detailed in section 7.4). The Lorenz gauge can be imposed in two ways. First, we can subsitute the relation $\partial_\mu A^\mu = 0$ into the Euler-Lagrange equations of motion (eqs. (6.2.17) and (6.2.18)), which results in an independant equation of motion for A_0. Alternatively, we can add the term $\frac{1}{2}\partial_\mu A^\mu \partial_\mu A^\mu$ to the lagrangian density $\mathcal{L}$. Note that we can check the numerics for a static vortex by checking that the gauge-invariant quantities remain consistent no matter the gauge choice.

Figure 7.5.1 shows snapshots of a dynamical simulation, in which we display the modulus of the Higgs field as a heat plot. The simulation on the left-hand side of each time stamp evolves with the temporal gauge imposed, $A_0 = 0$, whereas on the right, we impose the Lorenz gauge $\partial_\mu A^\mu = 0$. The simulation in question involves a critically coupled $N = 2$ vortex, with constant velocity in the x_1 direction. We see that with the temporal gauge, the vortex splits along the x_1 axis, which is an artefact of the difficulty to impose the temporal gauge. On the other hand, we notice that with the Lorenz gauge, the 2-vortex moves with constant velocity, maintaining its radial symmetry. This supports the choice of the Lorenz gauge for Abelian Higgs vortex dynamics.

7.6 Damping Boundary Conditions

Natural boundary conditions have been imposed to allow the phase to wind around the boundary as the fields evolve. Moreover, since we use a large intensity in exciting the vortex shape mode, the dynamical solution exhibits radiation. Therefore, we have implemented damping boundary conditions near the boundary. We subtract the first-order time derivatives of the fields orthogonal to the gauge orbit, multiplied by a function $K(x)$ from the equations of motion. Specifically, for the Higgs field, we modify the equation of motion to $\frac{\delta S}{\delta \phi} - K(x) D_0 \phi$, and for the gauge potential, we use $\frac{\delta S}{\delta A_i} - K(x) e_i$, where $e_i = \partial_i A_0 - \partial_0 A_i$. $K(x)$ has boundary conditions $K(0) = 0$ and $K(\infty) = 1$, and is of the form

$$K(x) = 1 - (1 - e^{\alpha(|x_1| - x_1^b)^2})(1 - e^{\alpha(|x_2| - x_2^b)^2}), \tag{7.6.1}$$

where x_i^b is the location of the boundary. This function ensures damping is applied only near the boundary, with the constant α chosen such that the damping region spans approximately 10% of the bulk from the boundary, minimising interference with the interior dynamics [53].

Although natural boundary conditions should allow for the radiation to pass through the boundary, some is reflected. The damping boundary conditions ensure that most of the radiation is absorbed so that it is not reflected back toward the bulk, affecting the behaviour the vortices.

Note that the damping boundary conditions are not perfect and that not all radiation is absorbed. To provide numerically accurate results, we altered the boundary conditions for a lattice of size 601×601 by varying the constant α, so that the solution matches that of a solution found in a lattice of size 2001×2001, whereby the grid is sufficiently large so that the radiation takes a long time to return to the system. Furthermore, we fine-tuned the boundary conditions by choosing the best α so that there is as little radiation as possible.

7.7 Zero Tracking

For analysing vortex dynamics, it is useful to track the zeros of the Higgs field to track the positions of the vortices. We design a tracking algorithm to identify and follow the positions of vortices in an Abelian Higgs model over a discretised two-dimensional spatial grid. We can interpret the vortices as point-like particles, treating the zero of the Higgs

field as the position of the vortices, $|\phi|^2 = 0$. The algorithm leverages a combination of field analysis, polynomial fitting, optimisation techniques, and intersection detection to locate these zeros with sub-grid precision. This section outlines the key methods employed in the algorithm.

Initially, we scan the entire grid to locate the vortex position. For each point on the grid (i, j), the modulus $|\phi|^2$ is evaluated. A point is considered a zero if $|\phi|^2 \leq 0.1$, a threshold chosen to identify regions near zeros of the field. This criterion is computationally efficient and ensures that potential vortices are not missed, although it requires further refinement.

To achieve sub-grid accuracy for the positions of the vortices that are close to each other, we fit a bivariate quadratic polynomial to the modulus $|\phi|^2$ in a local neighbourhood around each candidate point. We choose a 5×5 grid of data points to sample around the zero, centred at (i, j). The fitted polynomial is of the form

$$f(x) = ax_1^2 + bx_2^2 + cx_1 + dx_2 + e, \tag{7.7.1}$$

where a, b, c, d, e are coefficients determined by solving a linear system. The system is constructed as $A\mathbf{c} = \mathbf{b}$, where A is the design matrix with columns corresponding to $x_1^2, s_2^2, x_1, x_2, 1$, $\mathbf{b}$ is the vector of sampled values of $|\phi|^2$, and $\mathbf{c} = [a, b, c, d, e]^T$ is solved using Gaussian elimination. The minimum of this quadratic surface, found analytically as $x_1 = -c/(2a)$ and $x_2 = -d/(2b)$, provides an initial estimate of the position of the vortex, assuming $a, b > 0$, which indicates a local minimum. To refine this estimate, we employ two optimisation techniques. First, we consider the Nelder-Mead Simplex Method. An initial simplex is constructed around the candidate position and we evaluate the polynomial at the vortex position. The polynomial is minimised using the amoeba method, adjusting the simplex iteratively to converge on the minimum. If Nelder-Mead fails and a minimal solution is not found, a coordinate descent algorithm is used as a fallback, iteratively optimising x_1 and x_2 while keeping the other coordinate fixed. The resulting zero is stored as the vortex position if it is sufficiently distinct from previously identified vortices (checked via a distance threshold of 2 units).

For well separated vortices, it is computationally effective to consider tracking the zero contours of ϕ_1 and ϕ_2, the real and imaginary components of the Higgs field. We detect the zeros of ϕ_1 and ϕ_2 using linear interpolation between the grid points where ϕ_1 or ϕ_2 changes sign. Next, we fit polynomial curves up to second-order to the zero contours

using the Nelder-Mead method to minimise the sum of squared errors (SSE). To calculate the vortex zero, we find the intersection of the $\phi_1 = 0$ and $\phi_2 = 0$ contours. This method ensures robustness by directly targeting the field zeros rather than relying solely on the modulus.

The refined position is accepted only if it is sufficiently distinct from other vortices and it remains close to the position calculated in the subsequent time step. If these conditions fail, the algorithm may flip the vortex position across the origin (assuming a head-on scattering) or revert to the previous position, ensuring continuity.

7.8 Finite Difference Approximation

We employ finite difference approximations to discretise spatial derivatives in the equations of motion eqs. (6.2.17) and (6.2.18), enabling numerical evolution on a grid. These approximations replace derivatives with differences based on function values at discrete points, using Taylor expansions to determine their accuracy, which depends on the step size $\Delta x_1 = \Delta x_2 = h$. We define $f^{(i,j)}$ as the function value $f(x_1^{(i)}, x_2^{(j)})$ at grid point (i, j) on the $n_1 \times n_2$ lattice. The second-order centred difference approximations for the first degree derivative in x_1 and x_2 are

$$\partial_1 f^{(i,j)} = \frac{f^{(i+1,j)} - f^{(i-1,j)}}{2h} + O(h^2), \tag{7.8.1}$$

$$\partial_2 f^{(i,j)} = \frac{f^{(i,j+1)} - f^{(i,j-1)}}{2h} + O(h^2). \tag{7.8.2}$$

The second-order centred difference approximations for the second degree derivatives are given by

$$\partial_{11} f^{(i,j)} = \frac{f^{(i+1,j)} - 2f^{(i,j)} + f^{(i-1,j)}}{h^2} + O(h^2), \tag{7.8.3}$$

$$\partial_{22} f^{(i,j)} = \frac{f^{(i,j+1)} - 2f^{(i,j)} + f^{(i,j-1)}}{h^2} + O(h^2). \tag{7.8.4}$$

The fourth-order centred difference approximations for the first degree derivatives in x_1 and x_2 are

$$\partial_1 f^{(i,j)} = \frac{-f^{(i+2,j)} + 8f^{(i+1,j)} - 8f^{(i-1,j)} + f^{(i-2,j)}}{12h} + O(h^4),, \tag{7.8.5}$$

$$\partial_2 f^{(i,j)} = \frac{-f^{(i,j+2)} + 8f^{(i,j+1)} - 8f^{(i,j-1)} + f^{(i,j-2)}}{12h} + O(h^4). \tag{7.8.6}$$

The fourth-order centred difference approximations for the second degree derivatives are

$$\partial_1 1 f^{(i,j)} = \frac{-f^{(i+2,j)} + 16f^{(i+1,j)} - 30f^{(i,j)} + 16f^{(i-1,j)} - f^{(i-2,j)}}{12h^2} + O(h^4), \tag{7.8.7}$$

$$\partial_2 2 f^{(i,j)} = \frac{-f^{(i,j+2)} + 16f^{(i,j+1)} - 30f^{(i,j)} + 16f^{(i,j-1)} - f^{(i,j-2)}}{12h^2} + O(h^4). \tag{7.8.8}$$

since our simulations involve a two-dimensional 601×601 grid, we also require approximations for mixed derivatives. The fourth-order centred difference approximation for the mixed derivative $\partial_{12} f$ is

$$\partial_{12} f^{(i,j)} = \frac{f^{(i+1,j+1)} - f^{(i+1,j-1)} - f^{(i-1,j+1)} + f^{(i-1,j-1)}}{4h^2} + O(h^4), \tag{7.8.9}$$

where h is the uniform grid spacing. These methods, derived from Taylor expansions, underpin our 4^{th}-order finite difference operators, ensuring accurate spatial derivatives on the 601×601 grid.

7.9 Conclusions

This chapter has developed and implemented a variety of nonlinear numerical methods to investigate the dynamic solutions of the Abelian Higgs field equations, as defined in eqs. (6.2.17) and (6.2.18), with a focus on vortex scattering from initial conditions of well-separated, Lorentz-boosted vortices. By discretising the fields on a regular 601×601 grid with spacing $h = 0.1$, and employing 4^{th}-order finite difference operators for spatial derivatives, we constructed a discrete Lagrangian $\mathcal{L}_{\text{dis}}$ that approximates the continuous functional $\mathcal{L}[\Phi, A]$. The 2^{nd}-order Leapfrog method, with a time step $\Delta_t = 0.01$, proves to be effective for time evolution, balancing computational efficiency with symplectic conservation properties essential for long-term stability in vortex dynamics.

The incorporation of Lorentz transformations enabled the simulation of vortices with initial velocities, with the Lorenz gauge $\partial_\mu A^\mu = 0$ emerging as the optimal choice over the temporal gauge $A_0 = 0$. As demonstrated in figure 7.5.1, the Lorenz gauge preserves the radial symmetry of a critically coupled $N = 2$ vortex moving in the x_1 direction, avoiding numerical artefacts observed in the temporal gauge. This compatibility of the gauge with natural boundary conditions, detailed in (7.4.2), allowed radiation to exit the system, preventing reflections that destabilise the simulation, as evidenced by the smooth winding of the phase in figure 7.4.1.

To further enhance stability, damping boundary conditions with a carefully tuned function $K(x)$ absorbed residual radiation, aligning results with those of a larger 2001×2001 grid where boundary effects are minimised. The arrested Newton flow method, constrained by an arresting condition, provided a robust approach to evolve fields toward minimal static solutions. For vortex position analysis, we developed a zero-tracking algorithm, combining polynomial fitting, Nelder-Mead optimisation, and contour intersection, such that we achieved subgrid precision, effectively capturing both closely spaced and well-separated vortex dynamics.

Collectively, these methods yielded a stable, accurate framework for simulating Abelian Higgs vortex interactions. We suggest a significant importance of boundary conditions and gauge choices for maintaining physical stability when exploring complex vortex behaviours. Future work could extend these methods to higher-order integration schemes or adaptive grids to further refine resolution and computational efficiency, deepening our understanding of topological soliton dynamics in field theories.

Chapter 8

Linearisation

8.1 Introduction

This chapter includes work from [11, 13, 47]. In this chapter we will study the normal modes for vortices. This was first studied for several values of λ by Goodband and Hindmarsh in [36], and we will take a similar approach here. Recently, these modes have been studied in more detail using different methods for $\lambda = 1$ [8, 9] and all λ [14, 67].

8.2 One-Dimensional Spectral Flow

To proceed, we consider perturbations of the fields (ϕ, A) around the background of a static vortex solution (ϕ_s, a).

It is convenient to rewrite the vector gauge potential in terms of total angular momentum states

$$a_+ = a_1 + ia_2\,, \qquad\qquad a_- = a_1 - ia_2, \tag{8.2.1}$$

and hence consider the quantities

$$\psi(x) = \frac{\phi(x) - \phi_s(x)}{\epsilon}\,, \qquad\qquad \chi_\pm(x) = \frac{A_\pm(x) - a_\pm(x)}{\epsilon}\,, \tag{8.2.2}$$

where $a_- = \overline{a}_+$ and $(\phi_s(x), a_\pm(x))$ is the static solution of eqs. (6.2.17) and (6.2.18). Hence, the system is close to the static vortex precisely when the perturbations ψ and

$\chi_\pm$ are small. This gives a correction to the action eq. (6.2.1) of the form

$$S = S(\phi_s, a_\pm) + \epsilon^2 S_2 + \mathcal{O}(\epsilon^3)\,, \tag{8.2.3}$$

where $\epsilon \ll 1$ is the magnitude of the perturbation, and

$$S_2 = \frac{1}{2}\int \xi^\dagger \mathcal{D}\xi \; d^2x\,, \qquad \xi^\dagger(\mathbf{x}) = (\chi_- e^{i\omega t}, \chi_+ e^{-i\omega t}, \overline{\psi} e^{i\omega t}, \psi e^{-i\omega t})\,, \tag{8.2.4}$$

where ξ is a vector of the perturbations, ω is the angular frequency of the linear mode, and t denotes time. Note that the linear action term vanishes because (ϕ, A_μ) is a solution of the Euler-Lagrange equations of motion eqs. (6.2.17) and (6.2.18). Since ϵ is small we can neglect all terms higher than quadratic, leaving only linear corrections to the equations of motion.

Then, the total fields are

$$\begin{aligned} \phi(x) &= \phi_s(x) + \epsilon\psi(x)\, e^{-i\omega t}\,, & \overline{\phi(x)} &= \overline{\phi_s(x)} + \epsilon\overline{\psi(x)}\, e^{i\omega t}\,, \\ A_+(x) &= a_+(x) + \epsilon\chi_+(x)\, e^{-i\omega t}\,, & A_-(x) &= a_-(x) + \epsilon\chi_-(x)\, e^{i\omega t}\,. \end{aligned} \tag{8.2.5}$$

In order to set up the eigenvalue problem for the perturbations, we seek to remove the linear derivative terms by choosing the background gauge condition [27]

$$\partial_\mu \chi^\mu - (\overline{\psi}\phi_s - \overline{\phi_s}\psi) = 0\,. \tag{8.2.6}$$

This gauge choice removes the gauge degrees of freedom. Moreover, the Lorenz gauge $\partial_\mu A^\mu = 0$ is satisfied by this gauge condition. The Lorenz gauge is chosen for the full field theory dynamics because we found it to be the most suitable gauge choice for numerical simulations in chapter 7.

With the above ansatz, we obtain the eigenvalue equation from $\mathcal{D}$ by separating the time derivatives

$$\mathcal{D}_{BG} \begin{pmatrix} \chi_+ \\ \chi_- \\ \psi \\ \overline{\psi} \end{pmatrix} = \omega^2 \begin{pmatrix} \chi_+ \\ \chi_- \\ \psi \\ \overline{\psi} \end{pmatrix}\,, \tag{8.2.7}$$

where

$$\mathcal{D}_{BG} = \begin{pmatrix} D_1 & 0 & A & B \\ 0 & D_1 & C & E \\ E & B & D_2 & V_1 \\ C & A & V_2 & D_3 \end{pmatrix},$$

and

$$\begin{aligned} D_1 &= -\Delta + |\phi_s|^2\,, \\ D_2 &= -\Delta - i(a_+ + a_-)\partial_1 + (a_+ - a_+)\partial_2 + \frac{\lambda}{2}(2|\phi_s|^2 - 1) + a_+a_- + |\phi_s|^2\,, \\ D_3 &= -\Delta + i(a_+ + a_-)\partial_1 - (a_+ - a_-)\partial_2 + \frac{\lambda}{2}(2|\phi_s|^2 - 1) + a_+a_- + |\phi_s|^2\,, \\ A &= i\overline{\partial_1\phi_s} + \overline{\partial_2\phi_s} + \overline{\phi_s}a_s^+\,, & B &= -i\partial_1\phi_s - \partial_2\phi_s + \phi_s a_+\,, \\ C &= i\overline{\partial_1\phi_s} - \overline{\partial_y\phi_s} + \overline{\phi_s}a_-\,, & E &= -i\partial_1\phi_s + \partial_2\phi_s + \Phi a_-\,, \\ V_1 &= \frac{\lambda}{2}\phi_s^2 - \phi_s^2\,, & V_2 &= \frac{\lambda}{2}\overline{\phi_s}^2 - \overline{\phi_s}^2\,, \end{aligned} \tag{8.2.8}$$

with the Laplacian defined as $\Delta = \partial_{xx} + \partial_{yy}$.

We can use the radially symmetric ansatz (see eq. (6.5.3)) for ϕ, and note that

$$a_s^+ = \frac{ia_\theta(\rho)}{\rho}e^{-i\theta}\,, \qquad a_s^- = -\frac{ia_\theta(\rho)}{\rho}e^{i\theta}\,, \tag{8.2.9}$$

where $a_\theta(\rho)$ is a radial profile function found by solving eq. (6.5.5). We choose $(A_0, A_\rho, A_\theta) = (A_0, 0, a_\theta(\rho))$, where the radial gauge $A_\rho = 0$ is imposed.

The perturbations are given by [36]

$$\begin{aligned} \psi &= \sum_k s_k(\rho)e^{i(N+k)\theta}\,, & \overline{\psi} &= \sum_k \overline{s}_{-k}(\rho)e^{-i(N-k)\theta}\,, \\ \chi^+ &= \sum_k i\alpha_k(\rho)e^{i(k-1)\theta}\,, & \chi^- &= -\sum_k i\overline{\alpha}_{-k}(\rho)e^{i(k+1)\theta}\,, \end{aligned} \tag{8.2.10}$$

where N is the topological charge, and $k \in \mathbb{Z}$ is the wave number.

Substituting eq. (8.2.10) for the perturbations, eq. (8.2.9) for $a_\pm$ and eq. (6.5.3) for ϕ_s, we can reduce the eigenvalue problem, eq. (8.2.7), to a $1-$dimensional problem. We

hence have the eigenvalue problem

$$\begin{pmatrix} D_1 & 0 & A & B \\ 0 & D_2 & B & A \\ A & B & D_3 & V \\ B & A & V & D_4 \end{pmatrix} \begin{pmatrix} \overline{\alpha}_{-k} \\ \alpha_k \\ \overline{s}_{-k} \\ s_k \end{pmatrix} = \omega^2 \begin{pmatrix} \overline{\alpha}_{-k} \\ \alpha_k \\ \overline{s}_{-k} \\ s_k \end{pmatrix}, \tag{8.2.11}$$

where

$$\begin{aligned} D_1 &= -\partial_{\rho\rho} - \frac{1}{\rho}\partial_\rho + f^2 + \frac{(k+1)^2}{\rho^2}, \\ D_2 &= -\partial_{\rho\rho} - \frac{1}{\rho}\partial_\rho + f^2 + \frac{(k-1)^2}{\rho^2}, \\ D_3 &= -\partial_{\rho\rho} - \frac{1}{\rho}\partial_\rho + \frac{1}{\rho^2}(a_\theta - (N-k))^2 + f^2(\lambda+1) - \frac{\lambda}{2}, \\ D_4 &= -\partial_{\rho\rho} - \frac{1}{\rho}\partial_\rho + \frac{1}{\rho^2}(a_\theta - (N+k))^2 + f^2(\lambda+1) - \frac{\lambda}{2}, \\ A &= f' - \frac{f}{\rho}(N - a_\theta) \\ B &= -f' - \frac{f}{\rho}(N - a_\theta) \\ V &= \frac{1}{2}(\lambda - 2)f^2. \end{aligned} \tag{8.2.12}$$

We hence have a system of coupled ODEs

$$\omega^2\bar{\alpha}_{-k} = -\partial_{\rho\rho}\bar{\alpha}_{-k} - \frac{1}{\rho}\partial_\rho\bar{\alpha}_{-k} + \bar{\alpha}_{-k}(f^2 + \frac{(k+1)^2}{\rho^2}) + \bar{s}_{-k}(f' - \frac{f}{\rho}(N-a_\theta)) - s_k(f' + \frac{f}{\rho}(N-a_\theta)) \tag{8.2.13}$$

$$\omega^2\alpha_k = -\partial_{\rho\rho}\alpha_k - \frac{1}{\rho}\partial_\rho\alpha_k + \alpha_k(f^2 + \frac{(k-1)^2}{\rho^2}) - \bar{s}_{-k}(f' + \frac{f}{\rho}(N-a_\theta)) + s_k(f' - \frac{f}{\rho}(N-a_\theta)) \tag{8.2.14}$$

$$\begin{aligned} \omega^2\bar{s}_{-k} = &-\partial_{\rho\rho}\bar{s}_{-k} - \frac{1}{\rho}\partial_\rho\bar{s}_{-k} + \bar{s}_{-k}(\frac{1}{\rho^2}(a_\theta - (N-k))^2 + f^2(\lambda+1) - \frac{\lambda}{2}) + \cdots \\ &\cdots + \bar{\alpha}_{-k}(f' - \frac{f}{\rho}(N-a_\theta)) - \alpha_k(f' + \frac{f}{\rho}(N-a_\theta)) + \frac{1}{2}(\lambda-2)f^2 s_k \end{aligned} \tag{8.2.15}$$

$$\begin{aligned} \omega^2 s_k = &-\partial_{\rho\rho}s_k - \frac{1}{\rho}\partial_\rho s_k + s_k(\frac{1}{\rho^2}(a_\theta - (N+k))^2 + f^2(\lambda+1) - \frac{\lambda}{2}) + \cdots \\ &\cdots + \alpha_k(f' - \frac{f}{\rho}(N-a_\theta)) - \bar{\alpha}_{-k}(f' + \frac{f}{\rho}(N-a_\theta)) + \frac{1}{2}(\lambda-2)f^2\bar{s}_{-k}. \end{aligned} \tag{8.2.16}$$

We now employ a central second-order finite-difference scheme to discretise the system of coupled ODEs eqs. (8.2.13) to (8.2.16), and write the eigenvalue problem as a 4×4

block matrix, with entries of size $M \times M$. The whole matrix is then of size $4M \times 4M$. The set of discretised ordinary differential equations (DODEs) is as follows:

$$
\begin{aligned}
\omega^2 \bar{\alpha}_{-k}^{(i)} &= -\frac{\bar{\alpha}_{-k}^{(i+1)} - 2\bar{\alpha}_{-k}^{(i)} + \bar{\alpha}_{-k}^{(i-1)}}{h^2} - \frac{1}{ih}\frac{\bar{\alpha}_{-k}^{(i+1)} - \bar{\alpha}_{-k}^{(i-1)}}{2h} + \left[(f^{(i)})^2 + \frac{(k+1)^2}{(ih)^2}\right]\bar{\alpha}_{-k}^{(i)} \\
&\quad + \left(f'^{(i)} - \frac{f^{(i)}(N - a_\theta^{(i)})}{ih}\right)\bar{s}_{-k}^{(i)} - \left(f'^{(i)} + \frac{f^{(i)}(N - a_\theta^{(i)})}{ih}\right)s_k^{(i)}, \\
\omega^2 \alpha_k^{(i)} &= -\frac{\alpha_k^{(i+1)} - 2\alpha_k^{(i)} + \alpha_k^{(i-1)}}{h^2} - \frac{1}{ih}\frac{\alpha_k^{(i+1)} - \alpha_k^{(i-1)}}{2h} + \left[(f^{(i)})^2 + \frac{(k-1)^2}{(ih)^2}\right]\alpha_k^{(i)} \\
&\quad - \left(f'^{(i)} + \frac{f^{(i)}(N - a_\theta^{(i)})}{ih}\right)\bar{s}_{-k}^{(i)} + \left(f'^{(i)} - \frac{f^{(i)}(N - a_\theta^{(i)})}{ih}\right)s_k^{(i)}, \\
\omega^2 \bar{s}_{-k}^{(i)} &= -\frac{\bar{s}_{-k}^{(i+1)} - 2\bar{s}_{-k}^{(i)} + \bar{s}_{-k}^{(i-1)}}{h^2} - \frac{1}{ih}\frac{\bar{s}_{-k}^{(i+1)} - \bar{s}_{-k}^{(i-1)}}{2h} \\
&\quad + \left[\frac{(a_\theta^{(i)} - (N-k))^2}{(ih)^2} + (\lambda+1)(f^{(i)})^2 - \frac{\lambda}{2}\right]\bar{s}_{-k}^{(i)} \\
&\quad + \left(f'^{(i)} - \frac{f^{(i)}(N - a_\theta^{(i)})}{ih}\right)\bar{\alpha}_{-k}^{(i)} - \left(f'^{(i)} + \frac{f^{(i)}(N - a_\theta^{(i)})}{ih}\right)\alpha_k^{(i)} + \frac{1}{2}(\lambda-2)(f^{(i)})^2 s_k^{(i)}, \\
\omega^2 s_k^{(i)} &= -\frac{s_k^{(i+1)} - 2s_k^{(i)} + s_k^{(i-1)}}{h^2} - \frac{1}{ih}\frac{s_k^{(i+1)} - s_k^{(i-1)}}{2h} \\
&\quad + \left[\frac{(a_\theta^{(i)} - (N+k))^2}{(ih)^2} + (\lambda+1)(f^{(i)})^2 - \frac{\lambda}{2}\right]s_k^{(i)} \\
&\quad + \left(f'^{(i)} - \frac{f^{(i)}(N - a_\theta^{(i)})}{ih}\right)\alpha_k^{(i)} - \left(f'^{(i)} + \frac{f^{(i)}(N - a_\theta^{(i)})}{ih}\right)\bar{\alpha}_{-k}^{(i)} + \frac{1}{2}(\lambda-2)(f^{(i)})^2 \bar{s}_{-k}^{(i)},
\end{aligned}
\tag{8.2.17}
$$

where h is the step size in ρ, and the functions are evaluated at discrete points such that $g(ih) = g^{(i)}$ for $i = 1, 2, \ldots, M+1$. The coupled system of ODE's (eqs. (8.2.13) to (8.2.16)) have singular points as $\rho \to 0$. Thus, we must ensure regularity at the singular point $\rho = 0$. We do this by using the Frobenius method near the singular point. The Frobenius method assumes the solution $g(\rho)$ takes the form of a power series

$$
g(\rho) = \rho^s \sum_{j=0}^{\infty} u_j^{(g)} \rho^j, \tag{8.2.18}
$$

where $g \in \{\bar{\alpha}_{-k}, \alpha_k, \bar{s}_{-k}, s_k\}$, and $u_0^{(g)} \neq 0$. Using the asymptotic behaviour $f(\rho) \approx c\rho^N$, $a_\theta(\rho) \approx d\rho^2$ near $\rho = 0$, we derive the indicial equations. For $\bar{\alpha}_{-k}$, substituting

eq. (8.2.18) into the ODEs eq. (8.2.13) gives the recurrence relation

$$\sum_{j=0}^{\infty}\left[-(s+j)^2+(k+1)^2\right]u_j\rho^j+\sum_{j=2}^{\infty}\left[-\omega^2u_{j-2}\rho^j\right]+\mathcal{O}(\rho^{2N+2})=0. \tag{8.2.19}$$

Annihilation of the $j=0$ term gives the indical equation

$$\bar{\alpha}_{-k}: \quad -s^2+(k+1)^2=0 \implies s=\pm(k+1). \tag{8.2.20}$$

Choosing $s=k+1$ (since $k\geq 0$) to ensure regularity, the solution is

$$\bar{\alpha}_{-k}(\rho)\approx u_0^{(\bar{\alpha}_{-k})}\rho^{k+1}+u_2^{(\bar{\alpha}_{-k})}\rho^{k+3}+\cdots. \tag{8.2.21}$$

The recurrence relation between the odd coefficients of eq. (8.2.19) suggests that these coefficients vanish, hence we have the recurrence relation between even coefficients

$$u_{2m}^{(\bar{\alpha}_{-k})}=-\frac{\omega^2}{-4(m+k+1)}u_{2m-2}^{(\bar{\alpha}_{-k})}, \quad m=1,2,\ldots, \tag{8.2.22}$$

where $j=2m$, and $m=1,2,....$

For α_k, substituting eq. (8.2.18) into eq. (8.2.14), the leading terms give

$$\alpha_k: \quad -s^2+(k-1)^2=0 \implies s=\pm(k-1). \tag{8.2.23}$$

Choosing $s=|k-1|$ (since $k\in\mathbb{Z}$, adjusting for $k<2$ if necessary), the solution is

$$\alpha_k(\rho)\approx u_0^{(\alpha_k)}\rho^{|k-1|}+u_2^{(\alpha_k)}\rho^{|k-1|+2}+\cdots. \tag{8.2.24}$$

The recurrence relation for α_k from eq. (8.2.14) is

$$\left[-(s+j)^2+(k-1)^2\right]u_j^{(\alpha_k)}+\text{higher-order terms}=-\omega^2u_{j-2}^{(\alpha_k)}, \tag{8.2.25}$$

where for $j=0$, $s=\pm(k-1)$, and for $j=2m$, even coefficients satisfy

$$u_{2m}^{(\alpha_k)}=-\frac{\omega^2}{-4(m+|k-1|)}u_{2m-2}^{(\alpha_k)}, \quad m=1,2,\ldots. \tag{8.2.26}$$

For $\bar{s}_{-k}$, substituting eq. (8.2.18) into eq. (8.2.15), using $a_\theta(\rho) \approx d\rho^2$, the leading terms give

$$\bar{s}_{-k}: \quad -s^2 + (N-k)^2 = 0 \implies s = \pm(N-k). \tag{8.2.27}$$

Choosing $s = |N-k|$ (assuming $N > k$ for regularity, else adjust), the solution is

$$\bar{s}_{-k}(\rho) \approx u_0^{(\bar{s}_{-k})}\rho^{|N-k|} + u_2^{(\bar{s}_{-k})}\rho^{|N-k|+2} + \cdots. \tag{8.2.28}$$

The recurrence relation for $\bar{s}_{-k}$ from eq. (8.2.15) is

$$\left[-(s+j)^2 + (N-k)^2\right] u_j^{(\bar{s}_{-k})} + \text{higher-order terms} = -\omega^2 u_{j-2}^{(\bar{s}_{-k})}, \tag{8.2.29}$$

where for $j = 0$, $s = \pm(N-k)$, and for $j = 2m$, even coefficients satisfy

$$u_{2m}^{(\bar{s}_{-k})} = -\frac{\omega^2}{-4(m + |N-k|)} u_{2m-2}^{(\bar{s}_{-k})}, \quad m = 1, 2, \ldots. \tag{8.2.30}$$

For s_k, substituting eq. (8.2.18) into eq. (8.2.16), the leading terms give

$$s_k: \quad -s^2 + (N+k)^2 = 0 \implies s = \pm(N+k). \tag{8.2.31}$$

Choosing $s = N + k$ for regularity, the solution is

$$s_k(\rho) \approx u_0^{(s_k)}\rho^{N+k} + u_2^{(s_k)}\rho^{N+k+2} + \cdots. \tag{8.2.32}$$

The recurrence relation for s_k from eq. (8.2.16) is

$$\left[-(s+j)^2 + (N+k)^2\right] u_j^{(s_k)} + \text{higher-order terms} = -\omega^2 u_{j-2}^{(s_k)}, \tag{8.2.33}$$

where for $j = 0$, $s = \pm(N+k)$, and for $j = 2m$, even coefficients satisfy

$$u_{2m}^{(s_k)} = -\frac{\omega^2}{-4(m + N + k)} u_{2m-2}^{(s_k)}, \quad m = 1, 2, \ldots. \tag{8.2.34}$$

For boundary conditions at $\rho = 0$ ($i = 1$), if $g(0) = 0$, we set $g_1 = 0$ for $g \in \{\bar{\alpha}_{-k}, \alpha_k, \bar{s}_{-k}, s_k\}$. Otherwise, if $g(0)$ is constant, regularity requires $g'(0) = 0$, so using

a second-order forward difference formula [9]

$$g'(0) = \frac{-g^{(2)} + 4g^{(1)} - 3g^{(0)}}{2h} = 0 \implies g^{(0)} = \frac{4g^{(1)} - g^{(2)}}{3}. \tag{8.2.35}$$

Thus, the boundary conditions at $i = 1$ are

$$\omega^2 \bar{\alpha}_{-k}^{(1)} = -\frac{4}{3}\frac{\bar{\alpha}_{-k}^{(2)} - \bar{\alpha}_{-k}^{(1)}}{h^2} + \left[(f^{(1)})^2 + \frac{(k+1)^2}{h^2}\right]\bar{\alpha}_{-k}^{(1)} + \left(f'^{(1)} - \frac{f^{(1)}(N - a_\theta^{(1)})}{h}\right)\bar{s}_{-k}^{(1)} - \left(f'^{(1)} + \frac{f^{(1)}(N - a_\theta^{(1)})}{h}\right)s_k^{(1)}, \tag{8.2.36}$$

$$\omega^2 \alpha_k^{(1)} = -\frac{4}{3}\frac{\alpha_k^{(2)} - \alpha_k^{(1)}}{h^2} + \left[(f^{(1)})^2 + \frac{(k-1)^2}{h^2}\right]\alpha_k^{(1)} - \left(f'^{(1)} + \frac{f^{(1)}(N - a_\theta^{(1)})}{h}\right)\bar{s}_{-k}^{(1)} + \left(f'^{(1)} - \frac{f^{(1)}(N - a_\theta^{(1)})}{h}\right)s_k^{(1)}, \tag{8.2.37}$$

$$\omega^2 \bar{s}_{-k}^{(1)} = -\frac{4}{3}\frac{\bar{s}_{-k}^{(2)} - \bar{s}_{-k}^{(1)}}{h^2} + \left[\frac{(a_\theta^{(1)} - (N-k))^2}{h^2} + (\lambda+1)(f^{(1)})^2 - \frac{\lambda}{2}\right]\bar{s}_{-k}^{(1)} + \left(f'^{(1)} - \frac{f^{(1)}(N - a_\theta^{(1)})}{h}\right)\bar{\alpha}_{-k}^{(1)} - \left(f'^{(1)} + \frac{f^{(1)}(N - a_\theta^{(1)})}{h}\right)\alpha_k^{(1)} + \frac{1}{2}(\lambda-2)(f^{(1)})^2 s_k^{(1)}, \tag{8.2.38}$$

$$\omega^2 s_k^{(1)} = -\frac{4}{3}\frac{s_k^{(2)} - s_k^{(1)}}{h^2} + \left[\frac{(a_\theta^{(1)} - (N+k))^2}{h^2} + (\lambda+1)(f^{(1)})^2 - \frac{\lambda}{2}\right]s_k^{(1)} + \left(f'^{(1)} - \frac{f^{(1)}(N - a_\theta^{(1)})}{h}\right)\alpha_k^{(1)} - \left(f'^{(1)} + \frac{f^{(1)}(N - a_\theta^{(1)})}{h}\right)\bar{\alpha}_{-k}^{(1)} + \frac{1}{2}(\lambda-2)(f^{(1)})^2 \bar{s}_{-k}^{(1)}, \tag{8.2.39}$$

where h is sufficiently small, and $\bar{\alpha}_{-k}^{(0)} = \alpha_k^{(0)} = \bar{s}_{-k}^{(0)} = s_k^{(0)} = 0$ if the series starts at a positive power. At $i = M + 1$, we impose

$$\bar{\alpha}_{-k}^{(M+1)} = \alpha_k^{(M+1)} = \bar{s}_{-k}^{(M+1)} = s_k^{(M+1)} = 0. \tag{8.2.40}$$

The eigenfunctions are normalised using the L_2 normalisation condition

$$\pi \int_0^\infty \left(\alpha_k(\rho)^2 + \overline{\alpha}_{-k}(\rho)^2 + s_k(\rho)^2 + \overline{s}_{-k}(\rho)^2\right)\rho \, d\rho = 1\,. \tag{8.2.41}$$

If we consider a vortex solution of degree $N = 1$, and wave number $k = 0$ for the mode, then $s_0 = \overline{s}_{-0}$ and $\alpha_0 = \overline{\alpha}_{-0}$ and eq. (8.2.10) is simplified, giving the following ansatz

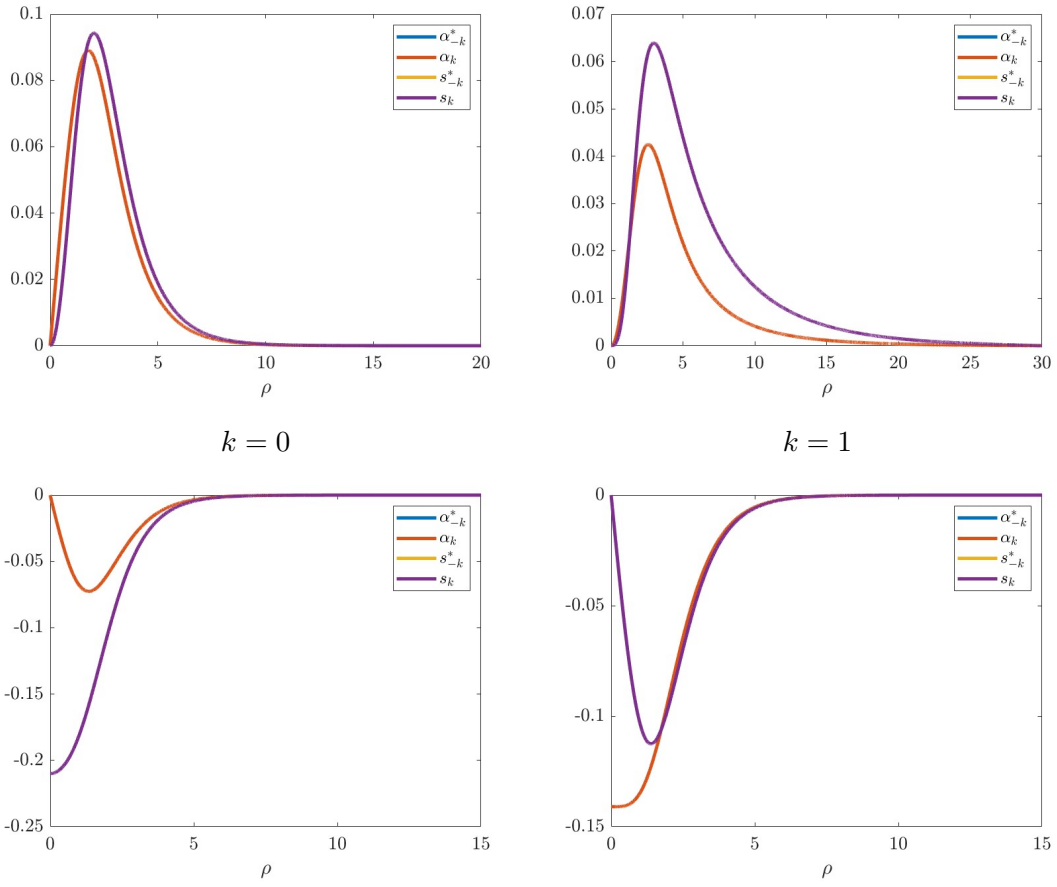

$k = 0$ $k = 1$

Splitting Mode Translation Mode

Figure 8.2.1: Discrete eigenfunctions for all wave number $k \leq N$, for a radially symmetric degree $N = 2$ vortex

for the perturbations

$$\begin{aligned}
\psi_1(x) &= \cos(\theta)\ s_0(\rho)\,, \\
\psi_2(x) &= \sin(\theta)\ s_0(\rho)\,, \\
\chi_1(x) &= -\sin(\theta)\ \alpha_0(\rho)\,, \\
\chi_2(x) &= \cos(\theta)\ \alpha_0(\rho)\,.
\end{aligned} \tag{8.2.42}$$

Therefore, the eigenvalue problem becomes

$$\begin{pmatrix} D_1 & A \\ A & D_3 \end{pmatrix} \begin{pmatrix} \alpha_0 \\ s_0 \end{pmatrix} = \omega^2 \begin{pmatrix} \alpha_0 \\ s_0 \end{pmatrix}\,, \tag{8.2.43}$$

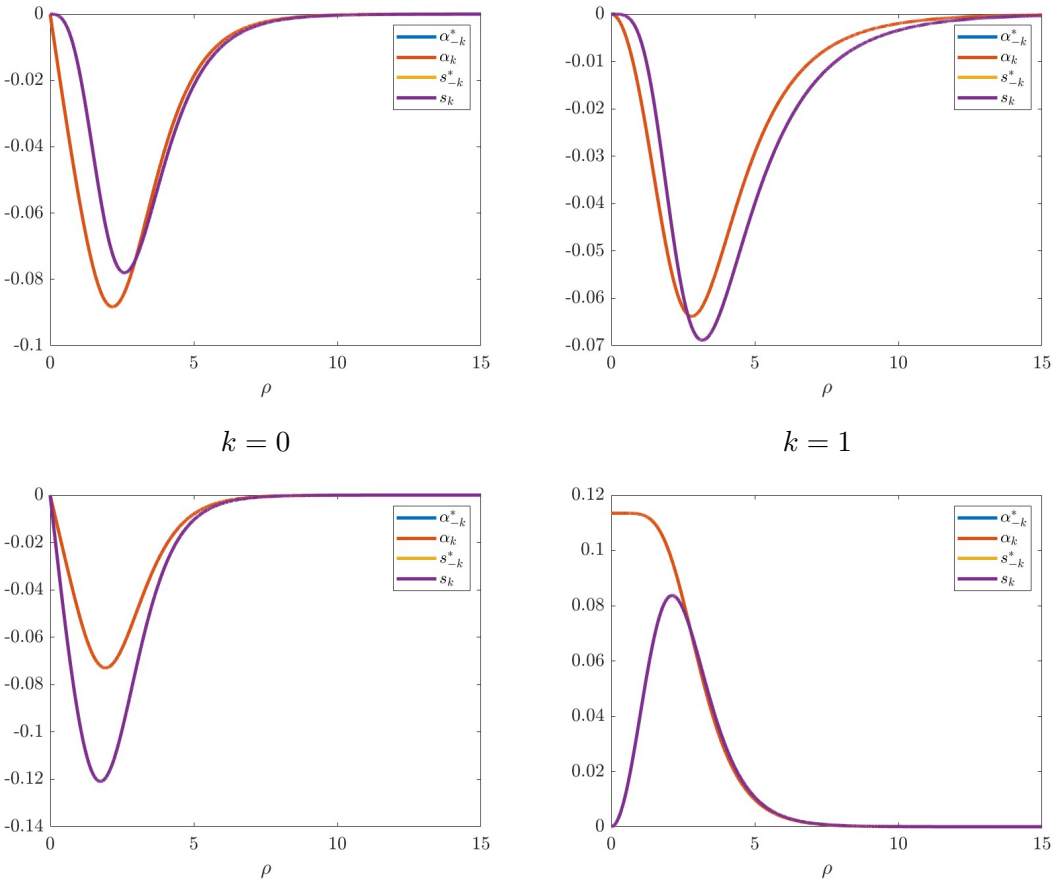

Figure 8.2.2: Discrete eigenfunctions for all wave number $k \leq N$, for a radially symmetric degree $N = 3$ vortex

where

$$
\begin{aligned}
D_1 &= -\left(\partial_{\rho\rho} + \frac{1}{\rho}\partial_\rho\right) + f^2 + \frac{1}{\rho^2}, \\
D_3 &= -\left(\partial_{\rho\rho} + \frac{1}{\rho}\partial_\rho\right) + \frac{\lambda}{2}\left(3f^2 - 1\right) + \frac{1}{\rho^2}\left(a_\theta - 1\right)^2, \\
A &= \frac{2f}{\rho}\left(a_\theta - 1\right).
\end{aligned} \tag{8.2.44}
$$

We hence have eigenfunctions of the form $\xi = (\alpha_0, \alpha_0, s_0, s_0)$, and the system eq. (8.2.7) has decoupled into two copies of equation eq. (8.2.44). The boundary conditions are the same as above for $k = 0$.

We now employ a central second-order finite-difference scheme to discretise the system of coupled ODEs eq. (8.2.44), and write the eigenvalue problem as a 2×2 block matrix, with entries of size $M \times M$. We then use MATLAB to find the eigenvalues of the block

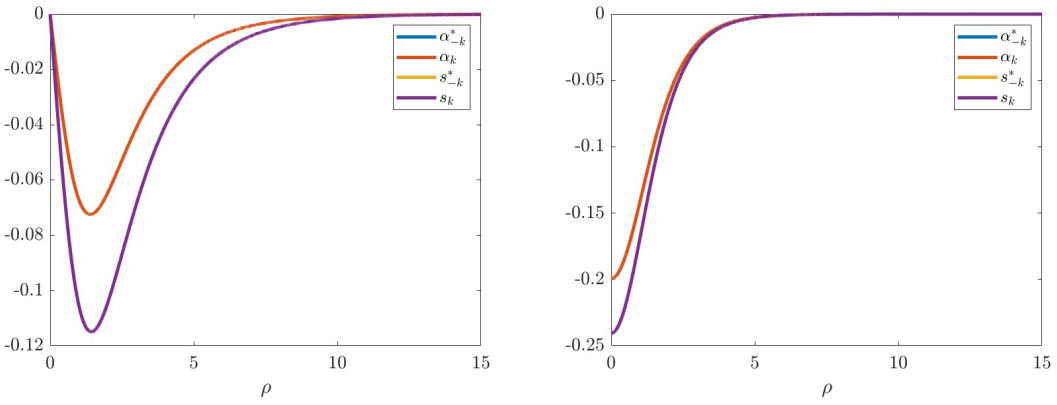

$k = 0$ Translation Mode

Figure 8.2.3: Discrete eigenfunctions for all wave number $k \leq N$, for a radially symmetric degree $N = 1$ vortex

matrix.

We find that for $N = 1$, we have only one normal mode, denoted the shape mode, which is a radially symmetric mode that causes fluctuations in gauge-invariant quantities. We find that the mode has the squared frequency $\omega^2_{1,0} = 0.77747$ and plot the eigenfunctions in figure 8.2.3. We have normalised the eigenfunctions using the L_2 norm

$$2\pi \int_0^\infty (\alpha_0(\rho)^2 + s_0(\rho)^2)\rho \, d\rho = 1 \,. \tag{8.2.45}$$

Figure 8.2.4 illustrates the resulting spectrum for the range $\lambda \in [0.1, 3]$ for $N = 1 \ldots 4$. The continuum threshold involves two distinct regions. The first is the mass threshold, at which point $\omega^2 = \lambda$, and a gauge threshold, where $\omega^2 = 1$. These thresholds arise due to the asymptotic behaviour of the spectral operator, where the fields approach the vacuum values such that $f \to 1$, and $a_\theta \to N$ as $\rho \to \infty$. Asymptotically, the perturbations decouple, hence

$$-\nabla^2\psi + m_H^2\psi = \omega^2\psi, \tag{8.2.46}$$

hence $\omega^2 = m_H^2 + k^2$, where $m_H = \sqrt{\lambda}$ is the Higgs mass. The continuous spectrum starts at the minimum energy with $k = 0$, hence the mass threshold is $\omega^2 = \lambda$.

Furthermore, we have that

$$-\nabla^2\chi_\pm + m_A^2\chi_\pm = \omega^2\chi_\pm, \tag{8.2.47}$$

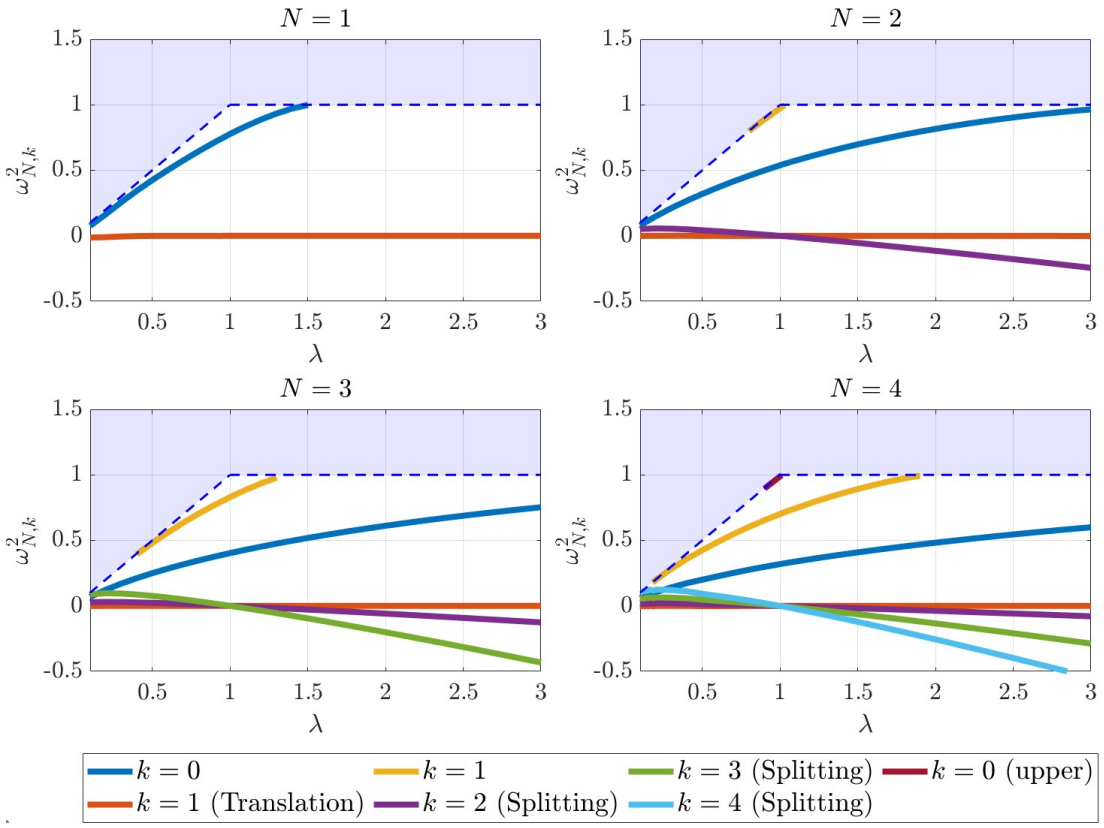

Figure 8.2.4: Plot to show the spectral structure as a function of $\lambda \in [0.1, 3]$ for $N = 1..4$ and wave number $k \leq N$. The shaded region indicates the continuous spectrum.

where m_A is the mass of the gauge field, which comes from the value of the covariant derivative at ∞, i.e. $|D_\mu \phi|^2 \approx A_\mu^2 = 1$, hence $m_A = 1$. We therefore have the value of the gauge threshold $\omega^2 = 1$. Note that at critical coupling, these two thresholds are the same.

For the case of $N = 1$, we have two discrete modes at $\lambda = 1$; see table A.1 for frequencies of the modes. We have the non-zero energy mode, which is the $k = 0$ shape mode (blue). We see that this squared frequency enters the continuous spectrum at $\lambda \approx 1.5$. We also have the zero-energy translation mode (orange), which is zero for all λ.

Next, for $N = 2$, we have four discrete modes at $\lambda = 1$, see table A.2. We have two non-zero energy modes, the $k = 0$ mode (blue), which is a radially symmetric shape mode and the $k = 1$ mode (yellow), which is a shape mode leading to oscillations from one half plane to the other, centred around the vortex core. The $k = 0$ shape mode enters the continuous spectrum at $\lambda \approx 3$. Furthermore, we see that the $k = 1$ mode exists in the discrete spectrum only for a bounded region in λ, that is, $\lambda \in [0.8, 1.03]$. Again, we have the $k = 1$ translation mode, which is a zero mode. Finally, we have

the $k = 2$ mode, whose excitation leads to a splitting of the vortices. This eigenvalue is zero at $\lambda = 1$, due to the absence of static forces between the vortex. For $\lambda > 1$, the eigenvalue is negative since in this region (type II) the static intervortex force is repulsive and static solutions for $N > 1$ are unstable.

The $N = 3$ spectrum has five discrete modes at critical coupling ($\lambda = 1$), see table A.3 for a full description of the frequencies. There exist two shape modes, at $k = 0$ (blue) and $k = 1$ (yellow). In the regions where we have calculated the frequency of the modes, we do not see where the $k = 0$ mode enters the continuum. However, we see that the $k = 1$ shape mode exists in the discrete spectrum for $\lambda \in [0.4, 1.3]$. Moreover, we have the $k = 1$ translation mode (orange), as well as two splitting modes for $k = 2$ (purple) and $k = 3$ respectively (green).

Finally, the $N = 4$ vortex has seven modes at critical coupling, see table A.4. In particular, we have two $k = 0$ modes, the shape mode (blue) and an upper mode (red). The shape mode exists for all the values of λ that we have calculated; however, the upper $k = 0$ mode exists in the discrete spectrum for $\lambda \in [0.9, 1.01]$. Furthermore, we have the $k = 1$ shape mode (yellow), which exists in the discrete spectrum for $\lambda \in [0.18, 1.9]$. Again, there is the $k = 1$ translation mode (orange), but we also have three splitting modes, that is, $k = 2$ (purple), $k = 3$ (green) and $k = 4$ (cyan). Any form of splitting of the $N = 4$ vortex would be a linear combination of these splitting modes, and similarly for all N.

8.3 2-dimensional Spectral Flow at Critical Coupling

Note that we can calculate the spectral flow of the shape modes for a vortex system in $2-$dimensions at critical coupling ($\lambda = 1$). To accomplish this, we simulate the full field theory in 2 dimensions with no excitations, with vortices centred at $\pm d_i$, where we take $d_i = [0 : 0.1 : 10]$. We perform an arrested Newton flow on this static configuration (see section 7.2), whereby we have pinned the vortices at the desired separation. We perform the pinning by setting the fields to zero at the required points.

We seek to numerically solve the eigenvalue problem (see eq. (8.2.7)). Since it is 2-dimensional, we discretise the spatial domain into a grid. We assume a square domain discretised into an $M \times M$ grid, where we have chosen $M = 401$, with grid spacing

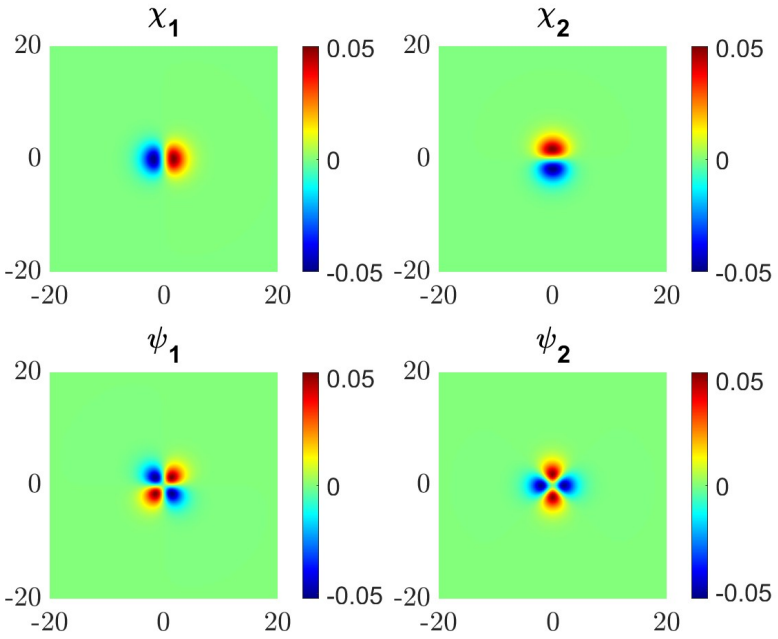

Figure 8.3.1: Heat plots for the field values of the perturbations ξ, corresponding to the $\omega_{2,0}$ shape mode.

$h = 0.1$. Each point in the grid (i, j) corresponds to a coordinate $(x_1^{(i)}, x_2^{(j)})$ and $i, j = 1, ..., M$. Let us focus on the perturbation ψ, as the other perturbation can be discretised in the same way. We map a two-dimensional grid to a one-dimensional vector, where $\psi(k) = \psi^{(i,j)}$, and $k = (j-1)M + i$. We then discretise the PDEs in eq. (8.2.8). The 2-dimensional Laplacian ($\Delta = \frac{\partial^2}{\partial x_1^2} + \frac{\partial^2}{\partial x_2^2}$) can be approximated using a second-order finite difference scheme, such that at the point (i, j)

$$\Delta\psi^{(i,j)} \approx \frac{\psi^{(i+1,j)} + \psi^{(i-1,j)} - 4\psi^{(i,j)} + \psi^{(i,j+1)} + \psi^{(i,j-1)}}{h^2} \tag{8.3.1}$$

Dirichlet boundary conditions have been imposed such that the eigenfunctions are zero at the boundary. For the right boundary, if $\mod(i, M) = 0$, then $\psi^{(i,j)} = 0$. For the left boundary, if $\mod(i, M) = 1$, then $\psi^{(i,j)} = 0$. For the bottom boundary, if $i \leq M$, then we set the perturbation to 0, and finally, for the top boundary, if $i \geq M \times M - M$, the perturbations are also zero.

8.3.1 2-Vortex Spectral Structure

This gives us the eigenfunctions in 2-dimensions. We can plot, for example, the modes at $d = 0$ for a 2-vortex system, see figures 8.3.1 and 8.3.2.

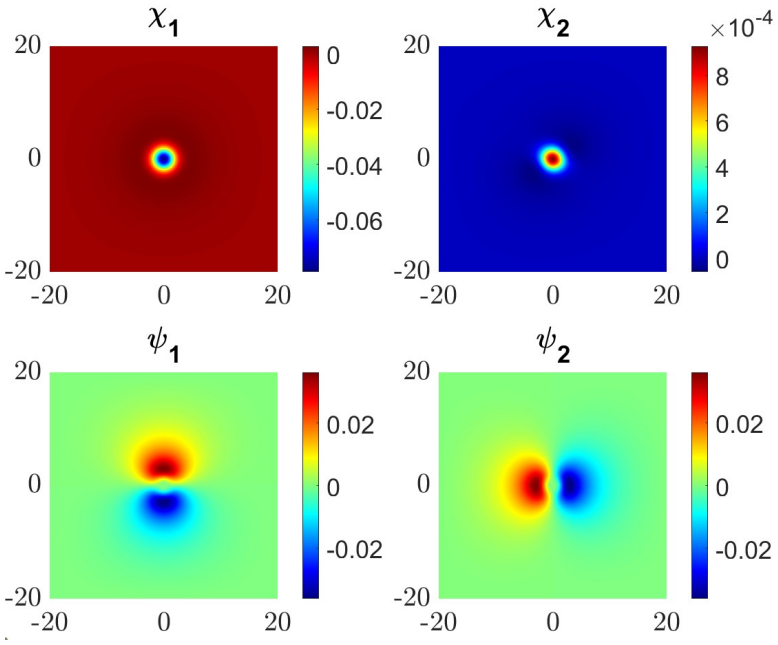

Figure 8.3.2: Heat plots for the field values of the perturbations ξ, corresponding to the $\omega_{2,1}$ shape mode.

We denote the spectral structure as the structure of the linear perturbations. It is important to note that although the N-vortex solution is degenerate on the moduli space, the spectral structure changes as a function of the separation of the vortices. We hence plot in figure 8.3.3 the flow of the modes as a function of the separation for a $2-$vortex system.

For concreteness, we assume that the vortices collide along the x_1-axis. Thus, their positions are $z = \pm d$ with $d \in \mathbb{R}_+$. ($d \in \mathbb{R}_-$ gives identical configurations). After the collision point, at $d = 0$, they pass to the x_2-axis. Thus, d becomes imaginary. For convenience, we chose $d \in i\mathbb{R}_-$. The separation is this $|2d|$.

In figure 8.3.3, we plot the spectral structure [9, 10, 39] for a 2-vortex system. Interestingly, we see that the number of bound modes changes with the separation.

When the vortices are well separated, we notice that there are two degenerate bound modes, the lowest mode (blue) denoted ξ_1, and the first upper mode, denoted ξ_2, (red). The squared frequency of this bound mode is $\omega^2_{1,0} = 0.777476$, which is the same as what we observed in the one-dimensional linearisation.

In terms of asymptotic initial states, there are two possible initial configurations. We denote the shape mode of the i^{th} single $1-$vortex as $|i\rangle$, $i = 1, 2..$ Here, we may excite two modes, ξ_1 and ξ_2. In fact, ξ_1 represents the in-phase superposition of the $N = 1$,$k = 0$

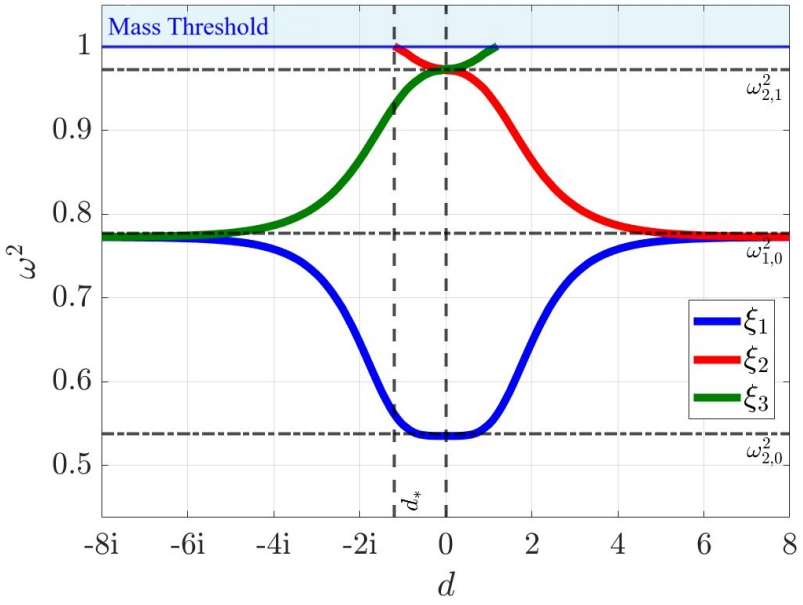

Figure 8.3.3: The spectral structure for the 2-vortex solution as a function of the vortex position parameter $d \in \mathbb{R}_+ \cup i\mathbb{R}_-$

shape mode on the vortices

$$\xi_1 = \frac{I(0)}{2}\left(|1\rangle + |2\rangle\right), \tag{8.3.2}$$

and ξ_2 represents the out-of-phase superposition

$$\xi_2 = \frac{I(0)}{2}\left(|1\rangle - |2\rangle\right), \tag{8.3.3}$$

where $I(0)$ is the initial intensity of the excitation such that $I(0) = \frac{1}{2}(\epsilon\omega)^2$.

As the vortices come closer together (decrease in d), the degeneracy is broken. In the case of the lower mode ξ_1, the squared frequency decreases monotonically to $\omega^2_{2,0} = 0.53859$ at $d = 0$. When the vortices are coincident at the origin ($d = 0$), the squared frequency of the lower mode takes a minimum value. In section 9.2, we explore the result of the decreasing squared frequency of the first mode and notice that we find an attractive intervortex force.

Alternatively, for the upper mode ξ_2, the squared frequency increases to $\omega^2_{2,1} = 0.97303$ at $d = 0$. We also notice the green curve in figure 8.3.3. This mode exists only for small values of $|d| < d_*$, where d_* is the value at which the green line, denoted as ξ_3, reaches the continuous spectrum. Furthermore, we have a mode crossing at $\omega^2_{2,1}$, where the two upper modes take the same value. Note that passing through the origin ($d = 0$) changes the vortex locations from x_1 to x_2-axis. This means that as d decreases further

to negative imaginary values, the second mode ξ_2 of the 2-vortex transitions to the third mode ξ_3, and hence the squared frequency increases further.

In section 9.3, we explore the flow of the upper two modes. Indeed, we find that the mode increasing induces a repulsive intervortex force. However, for a specific initial amplitude, explored in section 9.3, we find that the second mode indeed transitions into the third mode, and the excited vortices reach the point d_*, where the squared frequency hits the continuous spectrum.

8.3.2 3-Vortex Spectral Structure

We now discuss the spectral structure of the 3-vortex system, namely a superposition of three excited 1-vortices in the Abelian Higgs model at critical coupling. For $N = 1$, we have shown that there exists only one non-zero energy mode with eigenvalue $\omega^2_{1,0} = 0.77747$, which arises for angular momentum $k = 0$. This is the radially symmetric shape mode. For $N = 3$, the mode structure is more complicated. There are three shape modes: one radial mode ($k = 0$) with $\omega^2_{30} = 0.402708$ and two degenerate modes for $k = 1$, with squared angular frequency $\omega^2_{31} = 0.83025$. There are no possible bound states for $k = 2$, since the effective potential is pushed almost up to the continuum. The analysis of the flow of the shape modes for the $N = 3$ vortex is performed in a similar way as for the $N = 2$ vortex. To study the spectral flow, we consider paths within two 1-dimensional geodesic submanifolds of the reduced 2-dimensional moduli space with $y \to -y$ symmetry and centre of mass fixed at the origin, denoted $\mathcal{N}^{(1)}$ and $\mathcal{N}^{(2)}$. The subspace $\mathcal{N}^{(1)}$ consists of configurations where three critically coupled vortices are equidistant and collinear, aligned along the x-axis (before scattering) or y-axis (after scattering), with additional $x \to -x$ symmetry. The subspace $\mathcal{N}^{(2)}$ consists of configurations where three critically coupled vortices form an equilateral triangle, satisfying cyclic $\mathcal{C}_3$ symmetry (120° rotation). These submanifolds describe head-on collision dynamics, with $\mathcal{N}^{(1)}$ corresponding to 90° scattering and $\mathcal{N}^{(2)}$ to 60° scattering. Both subspaces support zero modes, which are energy-preserving perturbations (e.g., translations or rotations) defining the submanifold geometry, and non-zero energy shape modes, which are vibrational perturbations with frequencies ω^2_{Nk} (e.g., the radial mode for $k = 0$ and degenerate modes for $k = 1$). Both $\mathcal{N}^{(1)}$ and $\mathcal{N}^{(2)}$ are totally geodesic submanifolds of the reduced 2-dimensional moduli space for the 3-vortex system, as their geodesic flows, constrained by reflection symmetries for $\mathcal{N}^{(1)}$ and $\mathcal{C}_3$ symmetry

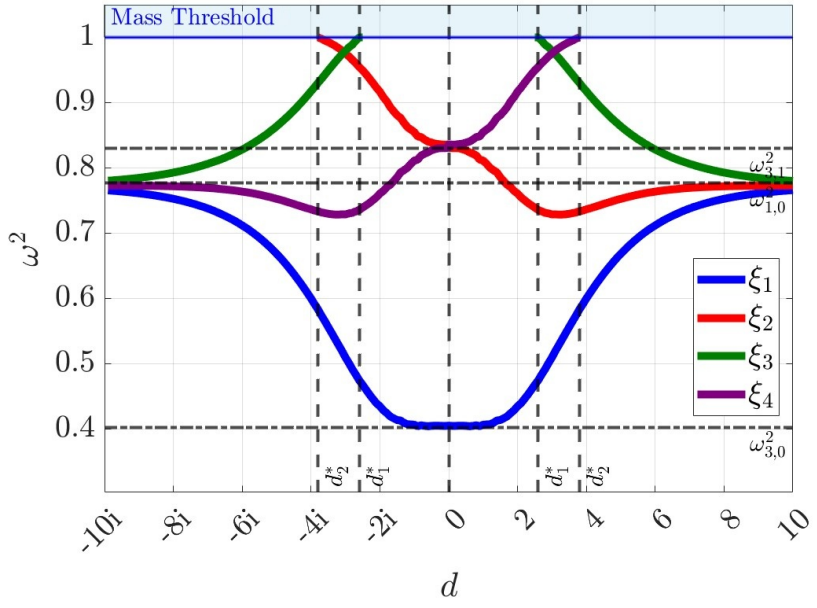

Figure 8.3.4: Spectral flow in the one-dim subspace $\mathcal{N}^{(1)}$ of three collinear 1-vortices. The coordinate d is the distance of the outer vortices from the origin.

for $\mathcal{N}^{(2)}$, have vanishing second fundamental forms, ensuring that geodesics starting tangent to each submanifold remain within it, consistent with the observed 90° and 60° scattering dynamics, respectively. We present the results in figure 8.3.4. We study the flow of the shape modes along the paths defined by the zero modes in the 1-dimensional subspaces $\mathcal{N}^{(1)}$ and $\mathcal{N}^{(2)}$ of the equidistant collinear and the equilateral triangle solutions, respectively.

8.3.2.1 Spectral flow in the subspace $\mathcal{N}^{(1)}$ of the collinear solutions

The first subspace is formed by three collinear vortices ($\lambda = 1$) separated by a distance d, with the centre of mass at the origin. For concreteness, we assume that the vortices are initially located on the x_1-axis.

The spectral flow for a collinear 3-vortex system is shown in figure 8.3.4. Although the number of discrete modes is the same at the origin, $d = 0$ (detailing a radially symmetric $N = 3$ vortex), and for infinitely separated vortices, ($d \to +\infty$), not all of the eigenvalues interpolate between them.

Using the 2-dimensional linearisation, we can also plot the $d = 0$ eigenfunctions for a 3-vortex system, see figures 8.3.5 and 8.3.6. First, we consider the blue line in figure 8.3.4, detailing the squared frequency of the lowest mode, denoted ξ_1. The squared frequency

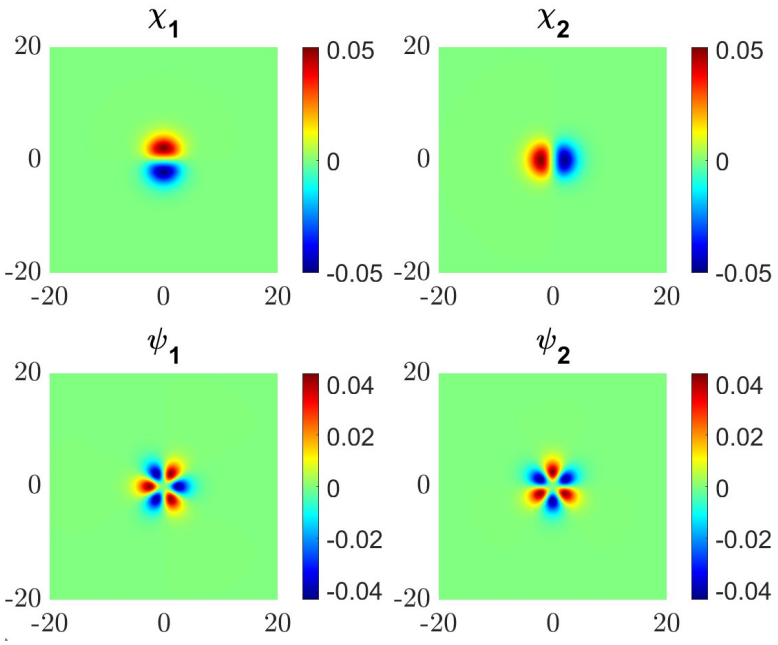

Figure 8.3.5: Heat plots for the field values of the perturbations ξ, corresponding to the $\omega_{2,0}$ shape mode.

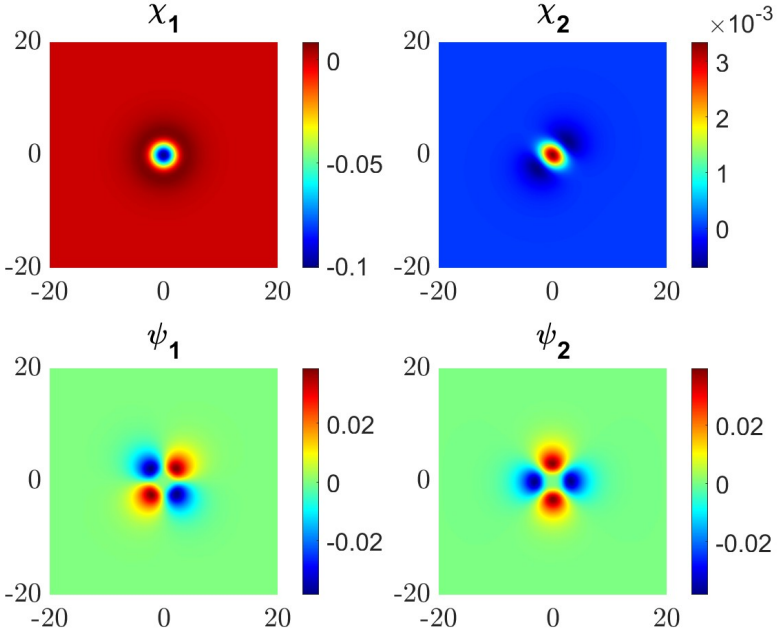

Figure 8.3.6: Heat plots for the field values of the perturbations ξ, corresponding to the $\omega_{2,1}$ shape mode.

grows from $\omega^2_{3,0} = 0.4027085$ at $d = 0$ to its asymptotic value, which is the value of the only existing eigenvalue in the discrete $N = 1$ vortex spectrum, $\omega^2_{1,0} = 0.77747$.

Next, we study the red line in figure 8.3.4, which shows one of the degenerate eigenvalues, labelled ξ_2. The squared frequency interpolates between $\omega^2_{3,1} = 0.8302566$ and the asymptotic value mentioned above. Interestingly, we see that there exists a local minimum in the squared frequency. This could suggest a region in which the vortices might become trapped in a quasi-stationary state. We discuss how this affects vortices away from critical coupling in chapter 10.

The third eigenvalue (see the purple line) existing for $d = 0$ has a surprising behaviour. The degeneracy of $\omega^2_{3,1}$ at $d = 0$ is broken immediately at $d \neq 0$ and the squared frequency increases as we move more positive in d, reaching the continuum threshold at d_2^*. We estimate the position in which the discrete mode enters the continuous spectrum to be in the region $d_2^* \in (3.5, 4)$.

Alternatively, the third degenerate eigenvalue associated with the configuration of three well-separated $N = 1$ vortices (see the green line in figure 8.3.4, labelled as ξ_3) emerges from the continuous spectrum in the region $d_1^* \in (2, 2.5)$ decreasing to the value ω^2_{10}. This means that for the range $d \in [2.5, 4]$ the spectrum involves four discrete eigenmodes. We note that there is also a value of d in this critical region where a level crossing of the two higher modes occurs.

The structure of the modes is symmetrically reflected as we go to the second part of the full subspace $\mathcal{N}^{(1)}$ which contains the collinear solutions placed on the x_2-axis. This takes into account the 90° scattering of the outer vortices when passing through the coincident configuration. This can be plotted in one graph assuming that $d \in i\mathbb{R}_- \cup \mathbb{R}_+$, where d is the distance of the outer vortices from the origin; see figure 8.3.4. Importantly, at $d = 0$ a novel phenomenon occurs. There exists a level crossing where the second mode ξ_2 continues as the third mode for $d \in i\mathbb{R}_-$. This level crossing will have a very important effect on the dynamics of the excited $N = 3$ vortex.

It is important to understand how these shape modes can be excited for asymptotic states where we have infinitely separated $N = 1$ vortices. Let us denote the shape mode of the i^{th} $N = 1$ vortex as $|i\rangle$, $i = 1, 2, 3$, where $i = 2$ is the vortex at the origin ($d = 0$), and $i = 1, 3$ are the outermost vortices. From the point of view of the asymptotic initial states, we may excite three modes. The lowest mode (blue curve in figure 8.3.4) is the

in-phase superposition of the shape modes of the 1-vortices

$$\xi_1 = \frac{I(0)}{\sqrt{3}}(|1\rangle + |2\rangle + |3\rangle). \tag{8.3.4}$$

The squared frequency of this mode decreases as d goes to 0. Then, for imaginary d it grows as $d \to -i\infty$, where the $N = 1$ vortices are infinitely separated along the x_2 axis. The second mode (red curve), which interpolates to ω_{31}^2 at $d = 0$, is given by the orthogonal superposition

$$\xi_2 = \frac{I(0)}{\sqrt{2}}(|1\rangle - |3\rangle), \tag{8.3.5}$$

The squared frequency of this mode increases as d decreases to 0. As we have already observed, after passing to imaginary d the squared frequency of this mode increases as d tends to $-id_2^*$, where it hits the continuous spectrum and disappears into the continuum. In this case, the mode enters the continuous spectrum *after* the vortices pass through the coincident configuration.

Finally, the third asymptotically available mode (green curve in figure 8.3.4) is excited by another linear superposition of the $N = 1$ vortex modes.

$$\xi_3 = \frac{I(0)}{\sqrt{6}}(|1\rangle - 2|2\rangle + |3\rangle). \tag{8.3.6}$$

This mode enters the continuum spectrum for a positive d_1^*, *before* the constituent $N = 1$ vortices are on top of each other.

8.3.2.2 Scattering of the subspace $\mathcal{N}^{(2)}$ of equilateral triangular configurations

Now we consider three critically coupled vortices located at the vertices of an equilateral triangle, at a distance d from the origin. The spectral flow for the equilateral triangular 3-vortex system is shown in figure 8.3.7. The spectral flow interpolates between the discrete spectrum found for the axially symmetric $N = 3$ vortex, and the eigenmode for three well separated $N = 1$ vortices.

The lower mode, labelled ξ_1 exhibits a plateau for small d, but monotonically increases with the separation after $d \approx 2$, reaching the asymptotic value, being the $N = 1$, $k = 0$ mode. Note that the degeneracy between the $k = 1$ eigenmodes is preserved for all d, so we do not see any spectral walls in this case. Furthermore, the squared frequency of the upper mode, labelled ξ_2 changes very little with separation. It decreases from

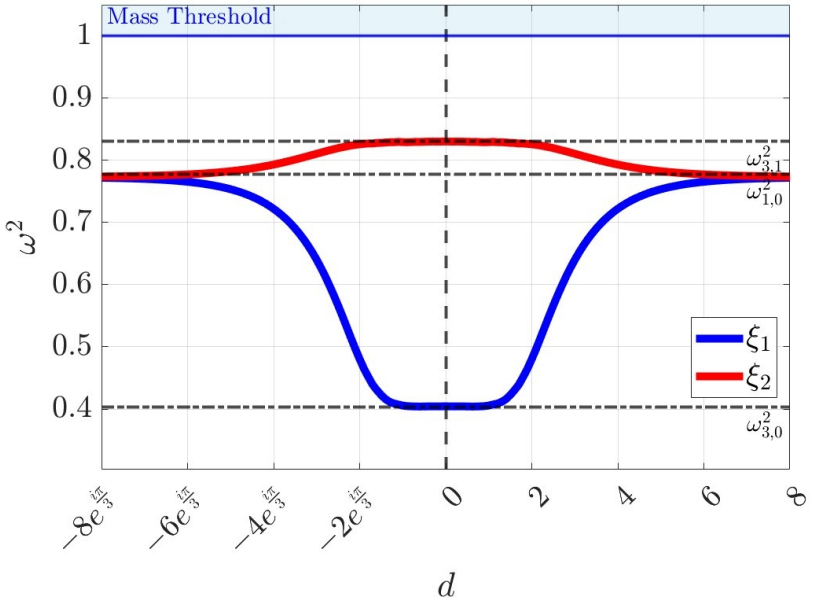

Figure 8.3.7: Spectral flow in the one-dimensional subspace $\mathcal{N}^{(2)}$ of an equilateral triangular configuration of 1-vortices. The coordinate d is the distance of the outer vortices from the origin.

$\omega^2_{3,1} = 0.83025$ for $d = 0$ to $\omega^2_{1,0} = 0.77747$. The structure of the modes is symmetric as the vortices pass the axially symmetric solution at $d = 0$, and the vortices exhibit a $60°$ scattering.

8.3.3 4-Vortex Spectral Structure

In this section we discuss the spectral structure of a 4-vortex system. At $d = 0$, we have the axially symmetric $N = 4$ vortex. We discuss four subspaces of this configuration space. Two of these subspaces are totally geodesic sub-manifolds of the moduli space, where the spectral structure is stabilised by symmetry. The first subspace $\mathcal{N}^{(1)}$ considers four vortices on the vertices of a square. The second subspace $\mathcal{N}^{(3)}$ considers an $N = 2$ vortex at the origin, with two $N = 1$ vortices centred with their zeros at $\pm d$ respectively. The other two subspaces are cross sections of a 2-dimensional space. Namely, the third subspace $\mathcal{N}^{(2)}$ considers two $N = 2$ vortices along the x_1 axis. Finally, the fourth subspace $\mathcal{N}^{(4)}$ considers four $N = 1$ vortices equidistant along the x_1 axis. To address the spectral structure, we consider paths within these subspaces of the reduced moduli space with center of mass fixed at the origin. The subspaces $\mathcal{N}^{(1)}$ and $\mathcal{N}^{(3)}$ are 1-dimensional totally geodesic submanifolds. The subspace $\mathcal{N}^{(1)}$ consists of configurations where four critically coupled vortices are located at the vertices of a square, satisfying

cyclic $\mathcal{C}_4$ symmetry (90° rotation) and dihedral symmetries including reflections. This submanifold describes head-on collision dynamics, corresponding to 45° scattering. The subspace $\mathcal{N}^{(3)}$ consists of configurations where an $N = 2$ vortex (two coincident vortices) is at the origin and two $N = 1$ vortices are equidistant at $\pm d$ along the x-axis (before scattering) or y-axis (after scattering), satisfying cyclic $\mathcal{C}_2$ symmetry (180° rotation) and reflection symmetries ($x \to -x$, $y \to -y$). This submanifold corresponds to 90° scattering. Both subspaces support zero modes, which are energy-preserving perturbations (e.g., rotations or translations defining the submanifold), and non-zero energy shape modes, which are vibrational perturbations. The subspaces $\mathcal{N}^{(2)}$ and $\mathcal{N}^{(4)}$ are not totally geodesic submanifolds but rather cross sections of 2-dimensional subspaces. For $\mathcal{N}^{(2)}$, the configurations involve two $N = 2$ vortices aligned along the x_1-axis, which may exhibit $\mathcal{C}_2$ and reflection symmetries but do not constrain the geodesic flow to remain entirely within a 1-dimensional submanifold due to additional degrees of freedom. Similarly, $\mathcal{N}^{(4)}$ involves four $N = 1$ vortices collinear and equidistant along the x_1-axis, with reflection symmetries, but it serves as a slice through a higher-dimensional space without the full symmetry stabilization required for totality geodesic property. $\mathcal{N}^{(1)}$ and $\mathcal{N}^{(3)}$ are totally geodesic submanifolds because their strong symmetries ($\mathcal{C}_4$ for $\mathcal{N}^{(1)}$ and $\mathcal{C}_2$ for $\mathcal{N}^{(3)}$) ensure that geodesics in the moduli space, starting tangent to the submanifold, remain within it, resulting in vanishing second fundamental forms. Note that for this section, we only discuss the spectral structure calculated from the 2-dimensional linearisation, and we do not discuss the full field theory numerical simulations.

8.3.3.1 Spectral structure of the subspace $\mathcal{N}^{(1)}$

In figure 8.3.8, we see that asymptotically, we only have one eigenmode, with squared frequency $\omega^2_{1,0}$. This is a degenerate mode that splits into 3 excitations. At $d = 0$, we have two eigenmodes, with squared frequencies $\omega^2_{4,0} = 0.31873565$ and $\omega^2_{4,1} = 0.70092248$. Note that the number of eigenmodes is not constant for all d. In fact, we see that for $|d| > 2$, we have three eigenmodes.

First, observe the blue line ξ_1 in figure 8.3.8. At $d = 0$, the squared frequency is $\omega^2_{4,0}$, which is the radially symmetric shape mode for the $N = 4$ vortex. This is the global minimum in terms of the squared frequency as a function of the distance d. Asymptotically, the squared frequency increases to $\omega^2_{1,0}$, which is the radially symmetric shape mode of the $N = 1$ vortex. This means that an excitation of the mode ξ_1 will

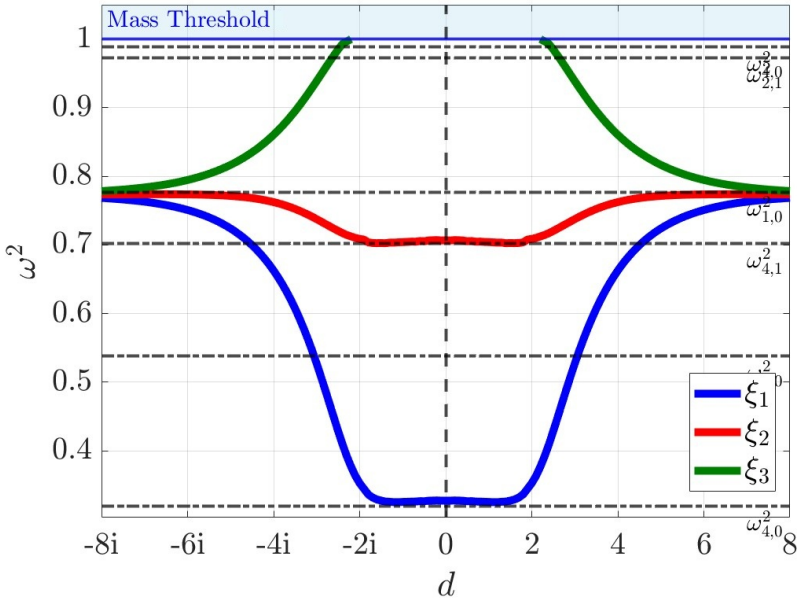

Figure 8.3.8: Spectral structure for a 4-vortex system, where the configuration of $N = 1$ vortices is the subspace $\mathcal{N}^{(1)}$, where the vortices are located on the vertices of a square, and d is the distance of the vortices from the origin.

introduce an attractive intervortex force. Previous results on 2-vortex systems and 3-vortex systems would suggest that this would lead to multiple bounces, whereby the vortices scatter at 90°, and we would expect to see a phase dependant fractal structure for the number of bounces.

Next, consider the red line ξ_2 in figure 8.3.8. The squared frequency at $d = 0$ is $\omega^2_{4,1}$, which is the $k = 1$, $N = 4$ mode. Asymptotically, the squared frequency also increases to $\omega^2_{1,0}$, suggesting that an excitation in this channel is also attractive, but not as strongly as ξ_1.

Finally, we consider the green line ξ_3 in figure 8.3.8. We observe with ξ_3 that there is a mode that reaches the continuous spectrum before the vortices scatter, suggesting the existence of a spectral wall.

8.3.3.2 Spectral structure of the subspace $\mathcal{N}^{(2)}$

Next, we consider the subspace $\mathcal{N}^{(3)}$ of four vortices, where we have an $N = 2$ vortex at the origin and two $N = 1$ vortices equidistant on the x_1 axis, and d is the distance from the outer $N = 1$ vortices to the origin. Interestingly, we see in figure 8.3.9 that we have the same number of modes at $d = 0$, and asymptotically ($d \to \infty$). For the $N = 4$ coincident configuration, we have three modes, a lower and upper $\omega^2_{4,0}$ mode, as well as

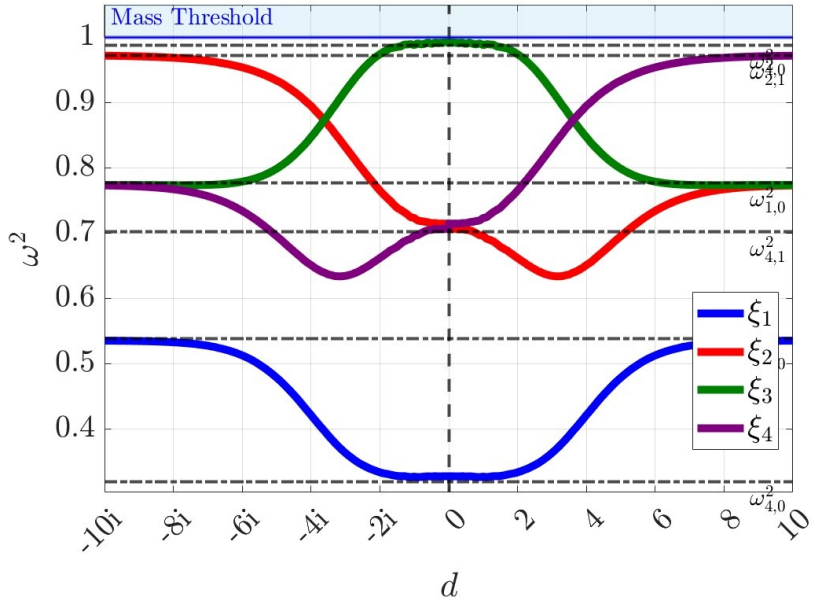

Figure 8.3.9: Spectral structure for a 4-vortex system, where the configuration is the subspace $\mathcal{N}^{(3)}$, where we have two $N = 1$ vortices equidistant on the x_1 axis, and a $N = 2$ vortex at the origin, and d is the distance of the vortices from the origin.

the $\omega^2_{4,1}$ shape mode. Asymptotically, we have the $\omega^2_{2,0}$ mode, the $\omega^2_{1,0}$ mode, and finally the $\omega^2_{2,1}$ mode.

First, consider the blue line ξ_1 in figure 8.3.9 which is the lowest excitation. We see that this excitation interpolates between the mode with squared frequency $\omega^2_{2,0}$ asymptotically, to the mode with squared frequency $\omega^2_{4,0}$ at $d = 0$. The squared frequency decreases as the vortices approach the axially symmetric $N = 4$ configuration, suggesting an attractive intervortex force. Note that this excitation is a global minimum.

Next, consider the red line ξ_2 in figure 8.3.9. The asymptotic value of the squared frequency of this mode is $\omega^2_{1,0}$, which is degenerate. As the vortices come closer together, the degeneracy is broken. As we decrease in d, the squared frequency decreases to $\omega^2_{4,1}$ at $d = 0$, where we have a mode crossing between ξ_2 and ξ_4 (the purple line in figure 8.3.9). After the vortices pass the axially symmetric $N = 4$ configuration, the squared frequency then increases to $\omega^2_{2,1}$ asymptotically. This suggests that the mode is attractive in $d \in \mathbb{R}^+$ and then changes to repulsive in $d \in \mathbb{R}^-$. Furthermore, we see that for small positive d, there is a local minimum, suggesting that vortices might become trapped in a quasi-stationary state where the squared frequency takes its minimum value.

Finally, we have the third mode ξ_3, see the green line in figure 8.3.9. We see that at

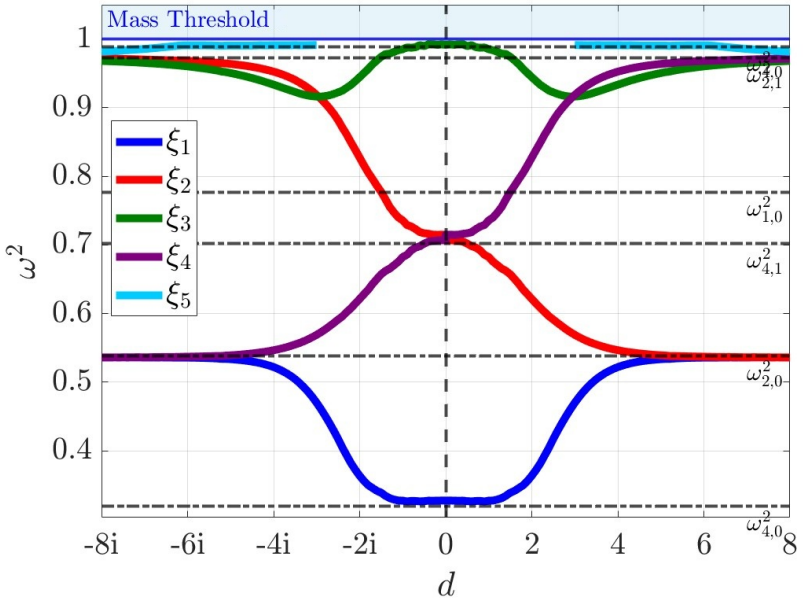

Figure 8.3.10: Spectral structure for a 4-vortex system, where the configuration is the subspace $\mathcal{N}^{(2)}$, where we have two $N = 2$ vortices equidistant on the x_1 axis, and d is the distance of the vortices from the origin.

$d = 0$, the excitation takes the value of the upper $\omega_{4,0}$ mode. As the vortices separate, the squared frequency decreases to $\omega^2_{1,0}$. This suggests a repulsive intervortex force. Furthermore, we have an additional mode crossing with the ξ_4 excitation (purple), which is the reflection of ξ_2.

8.3.3.3 Spectral structure of the subspace $\mathcal{N}^{(3)}$

Consider the subspace of two $N = 2$ vortices. At $d = 0$, we see that we have three modes, the lower ones with squared frequencies $\omega^2_{4,0}$, $\omega^2_{4,1}$, and the upper one with squared frequency $\omega^2_{4,0}$. Asymptotically, we have two degenerate modes, which are the two modes that exist for the $N = 2$ vortex with squared frequencies $\omega^2_{2,0}$ and $\omega^2_{2,1}$.

First, consider the blue line ξ_1 in figure 8.3.10. As in the case of the subspace $\mathcal{N}^{(1)}$, at $d = 0$ this mode is the global minimum, with squared frequency $\omega^2_{4,0}$. As two $N = 2$ vortices separate, we see that the squared frequency increases to $\omega^2_{2,0}$, suggesting an attractive intervortex force.

Next, we discuss the red line ξ_2 in figure 8.3.10. Asymptotically, we see that the degeneracy of the $\omega^2_{2,0}$ mode is broken. The mode increases to $\omega_{4,1}$ at $d = 0$. Note that there is a level crossing between ξ_2 and ξ_3 after the vortices pass through the axially

symmetric $N = 4$ configuration. The squared frequency continues to increase, reaching $\omega^2_{2,1}$. This would suggest a repulsive intervortex force.

There is also a third excitation; see the green line ξ_3 in figure 8.3.10. Asymptotically, the excitation has squared frequency $\omega^2_{2,1}$. This mode is also degenerate. The degeneracy is broken as the vortices come close together. The squaredfrequency initially decreases, suggesting an attractive force. There is a mode crossing with ξ_4 (the reflection of ξ_2). After this crossing, the squared frequency increases so that at $d = 0$, the squared frequency is that of the upper mode, with squared frequency $\omega^2_{4,0}$. This mode appears to be symmetric across the x_1 and x_2 axes. Hence, the vortices scatter through the upper $\omega_{4,0}$ configuration. Note that this overall increase in squared frequency suggests a repulsive intervortex force. Therefore, we see that an excitation of the form ξ_3 would induce an attractive-repulsive force as the separation of the vortices varies.

Finally, we observe the cyan line ξ_5 in figure 8.3.10. Again, the asymptotic value of this excitation is $\omega^2_{2,1}$. The degeneracy is broken once again as the vortices come closer together and the squared frequency quickly reaches the continuous spectrum at a finite distance $d \in [2, 3]$. This suggests that an excitation of this form could result in the formation of a spectral wall. Note that this excitation only slightly increases as the vortices come closer together, suggesting a weakly repulsive intervortex force.

8.3.3.4 Spectral structure of the subspace $\mathcal{N}^{(4)}$

Finally, for 4-vortex configurations, we consider the subspace $\mathcal{N}^{(4)}$ of four $N = 1$ vortices equidistant along the x_1-axis. Here, d is the distance of the outer vortices from the origin. The spectral structure is indeed quite similar to the spectral structure in the subspace $\mathcal{N}^{(2)}$, however, there are some key differences. We have the same number of modes at $d = 0$, however, the number of modes is not constant for all d.

Quite strikingly, notice the purple line ξ_4 in figure 8.3.11. Here we see that asymptotically the value of the excitation is $\omega^2_{1,0}$. As the vortices come closer together, the squared frequency increases rapidly, reaching the continuous spectrum at $d \in [5, 6]$. The would suggest the formation of a spectral wall *before* the vortices scatter.

We note that the lowest excitation ξ_1 (see the blue line in figure 8.3.11) is indeed quite similar to that in figure 8.3.9, hence we expect the same behaviour. Additionally, we see that the cyan line ξ_5 in figure 8.3.11 is in fact the same excitation as ξ_3 (green) in figure 8.3.9.

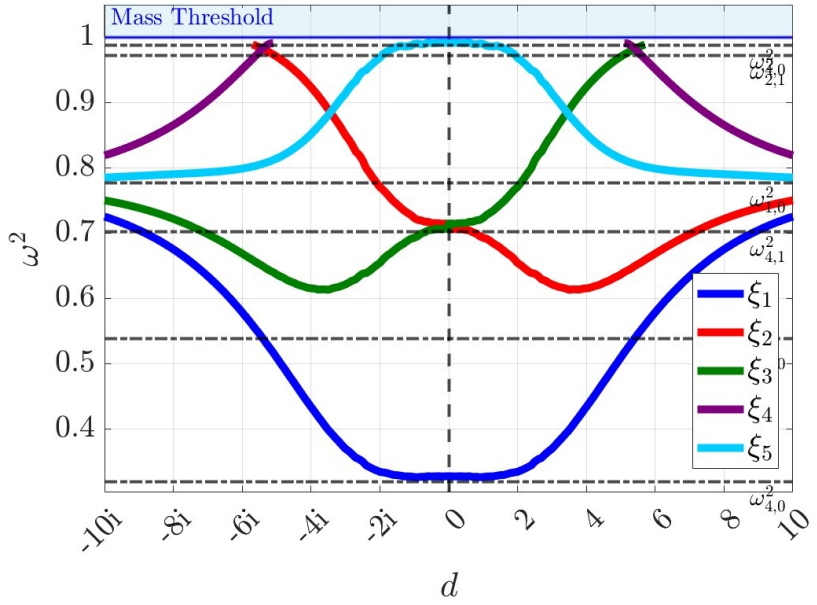

Figure 8.3.11: Spectral structure for a 4-vortex system, where the configuration is the subspace $\mathcal{N}^{(4)}$, where we have four $N = 1$ vortices equidistant on the x_1 axis. d is the distance of the vortices from the origin.

Next, consider the second excitation ξ_2, the red line in figure 8.3.11. Similarly to the subspace $\mathcal{N}^{(2)}$, we observe a local minimum where we might expect to see a quasi-stationary state. Surprisingly, after the vortices pass the axially symmetric $d = 0$ configuration, the path of the mode differs from that in the previous subspace. Here, we see that the squared frequency increases after the level crossing with ξ_3 (green), reaches the continuous spectrum at a position $d \in [-5i, 6i]$ *after* the vortices scatter.

8.4 Conclusions

In this chapter, we have investigated the spectral structure of vortices in the Abelian Higgs model, focusing on the linear perturbations and normal modes for $N = 1$, $N = 2$, $N = 3$, and $N = 4$ vortex configurations.

By employing a radially symmetric ansatz and a central second-order finite-difference scheme, we reduced the eigenvalue problem to a one-dimensional form, enabling the identification of discrete modes, including shape, translation, and splitting modes. For $N = 1$, we identified a single shape mode with squared frequency $\omega^2_{1,0} = 0.77747$, alongside a zero-energy translation mode. The $N = 2$ system revealed four discrete modes at critical coupling ($\lambda = 1$), with the $k = 0$ shape mode entering the continuum

at $\lambda \approx 3$. For $N = 3$, five discrete modes were found, with complex spectral flow indicating potential quasi-stationary states, particularly for the ξ_2 mode with a local minimum. The $N = 4$ system exhibited seven modes, with spectral walls suggested by modes reaching the continuum at finite separations.

The two-dimensional spectral flow analysis further showed how mode frequencies vary with vortex separation, indicating attractive and repulsive intervortex forces. For instance, the ξ_1 mode in the 2-vortex system decreases in squared frequency as vortices approach, suggesting an attractive force, while the ξ_2 mode's increase suggests a repulsive force, with mode crossings pointing to possible spectral walls. Similarly, the $N = 3$ and $N = 4$ systems displayed complex mode structures, with implications for scattering dynamics explored in subsequent chapters.

These findings, building on prior work [8, 9, 14, 36, 67], provide a robust foundation for understanding vortex interactions and their dynamic behaviours in the Abelian Higgs model.

Chapter 9

Excited Vortex Dynamics at Critical Coupling

9.1 Introduction

This chapter includes work from [11, 13, 47]. In this chapter, we will consider the second-order dynamics of vortices away from $\mathcal{M}_N$ by exciting the normal modes of the individual vortices. We will demonstrate that vortices do exhibit long-range forces at critical coupling when their normal modes are excited. We will then consider the effect of these excited modes on the scattering of vortices.

Several studies have considered the effect of excited normal modes on the scattering of solitons and antisolitons in 1-dimensional wobbling kinks [15]. The scattering of wobbling kink/anti-kinks (while exhibiting strong attractive static forces) are shown to bounce off each other depending on initial velocities and the intensities of the excited mode. The number of bounces has also been shown to be chaotic in nature. Further motivation arises during the scattering of $N > 1$ vortices, see section 6.8.2, where we observe the natural excitation of $N = 1$ vortex shape modes.

We explore the numerical techniques used in simulating vortex dynamics. We display results found from scattering vortices with excited shape modes.

9.1.1 Initial Configuration

We now explore a single vortex solution to the static equations of motion with excited shape mode. We can hence generalise an initial configuration for the vortex fields when

the shape mode is excited.

$$\begin{aligned}
\phi_1(t, x_1, x_2) &= \mathcal{R}((x_1 + ix_2)^N)F(x_1^2 + x_2^2) + \epsilon\psi_1(x)\cos(\omega t - \sigma(0)), \\
\phi_2(t, x_1, x_2) &= \mathcal{I}((x_1 + ix_2)^N)F(x_1^2 + x_2^2) + \epsilon\psi_2(x)\cos(\omega t - \sigma(0)), \\
A_\mu(t, x_1, x_2) &= \begin{pmatrix} 0 \\ -x_2 G(x_1^2 + x_2^2) + \epsilon\chi_1(x)\cos(\omega t - \sigma(0)) \\ x_1 G(x_1^2 + x_2^2) + \epsilon\chi_2(x)\cos(\omega t - \sigma(0)) \end{pmatrix},
\end{aligned} \tag{9.1.1}$$

where $\sigma(0)$ is the initial phase of the mode, ψ_i, χ_i are the perturbations, F and G are the solutions of eq. (6.5.9), ω is the angular frequency and ϵ is the magnitude of the perturbation.

We can now simulate a single vortex of degree N, with excited shape mode. We can hence study the intensity of the $N = 1$ excitation over time, by calculating the amplitude of the static potential energy. Figure 9.1.1 shows how the intensity of the excitation changes with time. Mathematically, the energy is conserved, however the damping boundary conditions (see chapter 7) remove radiation from the system that approaches the boundary. Thus, in a numerical sense, the total energy in the system decreases as radiation is absorbed.

The solid black line indicates the choice of ϵ used for the majority of our results. We denote the initial intensity of the excitation $I(0)$, where

$$I(0) = \frac{1}{2}(\epsilon\omega)^2. \tag{9.1.2}$$

We can see that there is an exponential decay by taking a logarithm of the intensity, see figure 9.1.2, whereby for $\epsilon < 0.7$, the resulting curves are straight lines. Initially, we see that for larger ϵ, the intensity of the shape mode decays faster. However, changing the initial intensity is the same as shifting through time, see figure 9.1.1, whereby we can shift along the time-axis such that all initial intensities can be considered as a decayed excitation along the same curve.

Figure 9.1.1 gives us a range of suitable intensities for the excitation of the shape mode

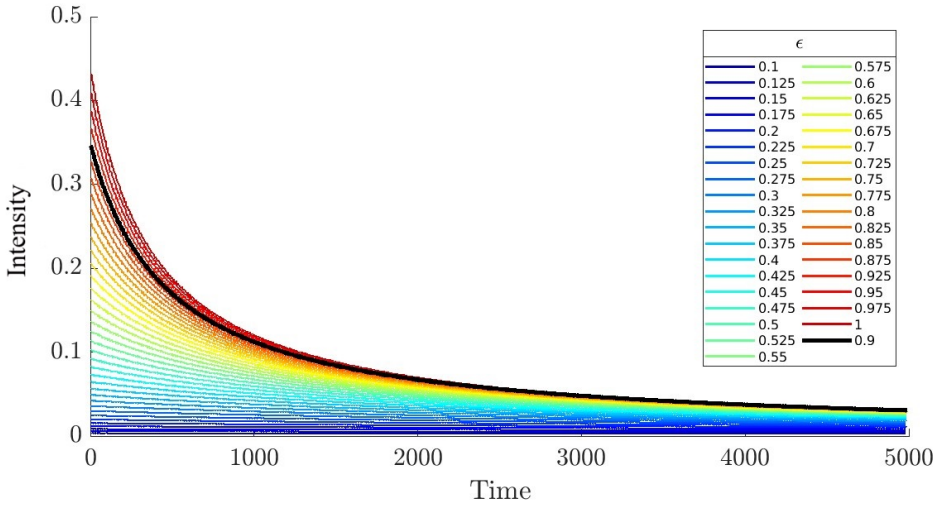

Figure 9.1.1: Change in intensity of the $N = 1$ vortex shape mode against time, where the intensity is the amplitude of the fluctuations in the static potential energy. The black line with $\epsilon = 0.9$ corresponding to $I(0) = 0.317$ is our default initial intensity in section section 9.2, where $I(0) = \frac{1}{2}(\epsilon\omega)^2$

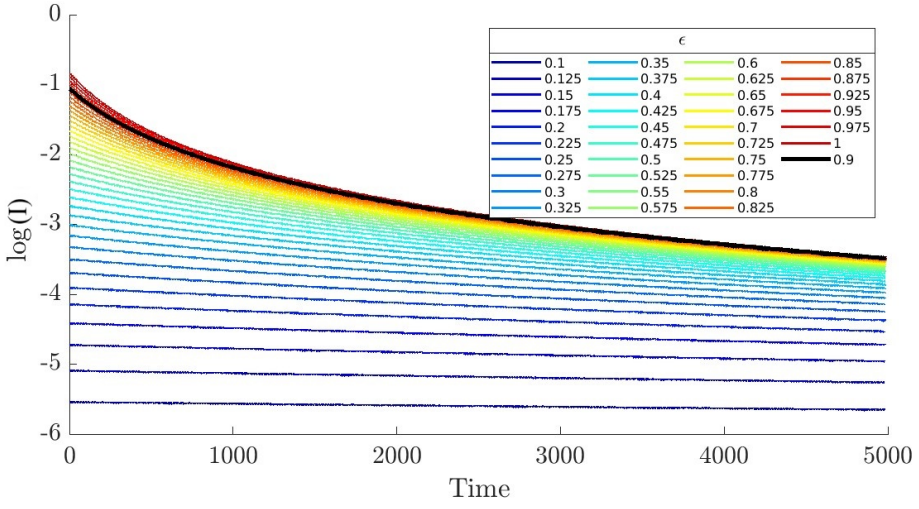

Figure 9.1.2: Log-plot of the intensity of the $N = 1$ shape mode against time, to show the exponential decay of the excitation. The black line with $\epsilon = 0.9$ corresponding to $I(0) = 0.317$ is our default initial intensity in section section 9.2.

to scatter excited vortices. We then boost the vortex eq. (9.1.1) using a Lorentz transformation, see section 7.1

$$\tilde{\phi_1}(t,x_1,x_2) = \mathcal{R}((\gamma(x_1+vt)+ix_2)^N)F(\gamma^2(x_1+vt)^2+x_2^2)+\epsilon\psi_1(\tilde{x})\cos\left(\omega\gamma(t+vx_1)-\sigma(0)\right),$$
$$\tilde{\phi_2}(t,x_1,x_2) = \mathcal{I}((\gamma(x_1+vt)+ix_2)^N)F(\gamma^2(x_1+vt)^2+x_2^2)+\epsilon\psi_2(\tilde{x})\cos\left(\omega\gamma(t+vx_1)-\sigma(0)\right),$$
$$\tilde{A}_\mu(t,x_1,x_2) = \begin{pmatrix} -\gamma v x_2 G(\gamma^2(x_1+vt)^2+x_2^2)+\gamma v\epsilon\chi_1(\tilde{x})\cos\left(\omega\gamma(t+vx_1)-\sigma(0)\right) \\ -\gamma x_2 G(\gamma^2(x_1+vt)^2+x_2^2)+\gamma\epsilon\chi_1(\tilde{x})\cos\left(\omega\gamma(t+vx_1)-\sigma(0)\right) \\ \gamma(x_1+vt)G(\gamma^2(x_1+vt)^2+x_2^2)+\epsilon\chi_2(\tilde{x})\cos\left(\omega\gamma(t+vx_1)-\sigma(0)\right) \end{pmatrix}. \tag{9.1.3}$$

For large initial intensities, the nonlinear terms in eq. (8.2.3) become significant, and we observe that the energy is phase dependent, varying up to order $\mathcal{O}(\epsilon^3)$ for a $\pi-$shift.
It is outlined in section 9.2.3 how to excite the same mode using a Derrick scaling. We find that the mode excitation can be well approximated by a scaling of the fields. However, this allows less freedom in the choice of the initial phase. To alter the phase using the Derrick's method, we must evolve the vortex in time to numerically change the initial phase of the mode, which results in a small decay in the energy. Using the method by which we alter the phase in the Derrick's approximation, we can also alter the phase the same way for eq. (9.1.3). By changing the phase this way, the intensity of the shape mode decays by approximately 10^{-4}, which is significantly less than the contribution to the energy of the higher order terms in the linearisation. Because of this, we will show in section 9.2 a phase space plot from both methods.
The initial field configurations eq. (9.1.3) are approximations to solutions of the dynamic equations of motion eqs. (6.2.17) and (6.2.18) and can be used to simulate a single degree N vortex with excited normal modes. We seek to study the scattering of excited $N=1$ vortices; hence we must create multi-vortex field configurations that are also solutions to the equations of motion eqs. (6.2.17) and (6.2.18). The Abikrosov ansatz [1] allows us to find field configurations detailing well-separated Lorentz boosted vortices with excited shape modes. The Abikrosov ansatz for a given vortex solution $(\tilde{\phi}(t,x),\tilde{A}_\mu(t,x))$ is

$$\hat{\phi} = \prod_i \tilde{\phi}(x-d_i), \qquad \hat{A}_\mu = \sum_i \tilde{A}_\mu(x-d_i), \tag{9.1.4}$$

where d_i are the positions of the vortex centres. The approximation works well when the vortices are well separated from each other, such that the separation is much larger

than the vortex core size, namely $2d_i \gg 1$.

9.2 Quasi-Bound States

In this section, we study the scattering behaviour of two $N = 1$ critically coupled vortices with excited shape modes, following the path of the first mode ξ_1; see figure 8.3.3. This means that we consider an initial excitation of the form eq. (8.3.2).

The excitation leads to an interesting scattering behaviour dependent on initial velocity, as well as intensity and phase of the shape mode. We look at snapshots of a numerical simulation which show the scattering of the excited vortices. We also plot different vortex trajectories, where we vary the initial phase of the shape mode. Furthermore, we show a plot summarising a sampling of scattering outcomes for a fixed intensity, where we vary the initial velocity and the phase of the shape mode. We then discuss how this summary is different if we change the initial intensity of the shape mode. Finally, we give a brief discussion regarding changing the relative phase of the shape mode between the two vortices.

For all simulations discussed in this section, the vortices are located at $d_i = \pm 10$, where d_i is defined in eq. (9.1.4). This separation was chosen so that the vortices are initially well separated and the forces between them can be neglected. Unless stated otherwise, we consider solutions for a fixed initial intensity $I(0) = 0.317$. This corresponds to $\epsilon = 0.9$, where ϵ is the magnitude of the perturbation, defined in eq. (8.2.5). We choose a sufficiently large initial intensity $I(0)$ such that there is enough energy in the shape mode for a considerable amount of interesting behaviour in the excited-scattering process. We label the initial phase of the shape mode with $\sigma(0) \in [0, 2\pi)$, defined in eq. (9.1.3). Unless stated otherwise, the two vortices are in phase with each other. We denote the initial velocity of the vortices by v_{in}.

9.2.1 Results

First, we show snapshots of a simulation for a 2-vortex scattering with excited shape modes in figure 9.2.1. The initial phase of the shape mode for each vortex is $\sigma(0) = 2.2612$, and the initial velocity is $v_{\text{in}} = 0.01$. We display the energy density as a heat plot and overlay the zeros of the Higgs field as black dots. We see that the energy density fluctuates as a result of the excited shape mode. At critical coupling, there are

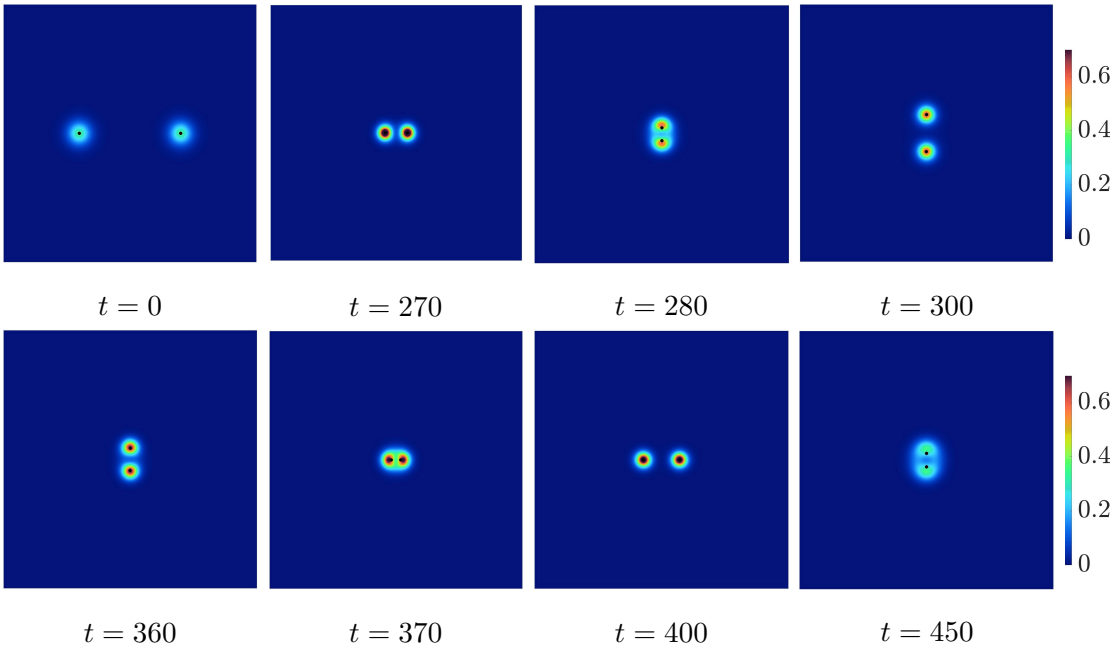

Figure 9.2.1: Heat plots of the energy density, showing snapshots through time of an excited vortex scattering, with initial phase $\sigma(0) = 2.2612$, initial velocity $v_{\text{in}} = 0.01$, and initial separation $s = 20$. The black dots indicate the zeros of the Higgs field. This figure shows how the vortices accelerate towards each other and then scatter at 90°. The vortices then slow before accelerating towards each other and scattering at 90° again, which repeats many times.

no static forces between vortices, and vortices scatter at right angles, in agreement with the moduli space approximation. We find that this is no longer the case for excited vortices. We refer to this multi-bounce behaviour as a quasi-bound state.

For a fuller picture of 2-vortex scattering, we can track the zeros of the Higgs field, as seen in figure 9.2.2. We plot half the separation of the zeros for a set of solutions to show the trajectories of the vortices as a function of time. We have only varied the initial phase $\sigma(0)$ for fixed velocity $v_{\text{in}} = 0.06725$. The solid blue line shows the the position (d) of the zeros of the Higgs field of the two vortices with excited shape mode from the origin, and the solid red line is the intensity $I(t)$ of the excitation. The dashed blue line shows the separation of two vortices with the same initial configuration but without excitation. The dashed red line indicates the intensity of a single vortex with the same mode excitation.

Let us begin by discussing the excited vortex scattering in general. We can see that the trajectories of the vortices with excited shape modes are different from those without excitation. Initially, there is no deviation between the vortex trajectories with or without excitation. There is also no curvature in the trajectories before $d \approx 8$, showing that the

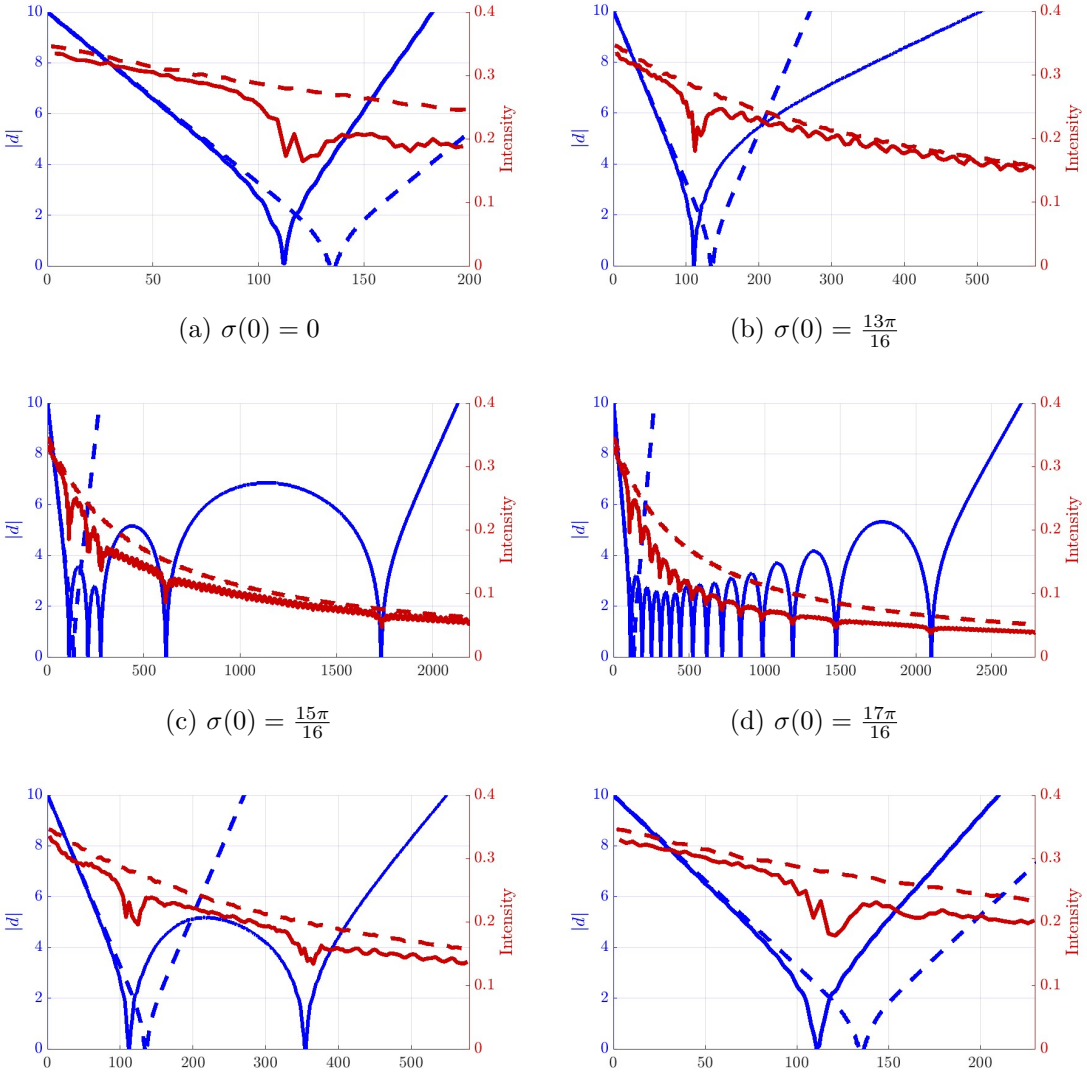

(a) $\sigma(0) = 0$ (b) $\sigma(0) = \frac{13\pi}{16}$

(c) $\sigma(0) = \frac{15\pi}{16}$ (d) $\sigma(0) = \frac{17\pi}{16}$

(e) $\sigma(0) = \frac{5\pi}{4}$ (f) $\sigma(0) = \frac{25\pi}{16}$

Figure 9.2.2: Tracking of position of the vortices with time, plotted in blue. Red indicates the intensity of the excitation per vortex. We show 6 plots, with different initial phases, and fixed initial velocity $v_{\text{in}} = 0.06725$. The dashed blue line indicates the standard scattering process with no excitation but with the same initial velocity. The dashed red line indicates the intensity of the excitation in the absence of the scattering.

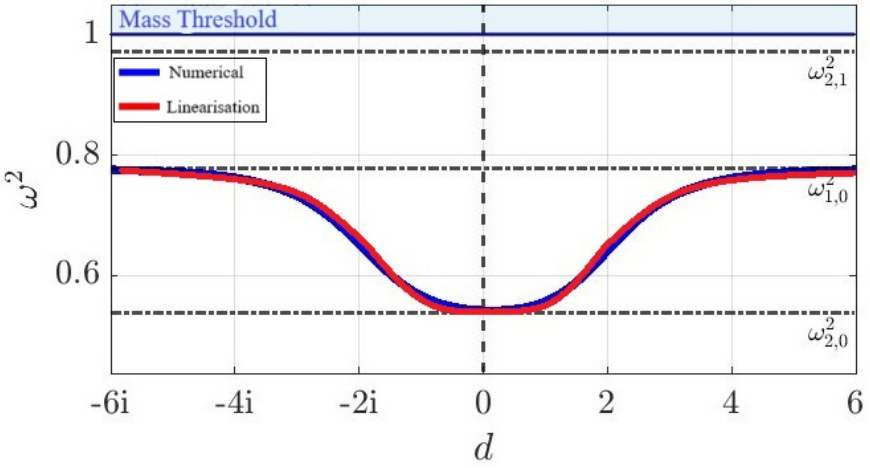

Figure 9.2.3: Numerically calculated flow of the squared angular frequency ω^2 from a dynamical simulation, as a function of the distance of the vortices to the origin d (blue), where $s = 2d$, and spectral flow calculated from the 2-dimensional linearisation (red). We choose an initial velocity of $v_{\text{in}} = 0.01$, and initial intensity $I(0) = 0.01$, where $I(0) = \frac{1}{2}(\epsilon\omega)^2$.

vortices travel initially at a constant velocity. This is because the length scale of the mode is approximately the same as the size of the vortices, which fall off exponentially at approximately $d = 8$, see figure 8.2.3.

For $d < 8$, the trajectory of the excited vortices begins to deviate from that of the standard scattering. We observe an increasing slope in the trajectory of the excited vortices, and the excited vortices also collide sooner than without excitation. We can hence see that the vortices begin to accelerate towards each other within this region. This interaction is similar to the behaviour of type I vortices, where vortices are attractive; see figure 6.6.1.

In all tracking plots, the intensity of the excitation drops after the vortices collide. We can see that this is a result of the collision as this is a deviation from the dashed blue line. This is due to the energy transfer mechanism, where energy from the mode is transferred to the kinetic energy of the vortex. After the excited vortices scatter, the intensity increases slightly, suggesting that the kinetic energy from the vortices is transferred back to the excitation. This is confirmed by studying figure 9.2.3, where we plot the flow of the angular frequency as a function of the separation of the vortices for a simulation where the vortices are not trapped in a quasi-bound state. We see that the frequency drops as the vortices scatter, suggesting that an excitation of this form is in the attractive channel. This confirms what we see from the lower mode ξ_1 in figure 8.3.3.

Furthermore, if there is more energy in the excitation, the vortices become more attractive, and hence we observe that they scatter again. Near the end of the simulation, we can see that the intensity of the excitation has decreased significantly, especially for figures 9.2.2c and 9.2.2d. It is possible that there is not enough energy left in the excitation, as it radiates energy as a result of the fast decay of the intensity. This means that not enough energy can be transferred to the kinetic energy, and hence the vortices escape.

There are some slight fluctuations in the intensity after the vortices collide. We believe this fluctuation to be a result of the Doppler effect as radiation is emitted from the vortices as they travel, which we have reproduced by studying the Doppler effect. Note that this is not displayed in this thesis.

Figures 9.2.2c to 9.2.2e display a quasi-bound state, where we have multiple bounces. Figure 9.2.2e shows a 2-bounce scattering solution, figure 9.2.2c shows a 4-bounce solution, and figure 9.2.2d shows a 13-bounce solution. We can see from the trajectories that the size of the bounce windows increases with time. This could be argued to be a result of the decay of the mode. As the mode decays, it loses energy, resulting in a reduced attractive quality as time progresses. This behaviour is expected as it is observed with kinks that we initially have noticeably short bounces that become longer as the simulation evolves [15].

9.2.2 Fractal Structure

Next, we study a phase space of solutions to help identify any patterns in the behaviour of the excited 2-vortex scattering. We find solutions for a range of initial phases and initial velocities, and hence generate a phase space of solutions, detailing the number of bounces as the number of times the vortices scatter through each other.

Figure 9.2.4b shows a sample of solutions for a set of initial phases $\sigma(0) \in [0, 2\pi)$, and initial velocities $v_{\text{in}} \in [0.01, 0.13]$. The number of bounces is indicated by the colour. The y-axis has been extended to be in the range $[0, 6\pi)$, since the phase coordinate is cyclic.

As stated above, we can alter the phase of the mode in two different ways. We can see the phase space of solutions for both these methods in figures 9.2.4a and 9.2.4b. Figure 9.2.4b shows solutions where the initial phase of the shape mode has been changed

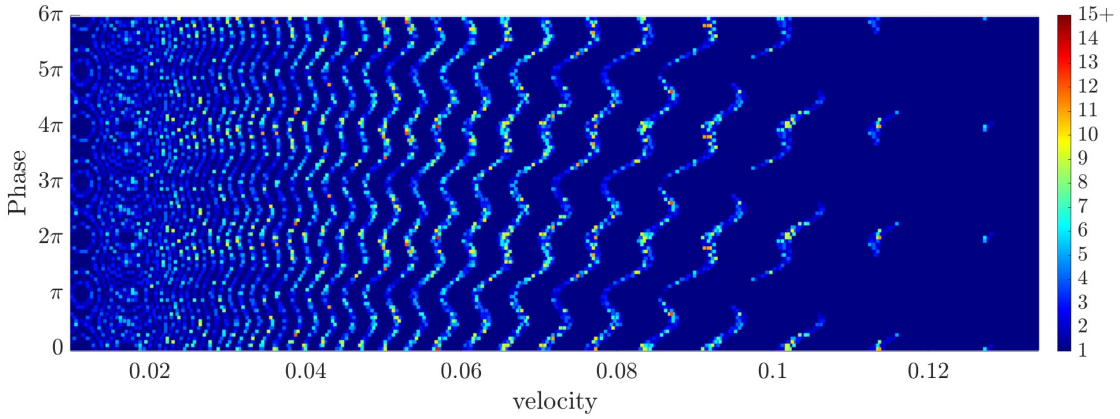

(a) Initial phase altered by changing $\sigma(0)$ in eq. (9.1.3).

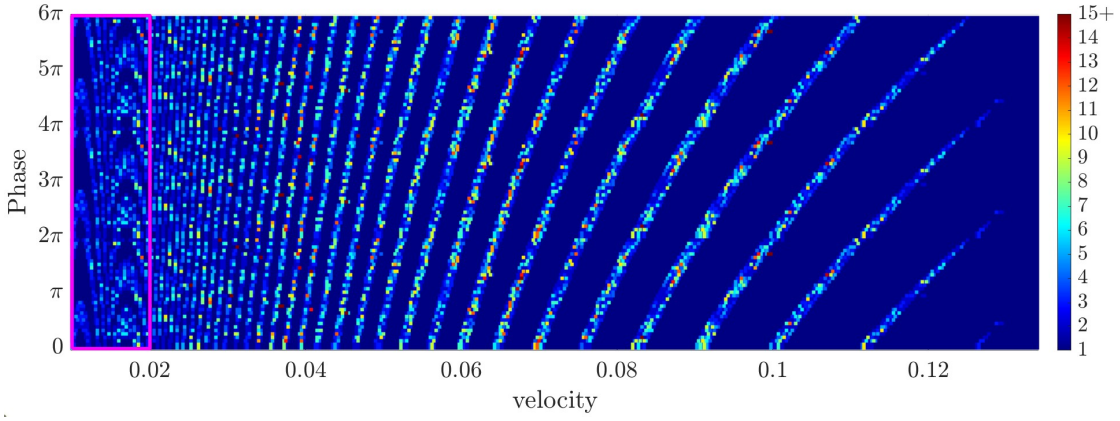

(b) Initial phase altered numerically using a displacement shift and evolving through time.

Figure 9.2.4: Phase space of excited vortex scattering solutions. We show solutions for different initial velocity and initial phase for fixed $\epsilon = 0.9$. The dark blue space indicates solutions that only have one bounce, i.e. the vortices scatter only once, which is the normal behaviour for vortices at critical coupling. The number of bounces is represented as a heat plot for the colour of each simulation, shown by the colour bar. The data is plotted three times along the y axis since the phase coordinate is cyclic, allowing us to get a clearer picture of the behaviour of the phase space. The purple rectangle corresponds to figure 9.2.5, where we show the phase space with higher resolution.

by shifting the initial vortex position d_i, and numerically evolve to alter the initial phase, and figure 9.2.4a shows solutions where the initial phase is changed using eq. (9.1.3). Due to the dependence of the energy on ϵ in eq. (9.1.3), which is maximal at a $\pi-$shift, we can see in figure 9.2.4a that the pattern of the results deviates most at this value, showing that the difference between these plots is an artefact of this phase dependence on the energy. We can hence assume that the plots should be identical, except that we have this deviation because of the method used.

We have shown that an in-phase excitation ξ_1 introduces an attractive force between

the single vortices. This, together with the resonant energy transfer mechanism between the kinetic and vibrational motion, triggers a fractal pattern of multi-bounces, where depending on the number of collisions the vortices are scattered under 90° or 180° angle. Indeed, precisely as in the kink-antikink collisions in ϕ^4 model [26, 56, 72], the energy initially stored in the kinetic motion can be temporarily transferred to the vibration mode and forces the vortices to collide again.

We observe in figure 9.2.4b regions of solutions that have multi-bounce scattering. We also observe in-between these regions sets of solutions that only scatter once. We see that the lines of solutions that have multi-bounces also have a curvature, rather than a fixed slope. This is quite intuitive, as we have a series of lines of decreasing gradient; however, we can clearly see that the lines curve. This means that changing the initial phase of the mode is equivalent to changing the initial velocity, up to a critical value where the initial velocity dominates the interaction of the vortices and they always escape. We can see that this critical velocity is around the region of $v_{\text{in}} = 0.13$. However, this is only a rough approximation. Extending the phase space in the y-direction also allows us to see more easily that for any given initial velocity below the critical region, you can always choose an initial phase such that the vortices scatter more than once.

For low velocities, the resolution of the phase space is too small to reveal the full structure of the phase space, hence the presence of the parabola in the parameter space of solutions figure 9.2.4b is a result of the resolution of the data. We observe in figure 9.2.5 that the fractal structure of repeated lines is observed for small velocities, but due to the increasing slope of this pattern at low velocities, it is difficult to capture the pattern as the lines become more vertical and narrow, meaning that it is easy to miss when scanning the parameter space.

We can hence see that the whole phase space shows a fractal structure of regions with multiple bounces, ranging from 2 to 30 bounces. The number of bounces does not appear to have any correlation to the phase space at large, but it could be argued that the resolution of the diagram is too low to give a definitive answer. We now turn to the question of why this fractal pattern appears. We can surmise that this is a result of the phase of the shape mode altering the state of the interaction for different velocities. We see that periodically, there are these dark blue regions (solutions that only scatter once) and then thin slices of solutions with multiple bounces, increasing in width and decreasing in slope as the initial velocity increases. Furthermore, these factors appear

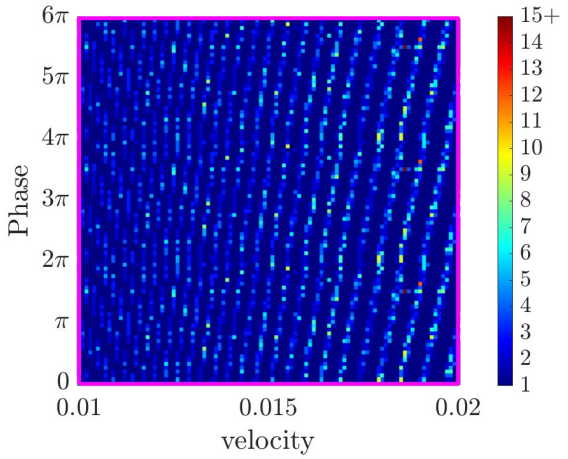

Figure 9.2.5: A higher resolution plot of the phase space plot. We plot the highlighted region of figure 9.2.4b, but using a smaller step in v_{in}.

to be constant for each region with respect to the phase.

We now discuss other initial intensities of the excitation. Take, for example, $\epsilon = 0.5$, i.e. $I(0) = 0.097$. For this initial intensity, the mode decays extremely slowly, and hence nonlinear effects are smaller. We find that for small velocities the vortices escape after one bounce. Hence, we can assume that for this intensity, the scattering is dominated by the velocity, and the mode excitation causes little interaction between the vortices as they scatter. This gives further evidence to the proposition that the vortices escape the bound state due to the decay of the excitation, as if the intensity is too small initially, they do not bounce more than once. Therefore, we examine one more initial intensity between these two values already discussed and take $\epsilon = 0.75$, such that $I(0) = 0.219$, which also decays slowly. We can see in figure 9.1.1 that this choice of ϵ corresponds to an initial intensity of approximately 60% of the previous intensity discussed, where $\epsilon = 0.9$ and $I(0) = 0.317$.

We see in figure 9.2.6 that we have the same fractal structure that dominates the phase space. There are some key differences between the phase space of solutions with $\epsilon = 0.9$ and $\epsilon = 0.75$. Firstly, we observe in figure 9.2.6 that there are only one bounce windows after an initial velocity of $v_{\text{in}} \approx 0.055$. This suggests that the interaction imposed by the mode is weaker than the strength of the initial velocity, further supporting the conjecture that the mode requires a certain amount of energy to dominate the interaction. We further see that the fractal lines are narrower in figure 9.2.6 than in figure 9.2.4b. However, they are significantly closer together, which could suggest that this set of solutions is just a scaled set of solutions compared to figure 9.2.4b. Note that for small

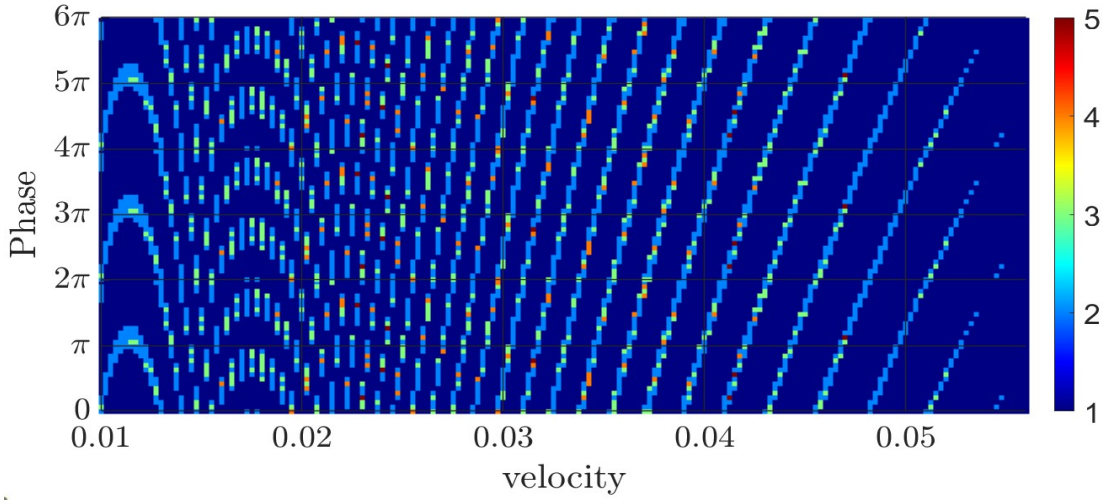

Figure 9.2.6: Parameter Solution space detailing the space of solutions computed using a 2^{nd} order Leapfrog method for time evolution. We show solutions for different initial velocity and initial phase for fixed $\epsilon = 0.75$. The dark blue space indicates solutions that only have one bounce, i.e. the vortices scatter only once, which is the normal behaviour for vortices at critical coupling. The number of bounces is represented as a heat plot for the colour of each simulation, shown by the colour bar. The data are plotted three times along the y axis since the phase coordinate is cyclic, allowing us to get a clearer picture of the behaviour of the phase space.

velocities, the line pattern is more difficult to see. This is due to the resolution of the phase space. With higher resolution, this part of the diagram would appear to fit the pattern of the rest of the data.

9.2.3 Derrick Scaling Approximation

This section seeks to show that the shape mode can be well approximated by a Derrick scaling of the fields.

we have Derrick's scaling argument in section 6.2. We can hence have the mode in terms of the Derrick scaling

$$\tilde{\psi} = \phi(\kappa x) - \phi(x), \tag{9.2.1}$$

$$\tilde{\chi}_\mu = \frac{1}{\kappa} A_\mu(\kappa x) - A_\mu(x). \tag{9.2.2}$$

It is important to perform the Derrick scaling on the fields before applying the Lorentz transformation, and the resulting initial condition is

$$\begin{aligned}\hat{\phi}(t,x) &= (\gamma(\kappa x_1 + vt) + i\kappa x_2)^N F(\gamma^2(\kappa x_1 + vt)^2 + \kappa^2 x_2^2), \\ \hat{A}_\mu(t,x) = (\hat{A}_0, \hat{A}_1, \hat{A}_2) &= \begin{pmatrix} Nv\gamma x_2 G(\gamma^2(\kappa x_1 + vt)^2 + \kappa^2 x_2^2) \\ -N\gamma x_2 G(\gamma^2(\kappa x_1 + vt)^2 + \kappa^2 x_2^2) \\ \frac{N\gamma(\kappa x_1 + vt)}{\kappa} G(\gamma^2(\kappa x_1 + vt)^2 + \kappa^2 x_2^2) \end{pmatrix},\end{aligned} \tag{9.2.3}$$

Hence we have an initial configuration for our two-dimensional dynamical simulations, detailing an axially symmetric vortex with an initial velocity and a Derrick mode excitation.

As stated above, we find the frequency of the shape mode to be $\omega^2_{1,0} = 0.777476$. By studying the potential energy of the Derrick scaled solution, we find a frequency of the approximated mode to be $\omega^2_{\text{Derrick}} = 0.770076$, which is within 1% of the frequency found through the linearisation of the full field theory. This gives us evidence that Derrick scaling the solution is indeed a good approximation to the shape mode.

We can determine how well the Derrick scaling approximates the mode, by calculating the 2-dimensional norm of the perturbation for both methods

$$\langle \mathbf{f}, \mathbf{g} \rangle = \int \mathbf{f} \cdot \mathbf{g} \; d^2x, \tag{9.2.4}$$

where $\mathbf{f}$ and $\mathbf{g}$ are vectors of the Higgs field and gauge fields for the Derrick scale perturbation, and the linearisation perturbation respectively, such that

$$\begin{aligned}\mathbf{f} &= (\tilde{\psi}_1(x,y), \tilde{\psi}_2(x,y), \tilde{\chi}_1(x,y), \tilde{\chi}_2(x,y))^T, \\ \mathbf{g} &= (\psi_1(x,y), \psi_2(x,y), \chi_1(x,y), \chi_2(x,y))^T.\end{aligned} \tag{9.2.5}$$

We see in figure 9.2.7 that the Derrick scaling mode approximation provides a partial approximation to the linearisation, with the normalised inner product between the perturbation vectors, representing the how well the Derrick scaling mode covers the linearisation ($\langle \mathbf{f}, \mathbf{g} \rangle / \sqrt{\langle \mathbf{f}, \mathbf{f} \rangle \langle \mathbf{g}, \mathbf{g} \rangle}$), ranging from approximately 0.9993 to 0.9753. For small perturbations around $\kappa = 1$, the deviation reaches a maximum of approximately 0.9993 at $\kappa = 0.98$, indicating a very close alignment, with the perturbation directions

differing by less than 0.07%. As the perturbation grows larger, the mode coverage decreases to 0.9753 at $\kappa = 0.5$ and 0.9797 at $\kappa = 1.5$, suggesting that the Derrick scaling approximation becomes less aligned with the linear mode, differing by up to 2.47% and 2.03% respectively. This indicates that the scale approximation is most effective near $\kappa = 1$, with alignment degrading as κ deviates, though it remains a reasonable method for exciting the mode across the tested range.

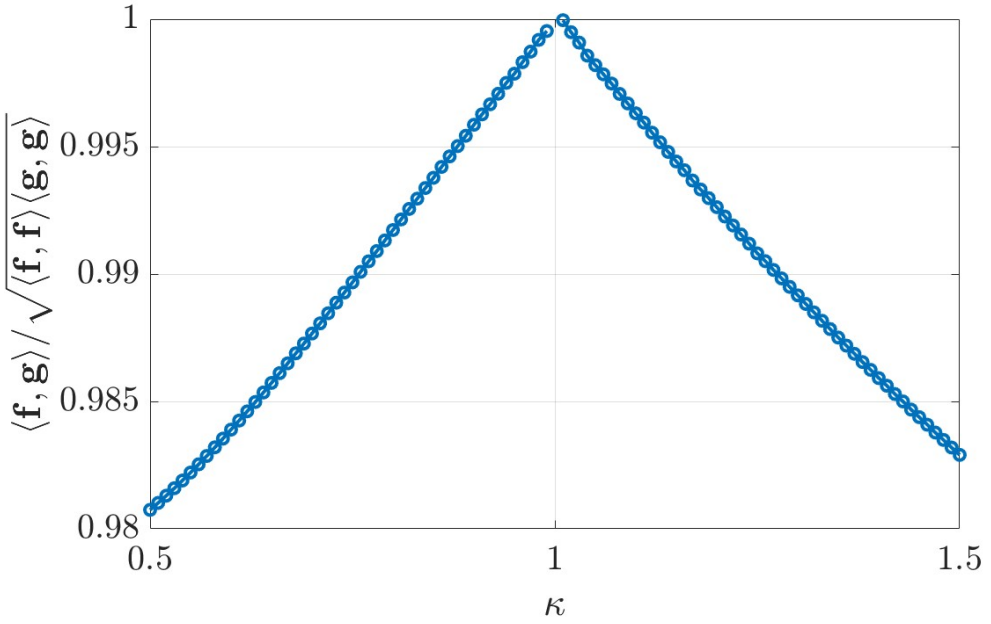

Figure 9.2.7: The normalised inner product $\langle \mathbf{f}, \mathbf{g} \rangle / \sqrt{\langle \mathbf{f}, \mathbf{f} \rangle \langle \mathbf{g}, \mathbf{g} \rangle}$, representing the deviation from perfect alignment between the Derrick scaling perturbation vector $\mathbf{f}$ and the linearisation perturbation vector $\mathbf{g}$, as a function of the scale factor κ. The deviation varies from approximately 0.9753 at $\kappa = 0.5$ (2.47% difference) to a maximum of 0.9993 at $\kappa = 0.98$ (0.07% difference), and decreases to 0.9797 at $\kappa = 1.5$ (2.03% difference), with an undefined value at $\kappa = 1.0$. These small deviations indicate the closest alignment near $\kappa = 1$, though the match is not as tight as initially expected across all κ.

It is a useful result that the shape mode can be approximated by a Derrick scaling. It has been shown in [36] and chapter 8 how to find eigenfunctions to excite the linear mode for all λ. The benefit of exciting the shape mode using a Derrick scaling is not only a simpler procedure, but it is applicable not only to critical coupling, but also for all λ, hence this method could be applied for all solitons, including those where the linearisation is not yet known. By approximating the shape mode by a Derrick scaling, we also begin to gain an understanding of the properties of interaction of the mode.

If we consider the spatial rescaling eq. (6.2.7), such that $\rho \to \kappa\rho$, then for $\rho \gg 1$, the equations eq. (6.6.1) rescale as

$$\begin{aligned} f(\rho) \to \tilde{f}(\rho) = f(\kappa\rho) &\approx 1 - \frac{q}{2\pi} K_0(\kappa\rho), \\ a_\theta(\rho) \to \tilde{a_\theta}(\rho) = a_\theta(\kappa\rho) &\approx 1 - \frac{m}{2\pi} \kappa\rho K_1(\kappa\rho). \end{aligned} \tag{9.2.6}$$

The magnetic field transforms under this rescaling. Starting with $B = \frac{1}{\rho}\frac{\partial a_\theta(\rho)}{\partial \rho}$,

$$\begin{aligned} B \to \frac{1}{\rho}\frac{\partial \tilde{a}_\theta(\rho)}{\partial \rho} &= \frac{1}{\rho}\frac{\partial}{\partial \rho}\left(a_\theta(\kappa\rho)\right) = \frac{1}{\rho}\cdot\kappa\frac{\partial a_\theta(\kappa\rho)}{\partial(\kappa\rho)} \\ &= \frac{\kappa}{\rho}\cdot\frac{\partial}{\partial(\kappa\rho)}\left(1 - \frac{m}{2\pi}(\kappa\rho)K_1(\kappa\rho)\right) \\ &= -\frac{\kappa}{\rho}\cdot\frac{m}{2\pi}\left[K_1(\kappa\rho) + (\kappa\rho)\frac{\partial K_1(\kappa\rho)}{\partial(\kappa\rho)}\right]. \end{aligned} \tag{9.2.7}$$

Using the derivative of the modified Bessel function, $\frac{\partial K_1(z)}{\partial z} = -K_0(z) - \frac{K_1(z)}{z}$, we get

$$\begin{aligned} B &= -\frac{\kappa}{\rho}\cdot\frac{m}{2\pi}\left[K_1(\kappa\rho) + (\kappa\rho)\left(-K_0(\kappa\rho) - \frac{K_1(\kappa\rho)}{\kappa\rho}\right)\right] \\ &= -\frac{\kappa}{\rho}\cdot\frac{m}{2\pi}\left[K_1(\kappa\rho) - (\kappa\rho)K_0(\kappa\rho) - K_1(\kappa\rho)\right] \\ &= \frac{\kappa}{\rho}\cdot\frac{m}{2\pi}(\kappa\rho)K_0(\kappa\rho) = \kappa^2\frac{m}{2\pi}K_0(\kappa\rho). \end{aligned} \tag{9.2.8}$$

Thus, the interaction energy at critical coupling, with s as the separation between two vortices, becomes

$$E_{int}(s) = -\frac{q^2}{2\pi}K_0(\kappa s) + \kappa^2\frac{m^2}{2\pi}K_0(\kappa s). \tag{9.2.9}$$

Therefore, we see that when $\kappa < 1$ the magnetic interaction is weaker, and hence there will be an attraction. Moreover, when $\kappa > 1$, the magnetic interaction is stronger, and hence there will be a repulsion between the vortices.

It is important to note that we have also developed the figures to excite the shape mode by a Derrick scaling of the fields. Indeed, using a Derrick scaling to excite the mode is only an approximation, and hence there is more radiation in the system when the excitation is carried out this way. However, it is much easier numerically to include a mode excitation of this form.

We show the phase space of solutions for a mode excitation of this form, see figure 9.2.8. Figure 9.2.8 shows that we can observe the same behaviour as in figure 9.2.4, confirming that using a Derrick scaling to excite the mode is a good approximation.

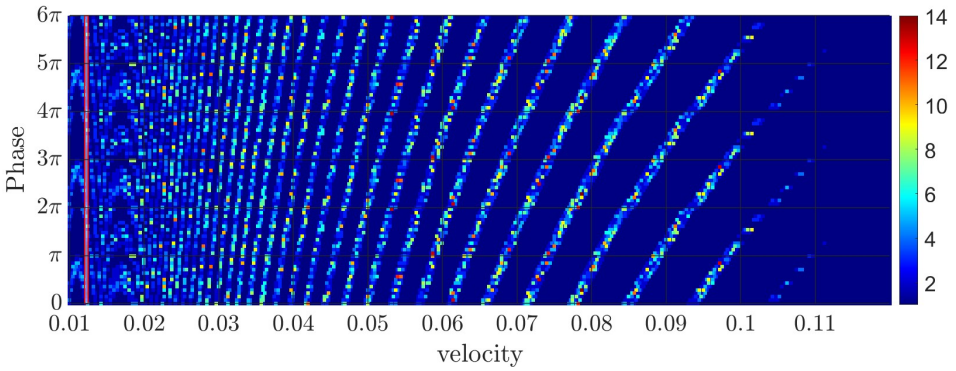

Figure 9.2.8: Phase space of scattering solutions. We show solutions for different initial velocity and initial phase for fixed Derrick factor $\kappa = 0.7$. The dark blue space indicates solutions that only have one bounce, i.e. the vortices scatter only once, which is the normal behaviour for vortices at critical coupling. The number of bounces is represented as a heat plot for the colour of each simulation, shown by the colour bar. The data are plotted three times along the y axis since the phase coordinate is cyclic, allowing us to get a clearer picture of the behaviour of the phase space.

9.3 Spectral Walls in 2-Vortex Scattering

We have shown that geodesic dynamics is significantly affected if a bound mode carried by the vortices is excited. If the lower mode ξ_1 is excited in a head-on 2-vortex scattering, the famous single 90° scattering is replaced by a chaotic fractal sequence of multi-bounces.

In this section, we will consider excitation of an out-of-phase superposition of shape modes of each of the vortices, which provides a repulsive intervortex force and therefore cannot lead to multi-bounces. This is an excitation of the form of eq. (8.3.3).

If the upper mode ξ_2 (see figure 8.3.3) is initially excited, then the intervortex force is repulsive. Thus, for a sufficiently large excitation, head-on scattering may occur without passing through the coincident configuration. In this case, the kinetic energy of the vortex motion is simply too small to overcome the repulsion triggered by the upper mode. As a result, there is no bounce and no 90° scattering. For a slightly smaller excitation, the vortices can reach $d = 0$, but still without 90° scattering.

Interestingly, for even smaller initial intensities we get two-bounce scattering. This is because the vortices pass through the $d = 0$ point and scatter at right angles. Now, the second mode changes to the third one, hence the frequency increases after collision. Consequently, the repulsion changes into an attraction between the vortices, which can dominate the kinetic motion. As the vortices scatter again, the modes cross once more.

The frequency drops with the separation, and the interaction becomes repulsive, and hence the vortices separate indefinitely.

For sufficiently small excitations of the upper mode, the kinetic energy is large enough to dominate the initial intervortex repulsion, and later attraction after scattering, resulting in the standard 90° scattering.

Moreover, we will show that the excitation of the upper modes in the 2-vortex collision leads to the existence of another phenomenon in soliton dynamics, which is the *spectral wall* [2]. The spectral wall phenomenon is an obstacle (barrier) in the dynamics of topological solitons because of the transition of a vibrational mode into the continuous spectrum. If the intensity of this mode is sufficiently large, the soliton is reflected by the spectral wall, whereas if the excitation is small enough, the soliton can pass through the spectral wall. For a particular value of the intensity, the soliton forms a long-living quasi-stationary state at a given spatial point, when the mode enters the continuum spectrum.

Spectral walls have only previously been observed in $(1+1)-$dimensional systems, see [4, 5]. In this section, we show that they exist also for vortices in the Abelian Higgs model. We have shown in figure 8.3.3 that there exists a point where the frequency reaches the continuum. Now, we seek to reproduce this using the full field theory dynamics. In our numerical simulations, we scatter two well separated single vortices. Initially, they are located at $x_1 = \pm 10$ ($d(0) = 10$) and are boosted towards each other along the x_1-axis with initial velocity v_{in}. The initial intensity of the normalised mode is $I(0)$, where $I(0) = \frac{1}{2}\epsilon^2\omega^2$. We use the same initial configurations as in section 9.2.

9.3.1 Results

In figure 9.3.1, we present the positions ($|d|$) of the vortices as a function of time, where $d = \frac{s}{2}$, with s being the separation of the vortices. We vary the initial intensity of the mode to display the different scattering behaviours in this channel, and choose a fixed initial velocity of $v_{\text{in}} = 0.01$.

The full field theory dynamics confirms the previous considerations gained from studying the spectral flow figure 8.3.3. For a large initial intensity, (see the purple line in figure 9.3.1) such that $I(0) \approx 3.8874 \times 10^{-3}$ the vortices never meet. Note that this is still a small initial intensity for the excitation; however, since we are at critical coupling and the vortices are slow moving, it is large enough that the repulsion dominates.

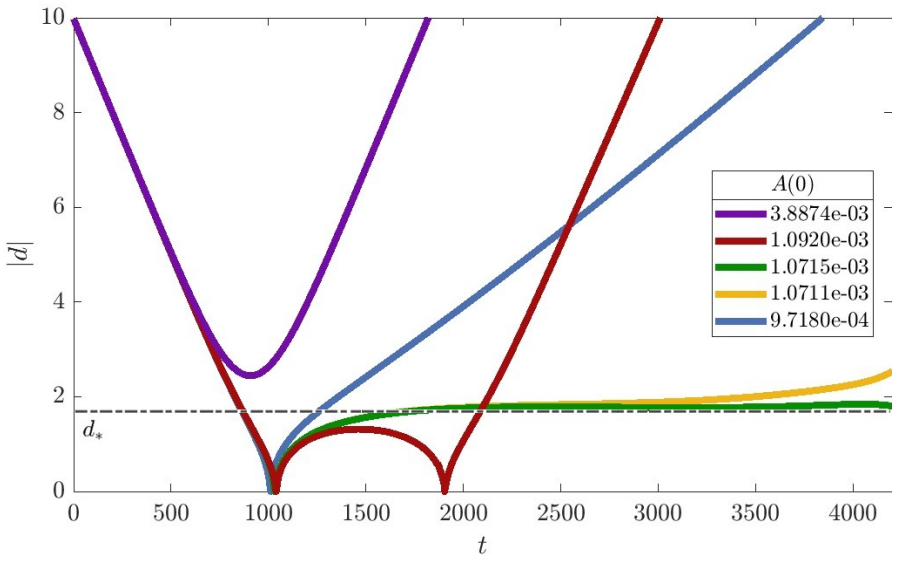

Figure 9.3.1: Dynamics of excited 2-vortex with $v_{in} = 0.01$. Time evolution of $|d|$ (half vortex-vortex separation). The dashed line labelled d^* indicates the position of the spectral wall.

Furthermore, if we decrease the intensity of the excitation, we observe the red line in figure 9.3.1 with $I(0) \approx 1.092 \times 10^{-3}$, where we get a 2-bounce solution, resulting in a 180°-scattering of the incoming vortices.

As the initial intensity further decreases, the vortices separate further after the first bounce. As explained, due to the mode crossing, the second mode ξ_2 becomes the third one ξ_3. The frequency tends to the continuous spectrum as the distance between the vortices along the x_2-axis increases. The spatial point at which the mode enters the continuum spectrum plays the role of a barrier in the solitonic dynamics, and this barrier is called a *spectral wall*.

We clearly see such a spectral wall in figure 9.3.1. Observe the green and yellow lines in figure 9.3.1. We notice that the trajectory flattens after scattering. This means that for a very long time the vortices almost stop with their centres located at $x_2 = \pm|d|_{sw}$, where $|d|_{sw} \approx 1.7$, forming a quasi-stationary state. It should be stressed that they remain at the same positions for a remarkably long time. That is, $t \approx 3000$, which can be compared with the time scale provided by the oscillation period of the excited mode. Furthermore, we see that this distance strongly agrees with the value estimated in figure 8.3.3, where $d_* \in [1, 2]$

If we further reduce the initial intensity of the mode, then the kinetic energy forces the vortices to pass through the spectral wall, exactly as in the case of kinks in (1+1) dimensions. Thus, for smaller initial intensities, we enter an adiabatic regime where

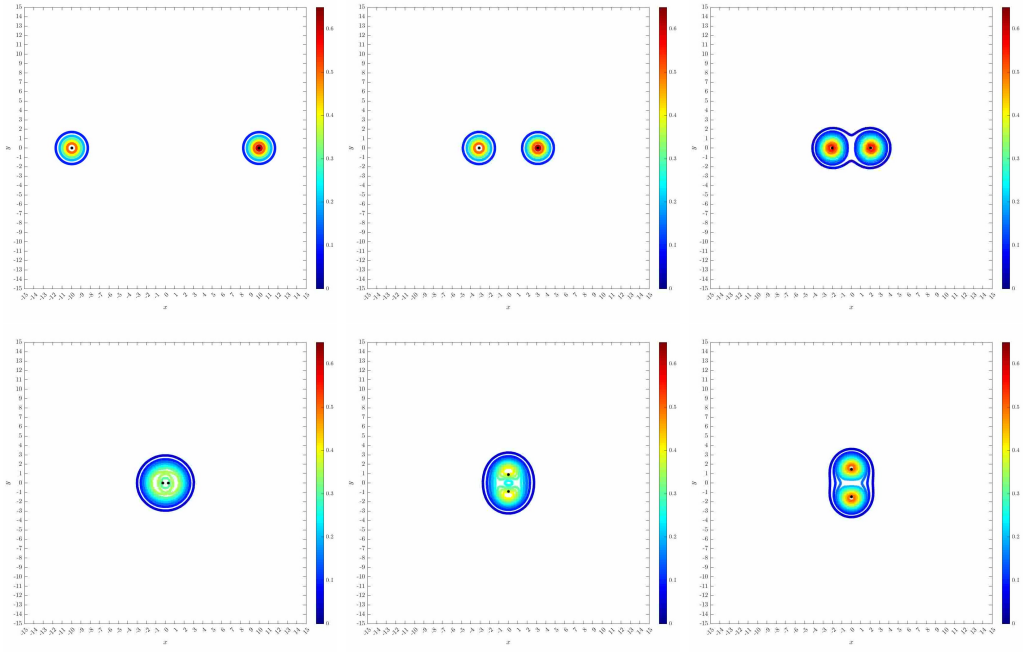

Figure 9.3.2: Snapshots of a dynamical simulation displaying a contour plot for the energy density for a critically coupled ($\lambda = 1$) two-vortex scattering, with internal shape modes excited out of phase, with initial velocity $v_{\text{in}} = 0.01$ and intensity $I(0) = 1.0715e - 03$, where $I(0) = \frac{1}{2}(\epsilon\omega)^2$.

the standard geodesic motion of the vortices is only weakly perturbed by the excited mode. Here we observe the standard one-bounce with 90° scattering, see the blue line in figure 9.3.1 with $I(0) = 9.718 \times 10^{-4}$.

We observe in figure 9.3.2 where we plot snapshots of a dynamical simulation, that the vortices are initially out of phase and well separated (note that the black dots indicate the zeros of the Higgs field). After the vortices scatter, the excitation enters the continuous spectrum, and the vortices cease to wobble in space. We can see that the vortices stop moving, forming a quasi-stationary state, as seen in figure 9.3.1, known as a spectral wall.

In figure 9.3.3, we plot the time evolution of the frequency of the second mode ξ_2. To numerically track the frequency, we calculate the static potential energy using Simpson's 3/8 rule at each time step δ_t. We therefore calculate the angular frequency, $\omega = \frac{\pi}{T_i}$, where T_i denote the periods of oscillations in the static energy. We notice that the frequency behaves as expected, which is consistent with the behaviour shown in figure 9.3.1.

Note that for higher initial velocities, there is a tendency for the vortices to form a stationary solution for slightly more negative imaginary d. This is not a surprising effect. A higher initial velocity v_{in} results in a higher intensity of the mode required to form the

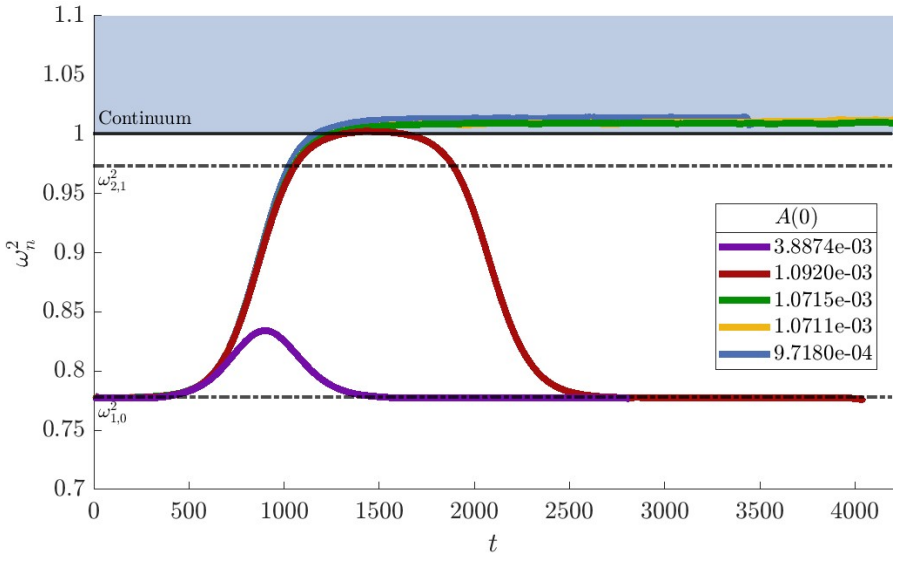

Figure 9.3.3: Time evolution of the squared angular frequency of the excited higher mode.

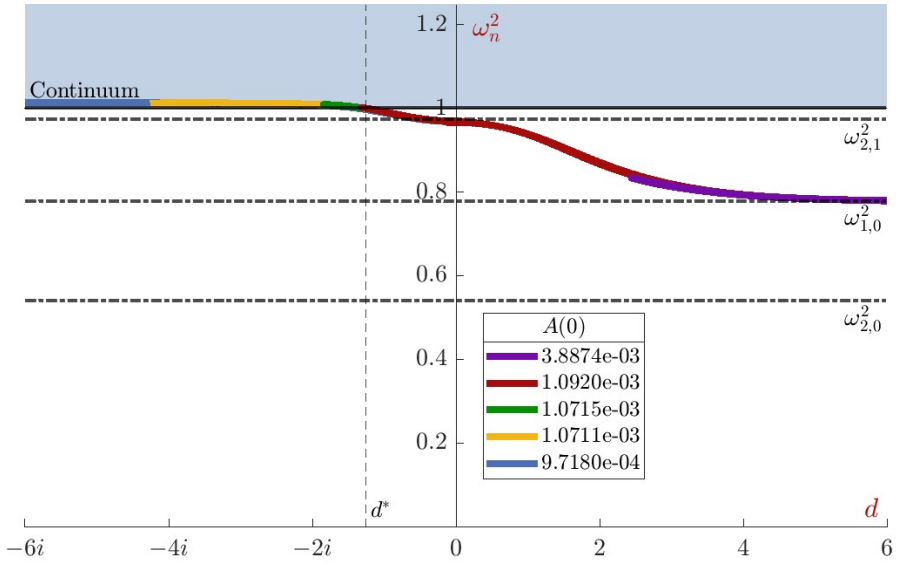

Figure 9.3.4: Frequency of the excited higher mode as a function of the vortex position parameter $d \in \mathbb{R}_+ \cup i\mathbb{R}_-$.

stationary solution. This means that corrections from higher order perturbation theory are significant, and some couplings between the modes may be important, affecting the position of the spectral wall. Similar effects were observed in $(1+1)$ dimensions [3, 4]. In figure 9.3.4 we show how the frequency of the mode depends on the position d of the vortex. We plot the numerically calculated frequency for all the simulations shown in figure 9.3.1. We observe that the frequency follows precisely the path of the second mode ξ_2 shown in figure 8.3.3. We can see that for the purple line, indicating a repulsive simulation where the vortices never meet, the frequency increases as they come close

together, confirming our intuitions about the repulsive force; however, it then decreases as the vortices escape to infinity. Interestingly, if we observe the yellow and green lines in figure 9.3.4, we notice that the frequency reaches the continuum at the distance d_*, where we observe the spectral wall. We also see from the red line, which corresponds to the two-bounce solution, that the frequency reaches the continuum after the vortices scatter. This indicates that the vortices are bouncing off the spectral wall in the x_2 direction, because the kinetic energy is not large enough to allow the vortices to pass through the spectral wall, and its energy is too large to allow for a quasi-stationary state.

9.4 Excited 3-Vortex Scattering

In this section, we aim to confirm the spectral structure shown in section 8.3.2 and study the full field theory dynamics of excited 3-vortices, namely a superposition of 3 excited 1-vortices. The dynamics are analyzed within the 1-dimensional geodesic submanifolds $\mathcal{N}^{(1)}$ and $\mathcal{N}^{(2)}$, defined in section 8.3.2, which are equipped with a Riemannian metric derived from the kinetic energy terms of the Abelian Higgs model's Lagrangian. For these 1-dimensional submanifolds, the metric function is a scalar function $g(d)$, where d is the coordinate parametrising the distance of the vortices from the origin, appearing in the metric $ds^2 = g(d)\,dd^2$. This metric governs the geodesic motion of the vortices along the submanifolds, describing force-free dynamics in the absence of shape mode excitations [11]. The metric function on the 1-dimensional subspaces $\mathcal{N}^{(1)}$ and $\mathcal{N}^{(2)}$ can be computed in two ways. In this thesis, we focus mainly on the numerical computation of slow-moving vortices, but it is shown in [11] how to find an analytical approximation to the metric near zero. The analytical method takes advantage of the fact that the solutions forming the subspaces arise by an action of the appropriate zero modes, namely the splitting mode. A complete calculation for the metric function is shown in [11]. For $d \to 0$, we have the metric function for 3 collinear vortices

$$g_{\text{collinear}}(d) = 0.984019\, d^2 + o(d^2). \tag{9.4.1}$$

Similarly, we find for 3 vortices in a triangle orientation, the metric function at $d \to 0$ is

$$g_{\text{triangle}}(d) = 0.584678\, d^4 + o(d^4). \tag{9.4.2}$$

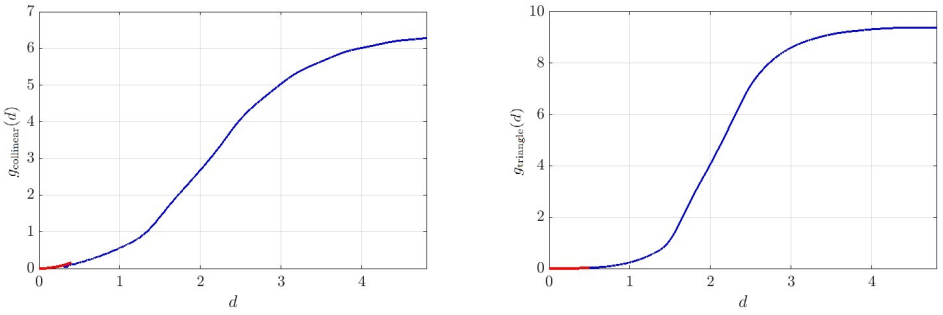

Figure 9.4.1: Metric on the one-dimensional collinear subspace $\mathcal{N}^{(1)}$ (left) and the equilateral triangle subspace $\mathcal{N}^{(2)}$ (right). The blue curve represents the numerically calculated metric, while the analytical approximation near the origin is plotted by the red curve.

These metric functions describe the geometry of $\mathcal{N}^{(1)}$ and $\mathcal{N}^{(2)}$ near the coincident solution ($d = 0$), with the quadratic and quartic dependence on d reflecting the distinct scattering angles (90° for collinear, 60° for triangular) as derived in [11]. The metric function can be deduced from the slow motion of vortices along the path defining the one-dimensional subspaces. In the initial state, we consider well-separated vortices with velocity v_{in}. The energy is conserved, allowing us to deduce the metric function from the time evolution of the distance of the vortices from the origin $d(t)$

$$g(d) = g^{\infty} v_{\text{in}}^2 \frac{1}{\dot{d}^2}, \tag{9.4.3}$$

where we ignore the potential energy which, for the slow motion of the critically coupled ($\lambda = 1$) solutions, is always the same. In figure 9.4.1 we plot the resulting metrics. It is numerically demanding to compute the metric when the vortices are close to each other, as the vortex positions are lost due to the accuracy of the discrete lattice. As such, we plot the numerically computed metric for $d > 0.3$ (collinear) and $d > 0.5$ (triangle) where the position is numerically robust. Otherwise, we are left with the analytical approximation.

9.4.1 Scattering in the subspace $\mathcal{N}^{(1)}$ of the collinear solutions

We have 3 possible scattering behaviours. The first behaviour arising from an excitation of the lowest mode eq. (8.3.4) introduces an attractive force between the $N = 1$ vortices. This triggers the resonant energy transfer mechanism, which results in an appearance

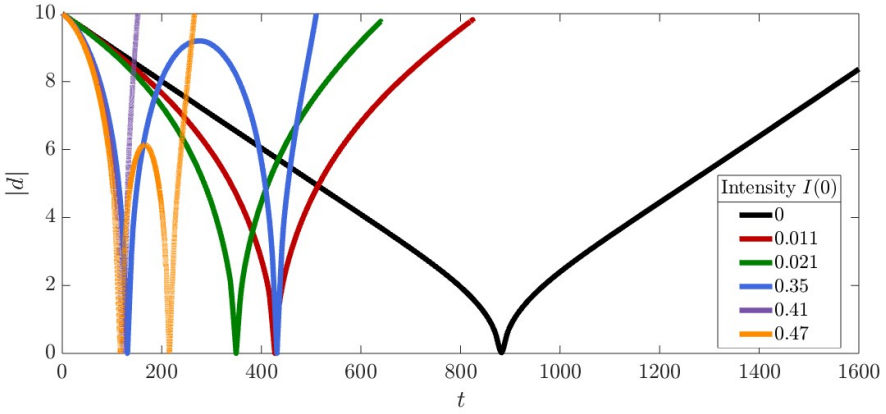

Figure 9.4.2: Full field theory figures for the scattering of vortices with the lowest mode excited eq. (8.3.4) in the collinear configurations, detailing distance $|d|$ of the outer vortices to the origin as a function of time, for a range of intensities, where $I(0) = \frac{1}{2}(\epsilon\omega)^2$.

of multi-bounces with a chaotic, and probably fractal, structure of multi-bounce windows. During a collision such that the vortices are coincident at the origin ($d = 0$), the energy stored in the kinetic motion can be transferred to the internal mode excitation. Moreover, it is the balance between the kinetic energy (kinetic motion of the $N = 1$ vortices) and the internal attractive energy (energy stored in the mode) that decides if the vortices can separate. If the intensity of the mode is too large, then the $N = 1$ vortices cannot overcome the attractive force and collide once again. At some point, the energy stored in the internal mode is transferred back to the kinetic energy, and the vortices eventually separate. In fact, whenever critically coupled vortices have a shape mode with the frequency decreasing with the intervortex distance, we find analogous behaviour, whereby the resonant energy transfer mechanism applies and a chaotic structure of multi-bounce windows arises. This mechanism explains the fractal structure in the kink-antikink collisions in the ϕ^4 model in $(1+1)$ dimensions [26, 56, 72]. Moreover, this behaviour has also been identified in the dynamics of an excited critically coupled 2-vortex system, see section 9.2, where the vortices are also subject to chaotic multi-bounces. Interestingly, depending on the number of bounces, we have 90° (odd) or 180° (even) scattering.

In figure 9.4.2, we plot the distance $|d|$ between the outer vortices from the origin. Notice the red line with initial intensity of the excitation, $I(0) = 0.011$, where we see that the motion of the vortices closely resembles geodesic motion, with only one bounce and the usual 90° scattering.

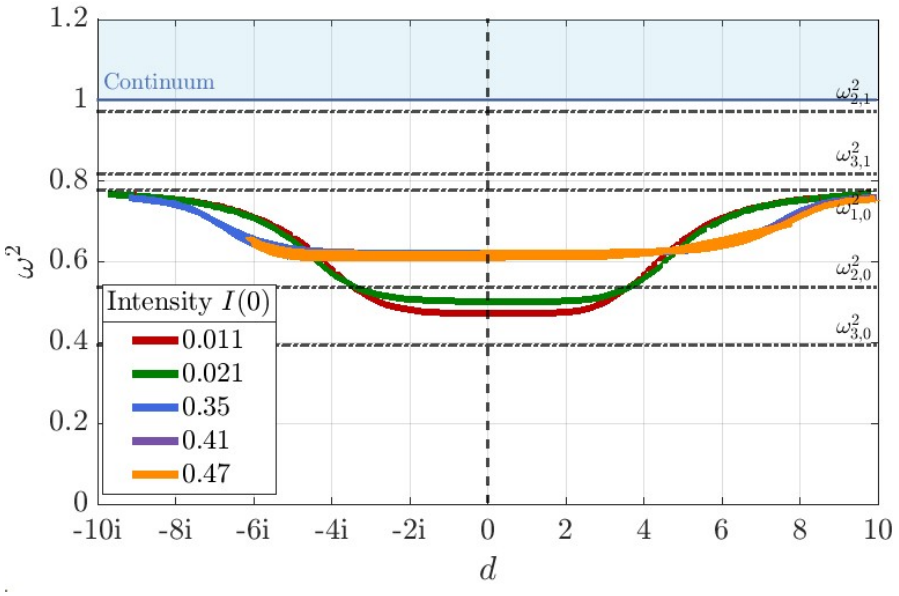

Figure 9.4.3: Full field theory figures for the scattering of vortices with the lowest mode excited eq. (8.3.4) in the collinear configurations, detailing the spectral flow as a function of the distance of the outer vortices from the origin, for a range of intensities, where $I(0) = \frac{1}{2}(\epsilon\omega)^2$.

For larger initial intensities, the geodesic approximation fails. We observe the blue and orange lines in figure 9.4.2 with $I(0) = 0.41$ and $I(0) = 0.47$, respectively, 2-bounce solutions with 180° scattering, where the outer vortices are scattered back to their initial positions.

We study figure 9.4.3, where we also show how the numerically calculated frequency of the mode varies during the evolution of the vortices. Our results here agree with the spectral analysis (see figure 8.3.4). We notice higher values for the plateau of ω^2 at $d = 0$ observed for higher initial intensities. This is a numerical artefact related to a very rapid motion of the vortices while passing the axially symmetric configuration, where the vortices move faster than the period of the oscillation, making it increasingly difficult to measure the frequency.

The second scattering behaviour arises from an excitation of the second mode eq. (8.3.5). An excitation of this form results in a repulsive-attractive force. When the vortices are initially well separated, we observe that the force is repulsive. If the kinetic energy is large enough (or the intensity of the mode sufficiently small) such that the vortices pass through the coincident configuration, the force changes sign and becomes attractive. This is because of the level crossing.

After passing through the coincident configuration, the frequency continues to increase.

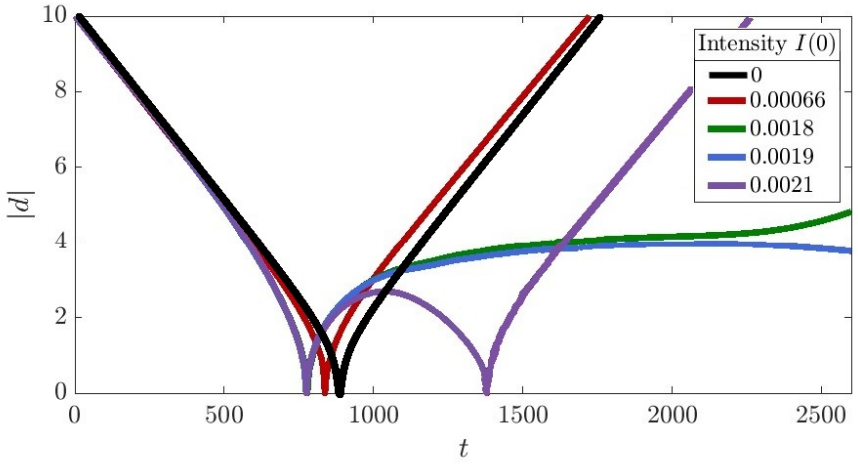

Figure 9.4.4: Full field theory figures for the scattering of vortices with the second mode eq. (8.3.5) excited in the collinear configurations, whereby we display the distance $|d|$ of the outer vortices to the origin as a function of time.

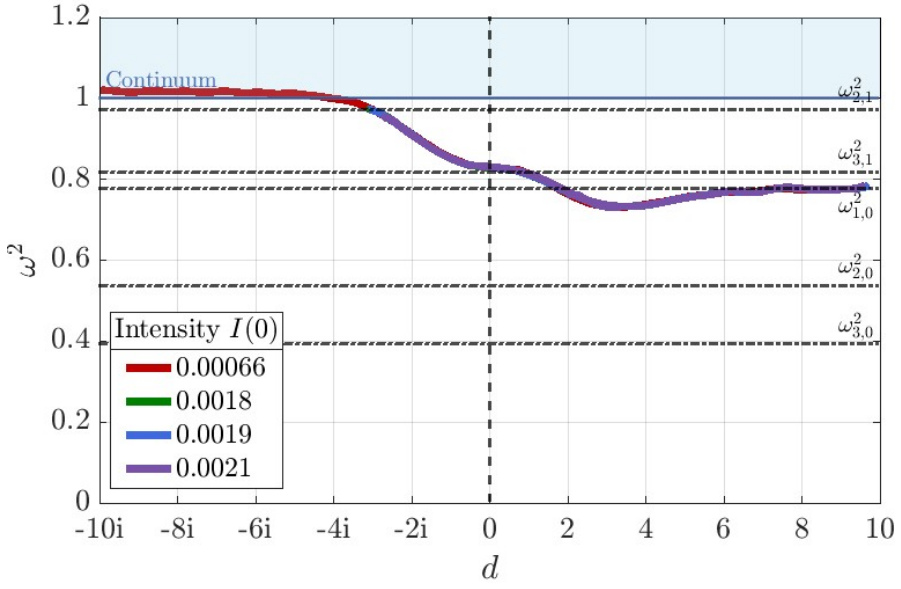

Figure 9.4.5: Full field theory figures for the scattering of vortices with the second mode eq. (8.3.5) excited in the collinear configurations, whereby we display the spectral flow as a function of the distance of the outer vortices from the origin.

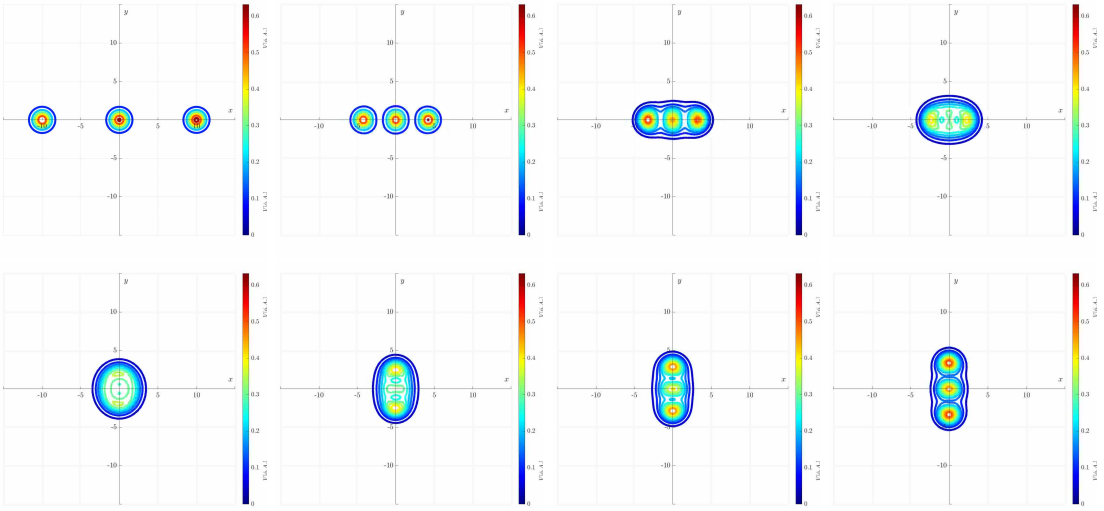

Figure 9.4.6: Snapshots of a dynamical simulation displaying a contour plot for the energy density for a critically coupled ($\lambda = 1$) three-vortex scattering, with excitation of the second mode eq. (8.3.5), where the initial intensity $I(0) = 0.0019$, where $I(0) = \frac{1}{2}(\epsilon\omega)^2$, and we have chosen the initial velocity of the outer two vortices $v_{\text{in}} = 0.01$.

Therefore, the attractive force can stop the vortices, leading them to backscatter, such that they are forced to pass through the coincident configuration again. As such, depending on the intensity of the excitation, we have the following possible scattering scenarios.

For large initial intensities, the vortices may not meet at all. This means no bounces and 180° scattering. For a smaller, fine-tuned intensity they can reach the coincident configuration. Hence, we have 1-bounce and still 180° scattering, see the red line in figure 9.4.4. For even smaller initial intensities (see the purple line), the vortices pass through the coincident configuration, but are forced to go back while they are on the x_2-axis. The vortices then pass through the coincident configuration once more, escaping to infinity along the x_1-axis. We therefore have a 2-bounce solution and 180° scattering. For even smaller intensities (see the green and blue lines in figure 9.4.4), the outer vortices have enough kinetic energy to overcome the repulsive force and pass through the coincident configuration. In this case, the vortices form a quasi-stationary state after scattering. By observing figure 9.4.5, we see that indeed, the frequency has entered the continuum, and hence we observe the formation of a spectral wall.

We show in figure 9.4.6 snapshots of the dynamical simulation corresponding to the blue line in figure 9.4.4. We indeed see that the outer vortices begin out of phase. After passing through the coincident configuration, we see that the vortices stop wobbling

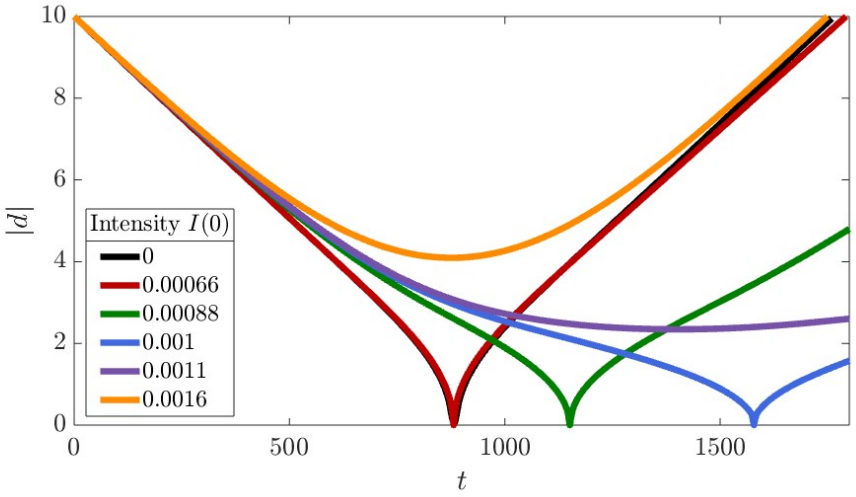

Figure 9.4.7: Full field theory figures for the scattering of vortices with the last mode eq. (8.3.6) excited in the collinear configurations, displaying the distance $|d|$ of the outer vortices to the origin as a function of time, for a range of intensities, where $I(0) = \frac{1}{2}(\epsilon\omega)^2$.

in space, as expected since the frequency has entered the continuous spectrum. The vortices remain at a fixed position in the x_2-plane for an extremely long time, namely $d_{sw} \approx 4$, which exactly agrees with the point on the moduli space where the mode hits the continuum, $d_2^* \in (3.5, 4)$, displaying this long-lived quasi-stationary state, known as the spectral wall.

Finally, we explore the excitation of the third mode, eq. (8.3.6). When we simulate the vortices in this way, we expect to see a spectral wall before the vortices collide.

We observe in figure 9.4.7 that the intervortex force induced by the excitation is repulsive, hence we only observe 0 or 1 bounce solutions. If the intensity of the excitation is large (see the purple line with $I(0) = 0.0016$), then the vortices repel before meeting the coincident configuration. Indeed, in figure 9.4.8 we see that the frequency increases as the vortices draw closer together but then decreases as they separate to infinity.

If we choose an initial intensity of $I(0) = 0.0011$ (see the orange line in figure 9.4.7), we observe a quasi-stationary state solution, whereby the vortices stop moving before the vortices collide. This is confirmed to be a spectral wall by studying figure 9.4.8, by which we notice that the frequency has entered the continuous spectrum. We note that the location of this spectral wall is $d_{sw} \approx 2.2$, which agrees well with the value found in the spectral analysis, where $d_1^* = (2, 2.5)$ (see figure 8.3.4).

It is worth noting that if the excitation is too small (see the red, green, and blue lines in figure 9.4.7), then the vortices will pass through the coincident configuration and scatter

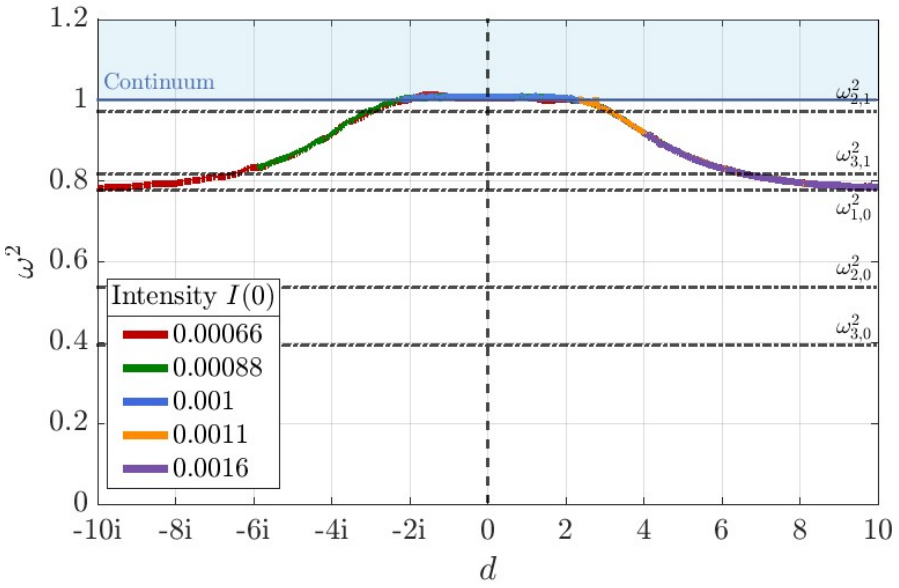

Figure 9.4.8: Full field theory Figures for the scattering of vortices with the last mode eq. (8.3.6) excited in the collinear configurations, displaying the spectral flow as a function of the distance, for a range of intensities, where $I(0) = \frac{1}{2}(\epsilon\omega)^2$.

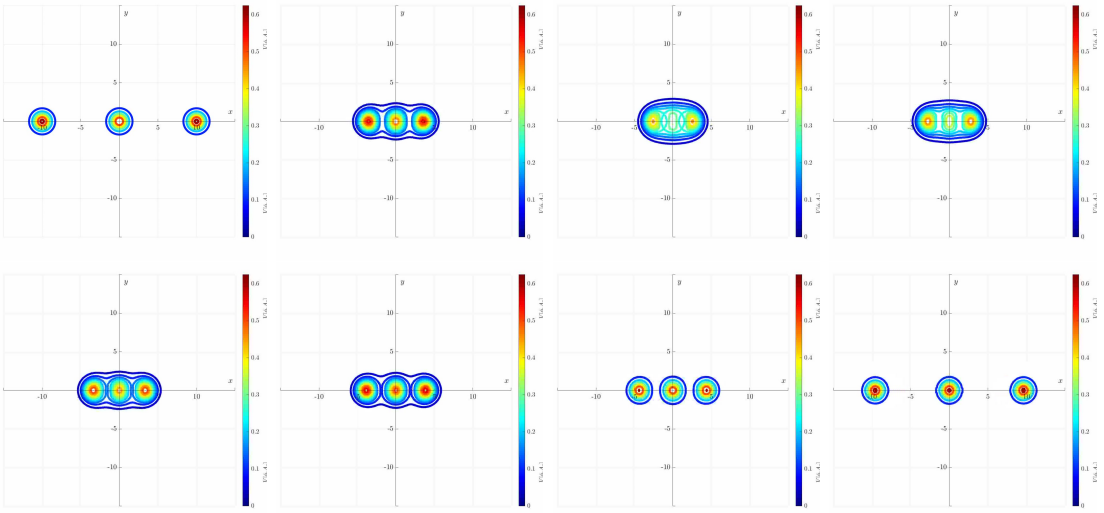

Figure 9.4.9: Snapshots of a dynamical simulation displaying a contour plot for the energy density for a critically coupled ($\lambda = 1$) three-vortex scattering, with excitation of the second mode eq. (8.3.6), where the initial intensity $I(0) = 0.0011$, with $I(0) = \frac{1}{2}(\epsilon\omega)^2$, and we have chosen the initial velocity of the outer two vortices $v_{\text{in}} = 0.01$.

once, and hence we have the standard 90° degree scattering. Moreover, from figure 9.4.8 we see that the frequency still passes into the continuous spectrum, but then emerges at the reflection point of d_{sw} on the x_2-plane.

We show in figure 9.4.9 the scattering simulation denoted by the yellow line in figure 9.4.4.

Figure 9.4.9 shows the formation of the quasi-stationary state before the vortices collide. We see that the outer vortices are excited in phase, with the vortex at the origin excited with twice the excitation but out of phase. As the vortices form the quasi-stationary state, we observe the excitation entering the continuum, as the vortices stop wobbling in space. The spectral wall eventually decays and the vortices escape to infinity back along the x_1-axis, whereby they wobble with the same initial excitation.

9.4.2 Scattering of the subspace $\mathcal{N}^{(2)}$ of equilateral triangular configurations

Now we consider three critically coupled vortices located at the vertices of an equilateral triangle, at a distance d from the origin.

Excitation of the lowest mode eq. (8.3.4) (ξ_1) in this scenario has the same effect as in the case of collinear configuration. As they are qualitatively very similar, we do not plot them.

Excitation of the two upper modes eq. (8.3.5) and eq. (8.3.6) introduces a very weak repulsive force. If the initial intensity is large, one may expect that the $N = 1$ vortices will be backscattered before passing the axially symmetric configuration. Hence, a 180° scattering can occur. In figure 9.4.10 (left) we present the time evolution of the vortex positions with an excitation of the ξ_2 mode. Here, the initial intensity is $I(0) = 0.0008$. The geodesic motion is practically not affected by the excitation of the mode. In figure 9.4.10 (right) we track the numerically calculated frequency and find that it exactly follows the pattern found in the linear perturbation theory.

9.5 Conclusions

In this chapter, we demonstrated that exciting the vortex shape mode in Abelian Higgs model at critical coupling induces fluctuations in gauge-invariant quantities, driving scattering behaviours akin to both type I and type II vortices. In-phase vortices predominantly exhibit attraction, as evidenced numerically and analytically, revealing a fractal phase-space structure tied to initial phase and velocity. This manifests in chaotic, multi-bounce scattering sensitive to initial conditions, rendering geodesic flow insufficient to explain excitation-induced attraction. The models in [12] proposed a potential-modified

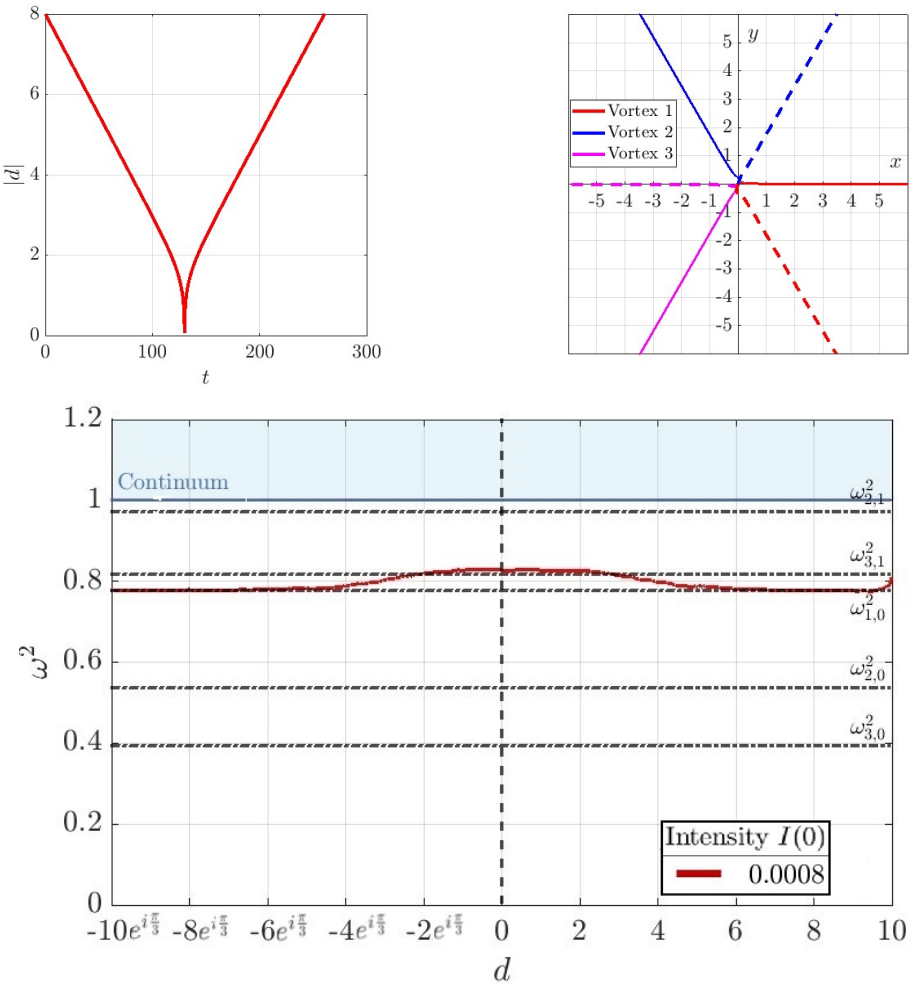

Figure 9.4.10: Full field theory figures for the scattering of vortices with the upper mode eq. (8.3.6) excited in the equilateral triangular configurations: Distance from the origin of the vortices as a function of time (left), Geodesic paths of the vortices (right), where the dashed lines are the paths after scattering, and spectral flow as a function of the distance (bottom).

geodesic flow on $\mathcal{M}$, corroborated by our findings and consistent with [47] for critically coupled two-vortex systems.

We found spectral walls, barriers that arise when a bound mode transitions to the continuum in the head-on 2-vortex dynamics, highlighting the pivotal role of internal modes, a feature well known in $(1+1)$ dimensions now extended to physically relevant models. In 3-vortex systems, the lowest mode induces an attractive intervortex force, producing multi-bounce solutions that shift 90° (collinear) or 60° (triangle) scattering to 180°. Higher modes in collinear cases produce repulsive-then attractive forces, forming spectral walls at separations d_{sw}.

These results have significant implications. Excited Abelian Higgs vortices in three dimensions, forming cosmic strings, may diverge from unexcited evolution due to spectral walls, impacting collision rates and gravitational wave signals [19, 20, 23, 39, 50, 51, 76]. In superconductors and Dirac materials such as graphene, mode transitions to the continuum could influence dynamics. We anticipate similar effects in solitons with vibrational modes, such as vortices with impurities [6, 18, 41, 42, 46, 74] or monopoles with quasinormal modes [21, 22, 33, 54], where Feshbach resonances may act analogously [34]. Even away from critical coupling (e.g., type I and type II vortices), stable modes with slow energy radiation [7] could reshape interactions. Bridging one and higher-dimensional soliton dynamics, our work underscores $(1+1)$-dimensional models as vital for understanding complex systems, with far-reaching theoretical and applied consequences.

Chapter 10

Vortex Dynamics away from Critical Coupling

10.1 Introduction

In this chapter, we seek to extend the work we have carried out on excited critically coupled vortices by discussing vortices away from critical coupling such that $\lambda \neq 1$. This chapter contains work from [48] We have shown in chapter 9 that the excitation of internal bound modes introduces attractive or repulsive forces dependent on the relative phase between the superposition of vortices, which interestingly changes the dynamics of the vortices. This is because the squared frequency of the mode usually changes with the intervortex separation. Away from critical coupling, we also have the static force as described in section 6.6, hence the interaction is more complex.

We will extend the analysis carried out on critically coupled vortices to discuss the scattering of excited vortices away from critical coupling. We discuss excited scattering simulations. Note that we cannot calculate the 2-dimensional spectrum as before in figures 8.3.3 and 8.3.4 due to the presence of the static forces arising from being away from critical coupling, and hence we rely on the numerically calculated squared frequency to discuss the mode induced interaction. We discuss the role of the spectral flow in vortex dynamics when coupled to the static interaction, and we present numerical results describing how the scattering behaviour is altered.

10.2 Type I Vortex Dynamics

Type I vortices are naturally attractive, hence for this section, we will consider mode excitations leading to a repulsive force. It has recently been shown in [8] and in section 9.3 that spectral walls exist in the critically coupled 2−vortex scattering with excited normal modes. In this case, the vortices were also excited to be repulsive. The squared angular frequency increases after the vortices scatter, entering the continuum at some fixed distance. We expect the same phenomena to occur here, except that because of the static force, it is unlikely that the vortices will become trapped in the spectral wall. Instead, we might observe the existence of a spectral wall by a change in velocity of vortices as the squared frequency enters the continuum. We have many regions of interest to consider. For the case of type I vortices, the excited scattering is not symmetric from x to y, noting that our initial configuration places the vortices on the x axis.

We can explore some snapshots of a dynamical simulation displaying a heat plot of the energy density. The simulation shown in figure 10.2.1 displays the scattering of two $N = 1$ vortices with $\lambda = 0.9$. We have excited the $k = 0$ shape mode on each vortex, with a relative phase of π to induce a repulsive force, i.e. an exitation of the from eq. (8.3.3). We have chosen an initial intensity of $I(0) = 0.3$, where $I(0) = \frac{\epsilon^2\omega^2}{2}$, with ω being the squared angular frequency of the vortex mode, and an initial velocity $v_{\text{in}} = 0.1$. Figure 10.2.1 shows how the vortices scatter multiple times, which is expected in the type I regime. It can also be seen that the vortices initially start out of phase, as seen by the difference in the peaks of the energy density. After the vortices scatter, the peaks are equivalent, highlighting the asymmetry in the scattering process.

We can gain more insight into the interaction between the vortices by tracking the squared angular frequency of the numerical simulation and plot it as a function of the separation; see figure 10.2.2. We calculate the angular frequency

$$\omega(t) = \frac{\pi}{\Delta t}, \tag{10.2.1}$$

where Δt is the time difference between two consecutive peaks or troughs in the static energy as a function of time t. We also track the positions of the vortices, allowing us to write ω^2 as a function of d, where d is half the separation.

It can be seen in figure 10.2.2 that as the vortices move closer to the origin, the squared frequency increases. For positive d, the squared frequency interpolates between the

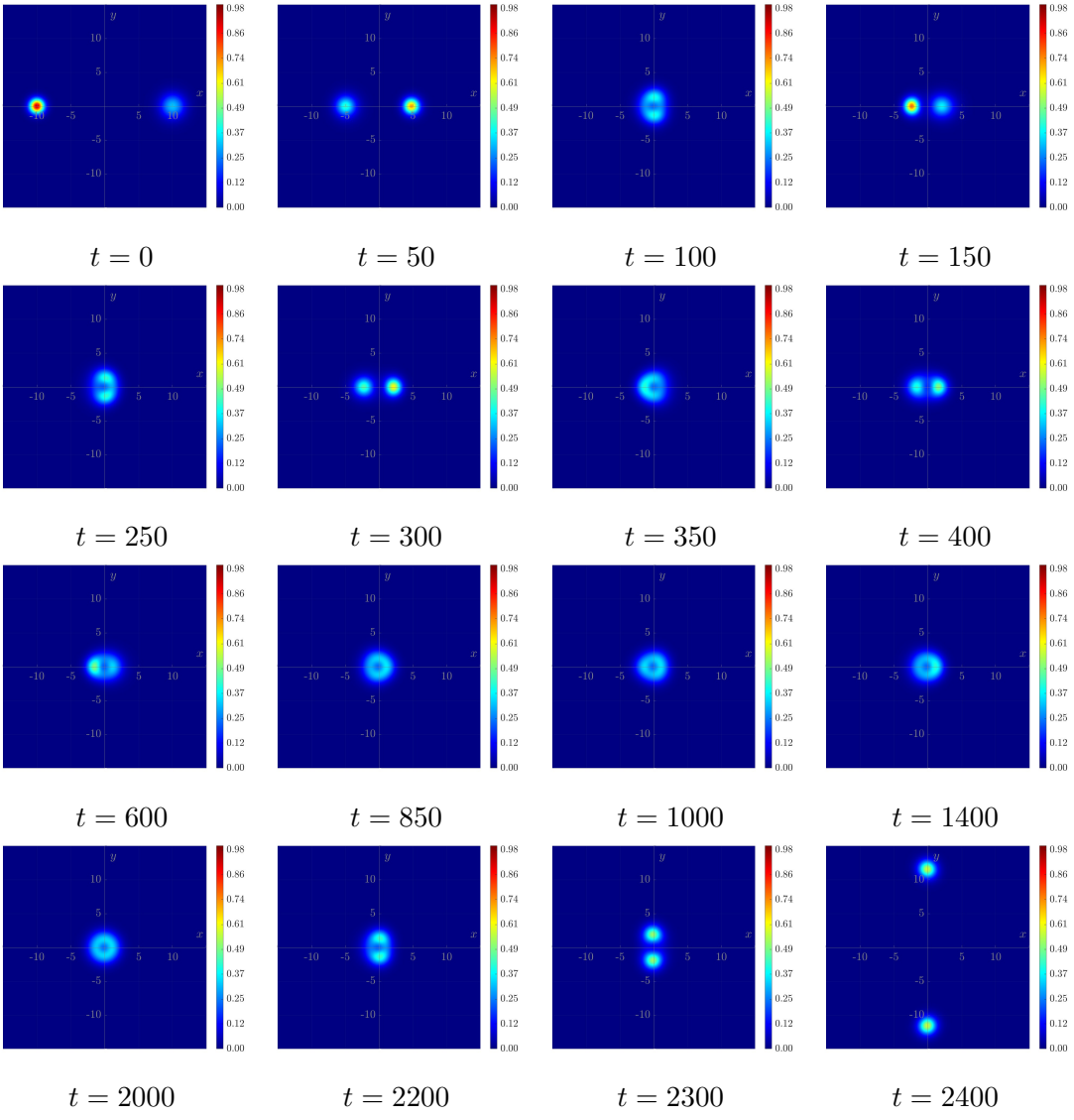

Figure 10.2.1: Snapshots of energy density for a two-vortex scattering ($\lambda = 0.9$, $v_{\text{in}} = 0.1$, $I(0) = 0.3$), with out-of-phase $k = 0$ shape modes, as seen in figure 10.2.3.

asymptotic values $\omega^2_{1,0} = 0.7136541$, which is the $N = 1$, $k = 0$ shape mode, and the $N = 2$, $k = 1$ mode at the coincident configuration, $\omega^2_{2,1} = 0.8883169$. We see that after the vortices pass through the coincident configuration, the squared frequency increases further, hitting the continuous spectrum at $d \approx -1i$. This would suggest the presence of a spectral wall. To confirm this, we can observe the trajectories of the vortices in a scattering solution, see figures 10.2.3 and 10.2.4.

We observe two interesting phenomena when observing the trajectories in figure 10.2.3. Note that blue is the position in x, and cyan is the position in y. Firstly, from the blue line we can see that the vortices initially travel at a near-constant velocity. After the

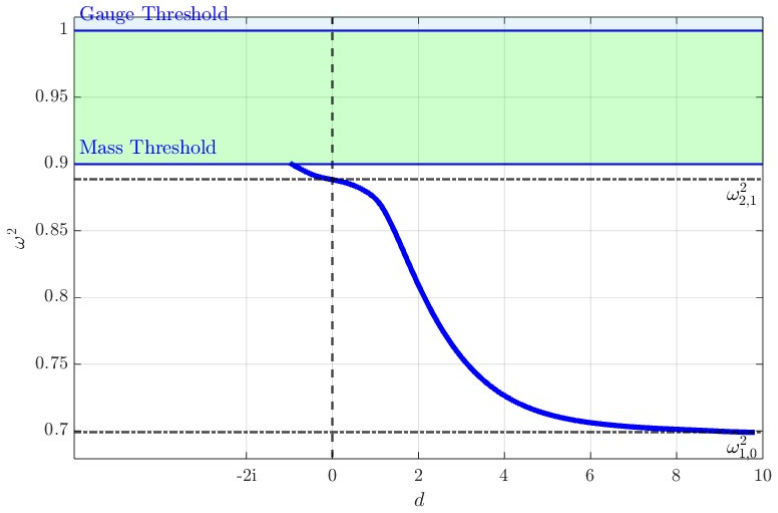

Figure 10.2.2: Flow of the squared angular frequency for a 2-vortex system (blue), with $\lambda = 0.9$, as a function of the distance from the origin of the vortices. The green area indicates the mass threshold, and the blue area the gauge threshold..

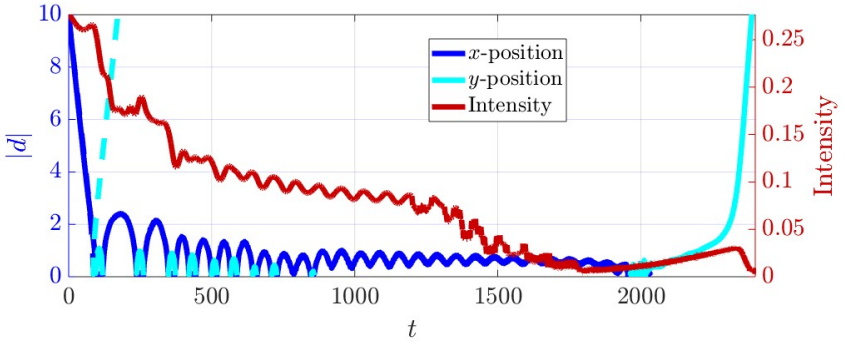

Figure 10.2.3: Trajectories of a two-vortex system ($\lambda = 0.9$, $v_{\text{in}} = 0.1$, $I(0) = 0.3$) as a function of time, where $I(0) = \frac{1}{2}(\epsilon\omega)^2$. The blue line shows the x-direction distance from the origin, cyan the y-direction, and red the excitation intensity per vortex. Dashed blue and cyan lines show unexcited scattering with the same parameters.

vortices scatter, we can see from the cyan line that the vortices hit the spectral wall and bounce back. This can be seen in the difference in the bounce size between the blue and cyan bounces. The distance in which the vortices bounce back in y is the same as the distance where the squared frequency hits the continuous spectrum, which confirms the presence of a spectral wall. Additionally, we can see that after the vortices have bounced a number of times, the vortices settle in the x-plane at a fixed distance. This is not a result of the spectral wall, instead it is due to the net force being zero. We notice that the intensity of the excitation, displayed as the red line in figure 10.2.3, decreases

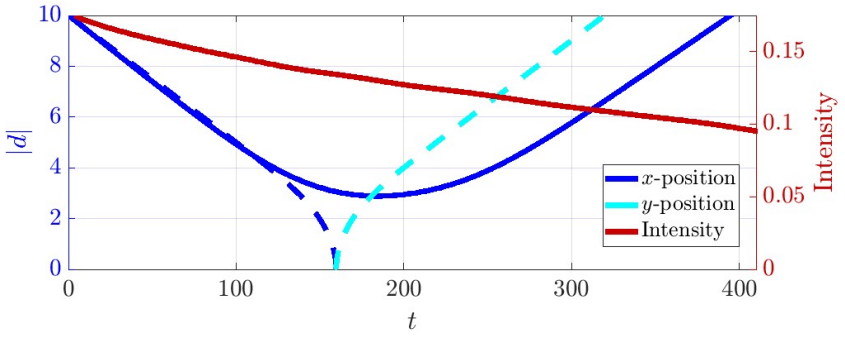

Figure 10.2.4: Trajectories of a 2-vortex system as a function of time, where $\lambda = 0.9$. We choose an initial velocity of $v_{\text{in}} = 0.05$, and initial intensity of the excitation $I(0) = 0.17$, where $I(0) = \frac{1}{2}(\epsilon\omega)^2$. The cyan line indicates the distance of the vortices from the origin in the y-direction, and the blue line indicates the x-direction. The red line shows the intensity of the excitation per vortex. The dashed blue and cyan lines show unexcited scattering in the x_1 and x_2-directions, respectively.

overall. This is due to a decay in the excitation as it radiates energy. Additionally, we observe temporary dips in the intensity as the vortices change direction, as seen at the peaks of the bounces in the x direction. This is due to the energy transfer mechanism, where the energy from the excitation is transferred to the kinetic energy. In addition, we see drops in intensity at the peaks of the bounces in the y-direction. This is because energy is transferred from the excitation to the spectral wall, and the resulting effect is that the vortices bounce off the spectral wall.

Figure 10.2.4 shows the scattering of a 2-vortex system at $\lambda = 0.9$, whereby the intensity of the excitation is large enough such that the repulsion from the mode dominates the scattering process. As such, the vortices never meet and are repelled towards infinity.

Next, we calculate the interaction energy, figure 10.2.5, whereby we have assumed that the intensity of the excitation is fixed for all d. The static force is calculated numerically; see section 6.6.

The mode interaction is calculated from the squared frequency displayed in figure 10.2.2, such that

$$E_{\text{Mode}}(d) = \frac{1}{2}\epsilon^2 \left(\omega^2(d) - \max_d \omega^2(d)\right), \tag{10.2.2}$$

where $\epsilon = \sqrt{\frac{I(0)}{\omega_{1,0}^2}}$, with $I(0)$ being the intensity of the excitation, and the energy is normalised such that it is asymptotically zero. We therefore have the total interaction energy per vortex, $E_{\text{Int}} = E_{\text{Static}} + E_{\text{Mode}}$.

We show the static force, seen on the left of figure 10.2.5, and the force induced by

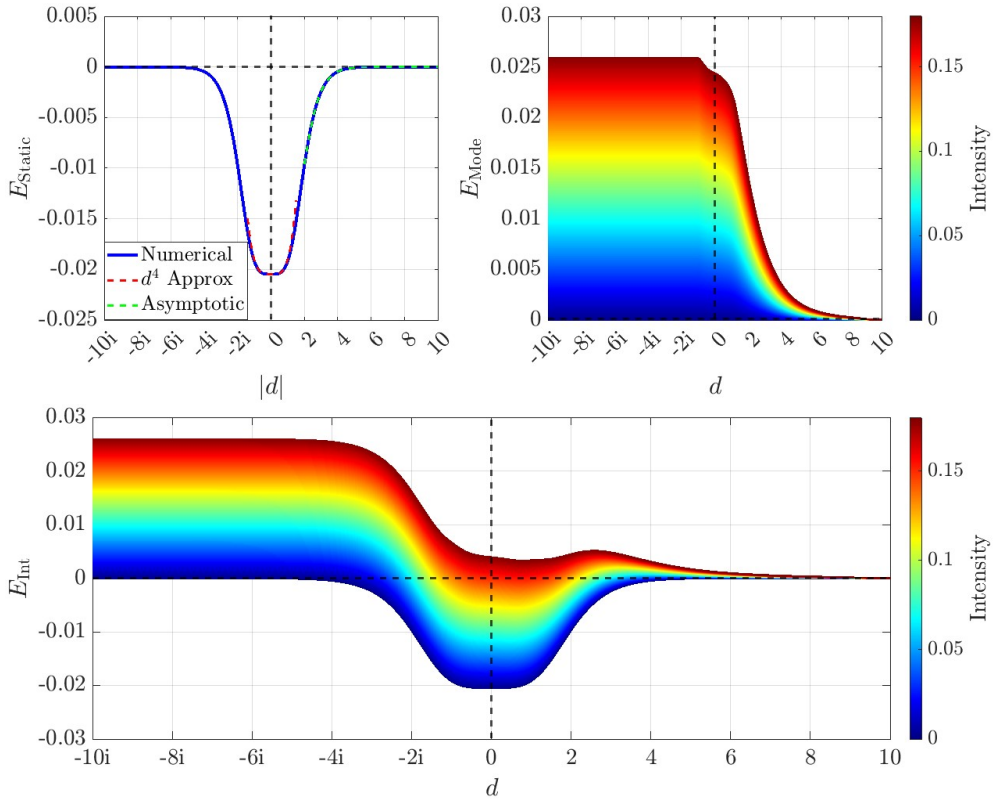

Figure 10.2.5: $\lambda = 0.9$ - Static force (left) in blue with d^4 approximation in dashed red for small d, and asymptotic approximation in dashed green. Interaction energy contribution from the mode (right) for a range of intensities. Total interaction energy (bottom) for a range of intensities.

excitation of the shape modes, seen on the right of figure 10.2.5. We are interested in the total interaction energy, being a sum of the static force and the mode interaction, as seen at the bottom of figure 10.2.5.

We interpret the interaction energy, seen from figure 10.2.5 as follows. For $|d| \ll 1$, the squared frequency and static force can both be approximated by d^4, therefore, if the coefficient of the interaction of the mode is smaller than that of the static force, then the two vortices will stay coincident at the origin; otherwise, the mode induced force will force them to separate. For $d > 1$, there exists a local extremum in the interaction energy at precisely the distance observed in figure 10.2.3. This explains the existence of this quasi-stationary state as the net force $F = -\frac{\partial}{\partial d} E_{\text{Int}} = 0$. For $d \in i\mathbb{R}_-$, we see that the interaction energy is highly positive due to the existence of the spectral wall. This makes it extremely difficult for vortices to move past this region. Additionally, for large d, we see that if the intensity of the perturbation is too large, then the vortices will never meet and will repel.

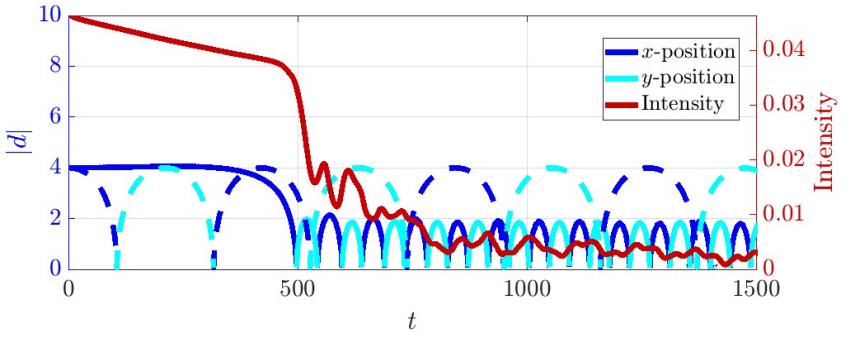

Figure 10.2.6: Trajectories of a 2-vortex system at $\lambda = 0.9$ starting near the local maximum, with initial velocity $v_{\text{in}} = 0$ and intensity $I(0) = 0.05$, where $I(0) = \frac{1}{2}(\epsilon\omega)^2$.

We can further explore the local extremum, by choosing an initial configuration where the vortices are situated at the local extremum; see figure 10.2.6.

It can be seen in figure 10.2.6 that initially the vortices form a quasi-stationary state, where they stay at a fixed position for a period of time. This is because the net force is zero. If the intensity of the excitation is large, the vortices will repel, as seen in figure 10.2.4, while if the intensity is small, then the static force will dominate and the vortices will be attracted toward the origin, as seen by the blue line in figure 10.2.6. We observe that this indeed happens in figure 10.2.6 as the intensity indicated by the red line decays, the quasi-stationary state decays and the vortices accelerate towards the origin.

It is important to note that the $k = 1$ mode exists in the discrete spectrum only for $\lambda > 0.8$, see chapter 8. As such, we must also explore what happens when two vortices scatter along the $x-$axis for $\lambda < 0.8$. In this regime, the angular squared frequency of the vortices will hit the continuous spectrum before the vortices collide. This could suggest the presence of a spectral wall, in which case we should see the vortices slow down in the region where the squared angular frequency hits the continuum.

We can plot the squared angular frequency as a function of the distance from the origin for a 2-vortex system with $\lambda = 0.5$, see figure 10.2.7.

It can be seen in figure 10.2.7 that as the vortices approach the origin, the squared frequency increases from the asymptotic value $\omega_{1,0}^2 = 0.4254454$, hitting the continuous spectrum at $d \approx 2.5$. To confirm the existence of a spectral wall, located at $d \in [2.2, 3]$, we will consider the trajectories of the vortices, see figure 10.2.8.

We can see in figure 10.2.8 that the bounces in y, indicated by the cyan lines, are smooth, which is expected as the squared frequency of the shape mode is in the continuous

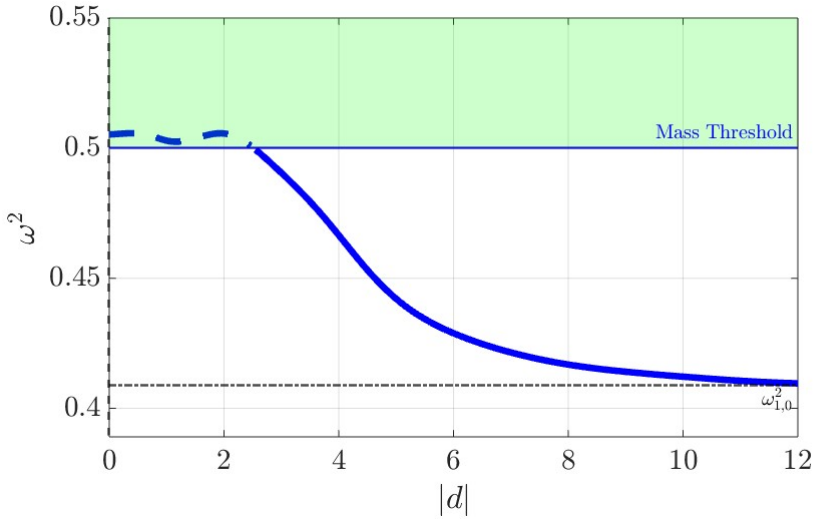

Figure 10.2.7: Flow of the squared angular frequency ω^2 for a 2-vortex system (blue), with $\lambda = 0.5$, as a function of the distance from the origin of the vortices. The green area indicates the mass threshold.

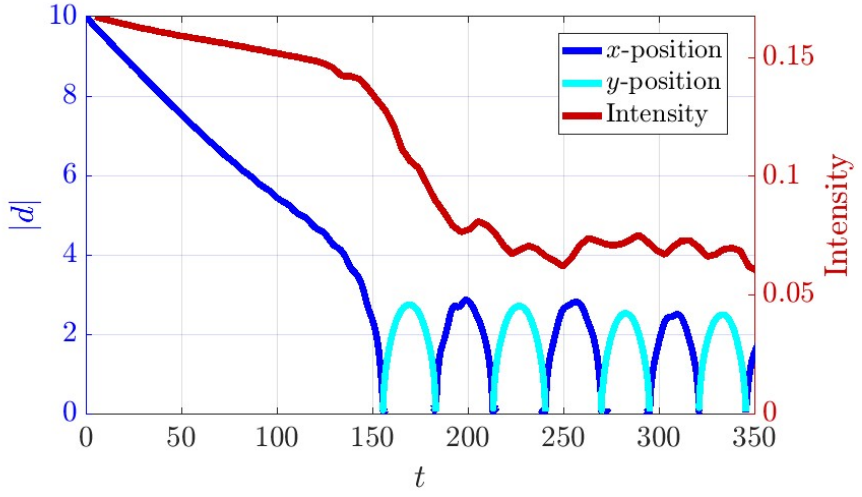

Figure 10.2.8: Trajectories of a 2-vortex system as a function of time, where $\lambda = 0.5$. We choose an initial velocity of $v_{\text{in}} = 0.05$, and initial intensity of the excitation $I(0) = 0.17$, where $I(0) = \frac{1}{2}(\epsilon\omega)^2$. The cyan line indicates the distance of the vortices from the origin in the y-direction, and the blue line indicates the x-direction. The intensity of the excitation $I(t)$ is displayed as the red line.

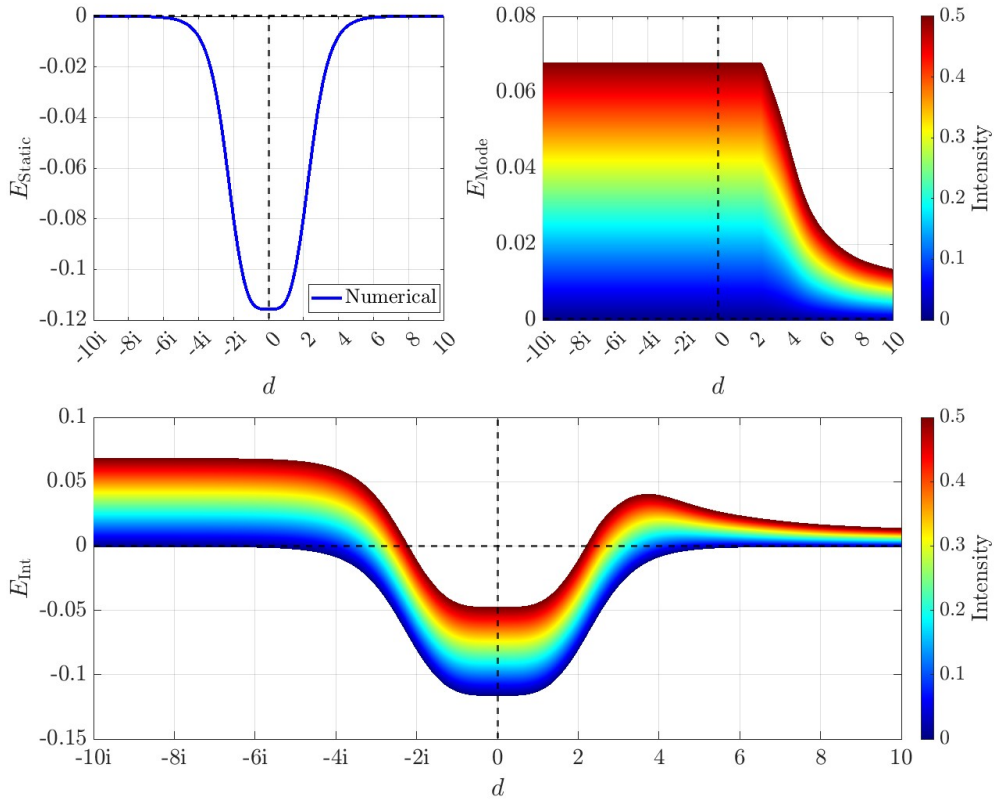

Figure 10.2.9: $\lambda = 0.5$ - Static force (left) in blue. Interaction energy contribution from the mode (right) for a range of intensities. Total interaction energy (bottom) for a range of intensities.

spectrum. More interestingly, the bounces in x, indicated by the blue lines, show some irregularities near the peak of the bounces. Little effect is noticed when the vortices first approach each other, due to the high acceleration as a result of the static force, so it is difficult to confirm the existence of a spectral wall.

Again, to gain insight into the full behaviour of the 2-vortex system with $\lambda = 0.5$, we can calculate the interaction energy; see figure 10.2.9.

We see from figure 10.2.9 that even though the frequency hits the continuous spectrum before the vortices coincide, there is also a local extremum at $d \in (3, 4.5)$, meaning that the vortices could form a quasi-stationary state at this fixed distance, as the net force is zero. The irregularities we observe in the blue line in figure 10.2.8 occur approximately at the the distance of the local extremum, suggesting that the vortices cannot move past this potential barrier, while the intensity of the excitation is large. For $|d| < 3$, that static force is large and hence the vortices want to attract, as seen by the negative interaction energy. This explains the bounces seen in figure 10.2.8, where the vortices bounce multiple times.

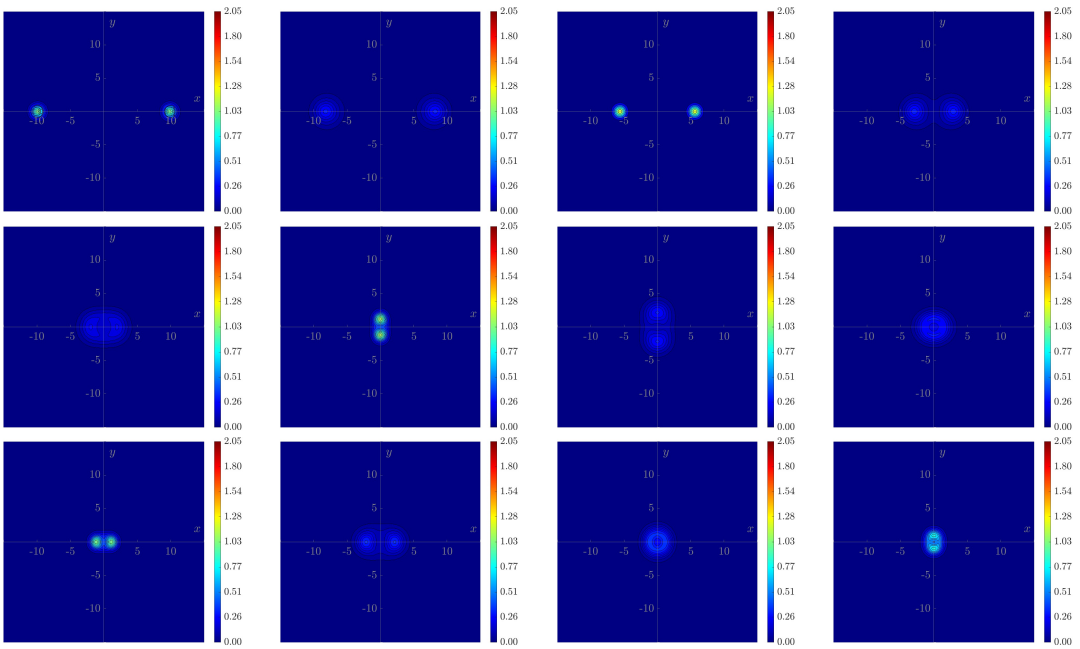

Figure 10.3.1: Snapshots of a dynamical simulation displaying a heat map for the static energy density for a 2-vortex scattering at $\lambda = 1.1$, with internal shape modes excited in phase, with intensity $I(0) = 0.3$, $I(0) = \frac{1}{2}(\epsilon\omega)^2$, and initial velocity $v_{\text{in}} = 0.1$.

10.3 Type II Vortex Dynamics

The static force for type II vortices is repulsive, hence it is natural to consider mode excitations in the attractive channel. As such, we consider the in-phase superposition of vortices with excited internal shape modes. Since we only consider the attractive channel, the spectral flow of the mode structure is symmetric from x to y.

We can explore some snapshots of a dynamical simulation displaying a heat plot of the energy density. The simulation shown in figure 10.3.1 displays the scattering of two $N = 1$ vortices with $\lambda = 1.1$. We have excited the $k = 0$ shape mode on each vortex to induce an attractive force, where $\omega_{1,0}^2 = 0.8352168$. We have chosen an initial intensity of $I(0) = 0.3$ and an initial velocity of $v_{\text{in}} = 0.1$.

We can observe in figure 10.3.1 that the vortices are in phase with excited $k = 0$ shape modes. We can see that the vortices move closer together, whilst oscillating in shape. We also observe the presence of a quasi-bound state where the vortices scatter multiple times. This is quite interesting because the static force in the II regime is repulsive, and therefore the vortices naturally want to move apart. We can gain more insight into the scattering process by discussing the trajectories of the vortices; see figures 10.3.2 and 10.3.3.

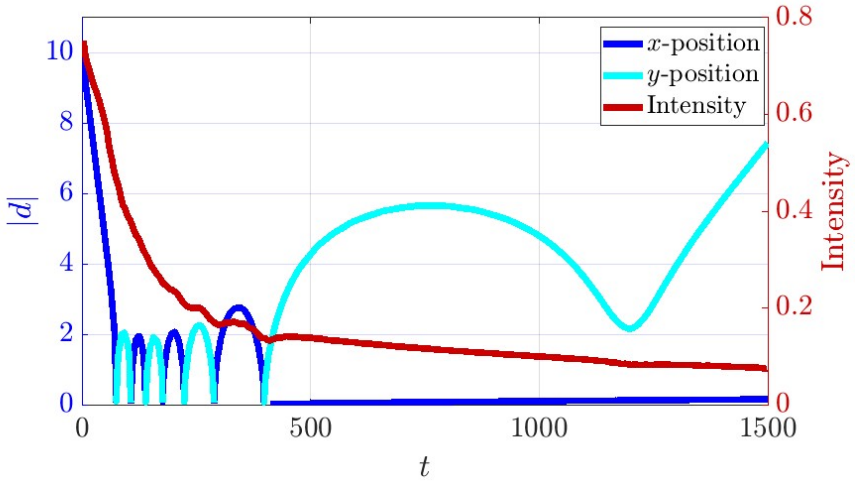

Figure 10.3.2: Trajectories of a 2-vortex system as a function of time, where $\lambda = 1.1$. We choose an initial velocity of $v_{\text{in}} = 0.1$, and initial intensity of the excitation $I(0) = 0.75$, where $I(0) = \frac{1}{2}(\epsilon\omega)^2$. The cyan line indicates the distance of the vortices from the origin in the y-direction, and the blue line indicates the x-direction.

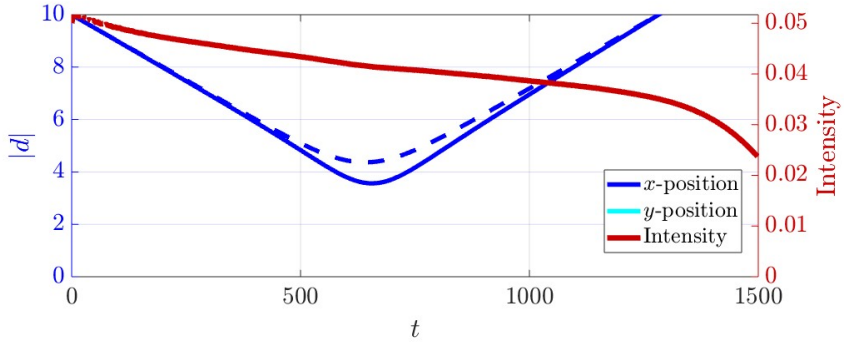

Figure 10.3.3: Trajectories of a 2-vortex system as a function of time, where $\lambda = 1.1$. We choose an initial velocity of $v_{\text{in}} = 0.01$, and initial intensity of the excitation $I(0) = 0.05$, where $I(0) = \frac{1}{2}(\epsilon\omega)^2$. The blue line indicates the distance of the vortices from the origin in the x-direction and dashed blue the unexcited scattering in the x-direction

We observe in figure 10.3.2 the distance of the vortices from the origin as a function of time. If the vortices lie on the $x-$axis, we plot their distance in blue, and if they lie on the $y-$axis, we plot the distance in cyan. We can see that initially, the vortices form a quasi-bound state, where they scatter multiple times. After some time, we see from the cyan line at $t \approx 500$ that the vortices separate significantly more, then move back towards each other. Interestingly, they do not move all the way to the origin, but instead slow, until they change direction and escape to infinity.

Figure 10.3.3 shows a simulation with an initial intensity of the excitation $I(0) = 0.01$,

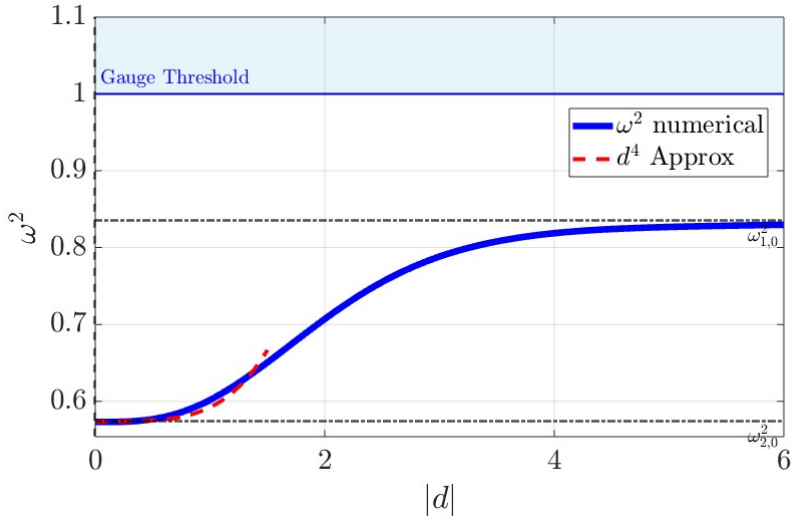

Figure 10.3.4: Flow of the angular frequency for a 2-vortex system, with $\lambda = 1.1$, as a function of the distance from the origin of the vortices. The light blue area indicates the gauge threshold.

and initial velocity $v_{\text{in}} = 0.05$. We see from the blue line indicating the position in the x-plane that the vortices do not meet the coincident configuration. This is because the excitation and kinetic motion of the vortices are too small to overcome the static force. We observe the red line in figure 10.3.3 that describes the intensity of the excitation as the vortices evolve. We note that the intensity drops as the vortices change direction and increases once they are moving back towards their initial position. This is because energy is transferred from the mode to the kinetic energy.

To begin to understand this behaviour, we can measure the squared angular frequency from the dynamical simulation (see figure 10.3.4). We plot the d^4 approximation for $d \to 0$. We see that the squared frequency interpolates between the value for the coincident $N = 2$ configuration with $\omega^2_{2,0} = 0.5738714$, and the asymptotic value describing well separated $N = 1$ vortices with $\omega^2_{1,0} = 0.8352168$. This suggests an attractive intervortex force induced by the in-phase excitation.

We can then calculate the energy contribution from the excitation (eq. (10.2.2)). This can be summed with the energy contribution of the static force, to give a space-dependent measure of the interaction energy for a type II 2-vortex system with excited shape modes, see figure 10.3.5.

We interpret the interaction energy (see figure 10.3.5) as follows. For small d, the interaction energy behaves similarly to the static force as d^4, hence the 2 vortices will remain at the origin if the mode is dominating, i.e. the intensity of the excitation is

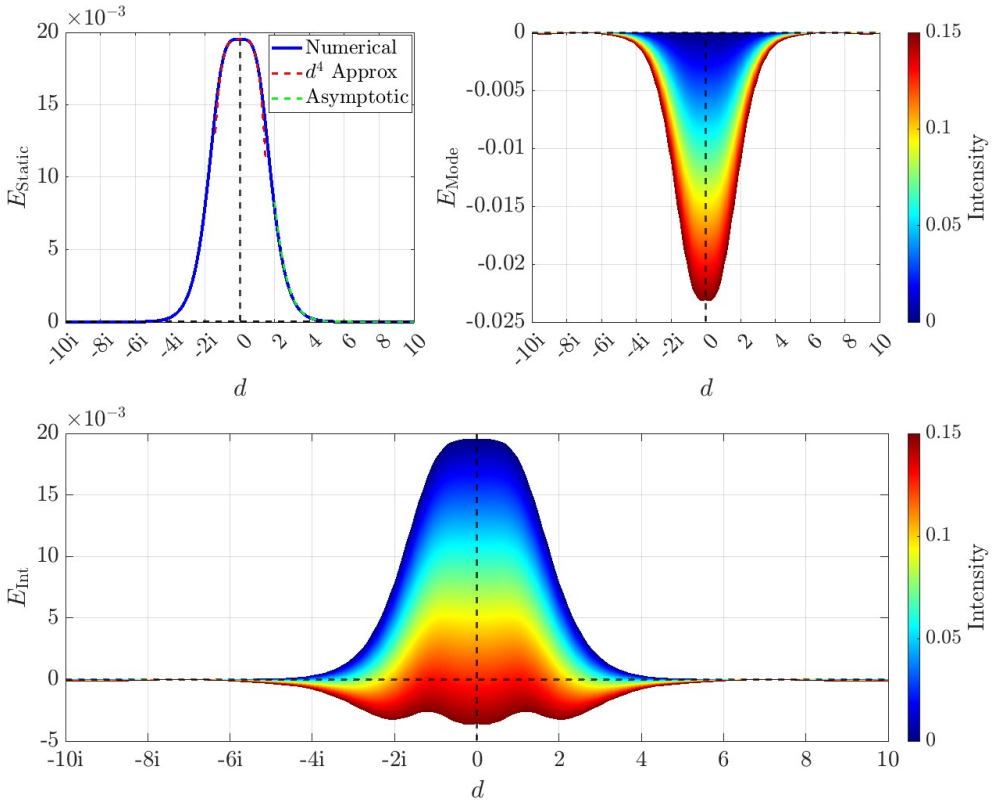

Figure 10.3.5: $\lambda = 1.1$ - Static force (left) in blue with d^4 approximation in dashed red for small d, and asymptotic approximation in dashed green. Interaction energy contribution from the mode (right) for a range of intensities. Total interaction energy (bottom) for a range of intensities.

large enough such that it is stronger than the static repulsion.

When the vortex separation is large, both the static force and the mode interaction asymptotically go to zero, hence there is no effect on vortex dynamics in this region. Alternatively, if we consider the scattering of vortices, when the intensity of the excitation is small, the vortices will back scatter due to the static force; however, if it is large enough, the vortices will be attracted towards each other.

In-between these two regions, vortex dynamics become highly nonlinear. There exists a local minimum in the interaction energy at $|d| \in (2, 4)$ that depends on the intensity of the mode. This suggests that vortices can become stuck at a fixed separation where the net force is zero, resulting in a quasi-stationary state, which explains the latter part of the trajectories in figure 10.3.2. We can confirm the existence of this bound state by considering another dynamical solution, see figure 10.3.6. The simulation in question begins with a saddle point solution, a radially symmetric $N = 2$ vortex centred at the origin. We then perturb the solution by adding a linear combination of the $k = 2$ splitting mode ($\omega^2_{2,2} = -0.0107688$) in the x direction and the $k = 0$ shape mode

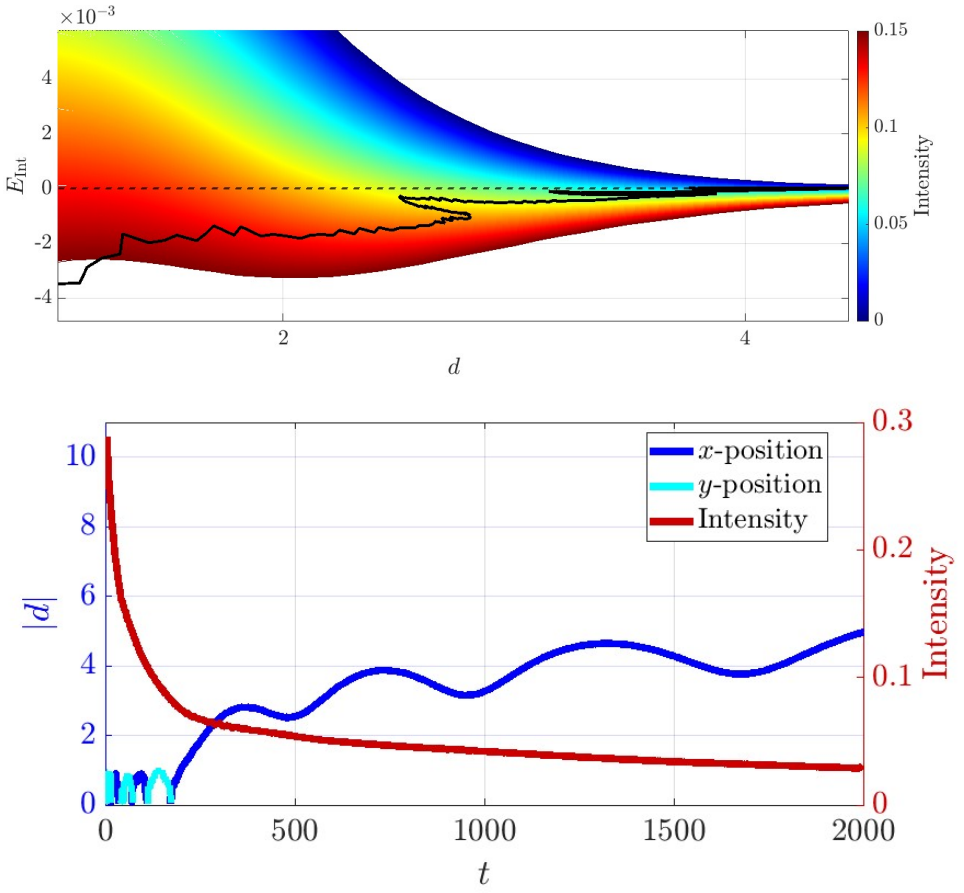

Figure 10.3.6: The solid black parametric curve indicates the path of the interaction energy of the simulation shown on the bottom. The solid blue and cyan lines on the bottom show the trajectories of the vortices in the x and y planes respectively.

$(\omega_{2,0}^2 = 0.5738714)$.

We see from the blue line denoting the distance from the origin of the vortices in the x-plane (see figure 10.3.6) that the vortex motion is slowed in the region of the local minimum of the interaction energy. In fact, we see that the vortices begin to oscillate in space within the region as the forces compete, until escaping as the intensity of the mode decays. The black parametric curve on the top of figure 10.3.6 can be followed to show how the intensity of the mode changes as the vortices evolve in time. It also shows that the vortices do indeed become trapped in this potential well. The colour-map shows the interaction energy assuming a fixed intensity, however, as seen in the bottom plot, the solid red line displays the intensity $I(t)$ as the vortices scatter, and it is not constant.

Similarly to figure 10.2.6, we can situate the vortices near the local minimum found in figure 10.3.5, see figure 10.3.7. Here, the vortices are initially positioned at $x = \pm 2$, with initial intensity $I(0) = 0.04$. The blue line indicates the position of the vortices

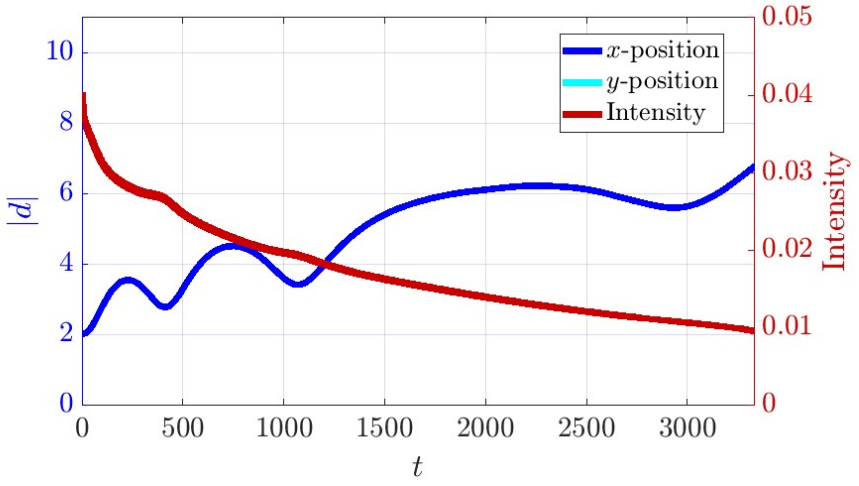

Figure 10.3.7: Trajectories of a two-vortex system at $\lambda = 1.1$ starting near the local minimum, with initial velocity $v_{\text{in}} = 0$ and intensity $I(0) = 0.04$, where $I(0) = \frac{1}{2}(\epsilon\omega)^2$.

on the $x-$axis as a function of time. We also show the intensity $I(t)$ in red. We can see that the vortices oscillate in space, within the potential well shown in figure 10.3.5. As the intensity of the excitation decays, the position of the potential well shifts to the right; hence, we see that the turning points of the position move out also. This clearly confirms the presence of a quasi-stationary state, whereby the vortices become trapped in the potential well and stay in a fixed region away from the origin, as long as the excitation is large enough.

We have calculated this interaction energy for a range of λ. It should be noted that the $N = 1$ shape mode exists only in the discrete spectrum up to $\lambda \approx 1.5$ (see chapter 8). The plots are not shown here; however, they show the same behaviour as figure 10.3.5. It is still of interest to consider the dynamics of vortices above this threshold, for $\lambda > 1.5$. For example, consider an $N = 2$ vortex at $\lambda = 2$, centred at the origin with an excited $k = 0$ shape mode, $\omega^2_{2,0} = 0.8161198$. This mode is still in the discrete spectrum; however, the $N = 1$ shape modes are not. As such we can consider the splitting of an $N = 2$ vortex, and monitor the dynamics of the constituent $N = 1$ vortices as they separate, see figure 10.3.8. One might assume that as the vortices separate, their frequencies will increase, and at some fixed distance the squared angular frequency will reach the continuous spectrum. This is a criterion for the existence of spectral walls, so it could be possible that the motion of the vortices is affected.

We can see from figure 10.3.8 that there exist some irregularities in the position at $|d| \approx 2$. This could suggest the presence of a spectral wall. Note that, due to the static

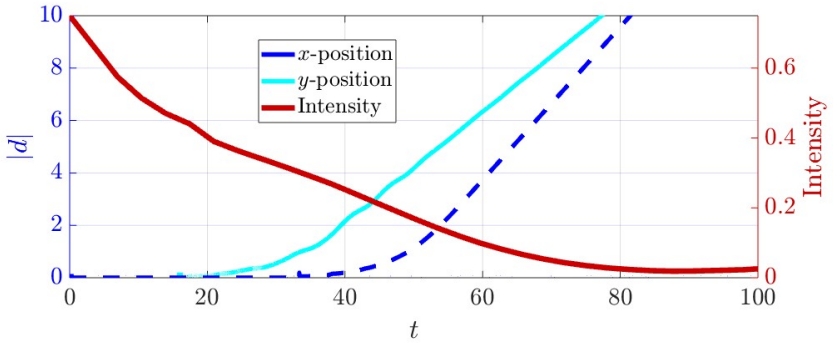

Figure 10.3.8: Trajectories of a 2-vortex system as a function of time, where $\lambda = 2$. We choose an initial intensity of the excitation $I(0) = 0.75$ per vortex, where $I(0) = \frac{1}{2}(\epsilon\omega)^2$. The cyan line indicates the distance of the vortices from the origin in the y-direction, and the dashed blue the unexcited scattering in the x-direction

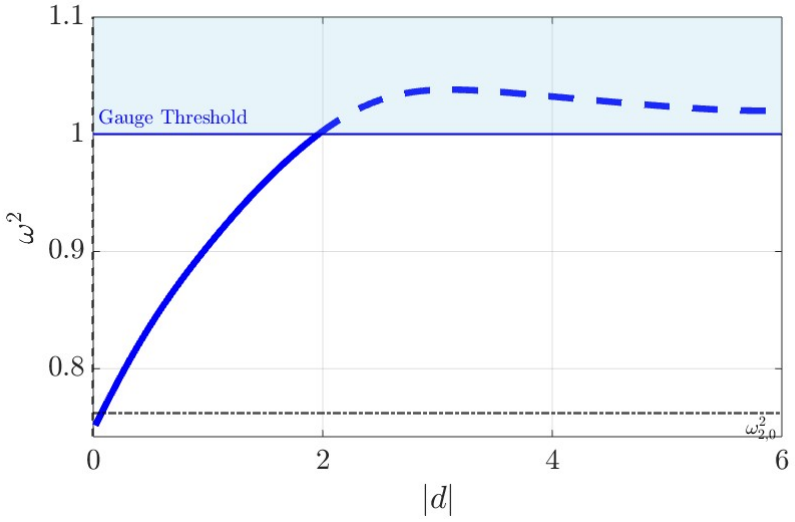

Figure 10.3.9: Flow of the squared angular frequency for a two vortex system, with $\lambda = 2$, as a function of the distance from the origin of the vortices. The light blue area indicates the gauge threshold.

repulsion, the vortices are not expected to form a quasi-stationary state; however, we do expect to see a change in velocity due to the presence of a spectral wall, which is what might be observed here. We can confirm that this irregularity is indeed a consequence of the spectral wall by tracking the squared angular frequency as the vortices separate; see figure 10.3.9.

We observe in figure 10.3.9 that the squared frequency rapidly increases from the coincident configuration with $\omega^2_{2,0} = 0.8161198$, as the vortices separate. We see that at $d \approx 2$, the squared frequency enters the continuous spectrum. This confirms the hypothesis of the existence of a spectral wall.

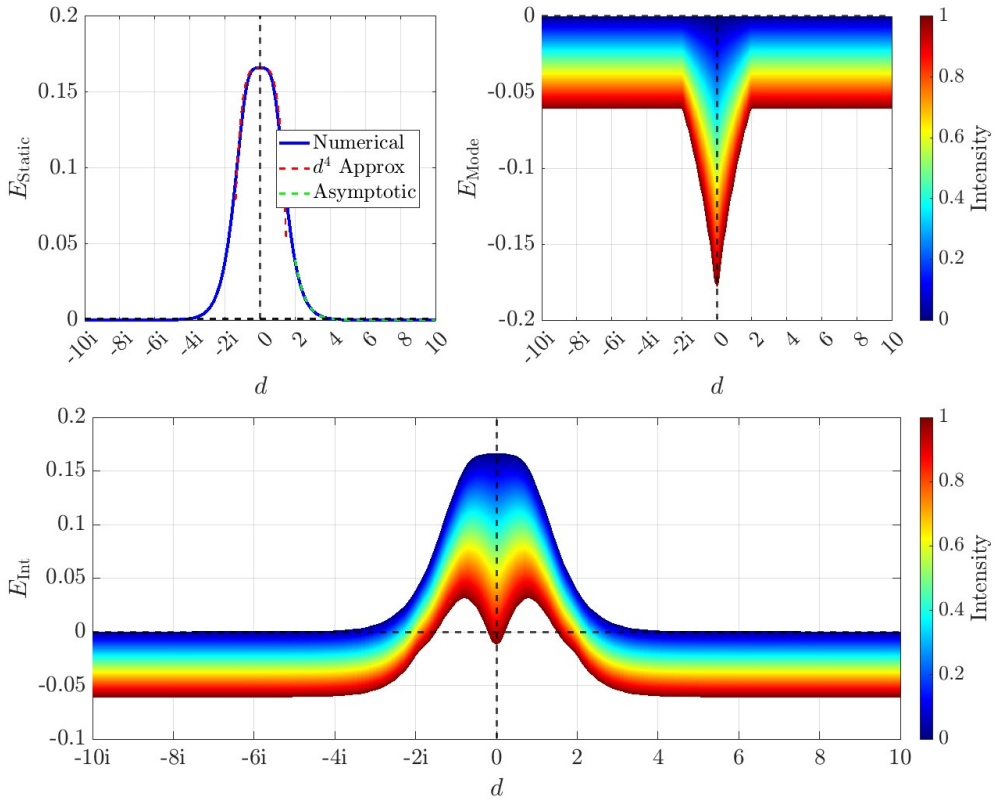

Figure 10.3.10: $\lambda = 2$ - Static force (left) in blue with d^4 approximation in dashed red for small d, and asymptotic approximation in dashed green. Interaction energy contribution from the mode (right) for a range of intensities, where $I(0) = \frac{1}{2}(\epsilon\omega)^2$. Total interaction energy (bottom) for a range of intensities.

Moreover, to fully understand the dynamics, we can again calculate the interaction energy, see figure 10.3.10. Firstly, for $|d| \ll 1$ there is a critical point in the interaction energy, suggesting that the $N = 2$ vortex can remain in the coincident configuration when excited. However, the excitation will quickly decay, and the vortices will separate. For well separated vortices, the squared frequency is in the continuous spectrum, hence all the energy from the excitation goes into the spectral wall, hence if the vortex is moving slow, it will bounce back towards the origin, or at least be slowed.

In [47] it was found that critically coupled vortices with excited shape modes in the attractive channel exhibit a chaotic bound structure, which we have shown in chapter 9. The vortices scatter more than once because of the energy transfer mechanism between the energy in the mode and the kinetic energy. We can perform the same analysis here. Although the static force of the type II vortices makes these quasi-bound states less likely to exist, they can still occur, as observed in figure 10.3.2.

We can vary the initial intensity of the perturbation and initial velocity of the vortices

to explore the chaotic nature of these multi-bounce solutions. We have done some initial calculations, but we do not present them here. Exploration of this chaotic multi-bounce structure is an avenue for future work.

10.4 Conclusion

In this chapter, we have extended our analysis of excited critically coupled vortices, see chapter 9, exploring the dynamics of vortices away from critical coupling. We have investigated how the excitation of internal bound modes influences vortex interactions when coupled with static forces, leading to a richer and more intricate scattering behaviour. The interplay between mode-induced forces, either attractive or repulsive, dependent on the relative phase of the excitation, and the inherent static interactions has been shown to significantly alter the dynamics of vortex scattering, as evidenced by our numerical simulations.

For type I vortex dynamics, where the static force is attractive, we have demonstrated that exciting repulsive modes can lead to complex scattering phenomena, including the presence of spectral walls. The interaction energy, comprising contributions from both the static force and the mode effects (figure 10.2.5), reveals regions where vortices may remain coincident, may separate, or may oscillate around a fixed position due to the presence of a local extremum creating a potential barrier. For $\lambda < 0.8$, where the discrete spectrum of certain modes ceases to exist, we observe that spectral walls still influence the dynamics, although their effects are subtler due to the dominance of the static attraction (figure 10.2.8).

In contrast, type II vortex dynamics, characterised by a repulsive static force, presents a slightly different dynamical landscape when attractive mode excitations are introduced. Our numerical results, namely, figures 10.3.1 and 10.3.2 showing the same simulation, highlight the formation of quasi-bound states where vortices scatter multiple times before separating or stabilising at a fixed distance, as seen in figures 10.3.6 and 10.3.7. The interaction energy analysis (figures 10.3.5 and 10.3.10) underscores the existence of critical points, which trap vortices in quasi-stationary configurations until the excitation intensity decays or the static repulsion prevails. For $\lambda > 1.5$, where the radially symmetric shape mode exists only in the continuous spectrum for $N = 1$, the spectral walls again play a role, slowing the vortex separation as frequencies reach the continuous spectrum (figures 10.3.8 and 10.3.9).

Across both regimes, the spectral flow of mode frequencies, coupled with static interactions, governs the scattering outcomes. The numerical results illustrate a delicate balance between forces, where initial conditions such as excitation intensity and initial velocity dictate whether vortices scatter symmetrically, form bound states, or repel to infinity. This complexity resembles findings at critical coupling, yet the departure from critical coupling introduces additional layers of nonlinearity, enriching the vortex dynamics.

We hence provided a comprehensive framework for understanding vortex interactions away from critical coupling, bridging the gap between theoretical predictions and numerical observations.

Chapter 11

Orbiting Vortices

11.1 Introduction

This chapter contains work from [48]. In this chapter, we discuss the full field theory dynamics for orbital vortex solutions, whereby the vortices undergo rotational motion around the origin. These orbits arise in various contexts. We will start to expand on the work in chapter 10, whereby we will take advantage of the attractive static force in type I superconductivity, and show that this attraction can lead to long-lived rotational states. We will discuss the role of the tangential velocity in balancing the centrifugal force with the mutual attraction of the type I vortices. Next, we will consider type II vortices. Here, the static intervortex force is repulsive, hence we will rely on the local minimum found in chapter 10, and discuss solutions with rotational motion inside this potential well. Moreover, we have studied the role of the mode-induced attractive force for critically coupled vortices in chapter 9. It is a natural progression to consider vortex orbits in this regime also, where we will again attempt to balance the attractive force with the repulsive centrifugal force to obtain long-lived vortex orbits. Finally, it is known that there is a strong attractive force for vortex-antivortex pairs. We will follow a similar procedure to that for type I vortices and show that we can achieve long-lived orbits.

11.2 Type I Vortex Orbits

When considering orbital vortices, it is first natural to consider the case of type I vortices, without excitation, see figure 11.2.1. Here, the only competing forces are the attractive

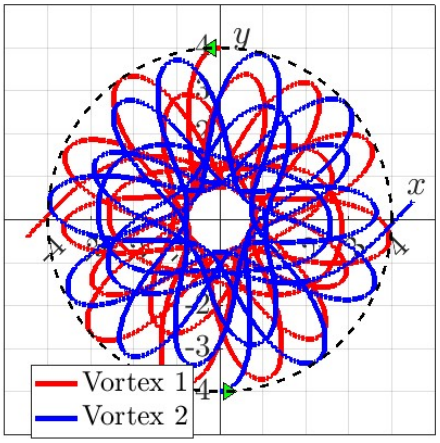

Figure 11.2.1: Trajectories of a 2-vortex system orbiting at $\lambda = 0.9$, with $v_{\text{in}} = 0.01$, and $I(0) = 0$, where $I(0) = \frac{1}{2}(\epsilon\omega)^2$.

static force and the repulsive centrifugal force. If the tangential velocity is small, then the vortices will be drawn towards the centre; see figure 11.2.1. If the velocity is large, the kinetic energy of the vortices will dominate the interaction and they will escape to infinity. For a fine-tuned velocity, dependent on the orbit size, the vortices may form a long-lived circular orbit.

In figure 11.2.1, we plot the trajectories of the vortices for a 2-vortex system at $\lambda = 0.9$. The initial velocity is $v_{\text{in}} = 0.01$, and the vortices are centred at $d_{\text{in}} = \pm 4$ in the y-direction. We can see from figure 11.2.1 that the vortices orbit the origin. Note that the orbit is not circular because of the magnitude of the static force. The kinetic motion, that is, the kinetic energy in the vortices, is not large enough to overcome the static attraction, hence the static force dominates the interaction. Note that the vortices do not meet the coincident configuration. Instead, they pass each other close to the origin and are accelerated past each other due to the increasing magnitude of the static force. Interestingly, the trajectories form peaks at precisely the distances they were initially configured.

Next, we attempt to approximate the perfect conditions for a circular orbit by studying the competing forces in the interaction. Consider a 2-vortex system with mass $m = V_1^{\lambda}$ per vortex, where the vortices have separation $s = |r_1 - r_2|$. We define the relative separation as $r = r_1 - r_2$. The reduced mass is thus $\mu = \frac{m}{2} = \frac{V_1^{\lambda}}{2}$.

In polar coordinates, we have that $r = (s\cos\theta, s\sin\theta)$. The relative kinetic energy is then

$$T_{\text{rel}} = \frac{m}{4}(\dot{s}^2 + s^2\dot{\theta}^2). \tag{11.2.1}$$

If we include a radial potential, then the reduced Lagrangian is then

$$L_{\text{red}} = \frac{m}{4}(\dot{s}^2 + s^2\dot{\theta}^2) - V(s). \tag{11.2.2}$$

Since the angular coordinate θ is cyclic, the angular momentum is then defined as

$$L_z = \frac{m}{4}s^2\dot{\theta} = \frac{V_1^\lambda}{4}sv, \tag{11.2.3}$$

where $v = s\dot{\theta}$.

Varying eq. (11.2.3) with respect to s gives

$$\frac{m}{4}\ddot{s} = \frac{m}{4}s\dot{\theta}^2 - \frac{dV}{ds}. \tag{11.2.4}$$

hence we have that

$$m\ddot{s} = \frac{16L_z^2}{ms^3} - 4\frac{dV}{ds}. \tag{11.2.5}$$

The centrifugal force is thus

$$F_{\text{centrifugal}} = \frac{16L_z^2}{V_1^\lambda s^3}. \tag{11.2.6}$$

We then have that the centrifugal part of the interaction energy per vortex is

$$E_{\text{centrifugal}} = -\frac{L_z^2}{V_1^\lambda d^2}, \tag{11.2.7}$$

where $s = 2d$, and $L_z = \frac{V_1^\lambda}{2}dv$

We can hence plot the interaction energy in this case, taking into account only that static force and centrifugal force, see figure 11.2.2.

We can see from figure 11.2.2 that for $d > 4$, the net force is asymptotically zero, where the force is the gradient of the interaction energy. Furthermore, we observe a critical point of the interaction energy for $d \in [0.5, 1.5]$. We can see from the force that we should be able to obtain vortex orbits for small d where the net force is zero. If the velocity is small, the static force will dominate and the vortices will accelerate towards the origin, see figure 11.2.1. We can predict the initial velocity required for the vortices

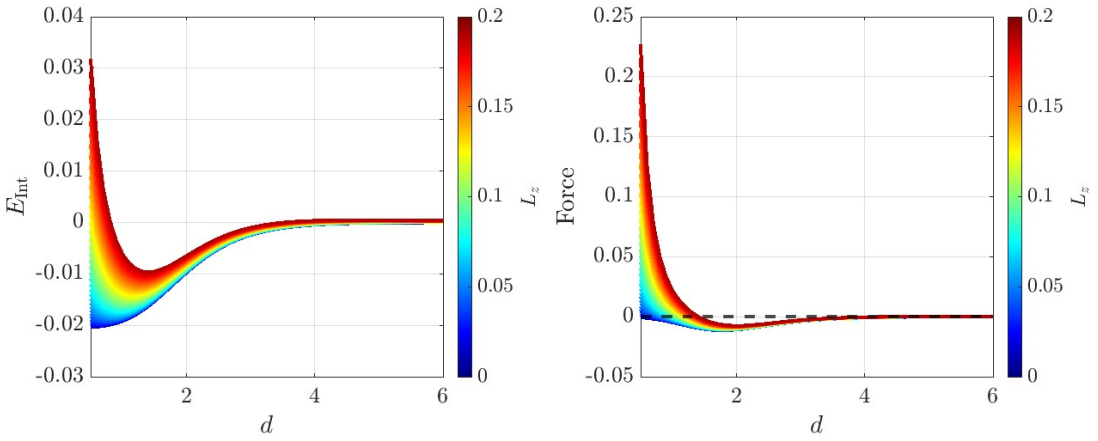

Figure 11.2.2: Sum of the static energy and the centrifugal kinetic energy (left) and the force (gradient of the interaction energy) (right), varying L_z, where $L_z = \frac{V_1^\lambda}{2} dv$, for $d \in [0.5, 6]$, the position of the vortices from the origin.

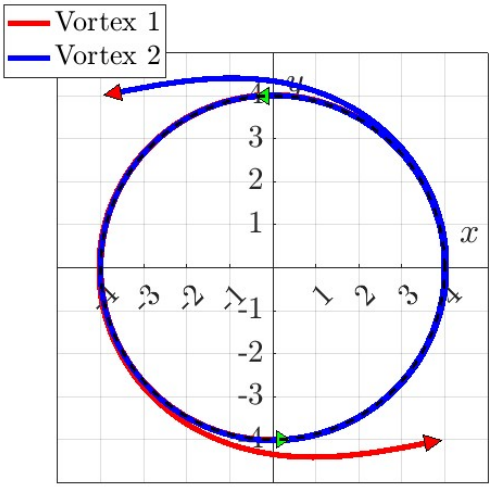

Figure 11.2.3: Trajectories of a two-vortex system orbiting at $\lambda = 0.9$, with $v_{\text{in}} = 0.03230815$ and $d = 4$.

to attempt to achieve a more circular orbit; see figure 11.2.3. We can calculate the expected tangential velocity of $v = 0.038246$, at a fixed distance of $d = 4$.

We see in figure 11.2.3 a long-lived circular orbit in which the vortices orbit the origin multiple times before escaping to infinity. We can plot snapshots of the corresponding dynamical simulation to gain a clearer picture of how the vortices orbit. We see in figure 11.2.4 that the vortices orbit the origin many times, before eventually escaping to infinity. This is because the net force is still slightly positive at this distance, see figure 11.2.2.

Furthermore, we can observe vortex orbits at the critical point in the interaction energy,

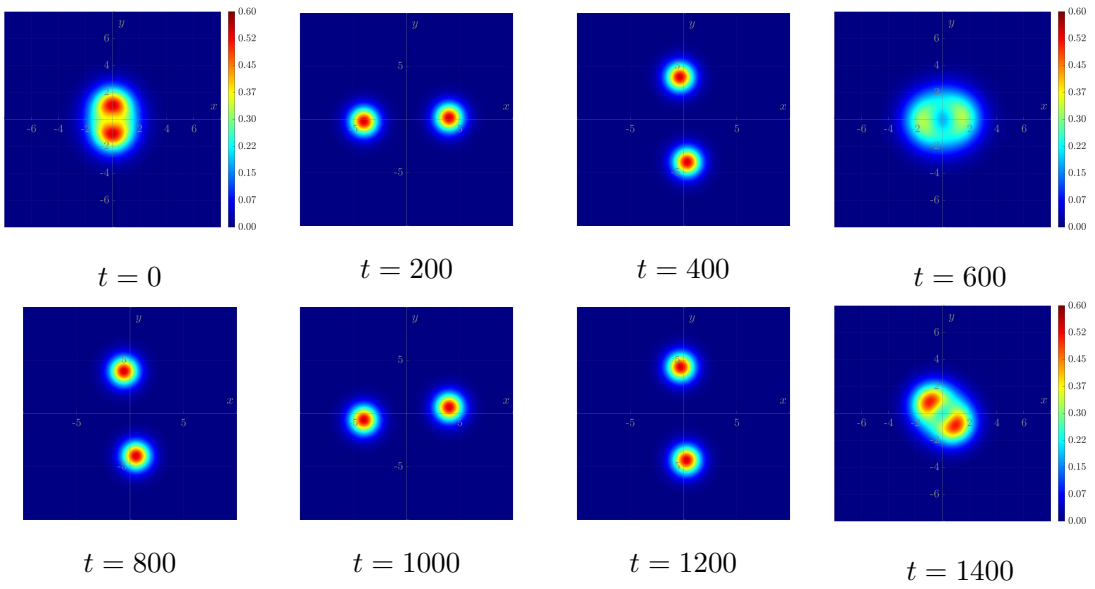

Figure 11.2.4: Snapshots of a dynamical simulation displaying a heat map for the energy density for a 2-vortex scattering with $\lambda = 0.9$ and initial velocity $v_{\text{in}} \approx 0.032$.

where $d \in [0.5, 1.5]$, see figure 11.2.5. We see that the vortices seem to orbit each other more than 10 times (up to when the numerics fail). The orbit is not perfectly circular. This could be due to the vortex oscillating in the potential well around the critical point in the interaction energy. Additionally, it could be a numerical artefact as a result of the vortices being initially positioned close together, such that the initial configuration is not a perfect approximation to the field theory. We can plot dynamical snapshots of the same simulation figure 11.2.5, displaying the static energy density as a heat plot; see figure 11.2.6.

11.3 Type II Vortex Orbits

We have shown in figure 10.3.5 that there exists a local minimum whereby the vortices can form a quasi-stationary state at a fixed distance away from the origin. This motivates us to consider type II vortices that orbit the origin.

The interaction energy will differ slightly, since not only do we still have the repulsive static force and the attractive mode interaction, but we will also have the centrifugal force. We can add the centrifugal force to the interaction energy, and approximate the ideal velocity for a circular orbit, given a fixed intensity. Let us first consider an intensity of $I(0) = 0.05$, see figure 11.3.1. We see in figure 11.3.1 that the net force is zero for

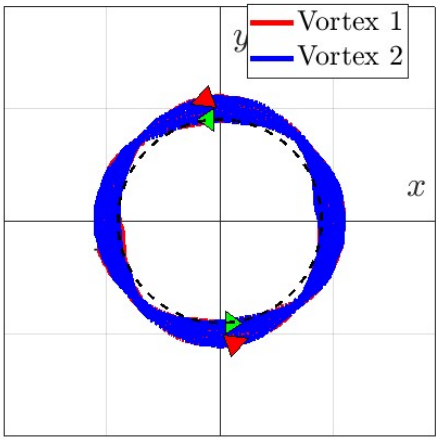

Figure 11.2.5: Trajectories of a two-vortex system orbiting for $\lambda = 0.9$ at $d = 0.9$, with $v_{\text{in}} = 0.045$

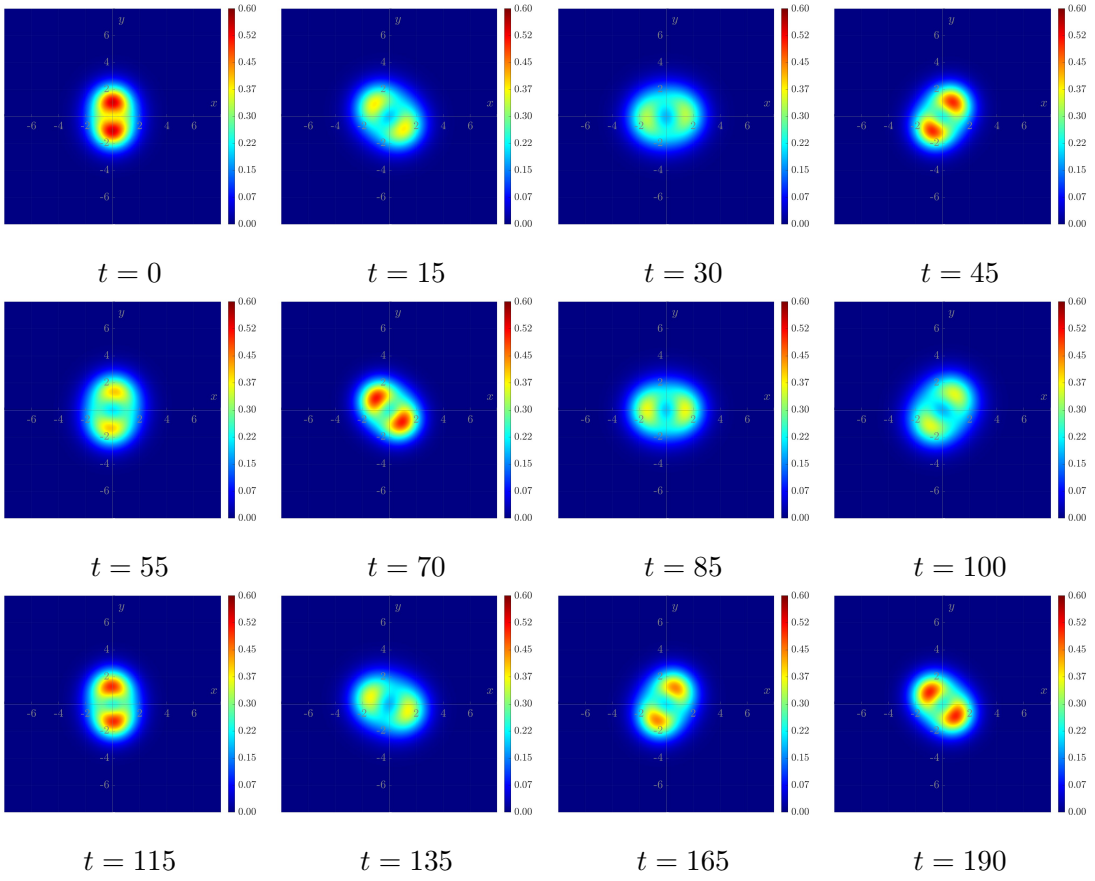

Figure 11.2.6: Snapshots of energy density for a two-vortex scattering ($\lambda = 0.9$, $v_{\text{in}} = 0.045$, $I(0) = 0$) at $d = \pm 0.9$, as seen in figure 11.2.5.

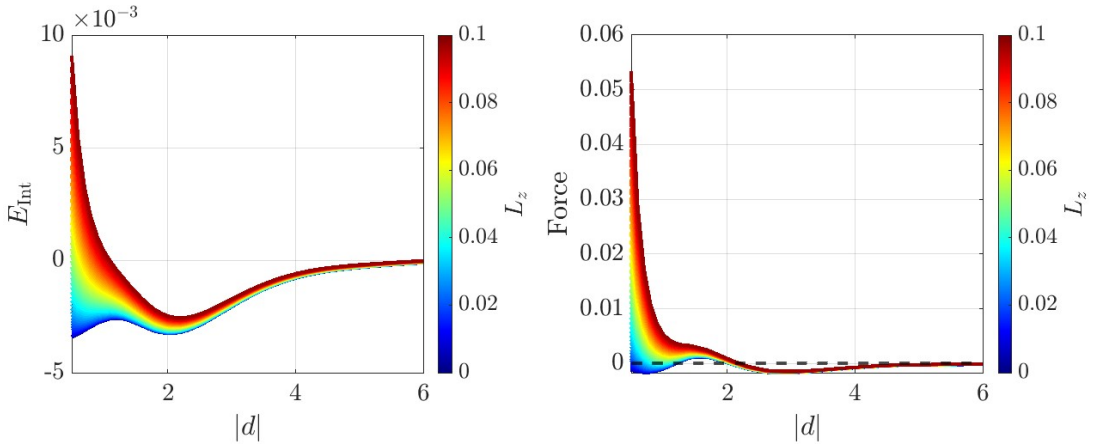

Figure 11.3.1: Interaction energy (left) and force (right) where $F = -\frac{\partial}{\partial d} E_{\text{Int}}$ for a 2-vortex system at $\lambda = 1.1$, with intensity $I(0) = 0.15$, where $I(0) = \frac{1}{2}(\epsilon\omega)^2$, and for a range of L_z, where $L_z = \frac{V_1^\lambda}{2} dv$. The interaction energy sums the static energy, the mode induced energy and the centrifugal energy, as a function of the radius of the orbit $d \in [0.5, 6]$.

$d > 4.5$, which means that if the vortices drift away, we should still be able to maintain a long-lived orbit at this distance, assuming that the intensity remains constant. Because the vortices are not initially well separated, the initial condition is not perfect. As such, the intensity will drop as the solution flows to the correct solution, which is why we have chosen an intensity of $I(0) = 0.15$. Furthermore, we see three critical points in the interaction energy. A shallow local minimum for $d \ll 1$, meaning that it might be possible to have vortex orbits in this regime. Furthermore, there is a second local minimum for $d \in [1.5, 2.5]$. This minimum is slightly more pronounced, making this distance a better candidate for long-lived vortex orbits. The local extremum at $d \approx 1$ suggests a potential barrier, that may help in stabilising vortex orbits.

Figure 11.3.2 shows the trajectories of two vortices with $\lambda = 1.1$, initial velocity $v_{\text{in}} = 0.019$ and intensity $I(0) = 0.1$. The blue line indicates the path of one vortex and the red line the other. The dashed black line displays the circle $x^2 + y^2 = d_0^2$, where $d_0 = 4.5$. We see that the orbit starts stable but deviates away from the black line. This is due to the intensity of the excitation decaying, and as such the static force and centrifugal force dominate the interaction, and the vortices escape to infinity.

If the initial intensity is large, the vortices will move towards the local minimum and oscillate back. This breaks the symmetry of the orbit; see figure 11.3.3. Instead, we can simulate the vortices to be initially located on top of the local minimum, at $d \approx 2$. We can expect the vortices to become trapped in the potential well, even with the additional

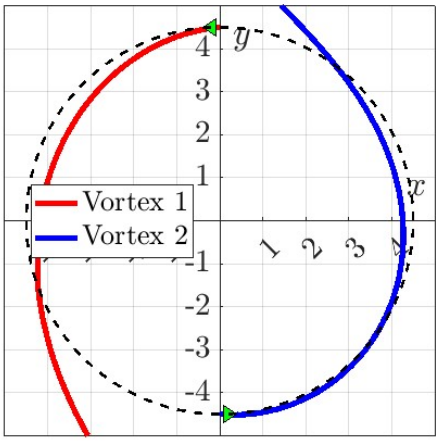

Figure 11.3.2: Trajectories of a 2-vortex system orbiting at $\lambda = 1.1$, with initial velocity $v_{\text{in}} = 0.019$ and intensity $I(0) = 0.1$, where $I(0) = \frac{1}{2}(\epsilon\omega)^2$.

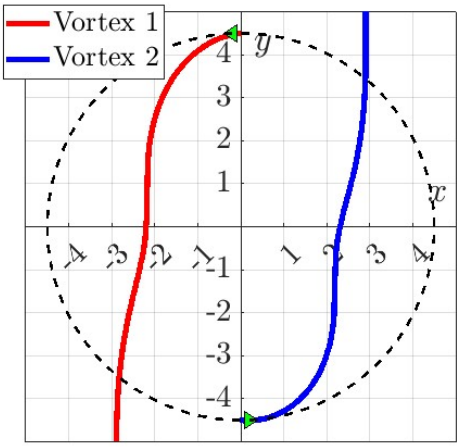

Figure 11.3.3: Trajectories of a 2-vortex system orbiting at $\lambda = 1.1$, with initial velocity $v_{\text{in}} = 0.015$ and intensity $I(0) = 0.015$, where $I(0) = \frac{1}{2}(\epsilon\omega)^2$.

centrifugal force, especially if the orbit is small. We see an example of this in figure 11.3.4 For $\lambda = 1.1$, $V_1^\lambda = 3.204508502$, so for a long-lived orbit at $d = 1$, for $I(0) = 0.2$, choosing $L_z = 0.07$, corresponding to the orange line in figure 11.3.1, we would require an angular velocity of $v_{\text{in}} = 0.043688$. We see an example of this in figure 11.3.5.

figure 11.3.5 shows a semi-stable orbit for type II vortices. The blue line indicates the path of one vortex and the red line the other. The dashed black line displays the circle $x_1^2 + x_2^2 = d_0^2$, where $d_0 = 1$.

We see in figure 11.3.5 that the vortices orbit twice around the origin before escaping.

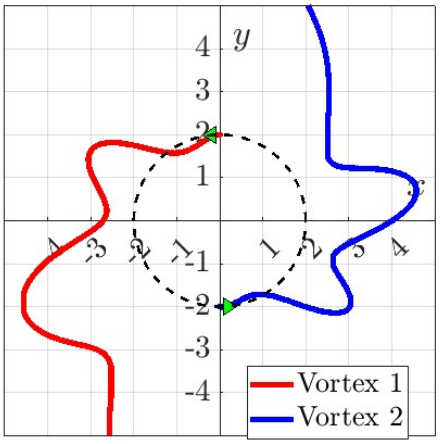

Figure 11.3.4: Trajectories of a 2-vortex system at $\lambda = 1.1$ with $y_{\text{in}} = 2$, initial velocity in the $x-$direction, $v_{\text{in}} = 0.01$ and initial intensity $I(0) = 0.08$, where $I(0) = \frac{1}{2}(\epsilon\omega)^2$.

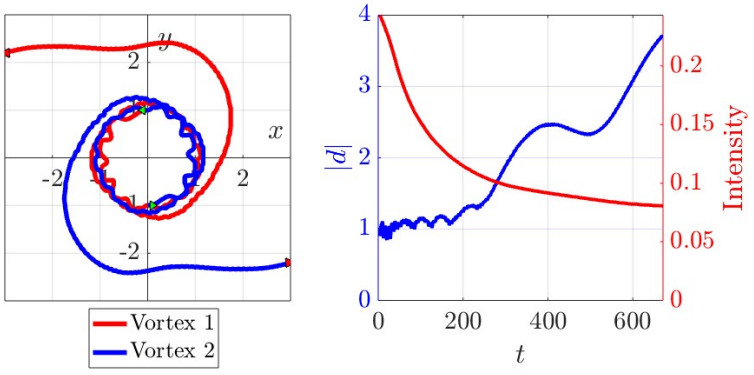

Figure 11.3.5: Left: trajectories of a two-vortex system ($\lambda = 1.1$, $v_{\text{in}} = 0.04$, $I(0) = 0.2$) at $x_2 = \pm 1$. The blue line shows the (x_1, x_2) position of one vortex, red the other. Right: intensity of the excitation per vortex as a function of time (red), and distance $|d|$ of the vortices from the origin as a function of time.

This is due to the intensity of the excitation decaying, as seen in the right of figure 11.3.4 with the magenta line displaying the intensity of the excitation per vortex as a function of time, and as such the static force and centrifugal force dominate the interaction, and the vortices escape to infinity.

11.4 Vortex Orbits at Critical Coupling

It was shown in section 9.2 that we can induce an attractive force to vortex scattering at critical coupling by including internal shape modes. It is natural to assume that we

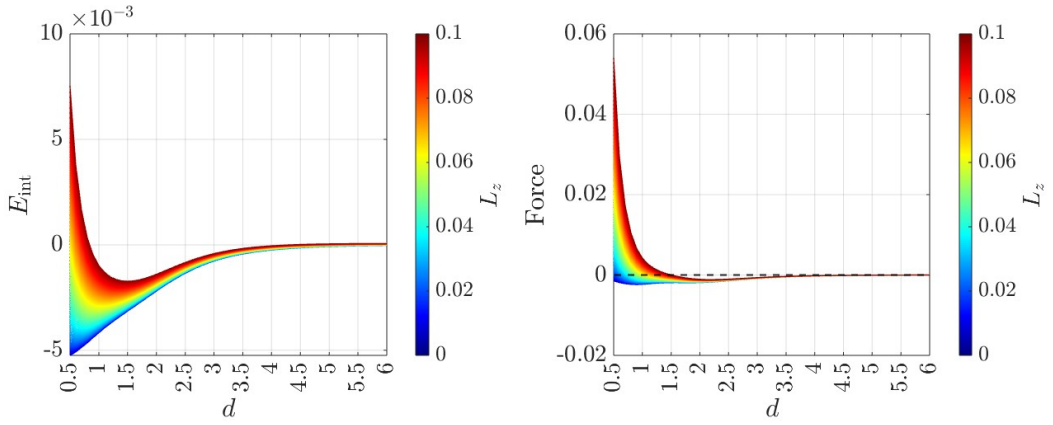

Figure 11.4.1: Interaction energy (left) and total force (right) for a two-vortex system ($\lambda = 1$) with initial intensity $I(0) = 0.025$ and angular momentum $L_z = \frac{V_1^\lambda}{2} d v_{\text{in}}$, as a function of orbit radius d.

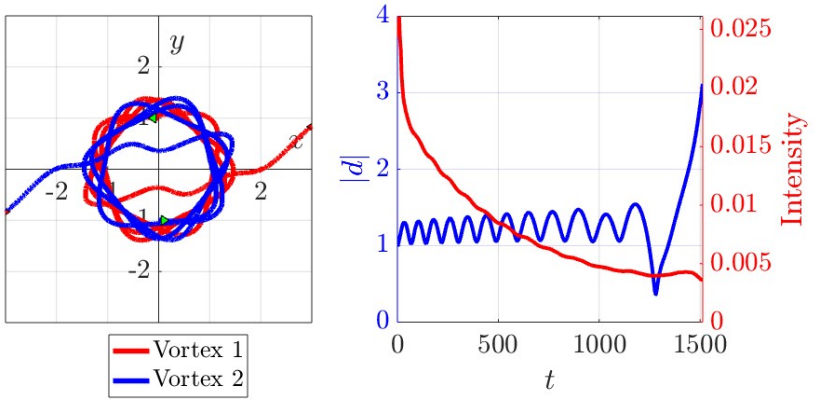

Figure 11.4.2: Left: trajectories of a two-vortex system ($\lambda = 1$, $v_{\text{in}} = 0.05$, $I(0) = 0.025$) at $x_2 = \pm 1$. The blue line shows the (x_1, x_2) position of one vortex, red the other. Right: intensity of the excitation per vortex as a function of time (red), and distance $|d|$ of the vortices from the origin as a function of time.

can hence find an orbital vortex pair at critical coupling.

We can gain some intuition for suitable orbits by studying the interaction energy, and hence the total force of the system. At critical coupling, the static force is zero, so the only competing forces are the attractive mode induced force, and the repulsive centrifugal force. We assume a fixed intensity of the excitation, and calculate the contributions to the interaction energy, see figure 11.4.1, where we have chosen a fixed intensity of $I(0) = 0.025$.

We see from figure 11.4.1 that for $I(0) = 0.025$, that the force crosses the x-axis at $|d| \approx 1$, i.e. there is a local minimum in the interaction energy (see left of figure 11.4.1). Choosing $L_z = 0.078$, we find that $v_{\text{in}} \approx 0.05$. We can test these parameters in figure 11.4.2.

We see in figure 11.4.2 that the vortices orbit the origin 6 times. The left plot shows the positions of the vortices in the x_1, x_2 plane, where blue shows the path of one vortex, and red the other vortex. The right plot shows the distance of the vortices from the origin as a function of time in blue, and the intensity of the excitation per vortex as a function of time in red. We can see from the distance of the vortices from the origin in the right plot (blue) that as the intensity of the excitation decreases, the size of the orbit increases, which is expected by observing figure 11.4.1. It is trivial that as the intensity of the excitation decreases, the attractive force induced by the mode also decreases, hence since the centrifugal force stays roughly the same (assuming a circular orbit), hence the local minimum where the interaction energy is zero, i.e. the force crosses the x_1-axis, moves out ($|d|$ increases).

We can show snapshots of the energy density for the simulation shown in figure 11.4.2.

We see in figure 11.4.3 that the vortices orbit the origin, whilst oscillating in shape, as well as oscillating about the local minimum in the interaction energy. The vortices orbit for a significantly long time, up to $t = 1500$, at which point the vortices escape after the orbit becomes breaks down and the vortices pass close to the origin.

11.5 Vortex Anti-Vortex Orbits

Finally, we will consider orbital solutions of vortex-antivortex pairs. Here, the static intervortex force is highly attractive, and if the pair collide, they will annihilate.

We can plot the trajectories of the vortices to observe the orbit. We expect two scenarios. If the initial velocity is small, the vortices will collide at the origin and annihilate. If the velocity is larger, the vortices will form a long-lived orbit, before either being pulled to the origin or escaping to infinity.

Consider a scattering solution with $v_{\text{in}} = 0.08$, see figure 11.5.1. We observe that the vortices initially form a semi-stable orbit; however, the tangential velocity is slightly too small and the vortices are drawn to the origin and annihilate before completing a full orbit. An artefact of this is the interesting yin-yang pattern in the trajectories.

If we increase the initial velocity to a fine-tuned value of $v_{\text{in}} = 0.08327$, we observe in figure 11.5.2 an orbital solution where a long-lived orbit is formed, and the vortices move around the origin multiple times before escaping to infinity.

We can also plot snapshots of the relevant dynamical simulation shown in figure 11.5.2, see figure 11.5.3. We display heat plots for the condensate $|\phi^2|$ and the magnetic field B.

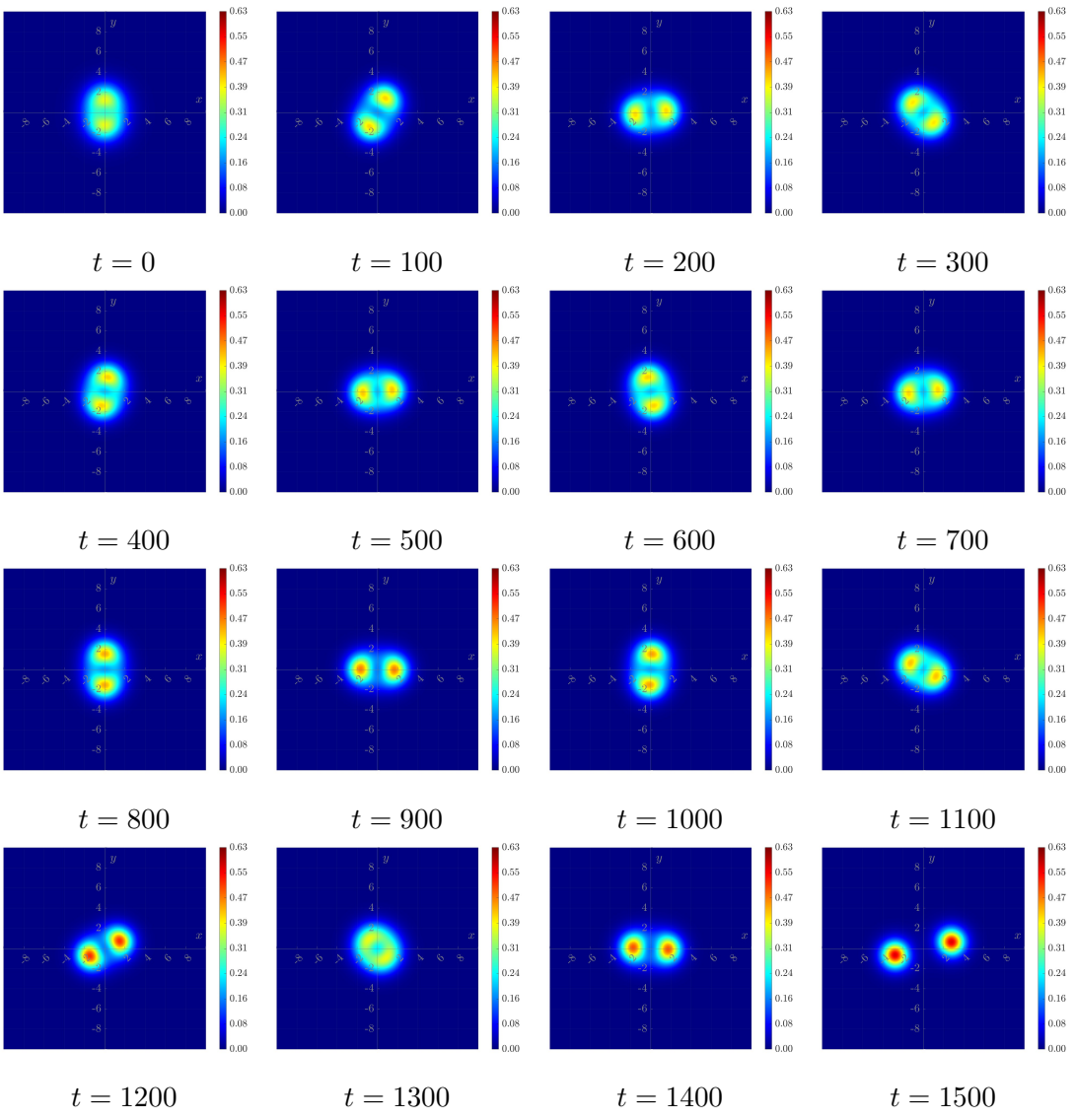

Figure 11.4.3: Snapshots of energy density for a two-vortex scattering ($\lambda = 1$, $v_{\text{in}} = 0.05$, $I(0) = 0.05$) at $d = \pm 1$, as seen in figure 11.4.2.

We can distinguish between the vortex and antivortex by the sign of the magnetic field. Note that in the magnetic field plots, red indicates positive and blue indicates negative; hence, we can see how the vortex and antivortex orbit the origin, before escaping to infinity.

11.6 Conclusion

In this chapter, we explore the dynamics of orbital vortex solutions across various regimes, demonstrating the interaction between static forces, centrifugal forces, and mode-induced interactions. Beginning with type I vortices, we discussed that long-lived

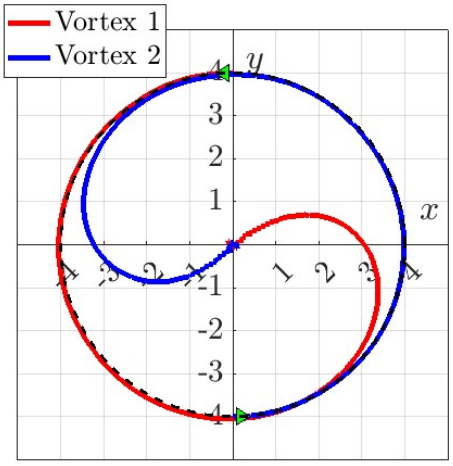

Figure 11.5.1: Trajectories of a vortex-antivortex pair. Red indicates the path of the vortex, and blue the antivortex. We see that the pair complete a half orbit, before being pulled to the origin an annihilating.

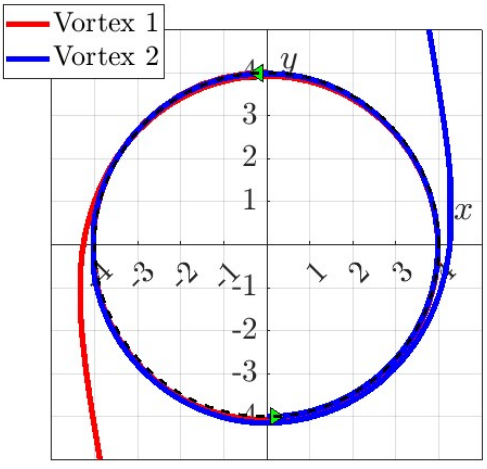

Figure 11.5.2: We plot the trajectories of the vortices. Here, the blue line indicates the path of the antivortex, and the red line shows the path of the vortex. The pair orbit the origin once, before escaping to infinity.

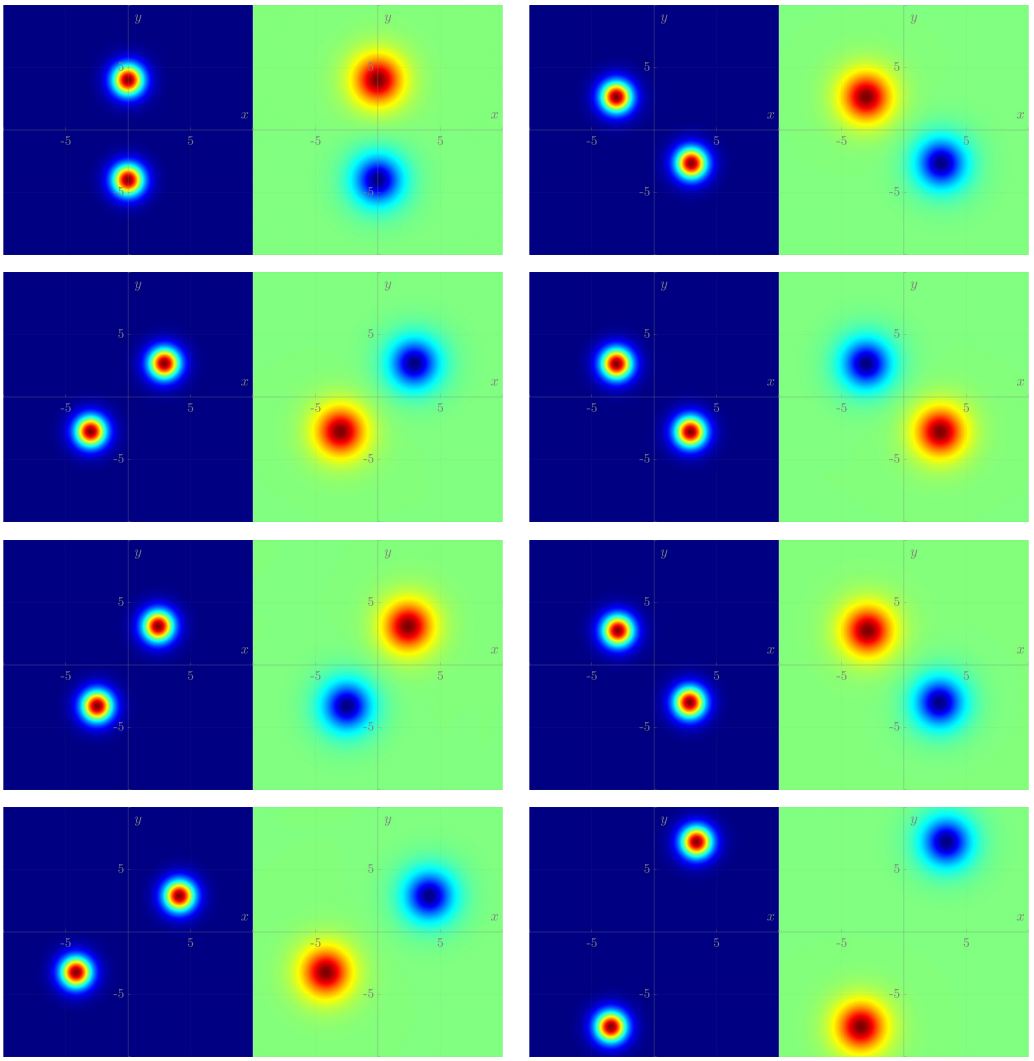

Figure 11.5.3: Heat plots for the condensate $|\phi^2|$ and the magnetic field B. We show a vortex-antivortex scattering with non-zero impact parameter. The scattering solution displays an orbital behaviour of the (anti)vortices around the origin.

orbits can be achieved when the tangential velocity precisely counterbalances the attractive static force. Through numerical simulations, we confirmed the existence of such orbits and identified conditions under which vortices either collapse towards the origin or escape to infinity, or form long-lived orbits inside a potential well.

For type II vortices, where the static force is repulsive, we examined the role of critical points in the interaction energy, observed in figure 11.3.1, in sustaining orbital motion. By introducing an additional mode-induced attraction, we demonstrated that vortex pairs can remain in bounded orbits within a potential well. However, we observed that as the excitation decays, the vortices may eventually escape, reinforcing the delicate balance required for sustained rotational motion.

Furthermore, we extended our analysis to critically coupled vortices, where shape mode excitations can introduce an effective attraction. Our simulations illustrated that this interaction can lead to vortex orbits at critical coupling, although the dynamic nature of the excitation prevents the formation of long-lived orbits.

Lastly, we considered vortex-antivortex pairs, where the strong attractive interaction necessitates careful velocity tuning to avoid annihilation. The results indicate that, under suitable conditions, vortex-antivortex orbits can exist, though their longevity is highly dependent on the specific initial conditions.

In general, this chapter has provided a comprehensive study of orbiting vortices, highlighting the interdependence of forces required to sustain such configurations. These findings may inform future studies on controlled vortex motion in various physical contexts.

Part IV

Conclusions

Chapter 12

Conclusions

This thesis started with a discussion on baby Skyrmions. Our analysis has primarily focused on static solutions and their energetic properties. A natural extension of this work would be to study the dynamical behaviour of baby Skyrmions under various perturbations. This includes exploring their scattering properties, rotational modes, and the possibility of quasi-bound states analogous to those found in vortex dynamics. Furthermore, higher charge solutions warrant further investigation, as they may exhibit novel structural formations, including global energy minimum that could serve as stable multi-Skyrmion configurations [61, 78].

In part III, we have conducted an in-depth investigation into the intricate dynamics of Abelian Higgs vortices, with a particular emphasis on how internal modes influence their interactions. Through a combination of analytical and numerical techniques, we have extended existing frameworks by considering vortex scattering, quasi-bound states, spectral walls, and orbital motion. Our results provide deeper insight into the role of internal mode excitation and its effect on vortex behaviour, particularly in regimes beyond critical coupling.

Building on the findings presented in this thesis, several promising avenues for future research emerge, providing opportunities to extend and deepen our understanding of vortex dynamics. The work presented here could be extended to study the dynamics of vortices of higher multiplicity, specifically multi-vortex scattering at critical coupling. This has many possibilities because higher-degree vortices also have more normal modes to excite.

An important result of this thesis is the existence of spectral walls in Abelian Higgs

vortex dynamics. One avenue is the identification of spectral walls in other higher-dimensional systems. The key requirement for the emergence of spectral walls is the presence of bound modes that, as they traverse the moduli space, enter the continuous spectrum. Additionally, we anticipate that spectral walls exist in BPS solitons with different topologies, with the most exciting candidates being BPS monopoles. If this effect extends to higher dimensions, it could enable the experimental observation of spectral walls in more realistic physical systems, including superconductors.

One of the key areas for future investigation involves studying vortex interactions in the presence of impurities. The introduction of defects in the medium can significantly alter vortex trajectories, potentially leading to novel bound states or chaotic scattering behaviour. Previous studies [18, 28] have shown that impurities can act as localised trapping sites, and incorporating this aspect into our framework could yield new stable configurations. Furthermore, the dynamics of vortices with magnetic impurities have been explored, providing insight into how impurities influence vortex motion [28].

Furthermore, an exciting avenue of research lies in the study of vortices within the Schrödinger-Chern-Simons model [30, 55]. Unlike the Abelian Higgs model, which features second-order dynamics, the Schrödinger-Chern-Simons system exhibits first-order conservative dynamics. The investigation of alternative materials with lower dissipation could lead to the emergence of additional internal modes, potentially enriching the dynamical landscape. Furthermore, the Schrödinger-Chern-Simons dynamics for vortices was discussed in [49] where it is shown that the vortices circle each other. Mode excitations could be an interesting avenue for future research in Schrödinger-Chern-Simons dynamics.

An additional avenue for future exploration lies in the study of vortex lattices, which offer a rich framework for understanding ordered vortex configurations in superconducting systems. Recent advances in [70, 80] have developed a method to compute minimal-energy vortex lattices in anisotropic Ginzburg-Landau models, revealing dynamic lattice structures that evolve with applied magnetic fields. These findings suggest investigating vortex lattices in the presence of internal mode excitations or impurities could thus bridge the dynamical phenomena observed in this thesis with macroscopic ordered states, potentially informing experimental observations in condensed matter systems.

Another promising direction is the extension of our vortex studies to cosmic strings.

The mathematical similarities between vortices in condensed matter systems and cosmic strings in cosmology suggest that many of the techniques developed in this thesis could be adapted to study string interactions in the early universe. It is shown in [75] that cosmic strings can form networks and undergo reconnection events, similar to vortex interactions. Understanding how mode excitations influence these processes could provide new insights into cosmic string evolution and their potential observational signatures.

In conclusion, this thesis has provided significant advancements in our understanding of vortex dynamics, particularly with the inclusion of internal modes for BPS vortices, as well as in the non-BPS regime. The interplay between mode excitations, intervortex forces, and orbital motion has been systematically analysed, leading to new insights that can inform future theoretical and experimental studies. The extensions outlined above present a rich landscape for further exploration, with potential implications spanning condensed matter physics, cosmology, and soliton theory.

Appendix A

Vortex Mode Frequencies

The squared angular frequencies $\omega_{N,k}^2$ computed by the MATLAB code are reliable to approximately 6 decimal places, limited primarily by the eigenvalue solver's tolerance of 10^{-6} and finite difference errors on the order of $h^2 = 4 \times 10^{-6}$.

λ	$k = 0$	$k = 1$ (T)
0.1	0.0758150	-0.0129376
0.2	0.1633020	-0.0108673
0.3	0.2560929	-0.0054384
0.4	0.3434223	-0.0021344
0.5	0.4254454	-0.0005528
0.6	0.5021804	-0.0005090
0.7	0.5760020	-0.0004885
0.8	0.6466050	-0.0004969
0.9	0.7136541	-0.0004948
1.0	0.7770676	-0.0002291
1.1	0.8352168	-0.0002416
1.2	0.8877518	-0.0002550
1.3	0.9336225	-0.0002596
1.4	0.9713502	-0.0002670
1.5	0.9983252	-0.0002860
1.6	-	-0.0002942
1.7	-	-0.0003132
1.8	-	-0.0003214
1.9	-	-0.0003422
2.0	-	-0.0003596
2.1	-	0.0000021
2.2	-	0.0000025
2.3	-	0.0000021
2.4	-	0.0000020
2.5	-	0.0000024
2.6	-	0.0000026
2.7	-	0.0000027
2.8	-	0.0000027
2.9	-	0.0000026
3.0	-	0.0000027

Table A.1: Squared angular frequencies $\omega^2_{N,k}$ for $N = 1$, for all $k \leq N$. (T) denotes a translation mode. Both the $k = 0$ and $k = 1$ modes here have degeneracy one.

λ	$k=0$	$k=1$ (T)	$k=1$	$k=2$ (S)
0.1	0.0789918	-0.0007159	-	0.0512741
0.2	0.1483615	-0.0001025	-	0.0558772
0.3	0.2105808	-0.0000096	-	0.0539602
0.4	0.2677272	-0.0000009	-	0.0493481
0.5	0.3192852	-0.0008482	-	0.0417627
0.6	0.3687888	-0.0007926	-	0.0345898
0.7	0.4149896	-0.0007993	-	0.0264856
0.8	0.4583296	-0.0007870	0.7984443	0.0177572
0.9	0.4989830	-0.0007977	0.8883169	0.0084556
1.0	0.5378953	-0.0004056	0.9724756	-0.0006509
1.1	0.5738714	-0.0004022	-	-0.0107688
1.2	0.6077165	-0.0004147	-	-0.0212523
1.3	0.6395990	-0.0004264	-	-0.0320366
1.4	0.6696357	-0.0004419	-	-0.0430984
1.5	0.6979666	-0.0004441	-	-0.0543849
1.6	0.7239046	-0.0009180	-	-0.0666735
1.7	0.7490566	-0.0009378	-	-0.0784261
1.8	0.7727572	-0.0009572	-	-0.0903705
1.9	0.7951064	-0.0009595	-	-0.1024658
2.0	0.8161198	-0.0009784	-	-0.1147567
2.1	0.8359077	-0.0009812	-	-0.1271782
2.2	0.8544807	-0.0009980	-	-0.1397720
2.3	0.8719014	-0.0010202	-	-0.1525159
2.4	0.8882325	-0.0010342	-	-0.1653795
2.5	0.9034858	-0.0010601	-	-0.1783907
2.6	0.9177515	-0.0010528	-	-0.1914653
2.7	0.9309928	-0.0010622	-	-0.2046847
2.8	0.9432418	-0.0010810	-	-0.2180313
2.9	0.9545307	-0.0010935	-	-0.2314733
3.0	0.9648639	-0.0010994	-	-0.2450055

Table A.2: Squared angular frequencies $\omega^2_{N,k}$ for $N = 2$, for all $k \leq N$. (T) denotes a translation mode, and (S) denotes a splitting mode. The $k = 0, 1(\mathrm{T}), 2(\mathrm{S})$ all have degeneracy 2, the $k = 1$ mode has degeneracy 4.

λ	$k=0$	$k=1$ (T)	$k=1$	$k=2$ (S)	$k=3$ (S)
0.1	0.0679526	-0.0008217	-	0.0274337	0.0881145
0.2	0.1227128	-0.0002553	-	0.0300880	0.0965833
0.3	0.1697435	-0.0000502	-	0.0291660	0.0941163
0.4	0.2115522	-0.0000094	0.3933655	0.0266270	0.0865239
0.5	0.2495440	-0.0000003	0.4797256	0.0232239	0.0759417
0.6	0.2845064	0.0000001	0.5603710	0.0192495	0.0632930
0.7	0.3169691	0.0000001	0.6354855	0.0148617	0.0490985
0.8	0.3473093	-0.0000001	0.7053603	0.0101529	0.0336815
0.9	0.3758143	-0.0000002	0.7702370	0.0051846	0.0172621
1.0	0.4027085	0.0000001	0.8302565	-0.0000005	-0.0000003
1.1	0.4281722	0.0000000	0.8854024	-0.0053696	-0.0179846
1.2	0.4523529	0.0000000	0.9353421	-0.0108991	-0.0365986
1.3	0.4753740	-0.0000001	0.9786845	-0.0165696	-0.0557680
1.4	0.4973393	-0.0000001	-	-0.0223660	-0.0754331
1.5	0.5183373	0.0000000	-	-0.0282764	-0.0955450
1.6	0.5384442	0.0000001	-	-0.0342903	-0.1160612
1.7	0.5577263	0.0000002	-	-0.0403995	-0.1369475
1.8	0.5762415	-0.0000002	-	-0.0465968	-0.1581733
1.9	0.5940412	0.0000000	-	-0.0528759	-0.1797126
2.0	0.6111707	0.0000001	-	-0.0592317	-0.2015431
2.1	0.6276709	0.0000000	-	-0.0656591	-0.2236438
2.2	0.6435771	0.0000000	-	-0.0721550	-0.2459979
2.3	0.6589224	0.0000002	-	-0.0787149	-0.2685889
2.4	0.6737361	0.0000005	-	-0.0853360	-0.2914031
2.5	0.6880456	0.0000000	-	-0.0920161	-0.3144280
2.6	0.7018746	0.0000000	-	-0.0987518	-0.3376510
2.7	0.7152464	-0.0000003	-	-0.1055404	-0.3610619
2.8	0.7281795	0.0000005	-	-0.1123813	-0.3846526
2.9	0.7406946	0.0000000	-	-0.1192708	-0.4084119
3.0	0.7528083	-0.0000003	-	-0.1262084	-0.4323327

Table A.3: Angular frequencies $\omega^2_{N,k}$ for $N = 3$, for all $k \leq N$. (T) denotes a translation mode, and (S) denotes a splitting mode. The $k = 0, 1(\mathrm{T}), 2(\mathrm{S}), 3(\mathrm{S})$ mode all have degeneracy 2, and the $k = 1$ mode has degeneracy 4.

λ	$k=0$	$k=1$ (T)	$k=1$	$k=2$ (S)	$k=3$ (S)	$k=4$ (S)	$k=0$ (U)
0.1	0.0597018	-0.0004676	-	0.0185135	0.0593157	-	-
0.2	0.1038126	-0.0001816	0.1972500	0.0199480	0.0644325	0.1237461	-
0.3	0.1407828	-0.0000422	0.2820540	0.0192449	0.0627045	0.1205088	-
0.4	0.1731786	-0.0000056	0.3587430	0.0175188	0.0576237	0.1108280	-
0.5	0.1998225	-0.0016302	0.4250953	0.0129110	0.0471123	0.0922926	-
0.6	0.2260267	-0.0019468	0.4877784	0.0098159	0.0380529	0.0752346	-
0.7	0.2518380	-0.0012650	0.5476264	0.0078877	0.0300327	0.0591256	-
0.8	0.2756647	-0.0008206	0.6027155	0.0054311	0.0206986	0.0407040	-
0.9	0.2978723	-0.0005342	0.6536530	0.0025972	0.0103722	0.0205305	0.8956216
1.0	0.3187357	-0.0003498	0.7009225	-0.0005073	-0.0007217	-0.0010059	0.9882124
1.1	0.3384593	-0.0002311	0.7448956	-0.0038108	-0.0124268	-0.0236312	-
1.2	0.3571987	-0.0001536	0.7858521	-0.0072649	-0.0246350	-0.0471547	-
1.3	0.3750754	-0.0001034	0.8239921	-0.0108365	-0.0372662	-0.0714325	-
1.4	0.3921842	-0.0000701	0.8594451	-0.0145030	-0.0502635	-0.0963607	-
1.5	0.4084210	-0.0001633	0.8919953	-0.0184203	-0.0638229	-0.1221844	-
1.6	0.4242607	-0.0001184	0.9222248	-0.0221884	-0.0773665	-0.1480978	-
1.7	0.4395149	-0.0000861	0.9495784	-0.0260268	-0.0911871	-0.1744864	-
1.8	0.4542315	-0.0000634	0.9735658	-0.0299262	-0.1052569	-0.2012994	-
1.9	0.4684533	-0.0000463	0.9929939	-0.0338783	-0.1195550	-0.2284982	-
2.0	0.4822159	-0.0000345	-	-0.0378782	-0.1340618	-0.2560463	-
2.1	0.4955512	-0.0000263	-	-0.0419210	-0.1487625	-0.2839159	-
2.2	0.5083785	-0.0000894	-	-0.0461107	-0.1637933	-0.3122807	-
2.3	0.5209603	-0.0000702	-	-0.0502069	-0.1788142	-0.3406815	-
2.4	0.5331833	-0.0000555	-	-0.0543415	-0.1940006	-0.3693471	-
2.5	0.5450684	-0.0000438	-	-0.0585109	-0.2093423	-0.3982590	-
2.6	0.5566327	-0.0000343	-	-0.0627135	-0.2248316	-0.4274015	-
2.7	0.5678959	-0.0000275	-	-0.0669464	-0.2404580	-0.4567581	-
2.8	0.5788705	-0.0000224	-	-0.0712086	-0.2562169	-0.4863179	-
2.9	0.5895704	-0.0000180	-	-0.0754979	-0.2721016	-0.5160696	-
3.0	0.6000094	-0.0000148	-	-0.0798128	-0.2881045	-0.5460005	-

Table A.4: Angular frequencies $\omega^2_{N,k}$ for $N = 4$, for all $k \leq N$. (T) denotes a translation mode, (S) denotes a splitting mode, and (U) denotes the upper mode. All of the modes here have degeneracy one.

Bibliography

[1] A. A. Abrikosov. On the Magnetic Properties of Superconductors of the Second Group. *Soviet Physics JETP*, 5:1174–1182, 1957.

[2] C. Adam, K. Oles, T. Romanczukiewicz, and A. Wereszczynski. Spectral Walls in Soliton Collisions. *Physical Review Letters*, 122(24):241601, 2019.

[3] C. Adam, K. Oles, T. Romanczukiewicz, and A. Wereszczynski. Kink-Antikink Collisions in a Weakly Interacting ϕ^4 Model. *Physical Review E*, 102(6):062214, 2020.

[4] C. Adam, K. Oles, T. Romanczukiewicz, and A. Wereszczynski. Spectral Walls in Antikink-Kink Scattering in the ϕ^6 Model. *Physical Review D*, 106(10):105027, 2022.

[5] C. Adam, K. Oles, T. Romanczukiewicz, A. Wereszczynski, and W. Zakrzewski. Spectral Walls in Multifield Kink Dynamics. *Journal of High Energy Physics*, 2021(8):147, 2021.

[6] C. Adam, J. M. Queiruga, and A. Wereszczynski. BPS Soliton-Impurity Models and Supersymmetry. *Journal of High Energy Physics*, 2019(7):164, 2019.

[7] A. Alonso-Izquierdo, J. J. Blanco-Pillado, D. Miguelez-Caballero, S. Navarro-Obregon, and J. Queiruga. Excited Abelian-Higgs Vortices: Decay Rate and Radiation Emission. *Physical Review D*, 110(6):065009, 2024.

[8] A. Alonso-Izquierdo, W. G. Fuertes, N. S. Manton, and J. Mateos Guilarte. Spectral flow of vortex shape modes over the BPS 2-vortex moduli space. *JHEP*, 01:020, 2024.

[9] A. Alonso-Izquierdo, W. Garcia Fuertes, and J. Mateos Guilarte. A Note on BPS Vortex Bound States. *Physics Letters B*, 753:29–33, Feb 2016.

[10] A. Alonso-Izquierdo, W. Garcia Fuertes, and J. Mateos Guilarte. Dissecting Zero Modes and Bound States on BPS Vortices in Ginzburg-Landau Superconductors. *Journal of High Energy Physics*, 2016(5):074, May 2016.

[11] A. Alonso-Izquierdo, N. S. Manton, J. Mateos Guilarte, M. Rees, and A. Wereszczynski. Dynamics of excited BPS three-vortices. *Phys. Rev. D*, 111(10):105021, 2025.

[12] A. Alonso-Izquierdo, N. S. Manton, J. Mateos Guilarte, and A. Wereszczynski. Collective Coordinate Models for 2-Vortex Shape Mode Dynamics. *Physical Review D*, 110(4):045012, Aug 2024.

[13] A. Alonso-Izquierdo, J. Mateos Guilarte, M. Rees, and A. Wereszczynski. Spectral Wall in Collisions of Excited Abelian Higgs Vortices. *Physical Review D*, 110(6):065004, Sep 2024.

[14] A. Alonso-Izquierdo and D. Miguelez-Caballero. Dissecting normal modes of vibration on vortices in Ginzburg-Landau superconductors. *Phys. Rev. D*, 110(12):125026, 2024.

[15] A. Alonso-Izquierdo, J. Queiroga-Nunes, and L. M. Nieto. Scattering Between Wobbling Kinks. *Physical Review D*, 103(4):045003, Feb 2021.

[16] R. F. S. Andrade. The leapfrog method for solving differential equations. *Computational Physics Communications*, 155(2):96–104, 2003.

[17] J. Ashcroft. *Topological Solitons and Their Dynamics*. University of Kent, 2017. Ph.D. thesis.

[18] J. Ashcroft and S. Krusch. Vortices and Magnetic Impurities. *Physical Review D*, 101(2):025004, Jan 2020.

[19] P. Auclair, J. J. Blanco-Pillado, D. G. Figueroa, A. C. Jenkins, M. Lewicki, et al. Probing the Gravitational Wave Background from Cosmic Strings with LISA. *Journal of Cosmology and Astroparticle Physics*, 2020(04):034, 2020.

[20] P. Auclair, K. Leyde, and D. A. Steer. A Window for Cosmic Strings. *Journal of Cosmology and Astroparticle Physics*, 2023(04):005, 2023.

[21] M. Bachmaier, G. Dvali, and J. S. Valbuena-Bermudez. Radiation Emission During the Erasure of Magnetic Monopoles. *Physical Review D*, 108(10):103501, 2023.

[22] M. Bachmaier, G. Dvali, J. S. Valbuena-Bermudez, and M. Zantedeschi. Confinement Slingshot and Gravitational Waves. *Physical Review D*, 110(1):016001, 2024.

[23] J. Baeza-Ballesteros, E. J. Copeland, D. G. Figueroa, and J. Lizarraga. Particle and gravitational wave emission by local string loops: Lattice calculation. *Phys. Rev. D*, 112:043540, Aug 2025.

[24] A. Bogdanov and D. A. Yablonskii. Thermodynamically stable vortices in magnetically ordered crystals. The mixed state of magnets. *Sov. Phys. JETP*, 68:101, 1994.

[25] E. B. Bogomol'nyi. The Stability of Classical Solutions. *Soviet Journal of Nuclear Physics*, 24(4):449–454, 1976.

[26] D. K. Campbell, J. F. Schonfeld, and C. A. Wingate. Resonance Structure in Kink-Antikink Interactions in ϕ^4 Theory. *Physica D*, 9(1-2):1–32, 1983.

[27] T.-P. Cheng and L.-F. Li. *Gauge Theory of Elementary Particle Physics*. Oxford University Press, Oxford, UK, 1984.

[28] A. Cockburn, S. Krusch, and A. A. Muhamed. Dynamics of Vortices with Magnetic Impurities. *Journal of Mathematical Physics*, 58(6):063509, Jun 2017.

[29] G. H. Derrick. Comments on Nonlinear Wave Equations as Models for Elementary Particles. *Journal of Mathematical Physics*, 5(9):1252–1254, 1964.

[30] A. T. Dorsey. Vortex Motion and the Hall Effect in Type-II Superconductors: A Time-Dependent Ginzburg-Landau Theory Approach. *Physical Review B*, 46(13):8376–8392, 1992.

[31] M. Elliot-Ripley and T. Winyard. Baby Skyrmions in AdS. *J. High Energy Phys.*, 2015:9, 2015.

[32] A. Fert, V. Cros, and J. Sampaio. Skyrmions on the track. *Nat. Nanotechnol.*, 8:152–156, 2013.

[33] P. Forgacs and M. S. Volkov. Destabilizing Tachyonic Vacua at or Above the BF Bound. *Physical Review Letters*, 92(15):151802, 2004.

[34] A. García Martín-Caro, J. Queiruga, and A. Wereszczynski. Feshbach resonances and dynamics of BPS solitons. *Phys. Rev. D*, 111(9):096002, 2025.

[35] V. L. Ginzburg and L. D. Landau. On the Theory of Superconductivity. *Zhurnal Eksperimental'noi i Teoreticheskoi Fiziki*, 20:1064–1082, 1950.

[36] M. Goodband and M. Hindmarsh. Bound States and Instabilities of Vortices. *Physical Review D*, 52(8):4621–4632, Oct 1995.

[37] J. Hesthaven and E. S. Mølgaard. A Sixth-Order Weighted Leapfrog Scheme for Wave Propagation. *Journal of Computational Physics*, 224(1):311–326, 2007.

[38] P. W. Higgs. Spontaneous Symmetry Breakdown Without Massless Bosons. *Physical Review*, 145(4):1156–1163, 1966.

[39] M. Hindmarsh, J. Lizarraga, J. Urrestilla, D. Daverio, and M. Kunz. Type I Abelian Higgs Strings: Evolution and Cosmic Microwave Background Constraints. *Physical Review D*, 99(8):083522, 2019.

[40] P. Jennings and T. Winyard. Broken planar Skyrmions — statics and dynamics. *J. High Energy Phys.*, 2014:122, 2014.

[41] S. Jeon, Y. Kim, and C. Kim. Existence and Uniqueness of BPS Vacuum and Multi-Vortices in Inhomogeneous Abelian Higgs Model, 2024. arXiv:2409.14054 [hep-th].

[42] S. Jeon, Y. Kim, and H. Song. Effect of Impurity on Inhomogeneous Vacuum and Interacting Vortices, 2025. arXiv:2501.02500 [math.AP].

[43] F. Jonietz, S. Mühlbauer, C. Pfleiderer, A. Neubauer, W. Münzer, A. Bauer, T. Adams, R. Georgii, P. Böni, R. A. Duine, K. Everschor, M. Garst, and A. Rosch. Spin Transfer Torques in MnSi at Ultralow Current Densities. *Science*, 330:1648–1651, 2010.

[44] J. Jäykkä and M. Speight. Easy plane baby Skyrmions. *Phys. Rev. D*, 82:125030, 2010.

[45] J. Jäykkä, M. Speight, and P. Sutcliffe. Broken baby Skyrmions. *Proc. R. Soc. A*, 468:1085–1104, 2012.

[46] Y. Kim, S. Jeon, O. K. Kwon, H. Song, and C. Kim. Vacuum and Vortices in Inhomogeneous Abelian Higgs Model, 2024. arXiv:2409.12451 [hep-th].

[47] S. Krusch, M. Rees, and T. Winyard. Scattering of Vortices with Excited Normal Modes. *Physical Review D*, 110(5):056050, Sep 2024.

[48] S. Krusch, M. Rees, and T. Winyard. Type I/II Vortex Dynamics With Excited Normal Modes, 2025. In preparation.

[49] S. Krusch and P. Sutcliffe. Schrödinger-Chern-Simons vortex dynamics. *Nonlinearity*, 19:1515–1534, 2006.

[50] J. Kume and M. Hindmarsh. Multi-Messenger Constraints on Abelian-Higgs Cosmic String Networks. *Journal of Cosmology and Astroparticle Physics*, 2023(04):045, 2023.

[51] J. Kume and M. Hindmarsh. Revised Bounds on Local Cosmic Strings from NANOGrav Observations. *Journal of Cosmology and Astroparticle Physics*, 2024(12):001, Dec 2024.

[52] P. Leask and S. B. Gudnason. Baby Skyrmion crystals. *Phys. Rev. D*, 105:025010, 2022.

[53] N. Manton and P. Sutcliffe. *Topological Solitons*. Cambridge University Press, 2004.

[54] N. S. Manton. A Remark on the Scattering of BPS Monopoles. *Physics Letters B*, 110(1):54–56, 1982.

[55] N. S. Manton. First Order Vortex Dynamics. *Annals of Physics*, 256(1):114–131, 1997.

[56] N. S. Manton, K. Oles, T. Romanczukiewicz, and A. Wereszczynski. Collective Coordinate Model of Kink-Antikink Collisions in ϕ^4 Theory. *Physical Review Letters*, 127(7):071601, Aug 2021.

[57] N. S. Manton and B. M. A. G. Piette. Understanding Skyrmions Using Rational Maps. In *European Congress of Mathematics*, volume 201 of *Progress in Mathematics*, pages 469–479. Birkhäuser, 2001.

[58] R. A. Matzner. Interaction of U(1) Cosmic Strings: Numerical Intercommutation. *Computers in Physics*, 2(5):51–64, Sep 1988.

[59] K. J. M. Moriarty, E. Myers, and C. Rebbi. Dynamical Interactions of Cosmic Strings and Flux Vortices in Superconductors. *Physics Letters B*, 207(4):411–418, 1988.

[60] E. Myers, C. Rebbi, and R. Strilka. Study of the Interaction and Scattering of Vortices in the Abelian Higgs (or Ginzburg-Landau) Model. *Physical Review D*, 45(4):1355–1365, 1992.

[61] B. M. A. G. Piette, B. J. Schroers, and W. J. Zakrzewski. Dynamics of Baby skyrmions. *Nuclear Physics B*, 439(1–2):205–235, 1995.

[62] P. J. Ruback. Vortex String Motion in the Abelian Higgs Model. *Nuclear Physics B*, 296(3):669–683, 1988.

[63] T. M. Samols. Vortex Scattering. *Communications in Mathematical Physics*, 145(1):149–179, 1992.

[64] E. P. S. Shellard and P. J. Ruback. Vortex Scattering in Two Dimensions. *Physics Letters B*, 209(2-3):262–270, 1988.

[65] T. H. R. Skyrme. A Non-Linear Field Theory. *Proceedings of the Royal Society of London. Series A. Mathematical and Physical Sciences*, 260(1300):127–138, 1961.

[66] J. M. Speight. Static Intervortex Forces. *Physical Review D*, 55(6):3830–3835, 1997.

[67] J. M. Speight and T. Winyard. Short-range intervortex forces. *Physical Review D*, 112(5):055024, Sep 2025.

[68] M. Speight and T. Winyard. Skyrmions and spin waves in frustrated ferromagnets at low applied magnetic field. *Phys. Rev. B*, 101:134420, Apr 2020.

[69] M. Speight, T. Winyard, and E. Babaev. Chiral p-wave superconductors have complex coherence and magnetic field penetration lengths. *Phys. Rev. B*, 100:174514, Nov 2019.

[70] M. Speight, T. Winyard, and E. Babaev. Symmetries, Length Scales, Magnetic Response and Skyrmion Chains in Nematic Superconductors. *Physical Review B*, 107, May 2023.

[71] M. Speight, T. Winyard, A. Wormald, and E. Babaev. Magnetic field behavior in $s+is$ and $s+id$ superconductors: Twisting of applied and spontaneous fields. *Phys. Rev. B*, 104:174515, Nov 2021.

[72] T. Sugiyama. Kink-Antikink Collisions in the Two-Dimensional ϕ^4 Model. *Progress of Theoretical Physics*, 61(5):1550–1550, 1979.

[73] C. H. Taubes. Arbitrary N-Vortex Solutions to the First Order Landau-Ginzburg Equations. *Communications in Mathematical Physics*, 72(3):277–292, 1980.

[74] D. Tong and K. Wong. Vortices and Impurities. *Journal of High Energy Physics*, 2014(1):090, 2014.

[75] T. Vachaspati and A. Vilenkin. Formation and evolution of cosmic strings. *Physical Review D*, 30(10):2036–2045, 1984.

[76] G. J. Verbiest and A. Achucarro. High Speed Collision and Reconnection of Abelian Higgs Strings in the Deep Type-II Regime. *Physical Review D*, 84(10):105036, 2011.

[77] A. Vilenkin. Cosmic Strings and Domain Walls. *Physics Reports*, 121(5):263–315, 1985.

[78] T. Weidig. The Baby Skyrme models and their multi-skyrmions. *Nonlinearity*, 12(6):1489–1503, 1999.

[79] T. Winyard. *The Skyrme Model: Curved Space, Symmetries and Mass*. PhD thesis, Durham University, 2016.

[80] T. Winyard and M. Speight. Vortex lattices and critical fields in anisotropic superconductors. *Physical Review B*, 111(14):144509, Apr 2025.

[81] H. Yoshida. Construction of higher order symplectic integrators. *Physics Letters A*, 150(5–7):262–268, 1990.

[82] X. Z. Yu, Y. Onose, N. Kanazawa, J. H. Park, J. H. Han, Y. Matsui, N. Nagaosa, and Y. Tokura. Real-space observation of a two-dimensional skyrmion crystal. *Nature*, 465:901–904, 2010.